



Development and Applications of X-ray Birefringence Imaging

by

RHIAN PATTERSON

**Thesis Submitted for
DOCTOR OF PHILOSOPHY**

**SCHOOL OF CHEMISTRY
CARDIFF UNIVERSITY**

July 2020

Acknowledgements

I would like to thank the following people, without whom I would not have been able to complete this PhD. My supervisors, Professor Kenneth Harris and Dr Steve Collins whose insight, knowledge and help guided me through this research. The opportunities they have provided have led to an incredible and rewarding PhD experience. I would like to acknowledge Cardiff University and the EPSRC for their funding.

I would also like to thank Diamond Light Source for their funding and providing use of the facilities at the synchrotron to perform research. Specifically I would like to thank the the beamline staff on B16 at Diamond Light Source for their knowledge and technical expertise; Dr Igor Dolbnya, Dr Ian Pape, Dr Oliver Fox and Andrew Malandain.

In addition to this I am thankful to Dr Colan Hughes for his help with my research specifically the determination of crystal structures from powder X-ray diffraction data and the interpretation of solid-state NMR data. I would like to acknowledge Dr Benson Kariuki for his help in interpretation of single crystal X-ray diffraction data. Furthermore, I am thankful to my other research group members Dr Yating Zhou, Dr Okba Al Rahal, Chris Smalley and Dr Andrew Williams for providing an enjoyable and exciting work environment.

Finally I would like to thank my family and friends for their support and encouragement during the course of my PhD. My parents for their patience and interest in my research. Tom, Alys and Jack for putting up with me during these last couple of months.

Abstract

The new technique of X-ray Birefringence Imaging (XBI) is the focus of this thesis. The research reported includes an expansion of previous theoretical work, explorations of new materials and the extension of the XBI technique to study new absorption edges. The final chapter covers another research topic, specifically crystal structure determination from powder X-ray diffraction (PXRD) data.

Chapter 1 provides an introduction to the interaction of electromagnetic waves with matter and the properties of matter that cause birefringence. Chapter 2 gives a detailed description of the different experimental techniques used in this thesis, focusing first on the XBI experimental setup and giving an overview of previous XBI studies. This chapter also describes the methodology for crystal structure determination from PXRD experimental data. Chapter 3 gives an in-depth discussion of the theoretical basis of XBI, showing how XBI behavior can be predicted theoretically for materials of known structure. A model system is discussed to demonstrate the methodology.

Chapter 4 includes XBI studies and XBI theoretical calculations of copper acetylacetonate and hexabromobenzene which are both examples of bending crystals, i.e., they are mechanically deformable under certain conditions. Animated videos of the XBI images recorded during bending for these materials are included in the digital data. Chapter 5 focuses on XBI studies of 1,2,4,5-tetrabromobenzene (TBB), focusing on XBI studies of a phase transition in this material, and the differences in XBI results for single crystals and twinned crystals of TBB. Animated videos of the XBI images recorded during the phase transition for the TBB crystals are included in the digital data.

Chapter 6 explores the expansion of the XBI technique to new X-ray absorption edges. Prior to the present work, all XBI studies have been carried out at the bromine K-edge. Included in this chapter are X-ray dichroism measurements at the sulphur, chromium, iron and copper K-edges. The most notable results are the XBI studies of CuBr_2 , carried out at both the bromine and copper K-edges. Chapter 7 discusses a research project involving structure determination from PXRD data, focusing on structure determination of a previously unidentified intermediate phase in the solid-state reaction from ammonium cyanate to urea.

Contents

1	Introduction	1
1.1	<i>Birefringence</i>	<i>1</i>
1.2	<i>Polarized light</i>	<i>8</i>
1.2.1	<i>Polarizing light microscopy</i>	<i>11</i>
1.3	<i>Interactions of materials with X-rays</i>	<i>15</i>
1.3.1	<i>X-ray Absorption</i>	<i>15</i>
1.3.2	<i>X-ray Diffraction.....</i>	<i>18</i>
1.3.3	<i>X-ray Dichroism.....</i>	<i>20</i>
2	Experimental Methods.....	22
2.1	<i>X-ray Birefringence Imaging.....</i>	<i>22</i>
2.1.1	<i>Experimental Setup</i>	<i>23</i>
2.1.2	<i>Previous work</i>	<i>39</i>
2.2	<i>Diffraction</i>	<i>47</i>
2.2.1	<i>Single Crystal X-ray Diffraction.....</i>	<i>47</i>
2.2.2	<i>Powder X-ray Diffraction</i>	<i>48</i>
3	Theoretical XBI Behaviour	52
3.1	<i>Interaction of incident X-rays with the Sample</i>	<i>53</i>
3.2	<i>Polarization State of Incident Beam.....</i>	<i>56</i>
3.3	<i>Interaction of X-ray beam with Polarization Analyzer</i>	<i>56</i>
3.4	<i>XBI calculation.....</i>	<i>57</i>

3.5	<i>Theoretical XBI Calculations for 1-bromoadamantane/thiourea</i>	57
4	XBI Studies of Mechanically Deformable Crystals	64
4.1	<i>Introduction</i>	64
4.2	<i>Copper (II) acetyl acetonate</i>	67
4.2.1	Results and Discussion.....	68
4.2.2	Theoretical XBI intensity of a single crystal of CuAcAc	78
4.3	<i>Hexabromobenzene</i>	89
4.3.1	Results and Discussion.....	91
4.4	<i>Conclusions</i>	101
5	XBI Studies of 1,2,4,5-Tetrabromobenzene	103
5.1	<i>Introduction</i>	103
5.2	<i>Results and Discussion</i>	107
5.2.1	XBI Studies of a Single crystal of TBB	109
5.2.2	XBI Studies of Twinned crystals of TBB	131
5.2.3	XBI Studies of ‘Hourglass’ TBB crystals.....	138
5.3	<i>Conclusions</i>	142
6	Extending the Application of the XBI technique to Elements Other than Bromine	144
6.1	<i>Introduction</i>	144
6.2	<i>Studies at the Sulphur K-edge</i>	150
6.3	<i>Studies at the Chromium K-edge</i>	155

6.4	<i>Studies at the Iron K-edge</i>	160
6.4.1	Ferrocene/thiourea.....	160
6.4.2	(η^4 -1,3-cyclohexadiene)Fe(CO) ₃ /thiourea and (η^4 -trimethylene methane)Fe(CO) ₃ /thiourea	165
6.5	<i>XBI Studies of Copper Dibromide</i>	170
6.6	<i>Conclusions</i>	180
7	PXRD studies of the solid-state transformation of Ammonium Cyanate to Urea.....	182
7.1	<i>Introduction</i>	182
7.2	<i>Experimental</i>	186
7.2.1	Powder X-ray diffraction	186
7.2.2	Solid-state NMR	187
7.3	<i>Results and Discussion</i>	187
7.3.1	Structure Determination.....	187
7.3.2	Proposed Mechanism for the Transformation from AC to Urea.....	197
7.3.3	Kinetics for the Transformation from AC to Urea.....	205
7.4	<i>Conclusions</i>	212
8	Conclusion.....	214
9	References	218
10	Appendices.....	232
10.1	<i>Appendix I</i>	232

1 Introduction

1.1 Birefringence

Birefringence finds its basis in the laws of electromagnetism first proposed by James Clerk Maxwell in 1813, where light is described as being composed of both electric (E) and magnetic (H) wave components. The electric and magnetic components vibrate in a sinusoidal manner perpendicular to each other (Figure 1.1). Light is a transverse wave, so there is therefore no component of the electric and magnetic fields in the direction of propagation of the light.

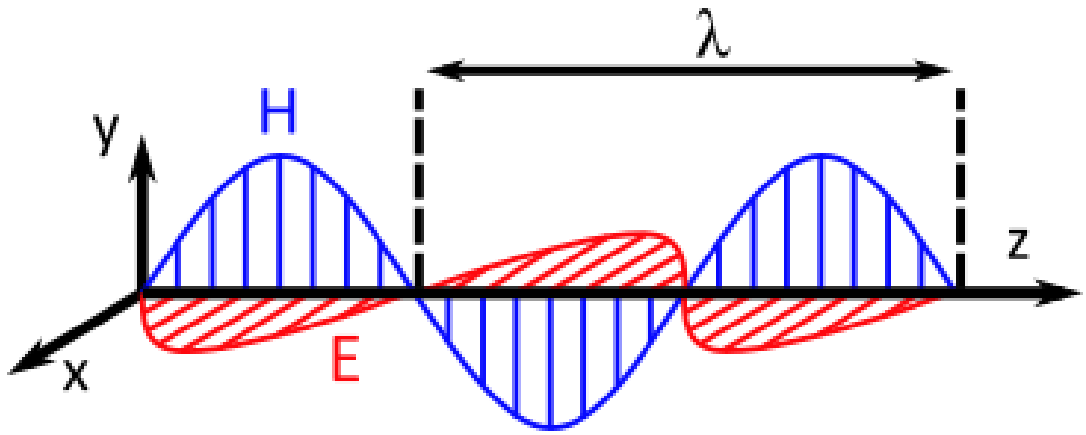


Figure 1.1 Electromagnetic wave propagating along z , where the magnetic field (blue) is vertical (aligned along the y -axis), the electric field vector (red) is horizontal (aligned along the x -axis). The axis system used here corresponds to the laboratory axis system used in XBI experiments, discussed in Chapter 2.

The phase velocity of light propagating through a material is affected by the interaction of the wave components with localized electromagnetic fields, determined by the relative electric permittivity/dielectric constant (ϵ) of the material. The velocity of light propagating through the material (v) can be related to the dielectric constant (ϵ) using:

$$v = \frac{c}{\sqrt{\epsilon \times m}} \quad (1.1)$$

where c is the speed of light in a vacuum and m is the relative magnetic permeability. The magnetic permeability is typically unity, and c/v is usually referred to as the refractive index (n) of a material. Therefore, the equation can be condensed to:

$$\varepsilon = n^2 \quad (1.2)$$

The refractive index naturally changes depending on the material as the localized electric fields in different materials are dissimilar, leading to the direction of the light wave changing when passing from one medium into another. Snell's law (Equation 1.3) relates the refractive indices of the two media to the angles of incidence (θ_1) and refraction (θ_2) as shown in Figure 1.2 (a).

$$\frac{\sin \theta_1}{\sin \theta_2} = \frac{n_2}{n_1} \quad (1.3)$$

We see Snell's law in practice whenever we view something submerged in water, with the object appearing to be displaced when submerged (Figure 1.2 (b)). In this case, light passes from air ($n = 1$) to water ($n = 1.33$) as there is an increase in refractive index the light will bend towards the normal and the pencil appears broken at the boundary between water and air.

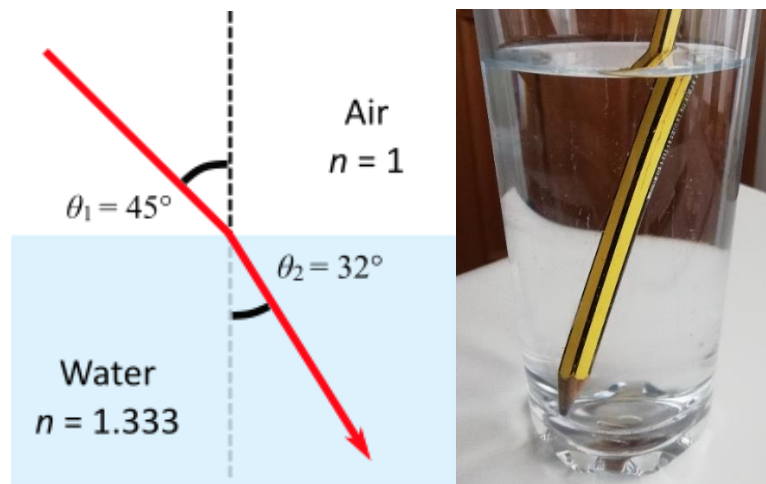


Figure 1.2 (a) Illustration of Snell's law with light at an incidence angle of 45° passing into water. The light ray bends towards the normal and using Snell's law the angle of refraction is 32° . (b) A pencil in water demonstrates Snell's law, with the pencil appearing broken at the boundary between water and air.

Optically isotropic materials such as crystals with a cubic crystal structure that have equivalent crystal axes, or water which has no long-range ordering, interact with light independent of orientation. Crystal structures that are not cubic are optically anisotropic, and local electromagnetic fields in different directions in the crystal are therefore inequivalent. An anisotropic crystal will thus exhibit different electrical properties and interact with light differently depending on the propagating direction of the incoming ray relative to the crystal axes.

Thus, the refractive index varies with orientation in anisotropic crystals and this property of the refractive index is responsible for the double refraction seen for birefringent crystals; an image viewed through a birefringent crystal will be doubled in certain orientations of the crystal (Figure 1.3). Iceland spar (a transparent crystal of calcite) is well known for its birefringent properties. These properties have in fact led to speculation that Iceland Spar's birefringence was used by Vikings to determine the position of the sun for navigation.^{1,2}

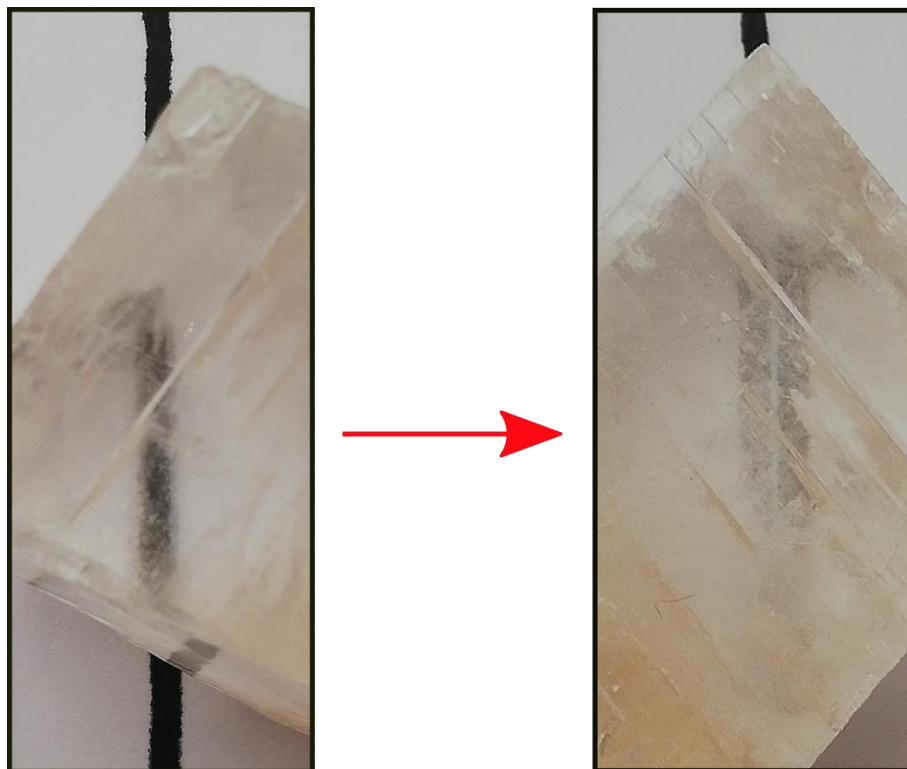


Figure 1.3 Left; calcite crystal oriented so no double refraction is observed. Right; calcite crystal has been rotated so the single black line is doubled.

For birefringent crystals, if light enters the crystal along “the optic axis”, the behaviour of the light is the same as for an isotropic crystal. Light entering in any other direction will be refracted into separate rays (ordinary and extraordinary) polarized with the electric vector vibration directions perpendicular to each other and travelling at different velocities. The ordinary ray (n_o) obeys Snell’s law, while the extraordinary ray (n_e) has a different refractive index and does not obey Snell’s law (Figure 1.4). The difference between these two refractive indices (Δn) is known as ‘birefringence’. From this, it follows that birefringence can be positive ($n_e > n_o$) or negative ($n_e < n_o$) depending on the magnitude of the respective refractive indices n_e and n_o .

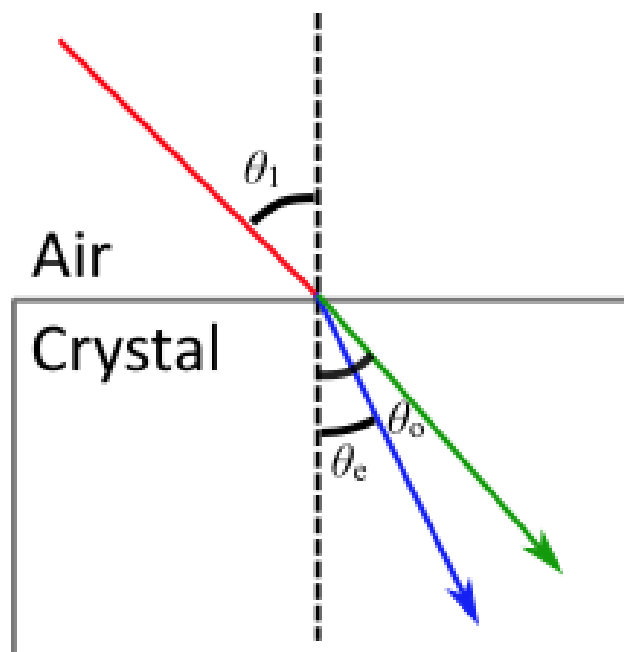


Figure 1.4 Unpolarized light (red) interacts with a birefringent crystal and is refracted into two polarized light rays: the ordinary ray (green) which obeys Snell’s law and is refracted by an angle θ_o , and the extraordinary ray (blue) refracted by angle θ_e .

As mentioned above, crystals in the cubic crystal system have isotropic properties. Other crystal structures are assigned to one of six crystal systems: triclinic, monoclinic, orthorhombic, tetragonal, trigonal and hexagonal. For all of these crystal systems, the crystal structures are anisotropic and thus may exhibit birefringence (Figure 1.5). The birefringent crystals systems can be further separated into uniaxial or biaxial.

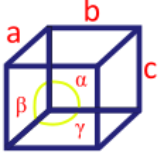




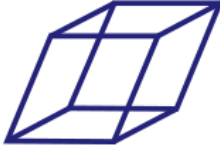

<p>Isotropic</p>	<p>Cubic $a = b = c$ $\alpha = \beta = \gamma = 90^\circ$</p> 		
<p>Uniaxial</p>	 <p>Tetragonal $a = b \neq c$ $\alpha = \beta = \gamma = 90^\circ$</p>	 <p>Rhombohedral $a = b = c$ $\alpha = \beta = \gamma \neq 90^\circ$</p>	 <p>Hexagonal $a = b \neq c$ $\alpha = \beta = 90^\circ, \gamma = 120^\circ$</p>
<p>Biaxial</p>	 <p>Orthorhombic $a \neq b \neq c$ $\alpha = \beta = \gamma = 90^\circ$</p>	 <p>Triclinic $a \neq b \neq c$ $\alpha \neq \beta \neq \gamma \neq 90^\circ$</p>	 <p>Monoclinic $a \neq b \neq c$ $\alpha = \gamma = 90^\circ, \beta \neq 90^\circ$</p>

Figure 1.5 The seven crystal systems are shown with their characteristic unit cell information and their assignment as isotropic, uniaxial and biaxial.

The classification of the crystal systems can be better understood using the refractive index ellipsoid, whereby the refractive indices in different directions are visualized using an ellipsoid (Figure 1.6). The refractive index ellipsoid is defined by assigning refractive indices to Cartesian axes, with the shape of the ellipsoid dependent on the refractive indices of the material.

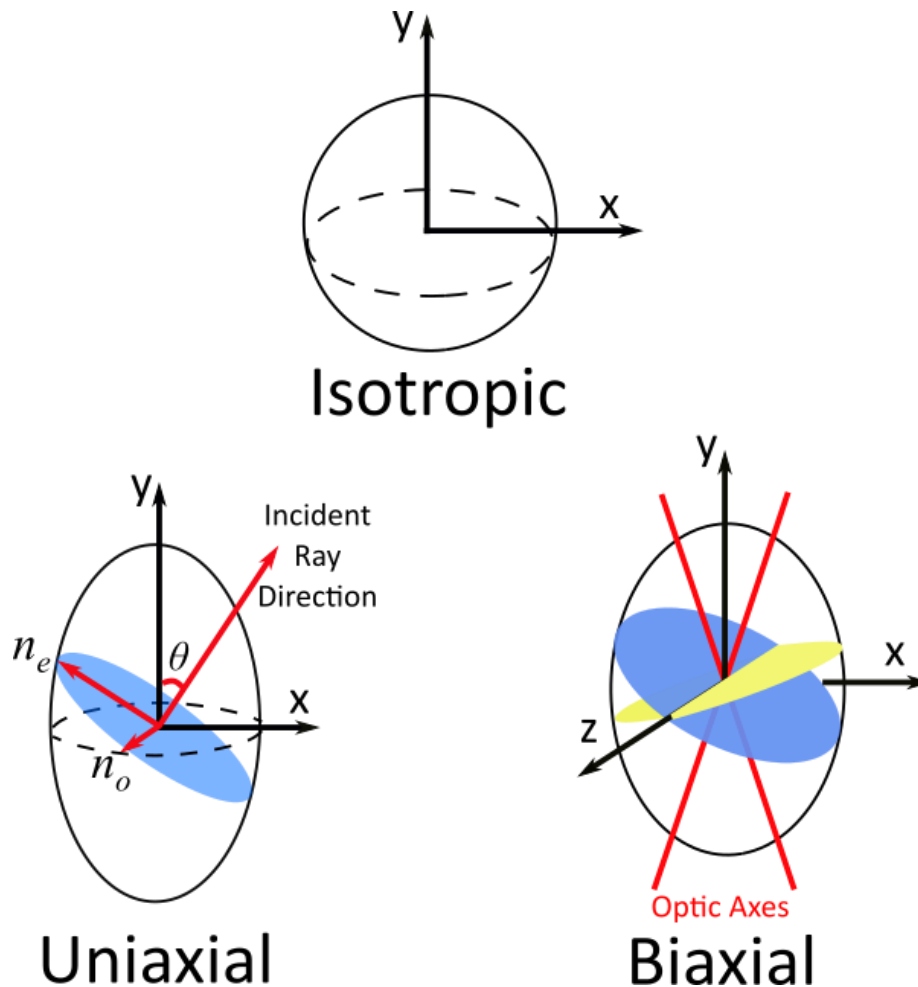


Figure 1.6 Refractive indices for isotropic, uniaxial and biaxial crystals. For the uniaxial crystal the y-axis corresponds to the optic axis and the blue ellipse is the plane perpendicular to the incident ray (red). The values for the refractive indices of the extraordinary (n_e) and ordinary ray (n_o) can be determined from equatorial and axial radii of the perpendicular plane. In the biaxial crystal the blue and yellow ellipses correspond to planes perpendicular to the two optic axes (red).

In an isotropic material, the refractive indices associated with each Cartesian axis are equal, and the refractive index ellipsoid is a sphere. Uniaxial materials have two equal refractive indices, but the third refractive index is different, along which the single optic axis lies. The y-axis is the optic axis for the uniaxial material shown in Figure 1.6. Along the direction of the optic axis, the material behaves as an isotropic crystal (all directions perpendicular to the optic axis are optically equivalent), and this rotation about the optic axis does not change the interaction of the light ray with the material.

The refractive index ellipsoid is crucial as it can be used to find the refractive indices associated with different directions of propagation of the incident light. Once the orientation of the refractive index ellipsoid relative to the incident light propagation direction is known, a plane is drawn perpendicular to the incident ray (uniaxial, Figure 1.6). The length of the two semi-axes of this planar ellipse gives the values of the refractive indices.

In biaxial materials, the refractive indices along each of the Cartesian axes are different. Thus, no axis exists for which rotation around the axis does not change the optical properties. However, there are two axes (known as binormals) where propagating light will not exhibit birefringence. These axes do not necessarily lie along any of the Cartesian axes and denote the angle where the different refractive indices are equal. Note that for monoclinic, one optic axis must lie along the b -axis (i.e. the unique axis), but the other optic axis can be anywhere in the ac -plane, i.e., not necessarily parallel to a or c axes.

Although this discussion has focused mainly on the birefringence of crystal systems, the phenomena of birefringence arises in many non-crystalline materials as long as some anisotropy is present. Birefringent materials can be separated into three different categories;

1. Intrinsic: the crystal systems discussed above fall into this category, as their anisotropy is intrinsic to their crystal systems.
2. Structural: materials with anisotropic formations which include many biological and synthetic materials such as cartilage,³ hair,⁴ and collagen.⁵
3. Induced: birefringence can be induced into materials through stress, strain and/or flow. Materials which exhibit this birefringence are not naturally anisotropic, but birefringence arises from external forces acting on the material to deform the structure. Glass or plastic polymers that have been stretched are common examples.⁶ Materials may also be aligned during the flow of a fluid⁷ (this typically requires molecules with anisotropic shapes such as rods or plates) as well as through application of an electric (Kerr effect) or magnetic field.⁸

Birefringence is a phenomenon caused by the anisotropy of a physical property. It should be noted that anisotropy does not necessarily equal birefringence, i.e., in cases for which the refractive indices are “accidentally” similar. However, of the materials which do exhibit birefringence, there is much of interest to study.

1.2 Polarized light

The light produced from the sun and, in fact, most natural and unnatural light sources are unpolarized. The light is described in this way based on the different characteristics of all the individual waves emitted by the light source (wave vector, frequencies, phases and polarization states). For this work, the most interesting property is the polarization state, as well as the energy (and monochromaticity) of the radiation. It is conventional to describe the polarization direction of light using the electric field vector rather than the magnetic field (Figure 1.1).

In unpolarized light, the electric field vectors are distributed equally in all planes parallel to the direction of propagation. Linearly polarized light has the electric field vector of all photons existing in one plane, and can be produced in several ways including birefringence, reflection and diffraction. To obtain linearly-polarized light from reflection, a specific incidence angle known as Brewster’s angle (or critical angle) is required:

$$n = \frac{\sin(\theta_i)}{\sin(\theta_r)} = \frac{\sin(\theta_i)}{\sin(\theta_{90-i})} = \tan(\theta_i) \quad (1.4)$$

where n is the refractive index of the reflecting medium, θ_i and θ_r stand for the angles of incidence and refraction, respectively. The incident light is both reflected and refracted, with the angle between these two rays equal to 90° . The refracted ray is only partially polarized, but the reflected ray is linearly polarized parallel to the reflecting surface (Figure 1.7).

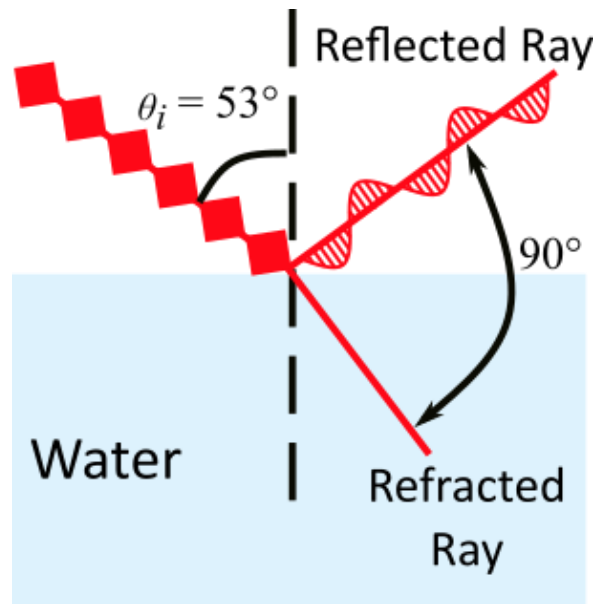


Figure 1.7 Illustration of Brewster's angle, with incoming unpolarized light undergoing reflection and refraction when incident on water ($n = 1.333$, $\theta_i = 53^\circ$).

As seen in Figure 1.7, light reflected off the water at the critical angle ($\theta_i = 53^\circ$) is polarized horizontal to the surface and is observed as glare. Glare occurs because the reflection comes from a horizontal surface; the light has the majority of its electric field vectors vibrating parallel to the water surface. To minimize glare, sunglasses incorporate polarizing filters into their lenses. Polarizing filters work by selectively transmitting light that is polarized parallel to the polarization direction of the filter (Figure 1.8).

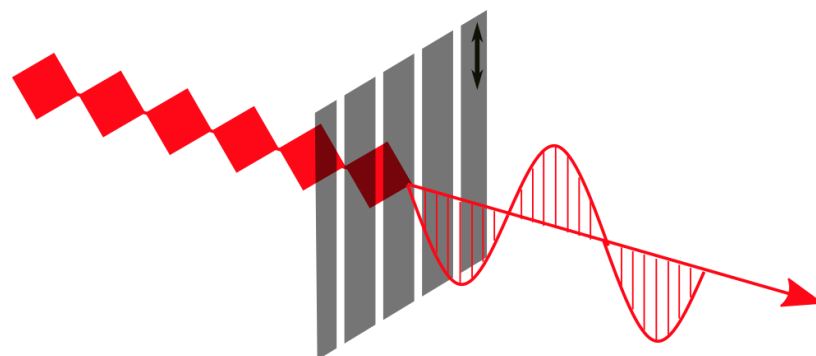


Figure 1.8 Unpolarized light transmitted through a polarizing filter, which transmits light polarized in the vertical direction; components of the incident light with electric vector vibrations in any non-vertical direction are blocked.

Polarizing filters have existed in various forms since the nineteenth century, first using a stack of glass plates as the polarizing filter,⁹ then a crystal of calcite (due to its birefringence) cut and joined to form a prism (Nicol's prism).¹⁰ Modern polarizing filters are typically made of polymer films embedded with crystals of iodoquinine sulfate all oriented in the same direction, developed by Dr Edwin H. Land, known today as Polaroid.¹¹

The discussion so far has focused on linearly-polarized light, but there are other forms of polarization, which are also relevant to this work: elliptical and circular. For elliptically polarized light, the electric field vector is described in terms of an ellipse perpendicular to the propagation direction, thus giving this form of polarization its name (Figure 1.9). Elliptical polarization can be described as either right-handed (clockwise) or left-handed (anticlockwise), depending on the rotation of the electric vector around the propagation direction. The specific case of elliptical polarization in which the polarization ellipse has equal major and minor axes is described as circular polarization. Similarly, to elliptical polarization, circular polarization can also be described as either right-handed or left-handed.

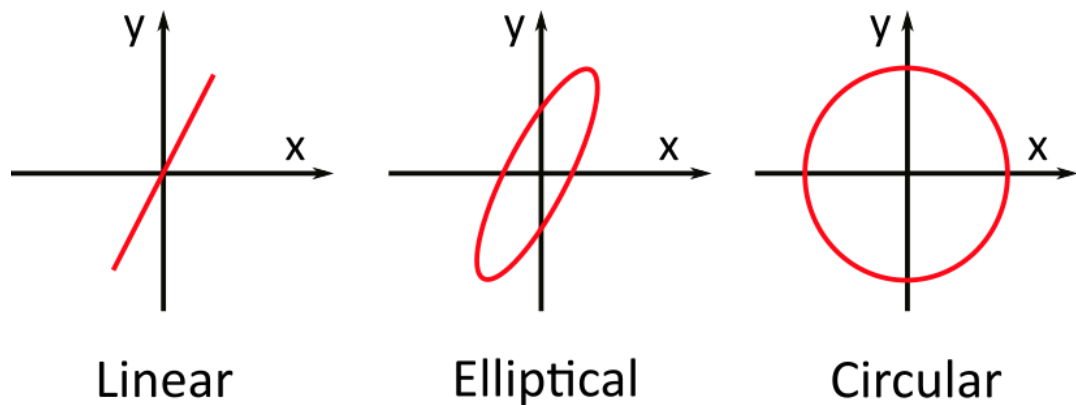


Figure 1.9 Linear, elliptical and circular polarization viewed along the propagating direction of the light ray (*z*-axis).

The state of polarization of light can be described using Stokes parameters (S_0 , S_1 , S_2 , S_3). The Stokes parameters may be described in terms of four polarizing filters.

1. S_0 : Filters out half of the incident light, indiscriminate to polarization
2. S_1 : Selects light polarized in the horizontal plane
3. S_2 : Selects light polarized at 45° from the horizontal plane
4. S_3 : Selects circularly polarized light with right-handed helices

By convention, the intensity that passes through S_0 is normalized to equal one. The Stokes parameters are typically shown as a four-component vector (S). The table below shows the vectors for unpolarized light, horizontal linear polarization and circular right-handed polarization.

Unpolarized	Horizontal Polarization	Circular Polarization (RH)
$I_0 \begin{pmatrix} 1 \\ 0 \\ 0 \\ 0 \end{pmatrix}$	$I_0 \begin{pmatrix} 1 \\ 1 \\ 0 \\ 0 \end{pmatrix}$	$I_0 \begin{pmatrix} 1 \\ 0 \\ 0 \\ 1 \end{pmatrix}$

Table 1.1 The Stokes parameters describing the polarization state for unpolarized, horizontally polarized and circularly polarized (right-handed) light.

Thus, if two waves have the same Stokes parameters, their polarization states are identical. In addition, if more than one wave propagates along the same path, the Stokes parameter of the resultant is the sum of the individual waves. A mathematical description for the state of polarization of light is essential for the theoretical calculations discussed in Chapter 3.

1.2.1 Polarizing light microscopy

Modern polarizing optical microscopes (POMs) use crossed polarizers to view birefringent samples. The crossed polarizer setup consists of two polarizing filters with their angle of polarization at 90° to each other. The first polarizing filter is known as the polarizer, the second as the analyzer. The polarizer restricts the unpolarized incident light passing through it to one plane, generating linearly polarized light. When the analyzer is oriented at 90° to the polarizer the light is completely extinguished. It is possible to control the amount of light passing through the set-up by keeping the polarizer fixed and changing the orientation of the analyzer.

When the polarizer and analyzer are parallel, the maximum amount of light is transmitted; when the polarizer and analyzer are oriented perpendicular (cross-polarizer), there is maximum extinction. Angles between parallel and perpendicular orientations produce different degrees of extinction, best illustrated in Figure 1.10.

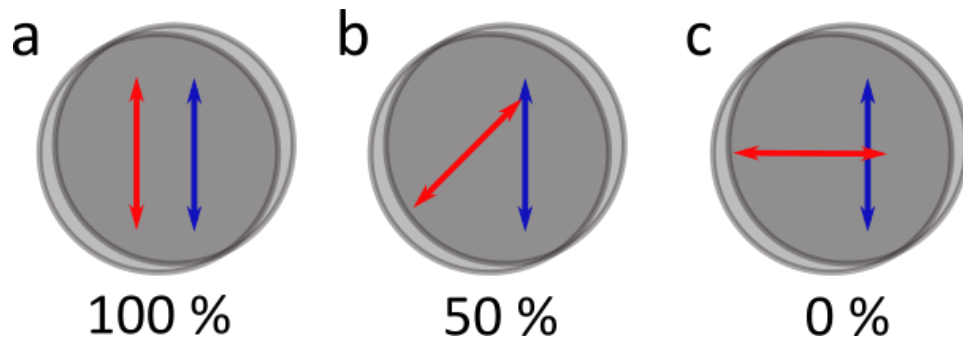


Figure 1.10 (a) Polarizing filters with polarization directions oriented parallel, thus giving maximum transmission. (b) The analyzer is oriented at 45° to the polarizer, giving transmitted intensity that is half of the incident intensity. (c) Polarizing filters oriented perpendicular give rise to zero transmitted light intensity.

Figure 1.10 (a) shows the parallel setup, and Figure 1.10 (c) shows the perpendicular setup. Image Figure 1.10 (b) shows the case with the analyzer at 45° relative to the polarizer, which reduces the amount of light transmitted by 50%. The amount of light that passes through the setup can be quantified using Malus' law:

$$I_F = I_0 \times \cos^2\theta \quad (1.5)$$

where I corresponds to intensity (I_0 incident intensity on the analyzer, I_F transmitted intensity) and θ is the angle between the polarizer and analyzer, thus giving a mathematical basis for extinction at $\theta = 90^\circ$ and maximum transmittance at $\theta = 0^\circ$ and 180° . The discussion so far has described the cross polarizer setup, but how is this used in the POM? In the POM, unfiltered white light enters the polarizer from the source and after passing through the polarizer is linearly polarized in the horizontal plane. Upon entering the birefringent sample (placed on the microscope stage), the polarized light is refracted into separate rays, which have electric vibration vectors perpendicular to each other. The two waves propagate with different speed and wavelength, meaning that the transmitted light now has elliptical polarization.

The analyzer oriented in the cross polarizer setup will select only the vertical component of the light ray to be transmitted to the detector (Figure 1.11). It should be noted that the POM typically has the propagation direction of the radiation in the vertical direction, as opposed to horizontal, as shown in Figure 1.11.

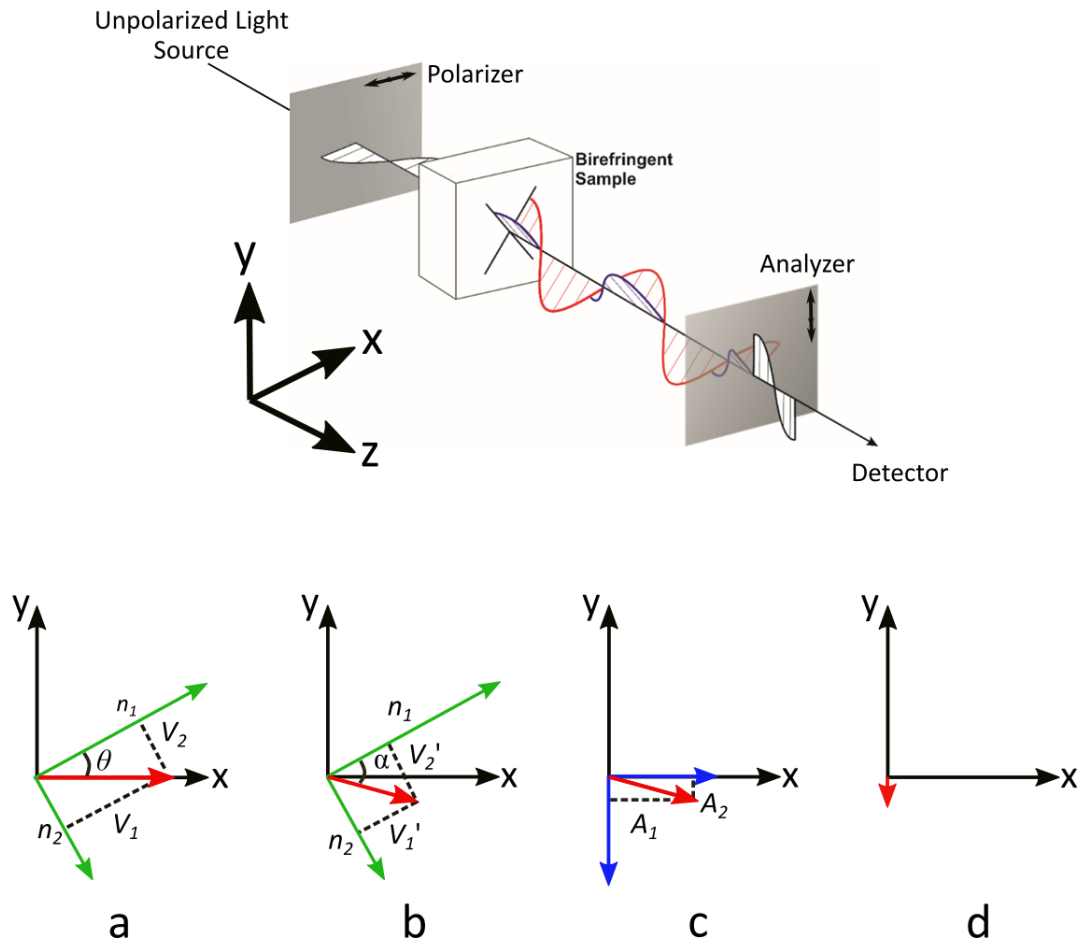


Figure 1.11 Top: Schematic of the crossed polarizer setup for the polarizing optical microscope, with a birefringent sample between the polarizer and analyzer. Bottom: The changes in the polarization vector as it passes through the setup, viewed along the propagation direction of the incident radiation (z -axis). (a) After transmitting through the polarizer the incoming radiation is polarized in the horizontal plane (red), and the refractive indices of the sample are denoted as n_1 and n_2 (green). (b) After passing through the sample, the light vector (red) has changed orientation. (c) The analyzer (blue) selects only the vertical component (A_2) of the radiation (red). (d) Only the vertical component of the radiation is transmitted to the detector.

The interactions that the polarized light experiences on passing through the sample can be explained more fully using vectors in the lower part of Figure 1.11, in which incident light polarized in the horizontal direction encounters a birefringent sample.

1. The principal axes of the refractive index ellipsoid are aligned with the refractive indices of the sample (n_1 and n_2). The principal axes are oriented at an angle θ relative to the polarizer (aligned along the x -axis) so that the polarization direction of the incident light is at an angle θ with respect to the principal axis n_1 . The linearly polarized light beam can be resolved into two orthogonal component vectors V_1 and V_2 .
2. The vector V_1 is retarded by the refractive index n_1 , and the vector V_2 is retarded by the refractive index n_2 . In this example, the light is retarded more in n_1 than in n_2 , resulting in the new vectors V_1' and V_2' . The new angle between the principal axes and the polarization direction of the transmitted light is denoted α .
3. The polarized light beam emerging from the sample then interacts with the analyzer, which is oriented at 90° with respect to the polarizer (i.e. the analyzer is aligned to the y -axis). The polarized light beam is resolved into two orthogonal vectors A_1 and A_2 perpendicular and parallel to the analyzer axis.
4. Only the component A_2 (parallel to the analyzer axis) passes through the analyzer, while the component A_1 is blocked. The amplitude of A_2 is a function of the angle θ and the birefringence properties of the sample.

Rotating the sample around the z -axis (χ rotation) affects the orientation of the electric vector vibration of the radiation emerging from the sample, thus determining the intensity of radiation transmitted through the analyzer. The variation in intensity as the sample is rotated is described mathematically by:

$$I_F = I_0 \sin^2(2\chi) \quad (1.6)$$

Similarly to Equation 1.5, I denotes intensity (I_0 is the incident intensity on the sample, and I_F is the transmitted intensity through the analyzer) and χ describes the rotation angle about the propagation direction (z -axis) of the light, where $\chi = 0^\circ$ corresponds to the crystal orientation with the optic axis parallel to the direction of linear polarization of the incident light.

1.3 Interactions of materials with X-rays

Electromagnetic waves with energies of roughly 100 eV to 100 keV are known as X-rays. X-rays interact with electrons present in a material through a variety of processes.

1.3.1 X-ray Absorption

When the energy from the X-ray is transferred to the sample, it can promote or eject a core electron producing an excited-state. Elements with a higher atomic number (Z) interact more strongly with incoming X-rays, and the binding energy of the core electrons increases nearly proportional to the square of the atomic number Z (Moseley's law). The degree to which an element absorbs X-rays can be described using the mass absorption coefficient (μ), which is known for all individual elements.¹² Thus, the mass absorption coefficient for a material can be determined when the chemical composition is known.

The mass absorption coefficient is also dependent on the energy of the incident X-ray. Upon increasing X-ray energy, the probability of X-ray absorption decreases, allowing greater transmission of X-rays through the sample. Therefore, the absorption coefficient shows a gradual decline with increasing energy. However, sharp jumps in transmission/absorption occur when the X-ray energy corresponds to an absorption edge (Figure 1.12). An absorption edge occurs at the binding energy for a core electron (corresponding to some form of transition) and is unique to each element. The absorption edge energy also varies slightly depending on the electronic environment of the element.

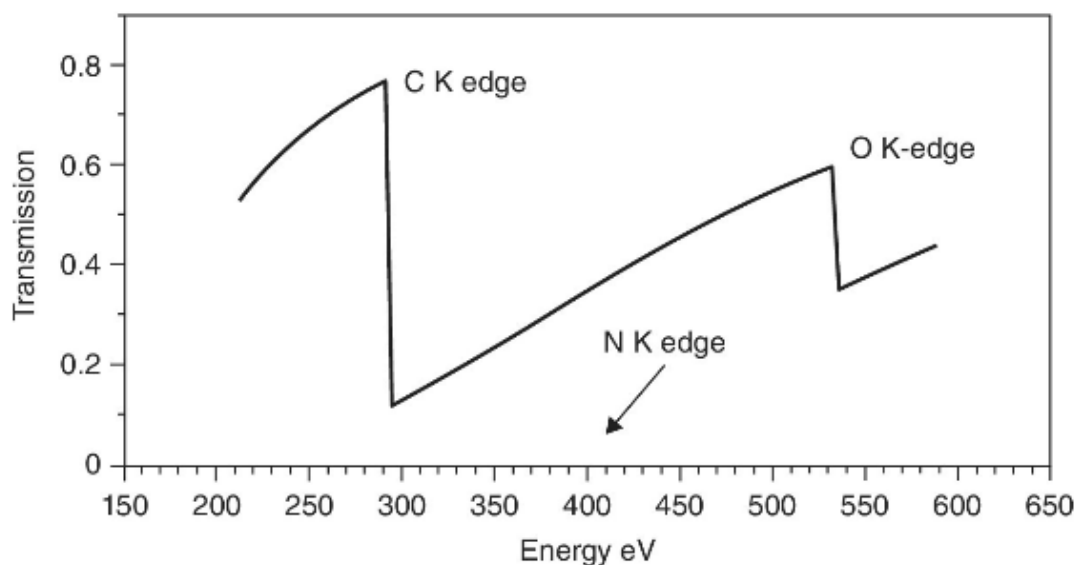


Figure 1.12 Transmission of X-rays as a function of energy for a 1 μm sample of ethanol. The K-edge energies for carbon, nitrogen and oxygen are labelled. Reprinted with permission from Reference 13.¹³

The precise energy and shape of the absorption edge can depend on many factors such as: oxidation state, the bonding environment of the atom, and the surrounding electronic environment. If the bonding of the element and/or the surrounding environment lowers the energy levels of the core orbitals, there will be an increase in binding energies and, therefore, the energy of the absorption edge will increase.

For a given element, there is an absorption edge corresponding to each occupied electron shell; therefore, the absorption edge is labelled according to the electron shell from which the promoted electron originated (Figure 1.13). The K-edge corresponds to a transition from the 1s orbital, i.e., the principal quantum number (n) is 1. The L-edge corresponds to transitions from $n = 2$ and the M-edge corresponds to transitions from $n = 3$.

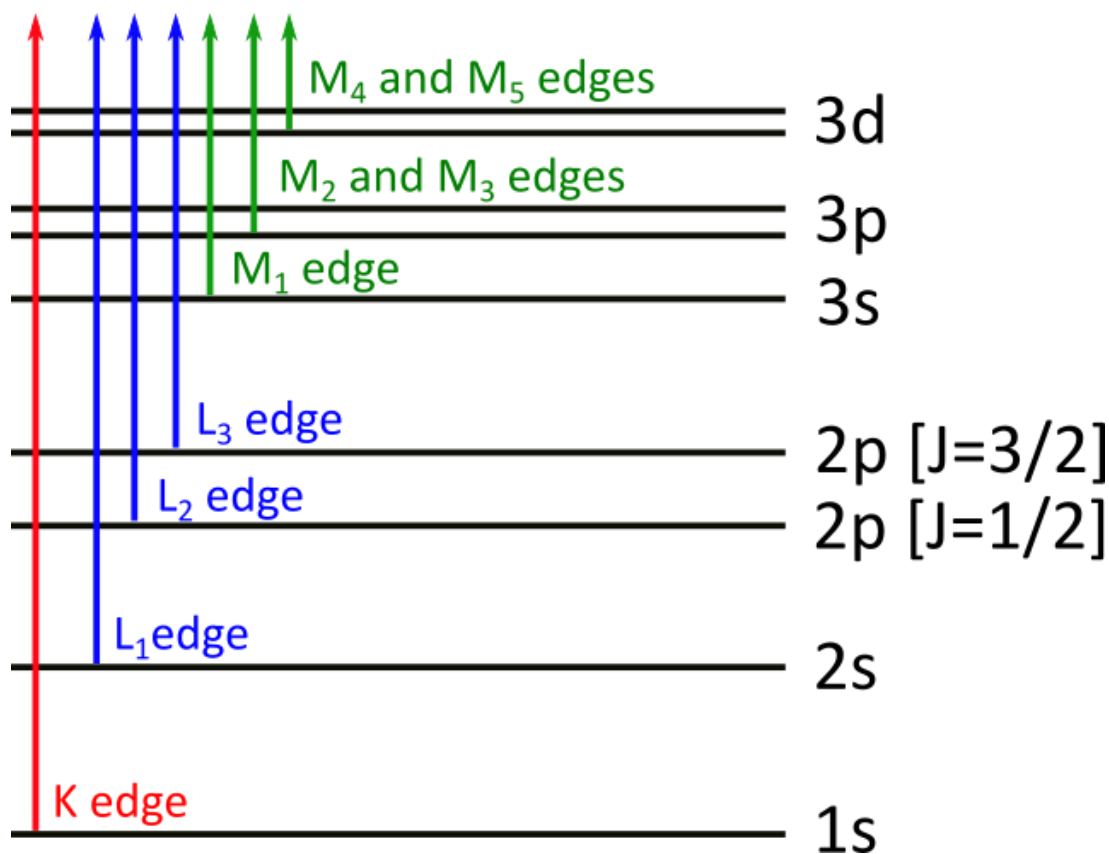


Figure 1.13 Possible transitions for electrons from each electron shell. Electron transition from the 1s orbital (K-edge) is in red. Electron transitions where the principal quantum number is 2 (L-edge) are in blue. Electron transitions where the principal quantum number is 3 (M-edge) are in green.

The promoted electron will either enter an empty orbital or be ejected from the atom. To be ejected, the X-rays must transfer sufficient energy. The empty orbitals may be localized on the absorbing atom or delocalized within bonds or neighbouring atoms. To determine which vacant orbitals to which the electron can be transferred, there are a number of rules.

1. The spin (S) of the electron cannot change ($\Delta S = 0$).
2. Laporte selection rule: transitions between orbitals of the same symmetry (pertaining to inversion) are forbidden.

1.3.2 X-ray Diffraction

X-ray diffraction results from elastic, coherent scattering of X-rays from atoms, which have long-range order. Bragg's law relates d_{hkl} (interplanar spacing associated with a specific set of "lattice planes" defined by Miller indices (hkl)) to the incident angle (θ_{hkl}) and the wavelength (λ) of the incoming X-rays, n is the order of reflection and always an integer.

$$n\lambda = 2d\sin\theta \quad (1.7)$$

The wavelength of X-rays is such that it is similar to the spacing of planes in a crystal lattice, meaning that interaction of X-rays with a sample can produce constructive interference and a diffracted ray when Bragg's law is satisfied (Equation 1.7, Figure 1.14).

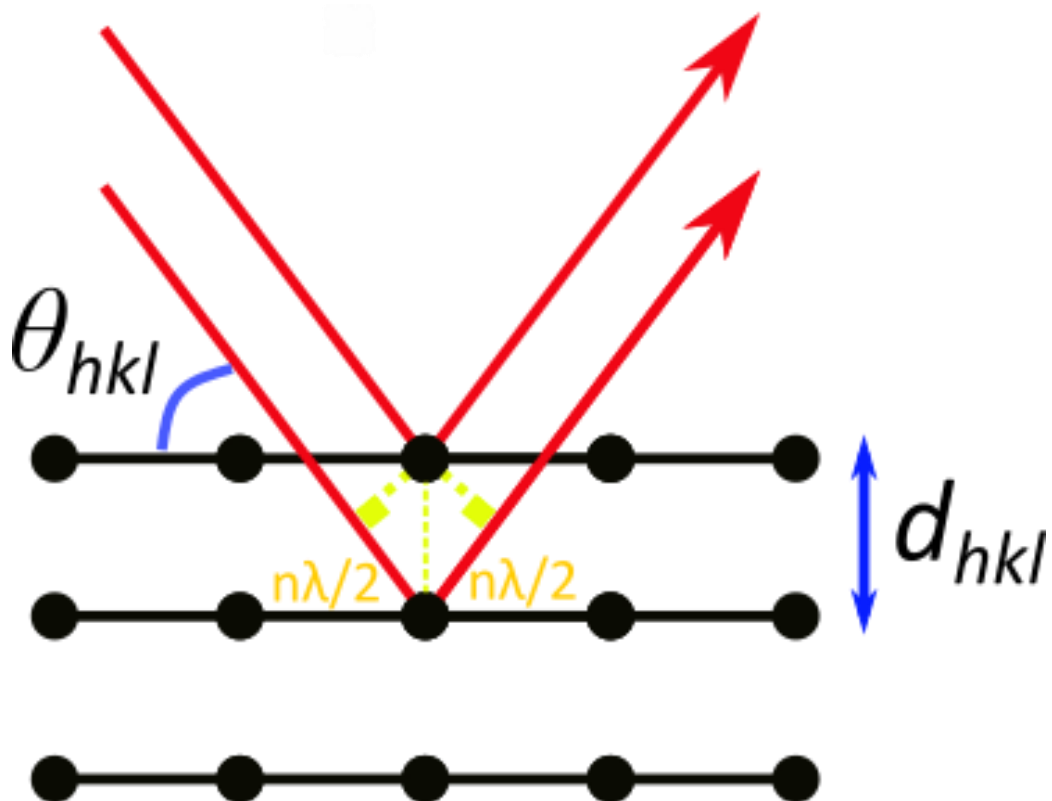


Figure 1.14 Illustration of Bragg diffraction, where incoming radiation with wavelength λ is diffracted by a set of lattice planes in the crystal (with interplanar spacing d_{hkl}).

1.3.2.1 Kinematic and Dynamical Diffraction

Kinematic theory is concerned with diffraction from non-ideal crystals. Dynamical theory looks at diffraction from perfect crystals. If the diffracting crystal is perfect, the incoming X-rays will experience multiple diffraction events (Figure 1.15). As, once the incoming X-ray has satisfied Bragg's law on one occasion, in a perfect crystal, it will satisfy Bragg's law multiple times. These diffracted rays will, therefore, interfere with each other. Dynamical diffraction is typically rare in the case of X-rays as most crystals are imperfect; however, the monochromator and polarization analyzer discussed in Chapter 2 are perfect crystals and dynamical diffraction comes into effect.

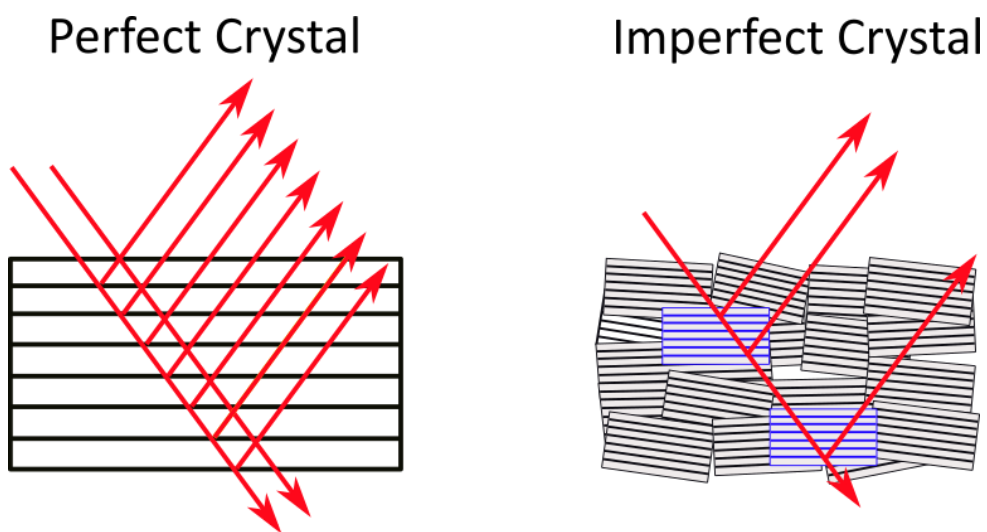


Figure 1.15 The perfect crystal (left) shows multiple diffraction events (red) from the incoming X-rays (red) and dynamical diffraction is observed. For the imperfect crystal (right), the crystal is made up of small domains with different orientations. Domains which satisfy Bragg's law (blue) for a specific direction of incident radiation will diffract (red), exhibiting kinematic diffraction.

Imperfect crystals, while possessing long-range order, can be thought of as small domains of crystal slightly miss-aligned with respect to each other (Figure 1.15). Therefore, not all of the domains satisfy Bragg's law for a specific direction of incident radiation; from this, it can be assumed that individual diffraction events do not interfere with each other. Kinematic diffraction is the most common form of diffraction and, unless explicitly stated in this thesis, kinematic diffraction can be assumed.

1.3.3 X-ray Dichroism

X-ray dichroism and X-ray birefringence are closely related, both phenomena concern the interaction of linearly polarized X-rays with an anisotropic structure.¹⁴⁻¹⁷ X-ray dichroism interrelates X-ray absorption, to a materials orientation with respect to the polarization direction of the incident linearly polarized X-ray beam. The intensity observed in X-ray dichroism measurements can be related to the angle (θ) between the incoming ray and the orbital direction (which is excited upon X-ray absorption) through Malus' law (Equation 1.5).

X-ray birefringence interrelates the speed of the wave propagation (real part of the complex refractive index), to a materials orientation with respect to the polarization direction of the incident linearly polarized X-ray beam. The intensity observed in X-ray birefringence measurements can be related to the angle (θ) between the incoming ray and the orbital direction (which is excited upon X-ray absorption) using Equation 1.6. Despite the different effects on linearly polarized X-rays the two phenomena produce, they rely on the same structural and symmetry properties of the material and can be related mathematically by a Kramers-Kronig transform.

$$\Delta\gamma''(E) = \frac{2}{\pi} P \int_0^{\infty} \frac{E' \Delta\gamma'(E')}{(E'^2 - E^2)} dE' \quad (1.8)$$

The Kramers-Kronig transform is shown in Equation 1.8, where E and E' represent the photon energy and P is the principal part of the integral. The linear absorption coefficient (γ) describes the fraction of intensity absorbed per unit thickness. The linear absorption coefficient (γ) can be extended into the complex linear absorption coefficient which is the sum of the real (γ') and imaginary (γ''), which correspond to dichroism and birefringence respectively. It should be noted that absorption is determined by the imaginary part of the complex refractive index in the optical region. Historically, X-ray absorption is described using a real absorption coefficient. So, to preserve this definition, the imaginary part is instead used to describe refraction and X-ray birefringence, with the real part used to describe X-ray dichroism, as stated above. X-ray dichroism spectra and the Kramers-Kronig transform are critical to the theoretical calculations detailed in Chapter 3.

Throughout this work, my aims have been to expand an understanding of the X-ray birefringence imaging (XBI) technique. There are a multitude of ways in which this objective has been achieved:

- Exploring structural properties of crystals, such as twinned crystals and twisted crystals, that have not been explored previously using XBI.
- Measurement of XBI data at absorption edges other than the bromine K-edge, at which all previous XBI work was carried out.
- Expansion of the theoretical framework of XBI to encompass materials containing more than a single C-Br bond orientation, as well as materials in which the X-ray absorbing element forms two or more bonds to neighbouring atoms.
- Development of a more complete, reproducible, and reliable protocol for setting up XBI experiments to make future XBI studies more accessible for other researchers.

As XBI studies can only be carried out at a synchrotron radiation source, there was some down time between scheduled XBI experiments, which permitted time for other research projects. These projects focused primarily on structure determination from powder X-ray diffraction data. A particularly interesting and challenging study in this regard is discussed in Chapter 7.

2 Experimental Methods

2.1 X-ray Birefringence Imaging

X-ray birefringence imaging (XBI) can be considered the X-ray analogue of the polarizing optical microscope (POM), which is in widespread use by both chemists and geologists. The POM utilises the visible spectrum of light to study the optical birefringence of materials, which depends on the overall crystal symmetry. It is surprising then that birefringence at X-ray energies has been studied so little,¹⁸⁻²¹ especially considering the related phenomena of X-ray dichroism has been studied extensively.^{14,16,17,21,22}

Using X-rays tuned to an elemental absorption edge means that the incident X-rays interact solely with the element of interest, thus allowing the local anisotropy of the bonding environment of the X-ray absorbing element to be studied. For XBI, the X-ray optic axis does not necessarily correspond to the optic axis as dictated by symmetry, or a crystallographic axis. Knowledge of local orientational properties and domain structures is invaluable in the understanding of materials and is linked to electronic, magnetic and optical properties of some materials, thus demonstrating the potential usefulness of this technique.

Previous experimental work utilising XBI and in this thesis has focused solely on excitations at K-edges. Thus, the excited electron has always originated from the 1s core-shell. The 1s shell has σ symmetry and, with knowledge of the dipole selection rules, the excited-state must contain a p-orbital component, although it may have σ or π symmetry. The probability of this transition is dependent on the relative orientations of the polarization of the incident beam and the excited-state orbital direction.^{14,16,23} The X-ray birefringence scales with the Q_{zz} component of the atomic quadrupole moment of the excited-state orbital.^{15,24} Previous XBI experimental work focused on the bromine K-edge (energy ~ 13.474 keV) as it is easily accessible. Additionally, the electron is excited into the bromine 4p shell via the σ^* antibonding orbital (Figure 2.1) of the C-Br bond.^{15,24} Thus, the XBI behaviour can be readily interpreted based on an effective X-ray optic axis parallel to the C-Br bond.

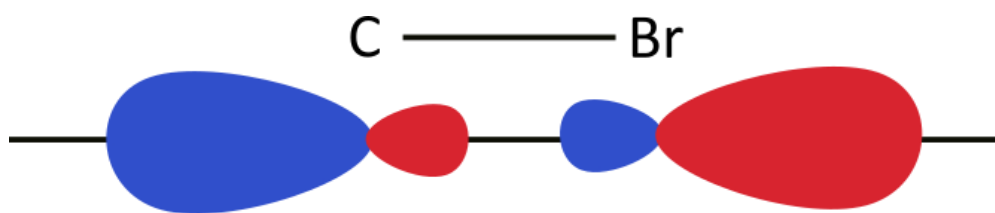


Figure 2.1 Atomic p orbitals for carbon and bromine, which are parallel to the C-Br bond direction, have combined with mismatched phases (red lobes have negative charge and blue positive charge) to form the σ^* antibonding orbital. A node of zero electron density can be seen equidistant between the carbon and bromine atoms.

It should be noted, however, that XBI is not capable of distinguishing bonds that are aligned anti-parallel to each other, as the phenomenon of X-ray birefringence is “parity even”.

2.1.1 Experimental Setup

XBI is not a standard experimental setup and requires a synchrotron source. For this reason, all XBI experiments were performed on B16, the test beamline at Diamond Light Source (DLS).²⁵ The synchrotron source is necessary for various reasons including;

1. The acceleration of the charged particles in the synchrotron is in the horizontal plane, therefore the resulting radiation is highly polarized with the electric component in the horizontal plane. Above and below this plane, the X-rays are elliptically polarized. XBI relies on the study of changes in the direction of linear polarization plane, hence the X-ray source must be linearly polarized.
2. The X-rays from a synchrotron are polychromatic and so the specific X-ray energy appropriate to a desired elemental absorption edge can be selected.

In the experimental coordinate system the propagation direction of the incident X-rays corresponds to the z -axis and the X-rays are linearly polarized along the x -axis (horizontal plane). Figure 2.2 shows a beamline schematic for B16 (some components not relevant to XBI experiments have been removed). Components which are indispensable to the XBI setup are labelled and will now be discussed in more detail.

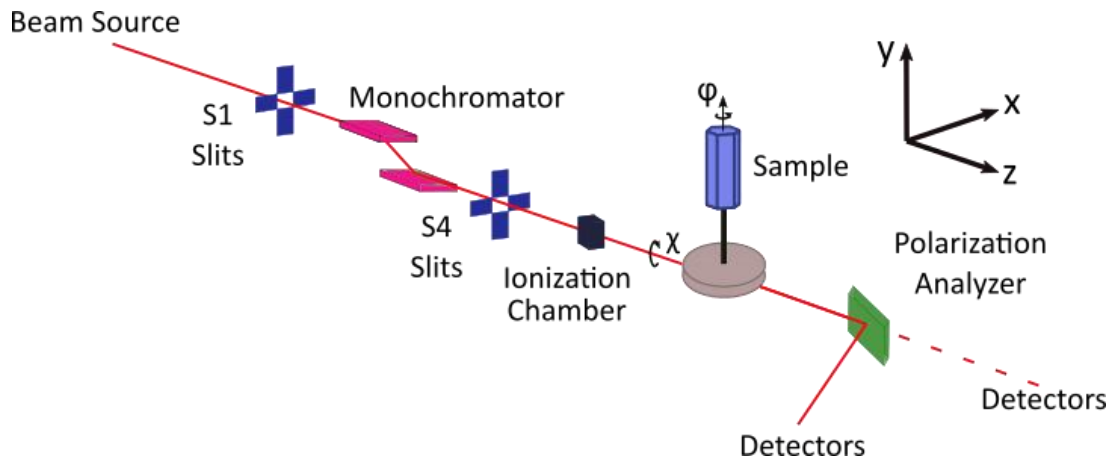


Figure 2.2 Beamline schematic for B16, shows selected components from the beamline important to the XBI setup; source, slits, monochromator, ionization chamber, diffractometer base (sample mount), polarization analyzer and detectors in the direct and diffracted path of the beam. Also pictured is the Cartesian axis system for XBI experiments with the z-axis corresponding to the propagation direction of the incident beam and the X-rays linearly polarized in the x-axis (horizontal).

2.1.1.1 Monochromator

The radiation from the beam source is polychromatic, encompassing a broad spectrum of energies. For the process of selecting a specific energy, a vertically deflecting double-crystal monochromator (typically silicon) is used, set to the (111) Bragg reflection. Utilizing Bragg's law (Equation 1.7) and having the capability to rotate the crystal monochromator, a different value of θ can be selected, thus changing the wavelength (λ) of the selected radiation. Therefore, the energy of the X-rays emerging from the monochromator can be tuned to the required elemental absorption edge.

A double crystal monochromator (consisting of two identical crystals, with identical Bragg planes parallel) is used so that both crystals diffract the X-rays, thus preventing a change in beam direction; instead, there is only a small displacement in the beam direction (Figure 2.3).²⁶ Perfect crystals are preferred for a monochromator as they diffract over a narrower angular range and are governed by dynamical diffraction.

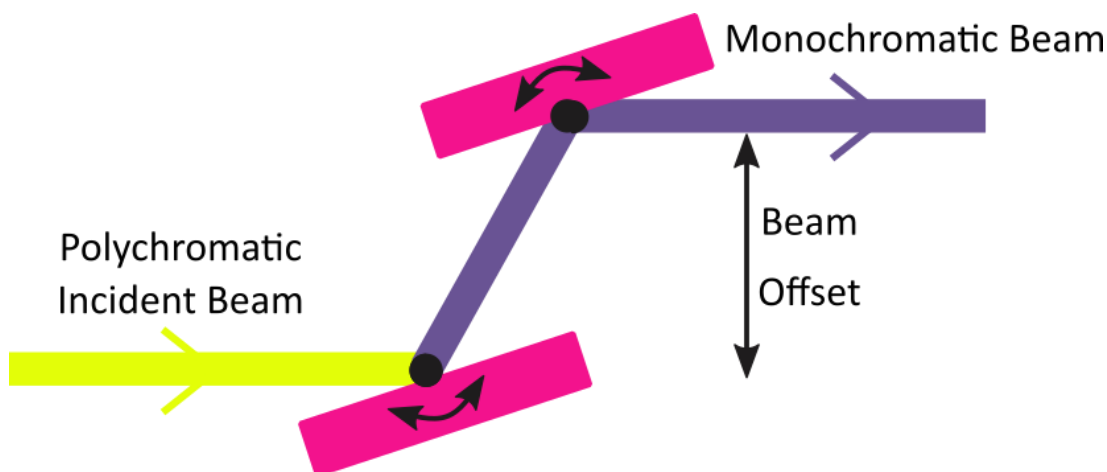


Figure 2.3 Polychromatic incident radiation (yellow) encountering a double crystal monochromator (pink) and exiting as monochromatic radiation (blue).

The monochromator is particularly sensitive to temperature, with thermal deformations being quite common. The primary source of heat comes from the beam. To counteract this problem, the monochromator has a cooling apparatus. However, even with cooling, there may be some deformation in the monochromator (and therefore incorrect energy selection), mainly when the monochromator is used for the first time after a period with no beam. The monochromator must consequently be recalibrated frequently, using materials with a known absorption edge.

2.1.1.2 Ionization chamber

Before encountering the sample, the X-rays pass through an ionization chamber recording the incident beam intensity, therefore allowing us to account for changes in the intensity of the incident beam due to fluctuations in the synchrotron source.

2.1.1.3 Sample mount (Huber diffractometer base)

The experimental axis has already been defined using the incident X-ray beam; direction of propagation corresponds to the z -axis and the direction of linear polarization to the x -axis. To discuss the rotations the sample can undergo it is first convenient to establish a reference axis for the sample. The reference axis typically corresponds to some well known feature of the sample or experimental setup. For single crystals a known crystallographic axis or the long axis of a needle-like crystal is often used as the reference axis.

The reference axis is maintained in the xy -plane throughout the XBI experiment regardless of rotation of the sample. A five-circle, vertical-scattering, Huber Eulerian diffractometer is used to mount the sample goniometer and rotates the goniometer (and sample) about the z -axis in the xy -plane, which is denoted as the χ rotation in XBI experiments (Figure 2.4). Therefore, the χ rotation changes the orientation of the reference axis with respect to the direction of linear polarization of the incident X-ray beam. For the current set-up on B16, the orientation with $\chi = 90^\circ$ corresponds to the orientation in which the sample reference axis is vertical (parallel to the y -axis).

The ϕ rotation corresponds to the sample rotation around the reference axis. Thus, the ϕ rotation changes the orientation of the sample with respect to the direction of linear polarization of the incident X-ray beam but not the orientation of the reference axis (Figure 2.4).

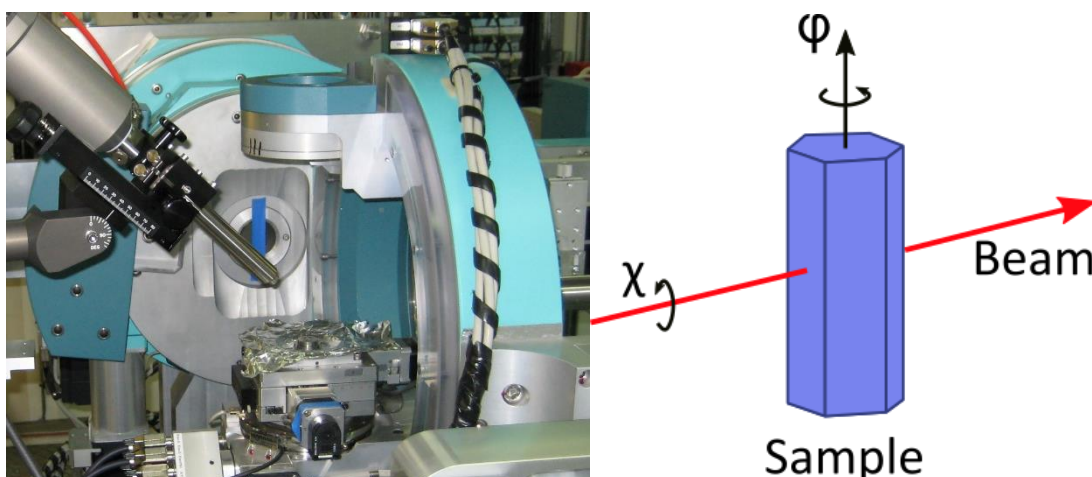


Figure 2.4 The Huber diffractometer and Cryostream on B16, and definition of sample rotation axes χ and ϕ . χ rotates around the beam direction, and ϕ rotates around the goniometer/reference axis.

The full range of χ and ϕ is dependent on the limits of the diffractometer movement; movements that are too large will lead to crashes between different parts of the setup. A minimum range of movement is around 180° in both χ and ϕ . The orientation of the sample when attached to the goniometer is of vital importance. For a needle like crystal, the long axis (reference axis) should be aligned exactly parallel to the goniometer axis, otherwise during the ϕ rotation the sample will move.

However, attaching the sample to the goniometer with the reference axis and goniometer axis parallel is difficult. Therefore, a goniometer which can accurately adjust the alignment of the sample after attachment is essential. The goniometer mount used for XBI experiments has a pair of perpendicular arcs which allow the orientation of the sample reference axis to be adjusted to match the goniometer axis after attachment of the sample (Figure 2.5).



Figure 2.5 Goniometer mount capable of adjusting the orientation of the sample relative to the laboratory reference frame.²⁷

A full understanding of the orientational properties of a sample may be developed by measuring XBI data as a two-dimensional scan, which consists of recording XBI images as a function of both χ and ϕ . Another standard scan is a temperature scan in which XBI data are recorded as a function of temperature for fixed sample orientation; in Figure 2.4, the Oxford Cryosystems Cryostream 700 nitrogen gas cooler, used to control the temperature of the sample is shown.

2.1.1.4 Polarization Analyzer

After the sample, a horizontally deflecting polarization analyzer is present in the beam path. The analyzer is mounted on a translation stage so it can be moved in and out of the beam path to perform XBI and X-ray absorption measurements respectively. The polarization analyzer selects only the vertical component of X-ray polarization, through diffraction of the beam at a Bragg angle close to 90° . X-rays tuned to different elemental absorption edges require polarization analyzers of different materials, which is related to the Bragg diffraction equation (Equation 1.7). As different absorption edges are at different energies, the X-ray wavelength (λ) changes, therefore requiring a suitable analyzer crystal with an inter-planar spacing (d_{hkl}), to allow diffraction to occur with a Bragg angle close to 90° for the specific wavelength:

$$d_{hkl} = \frac{a}{\sqrt{h^2 + k^2 + l^2}} \quad (2.1)$$

a = lattice parameter ($a = 5.431 \text{ \AA}$ for Si; $a = 5.658 \text{ \AA}$ for Ge)

For example, previous XBI studies have mainly focused on studies of the orientation of C-Br bonds using incident X-rays tuned to the Br K-edge absorption ($\sim 13.475 \text{ keV}$). In this situation, using Bragg's law (Equation 1.7) and the calculation for inter-planar spacing from the lattice parameter (Equation 2.1), it can be determined that the Si (555) or Ge (555) reflections would both be viable as the polarization analyzer, with angles of $\theta = 47.193^\circ$ and $\theta = 44.768^\circ$ respectively.

While the corresponding values of 2θ do not equal 90° exactly, the Bragg angles are sufficiently close to 90° that essentially only the vertical component of the polarized X-rays is diffracted to the detector. Thus, the polarization analyzer selects the X-rays polarized parallel to the y -axis (vertical). The original X-rays from the synchrotron source are linearly polarized parallel to the x -axis (horizontal), therefore, this setup corresponds to the crossed polarizer setup in the POM. As the specific Bragg reflection of the analyzer crystals does not correspond to a Bragg angle precisely equal to 90° ; the horizontal component of polarization is not entirely blocked by the analyzer. To calculate the effectiveness of the analyzer in selecting the vertical polarization, dynamical diffraction theory must be used as the analyzer is a perfect crystal.

The full theoretical calculations required to calculate the diffracted intensity of the *s*- and *p*-polarization (perpendicular and parallel to the horizontal plane respectively) using dynamical diffraction theory is discussed in Reference 28.²⁸ Ideally, the analyzer should operate such that the *p*-polarization (horizontal linear polarization) is minimized and the *s*-polarization maximized (vertical linear polarization). The *s*-polarization and *p*-polarization for Si (555) and Ge (555) are shown as ‘Rocking curves’ in Figure 2.6 as a function of the difference between the incidence angle at the analyzer and the ideal Bragg angle.

For the Ge (555) reflection, the *p*-polarization is almost completely suppressed, while for the Si (555) reflection, the *p*-polarization is also suppressed but not to the same extent. The difference observed in the suppression of the *p*-polarization is due in part to the Ge (555) reflection having a Bragg angle closer to the ideal value of $2\theta = 90^\circ$. However, the intensity of the *s*-polarization is considerably lower for the Ge analyzer compared to Si, which can be related to X-ray absorption (Section 1.3.1), as heavier elements such as Ge absorb more strongly.

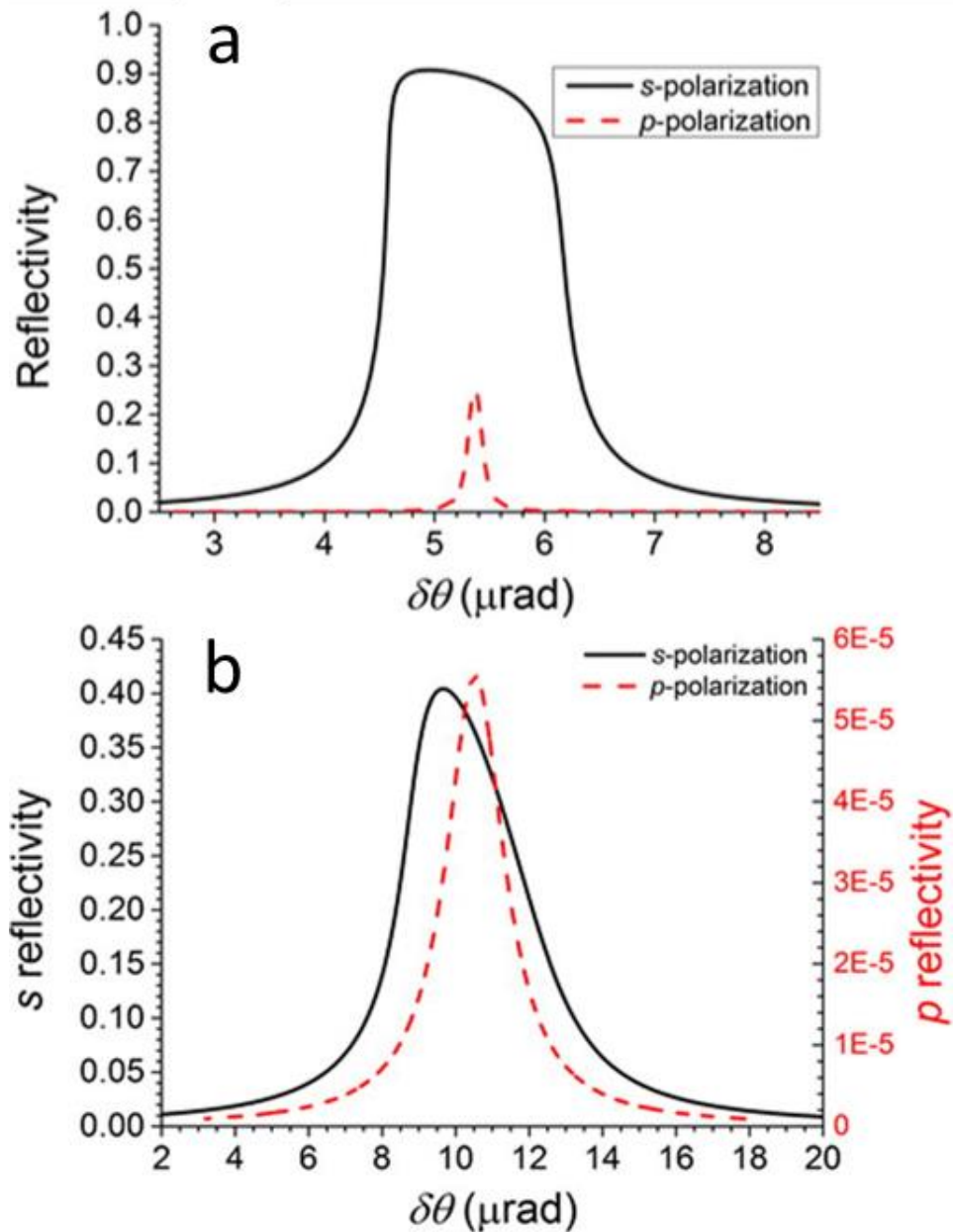


Figure 2.6 Rocking curves for (a) Si (555) and (b) Ge (555) for both *s*-polarized (solid line) and *p*-polarized (red dashed line) X-rays of 13.474 keV energy as a function of the difference ($\delta\theta$) between the incidence angle and the ideal angle ($\theta = 45^\circ$). Note that in (b) different scales are used for the reflectivity of the *s*-polarized and *p*-polarized X-rays. Adapted from Reference 28.²⁸

As seen in Figure 2.6, the diffracted intensity is very sensitive to the diffraction angle. When the analyzer crystal is setup on the beamline there is typically a small misalignment between the actual diffraction angle of the analyzer and the diffraction angle recorded by the rotation stage.

To correct for this, the analyzer crystal is rotated to the predicted diffraction angle and then intensity is recorded as a function of diffraction angle, usually $\pm 0.5^\circ$ from the predicted angle. The reflection is observed as two conjoined peaks in the intensity scan (Figure 2.7). The dip between the two peaks determines the optimal angle of reflection for the analyzer.

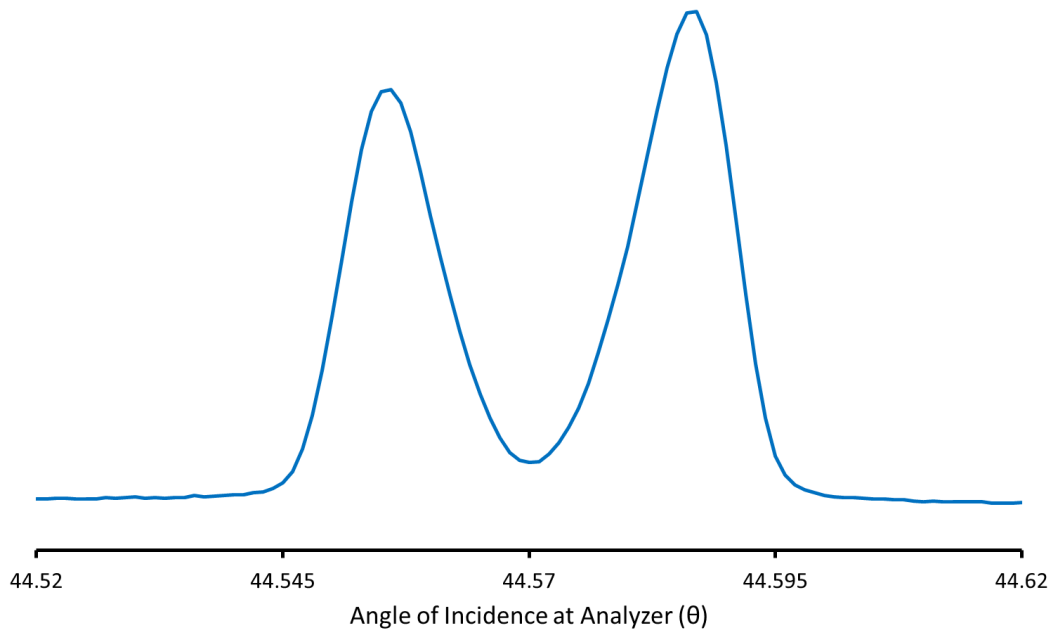


Figure 2.7 Intensity recorded as a function of incidence angle (θ) for the Ge (555) reflection at an energy of 13.476 keV.

2.1.1.5 Beam centre

There are two sets of slits in Figure 2.2, which control the shape and size of the beam. For optimal XBI setup, the slits should be centred to the beam centre (electron orbit plane), as the beam is perfectly linearly polarized only within the horizontal plane. Above and below the beam centre, the radiation is elliptically polarized, with the amount of elliptical polarization depending on the vertical angle, the electron energy (3 GeV) and the bending radius of the bending magnet (6.981 m).^{29,30} Figure 2.8 demonstrates the sensitivity of the polarization state to distance from the beam centre; it shows calculated plots for the horizontally and vertically polarized radiation on B16 at 13.474 keV as a function of the vertical angle β (where $\beta = 0$ corresponds to the electron orbit plane).²⁸ These data were simulated using SHADOW.³¹

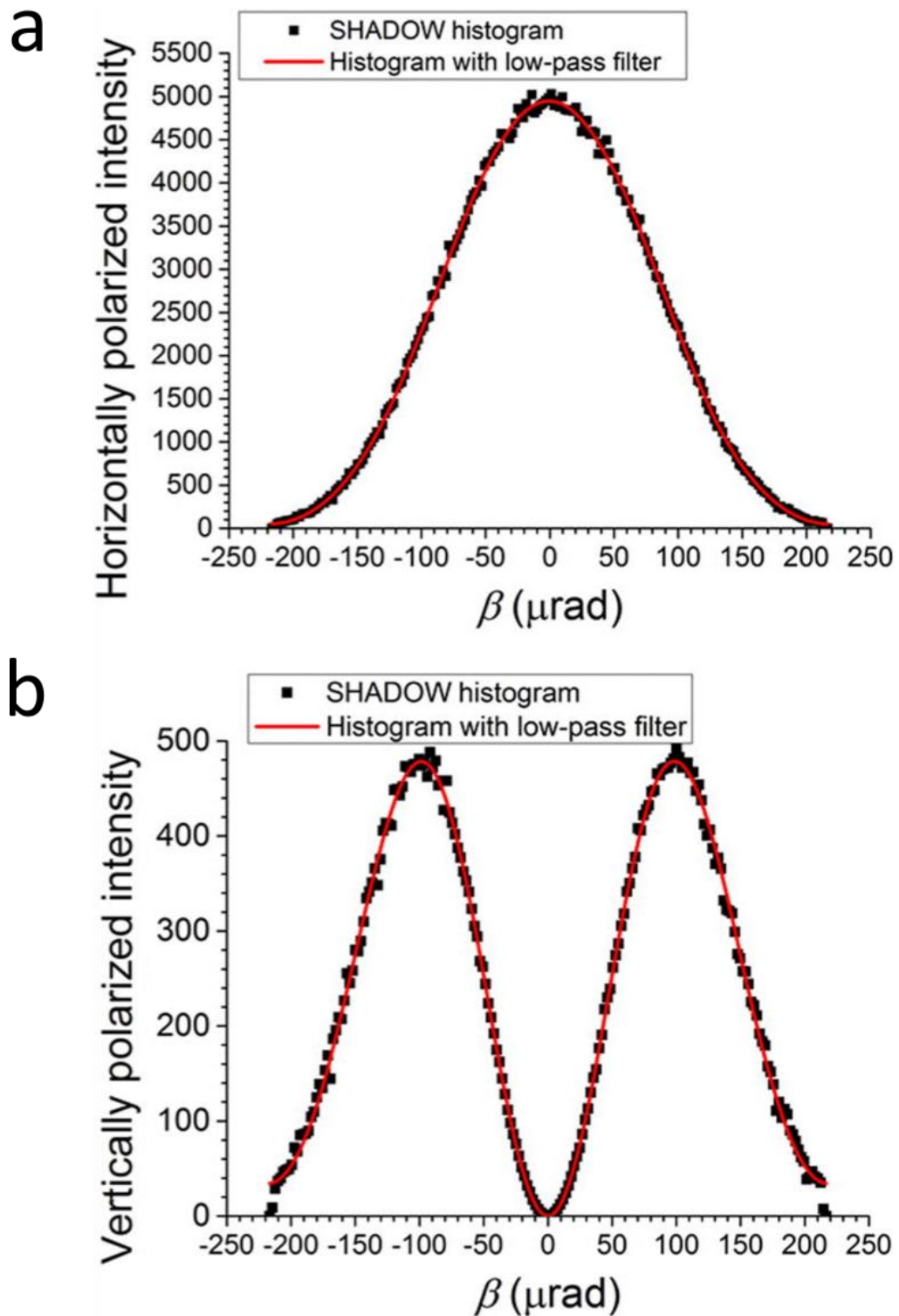


Figure 2.8 B16 DLS incident energy is 13.474 keV (a) horizontally polarized intensity (b) vertically polarized intensity as a function of β (vertical angle where $\beta = 0$ is the electron orbit plane). The simulated data from SHADOW is shown as black squares, to remove stochastic noise a Fourier transform low-pass filter was used and is shown as a red line. Reprinted with permission from Reference 28.²⁸

Figure 2.8 (a) shows a strong correlation between horizontal polarization and the electron orbit plane (vertical FWHM = 200 μrad); however, even for small deviations away from the electron plane, there is a marked increase in vertical polarization, dominated by two peaks at $\pm 100 \mu\text{rad}$ in Figure 2.8 (b), demonstrating the importance of determining the beam centre.^{28,30}

To determine the beam centre, a glass analyzer is used (the glass scatters at any angle, in contrast to the polarization analyzer, which gives diffraction only at specific Bragg angles). The S1 slit positions are moved vertically, while the intensity is scanned (Figure 2.9). The minimum intensity arises when vertical position of the slit is aligned to the beam centre. In Figure 2.9 the minimum is already positioned at a vertical offset of zero for the S1 slits, therefore, the slits are centered.

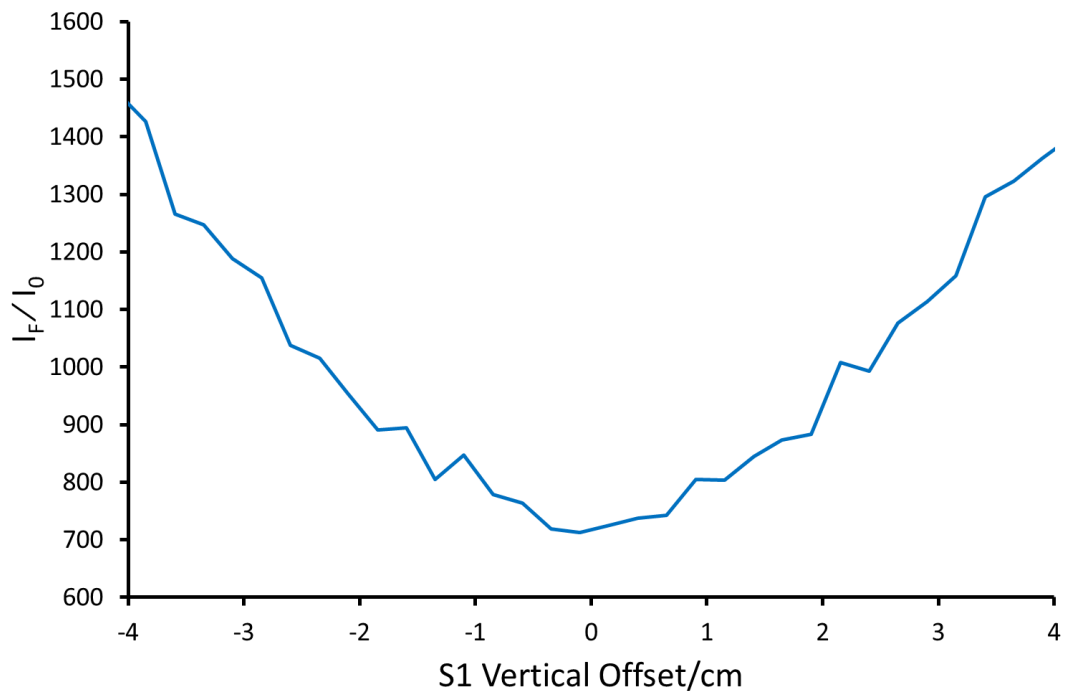


Figure 2.9 Scan of final intensity (I_F) divided by incident beam intensity (I_0) vs the vertical offset (cm) of the S1 slits using a glass analyzer. The minimum defines the beam centre position.

After finding the beam centre and positioning the slits, the centre of rotation of the diffractometer and the detectors can all be aligned to the beam centre, thus, minimizing the effects of elliptical polarization.

Elliptical polarization manifests as unequal maxima intensities upon χ rotation (from Equation 1.6, maxima in intensity are separated by $\chi = 90^\circ$). Figure 2.10 shows a χ scan for a single crystal of 1-bromoadamantane/thiourea recorded with a significant contribution from elliptical polarization in the incident beam. In this case, the maximum close to $\chi = 135^\circ$ is clearly lower in intensity than the maximum close to $\chi = 45^\circ$. If the polarization was perfectly linear, the two maxima would have identical intensity. While the disparity between peak maxima in Figure 2.10 is clearly understood and can be accounted for in theoretical calculations (Chapter 3) ensuring that the beam is properly centered is critical for obtaining high-quality data and is therefore an essential part of the XBI setup.

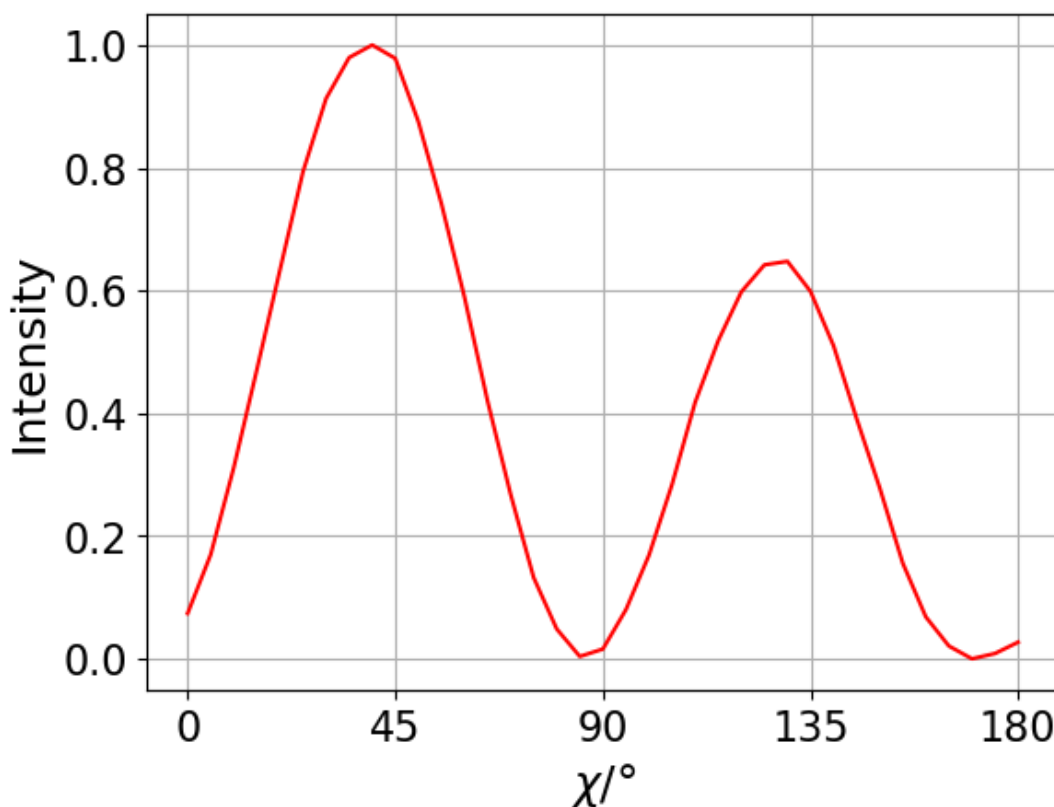


Figure 2.10 χ scan recorded for a single crystal of 1-bromoadamantane/thiourea ($\varphi = 0^\circ$) at 13.474 keV using the Ge (555) reflection. A significant component of elliptical polarization is present in the incident X-ray beam leading to unequal maxima in the two peaks.

2.1.1.6 Detectors

2.1.1.6.1 Measurement of XBI Images

The X-rays diffracted off the polarization analyzer, are measured using an area detector. In current operation, there are two detectors mounted on a translation stage: a Medipix merlin hybrid pixel detector (photon counting detector from Quantum Detectors; 55 μm pixel size; 256×256 pixels in the field of view) and an “X-ray eye” detector (12 bit **CCD** miniFDI camera from Photonic Science Ltd.; 6.5 μm pixel size; 1392×1040 pixels in the field of view). Each of these detectors have different pros and cons. Essentially, the Medipix has a better threshold and allows smaller differences in intensity to be detected. The CCD detector has greater spatial resolution and thus detects smaller physical differences in the XBI images. The detector can be changed remotely using a translation stage, allowing measurements to be made on a given sample using both detectors.

The resolution of the detector defines the limits of spatial resolution in the vertical direction for XBI images. However, in the horizontal direction, the resolution in XBI images is limited primarily by the dynamical diffraction extinction depth of the polarization analyzer. Previous calculations have shown that, for the Ge (555) reflection, the extinction depth is 7.9 μm .³² For the Si (555) reflection, the resolution is $\sim 28 \mu\text{m}$.³³ This difference arises because Ge is a heavier element, thus reducing the diffraction extinction depth. The extinction depth could potentially be reduced further using an analyzer based on heavier elements, although there is a trade-off with heavier elements absorbing X-rays more strongly.

The instrumental background of XBI images is dependent on the monochromator and the polarization analyzer. Bragg’s law determines that X-rays of a given wavelength (λ) are diffracted at an angle θ from a given material. If the wavelength of the incident X-rays is slightly different, diffraction will occur at a slightly different value of θ , producing a dispersion of diffracted wavelengths dependent on incidence angle (which is denoted β for the monochromator and α for the analyzer).

X-rays that are diffracted efficiently by both the monochromator and the polarization analyzer must be close to the intersection of the wavelength dispersions from the monochromator and the analyzer (Figure 2.11). Thus explaining the observed tilt in the intensity of the X-ray beam recorded in experimental XBI images with no sample present (which also represents the “background” intensity in XBI images recorded with a sample present (Figure 2.12)).

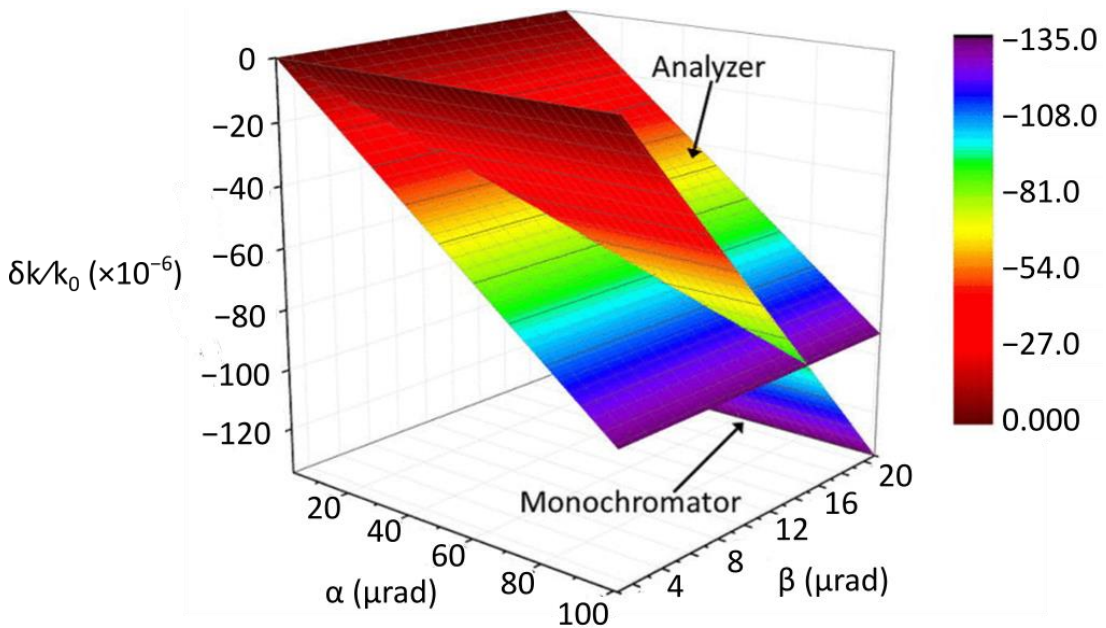


Figure 2.11 The Du Mond diagram in 3 dimensions showing X-rays diffracted by the monochromator (β , vertical deviation angle) and the analyzer (α , horizontal deviation angle) as a function of the wave vector magnitude ($\delta K/K_0$). Adapted from Reference 28.²⁸

The Bragg angle of the monochromator is fixed (for selection of a specific X-ray energy) but the Bragg angle at the polarization analyzer is different for different types of analyzer, causing a change in the tilt angle. For Si (555) and Ge (555), the theoretical tilt angles are 7.82° and 8.51° , respectively.²⁸ It is important to note that the direction of the tilt may change depending on whether the detector is positioned in the positive or negative direction along the x -axis, as viewed along the z -axis (Figure 2.12).

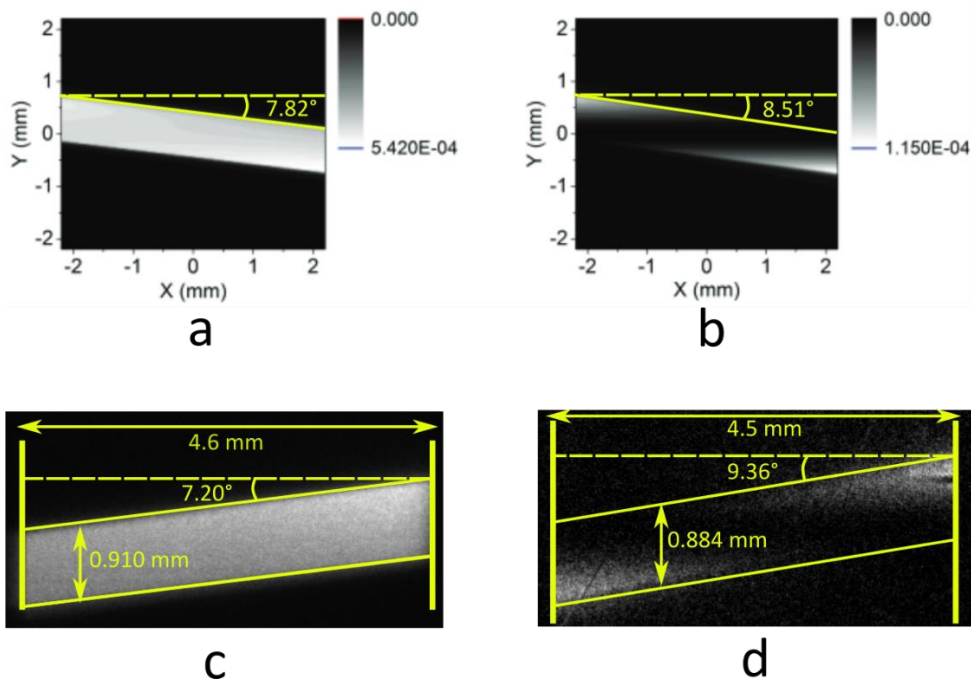


Figure 2.12 Theoretical background intensity recorded on the detector at 13.474 keV using (a) Si (555) and (b) Ge (555) as the analyzer reflections. Calculated tilt angles are 7.82° and 8.51° for the Si (555) and Ge (555) reflections respectively. Adapted from Reference 30.³⁰ Experimental background intensity at 13.474 keV using (c) Si (555) and (d) Ge (555) analyzer reflections. The measured tilt angles are roughly 7.20° and 9.36° for the Si (555) and Ge (555) reflections respectively. The difference in tilt direction between the experimental and calculated images is due to the detector being positioned in the positive direction along the x-axis in one case and positioned in the negative direction along the x-axis in the other case (as viewed along the z-axis).

The theoretical calculations shown in Figure 2.12 (a), (b) are clearly in excellent agreement with experimental data (Figure 2.12 (c), (d)). The intensity background in XBI images is dependent on both the vertical and horizontally polarized X-rays that are incident on the detector. The rocking curves shown in Figure 2.6 are therefore vitally important. For the Si (555) analyzer, there is a greater contribution from horizontal polarization compared to the Ge (555) analyzer, which is seen as a high-intensity background. For the Ge (555) analyzer, horizontally polarized X-rays from the electron orbit plane are almost entirely suppressed, appearing as a dark stripe in the XBI images and denoting the beam centre.²⁸

2.1.1.6.2 Measurement of X-ray Absorption/Dichroism

There are two detectors in the direct beam path (see Figure 2.2). One of these detectors is used to align the sample using another “X-ray eye” (12 bit **CCD** miniFDI camera from Photonic Science Ltd.; 6.5 μm pixel size; 1392 \times 1040 pixels in the field of view). The second detector, a PIPS (Passivated Implanted Planar Silicon) photodiode, is used to record X-ray absorption data. The detectors are mounted on a translation stage for ease of movement. X-ray absorption data are essential for selecting the correct X-ray energy to use in XBI experiments.

The effect of X-ray energy on birefringence is clearly illustrated in Figure 2.13, which shows X-ray absorption scans for 1-bromoadamantane/thiourea as a function of χ , with X-ray birefringence observed only within a very narrow region of energy (*ca.* 13.47 \pm 0.02 keV). Therefore, a method for selecting the correct X-ray energy for XBI experiments on any given material is of vital importance.

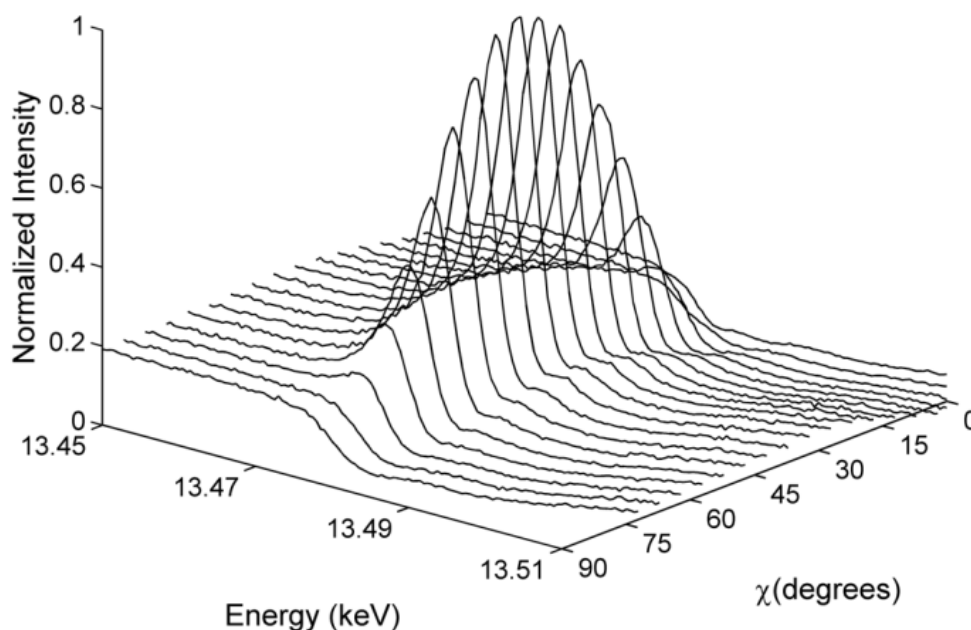


Figure 2.13 Plot of normalized intensity as a function of χ rotation and X-ray energy for a single crystal of 1-bromoadamantane/thiourea. The χ scan changes significantly with energy, when the energy is outside the range 13.47 \pm 0.02 keV no X-ray birefringence from is observed. Reprinted with permission from Reference 23.²³

To determine the X-ray energy for use in XBI experiments, X-ray absorption spectra are recorded for two orientations of the sample. Figure 2.14 (a) shows an example for 1-bromoadamantane/thiourea, with X-ray absorption at the Br K-edge. The X-ray dichroism spectra is calculated by taking the difference from the two X-ray absorption spectra, where the X-ray absorption spectra have a difference in χ of 90° . The X-ray birefringence spectra is then calculated from the X-ray dichroism spectra using the Kramers-Kronig transform (Equation 1.8). Figure 2.14 (b) shows that the energy corresponding to maximum X-ray birefringence is equivalent to halfway up the K-edge in the X-ray absorption spectrum recorded with the crystal horizontal, leading to better contrast in the XBI images.^{23,32}

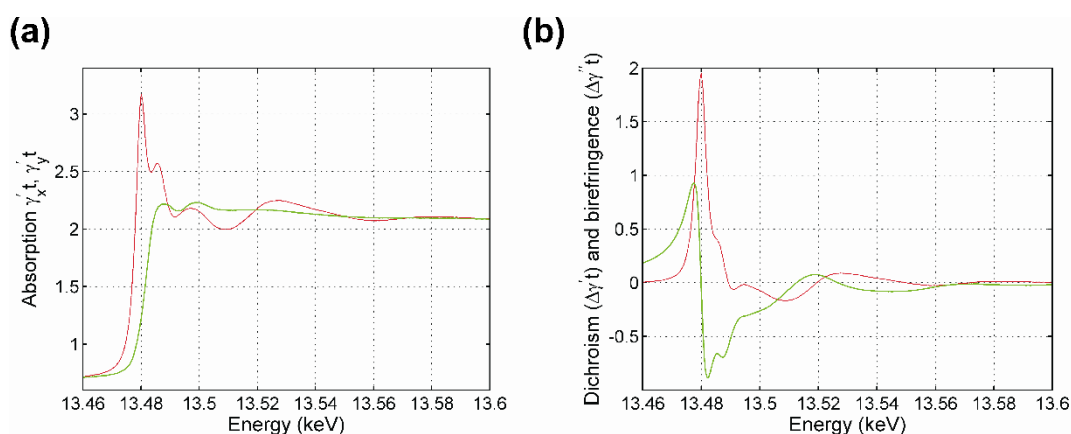


Figure 2.14 (a) X-ray absorption spectra for a single crystal of 1-bromoadamantane/thiourea with the *c*-axis oriented parallel (red) and perpendicular (green) to the direction of polarization of the incident linearly polarized X-ray beam. (b) X-ray dichroism calculated from the difference of the two spectra in part a (red) and the X-ray birefringence spectrum (green) calculated using the Kramers-Kronig transform. Reprinted with permission from Reference 23.²³

2.1.2 Previous work

2.1.2.1 X-ray birefringence from a model anisotropic material

Initial experiments determined that an ideal model material to study X-ray birefringence would have all bonds of interest aligned parallel. In the case of XBI studies at the Br K-edge the 1-bromoadamantane/thiourea inclusion compound proved ideal in this regard.

Thiourea inclusion compounds form a tunnel structure (with the long needle axis of the crystal parallel to the tunnel axis) with the guest molecules confined within the thiourea host tunnel. In the case of 1-bromoadamantane/thiourea, the C-Br bonds are aligned parallel to the tunnel axis and hence parallel to the long needle axis of the crystal morphology (Figure 2.15 (c)). Given the highly anisotropic distribution of the C-Br bond orientations, the material is expected to exhibit significant X-ray birefringence at the Br K-edge.

The C-Br bonds are parallel to the x -axis when $\chi = 0^\circ$, rotating the crystal around the beam direction showed a significant variation in intensity with a maximum at a bond orientation of $\chi = 45^\circ$ (Figure 2.15 (a)). Behaving as would be expected for birefringence observed using a POM and following the sine curve predicted from Equation 1.6. Rotating the crystal about its long axis (ϕ) showed very little change in intensity; this is expected as the X-ray optic axis (parallel to the C-Br bond axis) is parallel to this rotation axis (Figure 2.15 (b)). Thus, the first demonstration of X-ray birefringence to study anisotropy in a material proved successful.²³

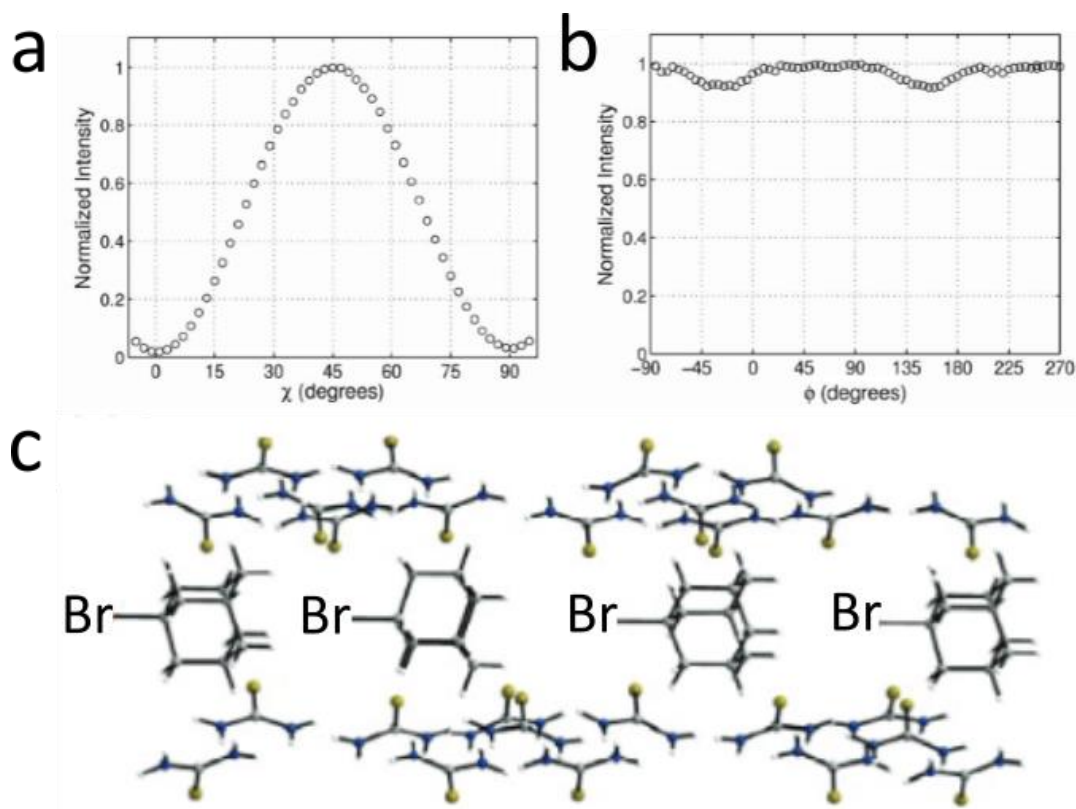


Figure 2.15 X-ray birefringence normalized intensity for a single crystal of 1-bromoadamantane/thiourea (a) as a function of the χ rotation and (b) as a function of the ϕ rotation. (c) Crystal structure of the 1-bromoadamantane/thiourea inclusion compound viewed perpendicular to the thiourea tunnel with 1-bromoadamantane as the guest molecule. Adapted from Reference 23.²³

2.1.2.2 Orientational Changes due to Phase Transitions

The next material to be studied was the bromocyclohexane/thiourea inclusion compound; the material was of interest due to a known order/disorder phase transition at 233 K. At high temperature (298 K) the guest molecules undergo isotropic reorientational motion. At low temperature, the guest motion becomes gradually more restricted, and exhibits a well-defined orientation of the C-Br bonds (Figure 2.16).²⁴

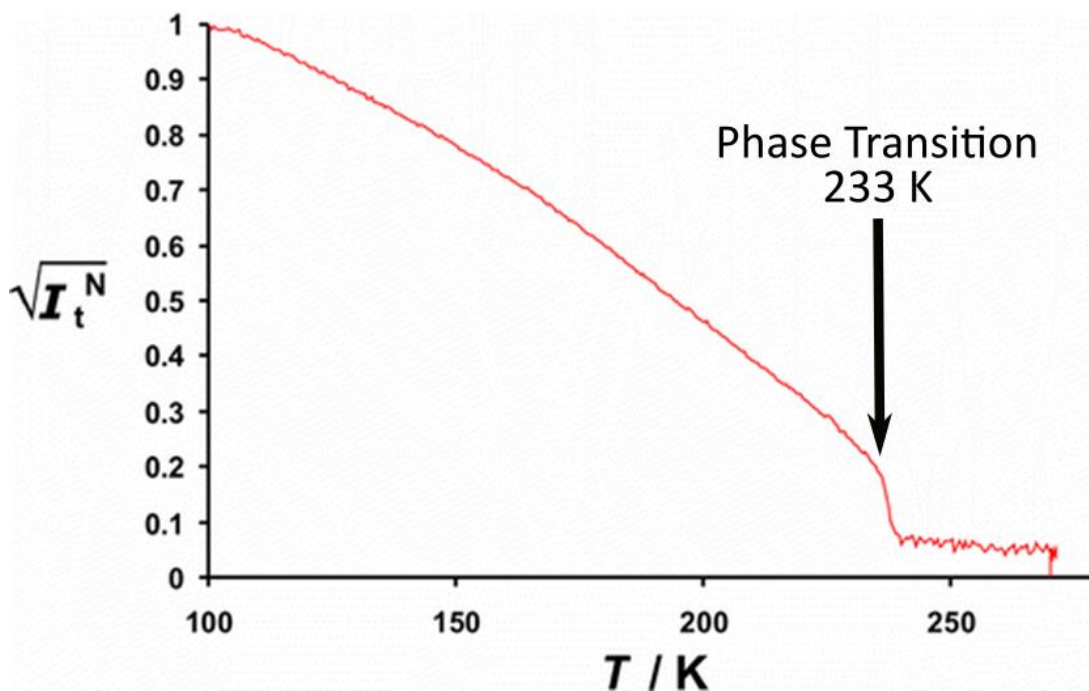


Figure 2.16 Normalized X-ray birefringence intensity as a function of temperature for a single crystal of bromocyclohexane/thiourea oriented at $\chi = -10^\circ$ and $\varphi = 0^\circ$. A gradual increase in intensity as the bromocyclohexane guest molecule becomes more ordered as the temperature is decreased. Adapted from Reference 24.²⁴

XBI images of the low-temperature phase show that the crystal forms domains (Figure 2.17) with a bright region in the centre and dark regions to either side. The intersection of the domains of the c -axis (long needle axis) at an angle of roughly 136° , meaning that the domain boundary can be assigned to the crystallographic $(10\bar{1})$ plane.³³

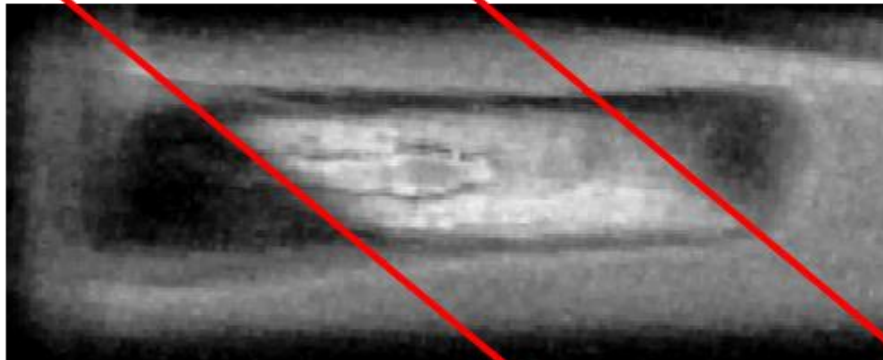


Figure 2.17 XBI image recorded at 20 K for the low-temperature phase of bromocyclohexane/thiourea oriented at $\chi = 10^\circ$ and $\varphi = 180^\circ$. At $\chi = 10^\circ$, the angle of the C-Br bond (the effective X-ray optic axis) with respect to the incident polarized X-rays is ca. 62° . Pictured in the image are the domains in the crystal, which have different orientations of the C-Br bonds and hence a difference in XBI intensity.³³

This material is also interesting as it highlights the difference between XBI and POM. Figure 2.18 shows both the XBI images and POM images for the high-temperature phase of bromocyclohexane/thiourea. The XBI images show no change in intensity with orientation, as the bromocyclohexane guest molecules (and hence the C-Br bonds) are isotropic in the high temperature phase. The POM images show uniaxial behaviour as illustrated by the changes in intensity with a change in orientation of the crystal. The optic axis in this case is dependent on the rhombohedral crystal symmetry of the thiourea tunnel structure.

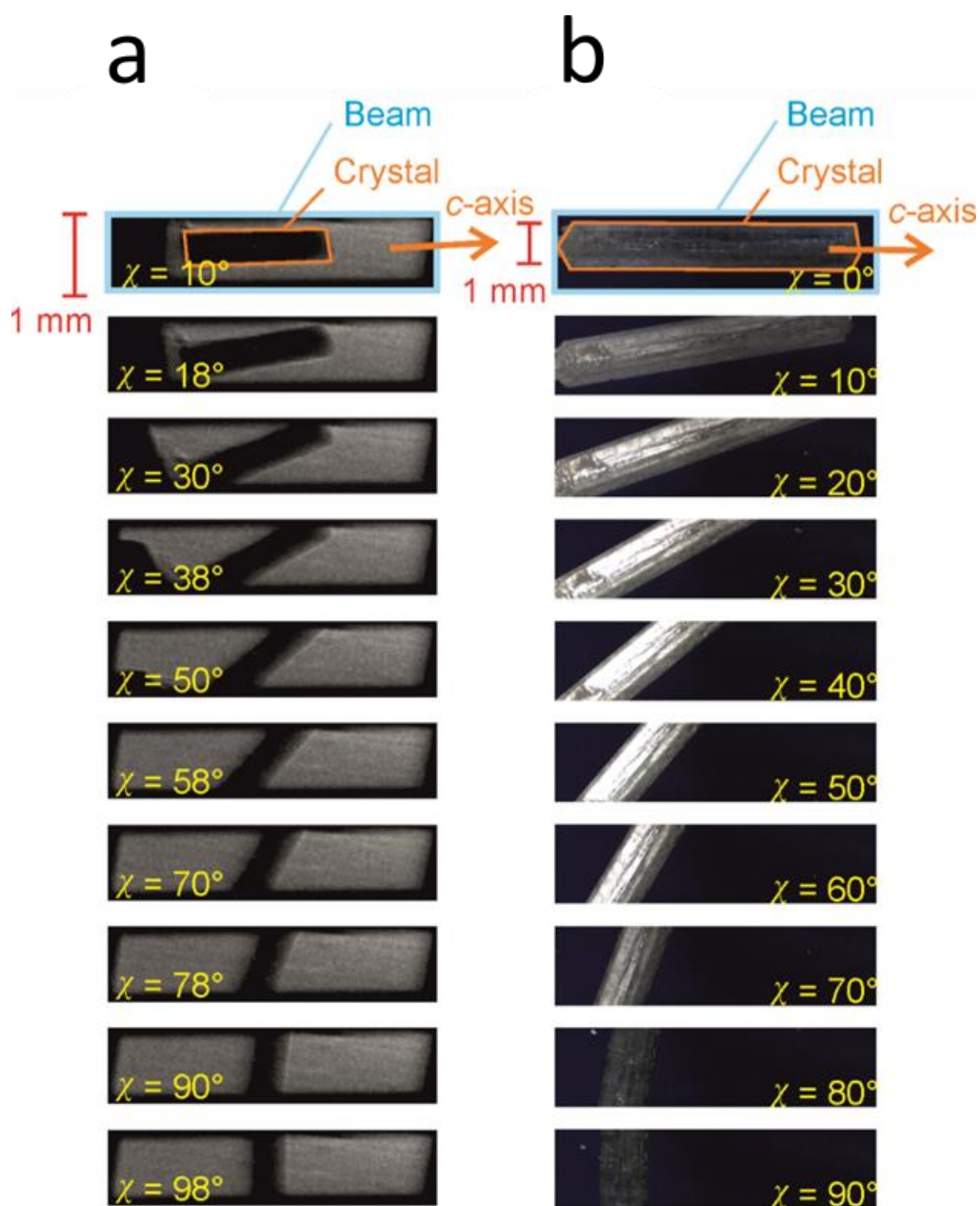


Figure 2.18 Images of a single crystal of bromocyclohexane/thiourea as a function of χ rotation for (a) XBI (298 K) and (b) POM (293 K). Adapted from Reference 33.³³

2.1.2.3 Time-Averaged Resultant of Orientational Distribution

Next studied was the effects of anisotropic molecular dynamics on XBI behaviour, using 1,8-dibromooctane/urea and 1, 10-dibromodecane/urea inclusion compounds. In these materials, the C-Br bonds are not aligned directly along the tunnel axis but are instead distributed on a cone by rotation around the tunnel axis (Figure 2.19).

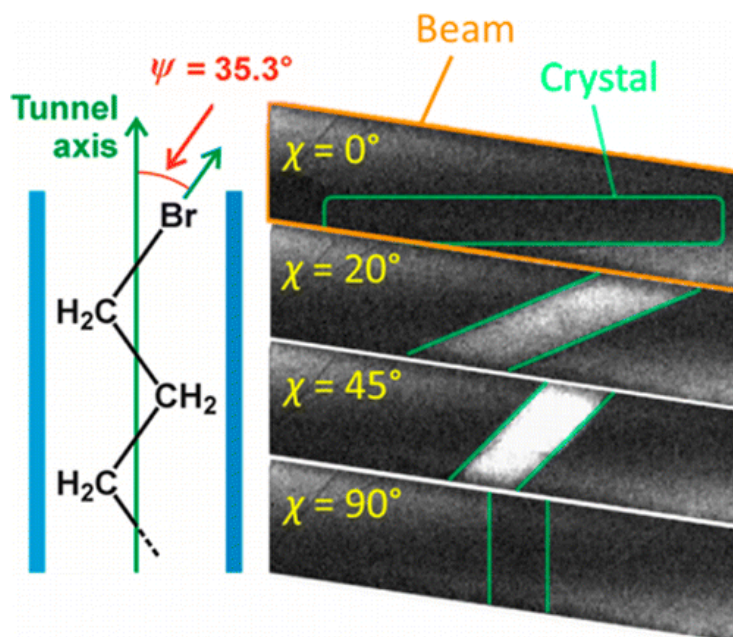


Figure 2.19 Orientation of the C-Br bond of an α,ω -dibromoalkane guest molecule in the urea tunnel and XBI images of a single crystal of 1,10-dibromodecane/urea as a function of χ rotation.³²

However, the XBI results were comparable to the 1-bromoadamantane/thiourea inclusion compound (Section 2.1.2.1), with minima in intensity observed at $\chi = 0^\circ$ and $\chi = 90^\circ$ and a maximum at $\chi = 45^\circ$. Thus indicating that the resultant C-Br bond vector (representing a time-averaged orientation) is projected along the long axis of the single crystal. In the low-temperature phase, the results do not necessarily correspond to a time average but could instead be a space average.³²

2.1.2.4 Liquid Crystals

XBI has also been utilized to study molecular orientational ordering in liquid-crystalline phases. A magnetic field was used to align the molecular axis of the liquid crystal parallel to the magnetic field direction (Figure 2.20).

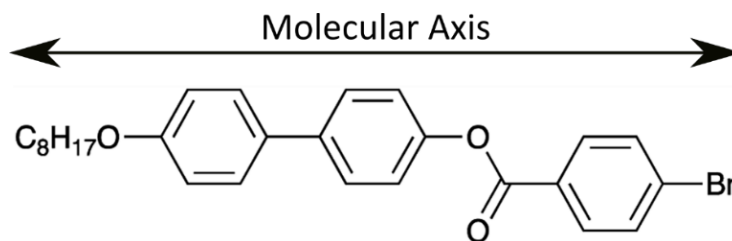


Figure 2.20 Liquid crystal used for XBI measurements. Molecular axis is parallel to the C-Br bond direction.

As the C-Br bond is parallel to the molecular axis, XBI using linearly polarized incident X-rays tuned to the bromine K-edge can be used to report on molecular alignment. The sample cell is mounted on the beamline and the sample and the magnetic field are rotated together so, in this case, χ denotes rotation of the magnetic field (magnetic field direction is acting as the reference axis). There is also a variable temperature capability built into the cell, as the degree of ordering of the molecule in the magnetic field is dependent on temperature (Figure 2.21).

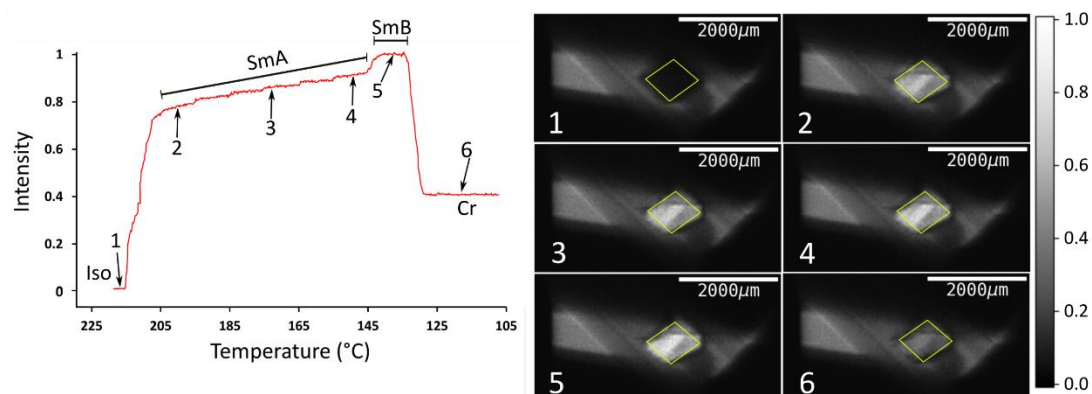


Figure 2.21 Transmitted X-ray intensity as a function of temperature for a liquid crystal along with XBI images at selected temperatures. Magnetic field is fixed at $\chi = 45^\circ$. Adapted from Reference 8.⁸

In this experiment, transmitted X-ray intensity was recorded as a function of temperature with the magnetic field fixed at $\chi = 45^\circ$. An increase in intensity or brightness corresponds to greater orientational ordering, corresponding to a greater degree of alignment of the C-Br bonds, along the magnetic field direction. The first phase imaged was the isotropic (Iso) liquid phase where the C-Br bonds are completely randomly oriented, and the intensity is therefore essentially zero.

Upon decreasing the temperature, there is a large and sharp increase in intensity at around 215°C as the sample becomes more ordered (nematic phase). There is an increase in intensity as the temperature is lowered due to the liquid crystal going through different phases (SmA, SmB), which get progressively more ordered until crystallization (Cr), at which the intensity drops as the sample is polycrystalline.⁸

XBI imaging has been revealed to be a powerful technique for determining the local orientational properties of anisotropic materials as long as the incident X-ray energy is tuned to the absorption edge of an element in the material. XBI has the capability to examine partially ordered materials and order-disorder phase transitions, revealing the formation of orientationally distinct domains, and with the potential to study the propagation and change in domain boundaries during phase transitions.

2.2 Diffraction

Scattering of X-rays from a crystal produces a diffraction pattern. The positions and relative intensities of the scattered X-rays depend on the arrangement of the atoms in the crystal structure. Bragg's law (Equation 1.7) can be used to convert the diffraction peak positions into d-spacings, which are unique to each crystal structure. Analysis of peak positions (d-spacing) is used to determine unit cell information. Analysis of relative intensities of diffracted beams gives the arrangement of atoms within the unit cell.

2.2.1 Single Crystal X-ray Diffraction

For single crystal X-ray diffraction (SCXRD), a full diffraction pattern appears as a pattern of spots (diffraction maxima) oriented in 3D space (recorded for different orientations of the crystal, using a 2D detector). The positions of the spots relate to the unit cell of the crystal structure, and the relative intensities relate to the arrangement of atoms within the unit cell.

In the present work, single crystal XRD data were collected on an Agilent SuperNova Dual Atlas diffractometer with a mirror monochromator [using either Cu K_{α} ($\lambda = 1.5418 \text{ \AA}$) or Mo K_{α} ($\lambda = 0.7107 \text{ \AA}$) radiation], equipped with an Oxford Cryostreams cooling apparatus.

2.2.2 Powder X-ray Diffraction

X-ray powder diffraction (PXRD), rather than discrete diffraction data as for SCXRD, produces diffraction cones, but the 1D detector used in powder diffraction only detects a thin slice of this overall cone. The diffraction pattern is seen as a continuous line with peaks corresponding to the intersection of cones of scattering by the detector (Figure 2.22). Similarly to SCXRD, PXRD can be used to determine a crystal structure, although the process is more complicated due to loss of information as the 3D information provided by SCXRD is compressed into 1D data.

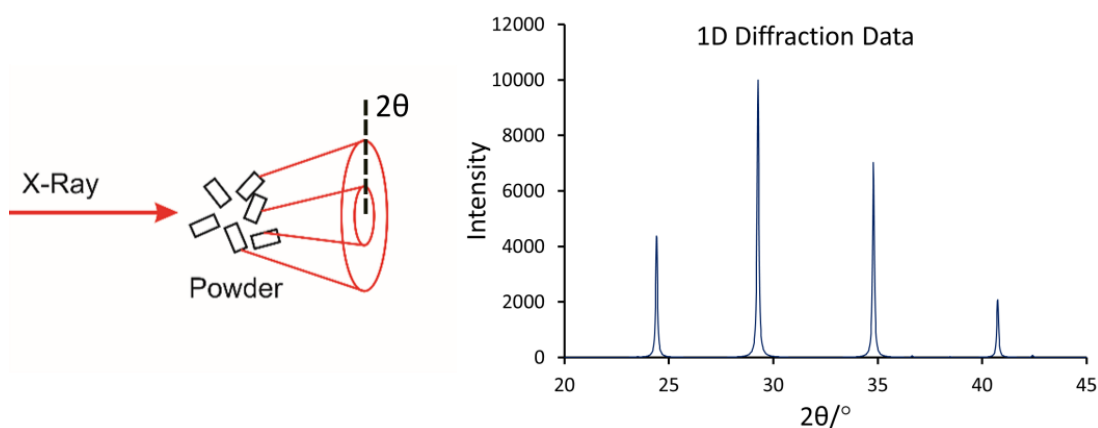


Figure 2.22 Diffraction cones produced when a powder sample is exposed to X-rays. PXRD data is recorded as a slice of the cone, with peaks corresponding to the intersection of the scattered cones. PXRD pattern shown corresponds to the ammonium cyanate crystal structure.³⁴ Adapted from Reference 35.³⁵

There are multiple steps to the determination of a crystal structure from powder XRD data.

1. Indexing (determination of unit cell parameters and space group)
2. Profile fitting (Le Bail or Pawley)
3. Structure Solution
4. Rietveld Refinement

The program CRYSFIRE³⁶ uses a variety of algorithms to index the peak positions in the diffraction pattern and therefore to find the unit cell and a likely space group (symmetry present in the unit cell).

Space groups are determined from consideration of systematic absences (certain symmetry elements cause destructive interference between diffracted rays for certain scattering directions, and no maxima are observed at these positions). Thus, a probable space group can be determined. The contents of the asymmetric unit (the smallest portion of the unit cell that cannot be repeated by symmetry) can be established during indexing. The unit cell volume and relative atomic mass are used to calculate a density. The calculated density can be compared to the density of similar compounds to determine the number of molecules in the asymmetric unit.

A common problem with PXRD is the presence of impurity phases, as these unwanted phases will also produce diffraction maxima. Assigning peaks to each phase can be time-consuming and sometimes impossible if the impurity phase also has an unknown crystal structure and therefore unknown diffraction pattern.

The Le Bail method³⁷ is used to fit the profile of the powder diffraction pattern by optimizing the unit cell parameters and peak profile parameters, which are required in the following stage of the structure determination. The structures in this thesis have been solved by the direct-space strategy, implemented using a genetic algorithm³⁸⁻⁴⁰ (GA) within the program EAGER. The direct-space strategy efficiently samples “trial structures” using global optimisation algorithms to find the crystal structure with a simulated powder pattern representing the best fit to the experimental powder pattern.

Within EAGER in the first generation (P_j) of the GA calculation, the population comprises of randomly generated crystal structures, each defined by a unique set of variables (Γ). The GA then uses a variety of processes to mimic biological evolution. These operations include natural selection, mating and mutation (Figure 2.23). These operations convert the population in a given generation (P_j) into an improved population in the next generation (P_{j+1}). It should be noted that the number of trial structures in the population in each generation is constant. During the evolution from P_j to P_{j+1} , N_m mating and N_x mutation operations are carried out.

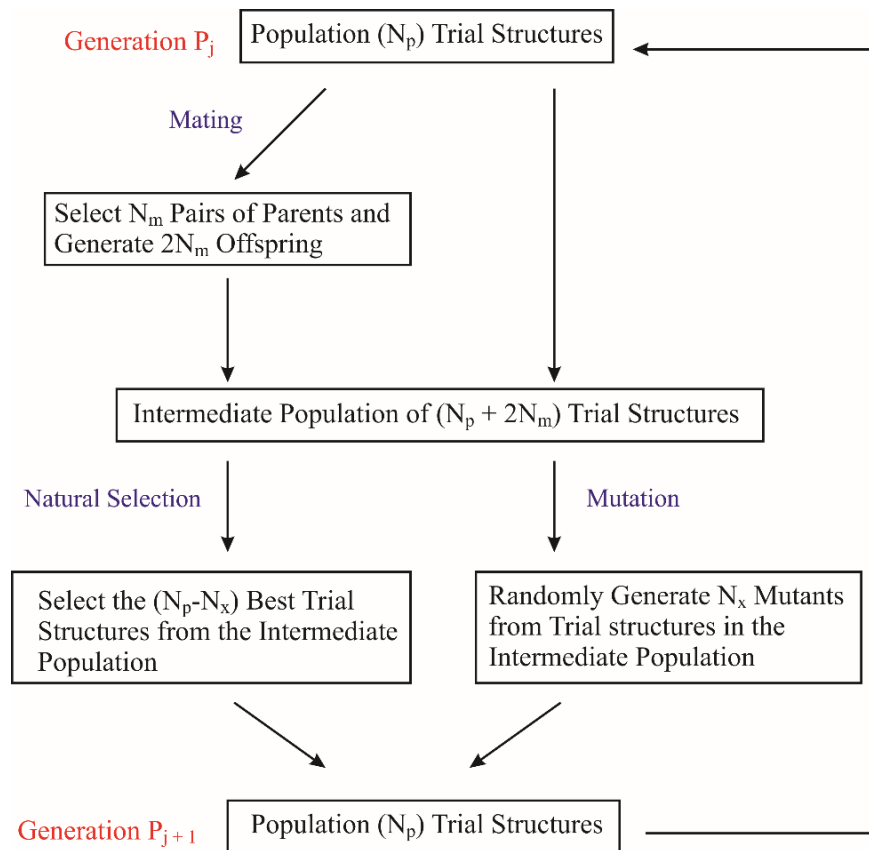


Figure 2.23 Flow diagram showing the operations carried out during the evolution of the population of trial crystal structures from one generation (P_j) to the next generation (P_{j+1}) in the GA technique for structure solution. Each generation has N_p trial structures and N_m mating and N_x mutation operations are carried out. Adapted from Reference 41.⁴¹

As shown in Figure 2.23, N_m parents are selected from the population to undergo mating operations. By distributing the unique structural variables (Γ) of the two parent structures between the “offspring”, two new structures are produced. No new variables are produced during the mating operation, whereas the mutation operation is used to produce new variables by changing random variables in a number (N_x) of structures randomly selected from the population. The mutation can take two forms:

- Static mutation – completely random values of selected variables
- Dynamic mutation – a new value for selected variables is derived from the previous value by a small random change.

The simulated powder pattern calculated for each crystal structure in the population and the experimental powder pattern are compared to assess their similarity. The difference between the simulated and experimental powder pattern is measured using R_{wp} (the weighted profile R-factor).

$$R_{wp} = 100 \times \sqrt{\frac{\sum_i w_i (y_i - y_{ci})^2}{\sum_i w_i y_i^2}} \quad (2.2)$$

where y_i denotes the intensity of the i th data point in the experimental powder XRD pattern, y_{ci} denotes the intensity of the i th data point in the calculated powder XRD pattern and w_i is the weighting factor of the i th point.

Finally, Rietveld refinement⁴² optimizes the structure solution by allowing refinement of the atomic positions and atomic displacement parameters. The least-squares method is used to refine the variables defining the simulated crystal structure and the profile of the powder pattern to get the best fit between the simulated and experimental data (assessed again using R_{wp}). In Rietveld refinement, constraints are used to maintain molecular geometries, bond lengths, angles and planes at chemically and structurally reasonable values. For more information on powder diffraction, please see a review by Kenneth D. M. Harris and Eugene Y. Cheung (2004).⁴¹

3 Theoretical XBI Behaviour

In this Chapter, we describe a procedure to allow XBI behaviour to be predicted for known structures and extending previous work to materials containing two or more distinct orientations of the C-Br bonds. The modelling described in this Chapter is only semi-quantitative. Samples that are studied using XBI and upon which theoretical calculations are performed, are often inhomogeneous because the aim is to image a variation in properties. This inhomogeneity is not easily included in the theoretical models, so rather than giving quantitative results, the theoretical calculations confirm a feasible explanation for the underlying physics.

The methodology developed here describes the change in intensity of a linearly polarized X-ray as it passes through the XBI experimental setup, and is an extension of previous work.^{23,43} The calculations are suitable for any sample for which electric dipole transitions dominate the X-ray absorption, and allow any orientation of the sample relative to this experimental set-up to be considered. Other factors taken into account include non-perfect linear polarization and a non-ideal polarization analyzer. Using this methodology, it is shown that XBI data can be predicted with remarkable accuracy.

The X-ray absorption by an isotropic material can be described using:

$$\varepsilon_1 = \varepsilon_0 e^{-\gamma t/2} \quad (3.1)$$

$$\frac{I_1}{I_0} = \frac{|\varepsilon_1|^2}{|\varepsilon_0|^2} = e^{-\gamma t} \quad (3.2)$$

These equations refer to the amplitude (ε) and intensity (I) of X-rays transmitted through an isotropic material of known thickness (t) and absorption coefficient (γ), where the subscript 0 indicates the incident X-rays and subscript 1 indicates the transmitted X-rays. The absorption coefficient (γ) can be determined experimentally or determined from the crystal structure of the sample.

3.1 Interaction of incident X-rays with the Sample

An anisotropic sample must be considered in three dimensions, due to the symmetry properties of the sample and dependence on the orientation of the sample relative to the experimental set-up. Therefore, the absorption coefficient of the sample must be described using a symmetric second-rank tensor $\underline{\gamma}$. Adopting the framework of Cartesian tensors, $\underline{\gamma}$ is determined by the following equation:

$$\underline{\gamma} = a(E) + b(E)\hat{\varepsilon}_i\hat{\varepsilon}'_jT_{ij} \quad (3.3)$$

The tensor describing the absorption coefficient can also be written as:

$$\begin{bmatrix} a(E) + b(E)T_{11} & b(E)T_{12} & b(E)T_{13} \\ b(E)T_{21} & a(E) + b(E)T_{22} & b(E)T_{23} \\ b(E)T_{31} & b(E)T_{32} & a(E) + b(E)T_{33} \end{bmatrix} \quad (3.4)$$

The scalar $a(E)$ is the isotropic absorption coefficient, while the scalar $b(E)$ gives the anisotropic absorption coefficient. If $a(E)$ and $b(E)$ are determined from a simple system with well-defined C-Br bonds, then they can be used to calculate any average anisotropy for multiple bonds within a unit cell. In previous cases, we have assumed that $a(E)$ and $b(E)$ are close to one (for a sample with strong dichroism and optimum thickness, they tend to be close to one).

The $\hat{\varepsilon}_i^{(n)}$ notation corresponds to the components of photon polarization (electric field) along three Cartesian axes, i.e. $\varepsilon_1 = \hat{\underline{\varepsilon}} \cdot \hat{\underline{x}}$, $\varepsilon_2 = \hat{\underline{\varepsilon}} \cdot \hat{\underline{y}}$, $\varepsilon_3 = \hat{\underline{\varepsilon}} \cdot \hat{\underline{z}}$. As XBI uses an experimental coordinate system which has the z -axis as the propagation direction of the incident X-ray beam and as light is a transverse wave, $\hat{\underline{\varepsilon}} \cdot \hat{\underline{z}}$ is equal to zero.

In Equation 3.3, T_{ij} is a traceless symmetric tensor determined from the bond vectors (containing the X-ray absorbing element) in the unit cell. To determine T_{ij} , we assume that the bonding is uniaxial. Therefore, the net response of multiple bonds in a material is the resultant vector summation of all the individual bond orientations. Thus, assuming N bonds in a unit cell, Equation, 3.5 is produced.

$$T_{ij} = \frac{1}{N} \sum_{n=1}^N \begin{bmatrix} x_n^2 - \frac{1}{3} & x_n y_n & x_n z_n \\ y_n x_n & y_n^2 - \frac{1}{3} & y_n z_n \\ z_n x_n & z_n y_n & z_n^2 - \frac{1}{3} \end{bmatrix} \quad (3.5)$$

Where x_n , y_n and z_n are the Cartesian unit vector components for the n^{th} bond. The tensor for a unit cell can be determined by calculating the vectors for each bond of interest. Before the vectors are calculated, a transformation (Equation 3.6) is needed to convert the fractional coordinates (u , v , w) into a Cartesian coordinate system (x_s , y_s , z_s).

$$\begin{bmatrix} x_s \\ y_s \\ z_s \end{bmatrix} = \begin{bmatrix} a & b \cos(\gamma) & c \cos(\beta) \\ 0 & b \sin(\gamma) & c \frac{\cos(\alpha) - \cos(\beta) \cos(\gamma)}{\sin(\gamma)} \\ 0 & 0 & \frac{V}{ab \sin(\gamma)} \end{bmatrix} \begin{bmatrix} u \\ v \\ w \end{bmatrix} \quad (3.6)$$

Where a , b , c , α , β , γ correspond to lengths and angles of the unit cell and V is the unit cell volume. The vectors are calculated by subtracting the coordinates of one atom (x_s^B , y_s^B , z_s^B) from the bonded atom (x_s^A , y_s^A , z_s^A).

$$r_x, r_y, r_z = x_s^A, y_s^A, z_s^A - x_s^B, y_s^B, z_s^B \quad (3.7)$$

Inputting the vectors into Equation 3.5 thus gives a tensor (T) describing the bond orientations, which can be expressed as a three dimensional ellipsoid. However, at this point the tensor (T) is still a Cartesian frame that needs to be rotated to the laboratory frame, using a unitary transformation (V), where T is the rotated tensor:

$$T \rightarrow VTV' \quad (3.8)$$

The unitary transformation is calculated from three separate rotations. The χ and ϕ rotations of the crystal relative to the laboratory reference frame each have their rotation matrix and correspond to the χ and ϕ rotations in XBI experiments discussed in detail in Section 2.1.1.3. U denotes the rotation matrix that brings the Cartesian frame produced from Equation 3.6 and laboratory frame into coincidence when $\chi = 0^\circ$ and $\phi = 0^\circ$.

$$V = R_z(\chi)R_x(\varphi)U = \begin{bmatrix} \cos \chi & -\sin \chi & 0 \\ \sin \chi & \cos \chi & 0 \\ 0 & 0 & 1 \end{bmatrix} \begin{bmatrix} 1 & 0 & 0 \\ 0 & \cos \varphi & -\sin \varphi \\ 0 & \sin \varphi & \cos \varphi \end{bmatrix} U \quad (3.9)$$

As discussed earlier, in anisotropic materials, the transmitted X-ray intensities along x and y are different. There is no z -component as X-rays are a transverse wave propagated along the z -axis. Consequently, the complex absorption coefficient can be written as a 2×2 matrix:

$$\Gamma = \begin{bmatrix} \gamma_{xx} & \gamma_{xy} \\ \gamma_{yx} & \gamma_{yy} \end{bmatrix} \quad (3.10)$$

where the absorption coefficient and the tensor description (Equation 3.4) of the crystal are related by the following equations:

$$\gamma_{xx} = a(E) + b(E) T_{11} \quad (3.11)$$

$$\gamma_{yy} = a(E) + b(E) T_{22} \quad (3.12)$$

$$\gamma_{xy} = \gamma_{yx} = b(E) T_{12} = b(E) T_{21} \quad (3.13)$$

The amplitude and polarization of the X-rays as they propagate through a material is described by the transmittance matrix A . The relationship of the absorption coefficients to the scattering operator is complicated due to having to calculate the exponential of a matrix.

$$A = e^{-\Gamma t/2} \quad (3.14)$$

$$A = e^{-(\gamma_{xx} + \gamma_{yy})t/4} \begin{bmatrix} \cosh \Phi - \frac{(\gamma_{xx} - \gamma_{yy})t \sinh \Phi}{4\Phi} & \frac{\gamma_{xy} t \sinh \Phi}{2\Phi} \\ \frac{\gamma_{yx} t \sinh \Phi}{2\Phi} & \cosh \Phi + \frac{(\gamma_{xx} - \gamma_{yy})t \sinh \Phi}{4\Phi} \end{bmatrix} \quad (3.15)$$

$$\Phi = \frac{t}{4} \sqrt{(\gamma_{xx} - \gamma_{yy})^2 + 4\gamma_{xy}\gamma_{yx}} \quad (3.16)$$

3.2 Polarization State of Incident Beam

The state of polarization of the incident beam is described using the polarization density matrix μ . The matrix μ is expressed in Stokes parameters (Equation 3.17), where P_3 is linear polarization along x , P_2 is the circular or elliptical polarization, and P_1 is the linear polarization at 45° from x in the xy -plane. With almost perfect linear polarization $P_1 = P_2 = 0$ and $P_3 = 1$. Note that we follow the definitions of Stokes parameters from References 19 and 44.^{19,44}

$$\mu = \frac{1}{2} \begin{bmatrix} 1 + P_3 & P_1 - iP_2 \\ P_1 + iP_2 & 1 - P_3 \end{bmatrix} \quad (3.17)$$

3.3 Interaction of X-ray beam with Polarization Analyzer

A_p is the transmittance matrix of the polarization analyzer and describes the change in the X-ray beam after encountering the polarization analyzer. This matrix is derived from the product of two rotation matrices relevant to the polarization analyzer.

One matrix describes rotation about the beam direction:

$$R_\eta = \begin{bmatrix} \cos \eta & -\sin \eta & 0 \\ \sin \eta & \cos \eta & 0 \\ 0 & 0 & 1 \end{bmatrix} \quad (3.18)$$

where η is the angle between transmitted polarization by the polarization analyzer and x -axis. As the polarization analyzer selects the vertical component (y -axis) the angle η is always taken as 90° .

The other rotation matrix describes the deflection of the X-ray beam by 2θ at the analyzer (Equation 3.19). The 2θ value is determined using Bragg's law (Equation 1.7) and will vary depending on the X-ray energy and polarization analyzer used (see Page 28).

$$R_{2\theta} = \begin{bmatrix} 1 & 0 & 0 \\ 0 & \cos 2\theta & -\sin 2\theta \\ 0 & \sin 2\theta & \cos 2\theta \end{bmatrix} \quad (3.19)$$

The transformation $R_{2\theta}R_\eta$ gives:

$$A_p = \begin{bmatrix} \cos \eta & -\sin \eta & 0 \\ \cos 2\theta \sin \eta & \cos 2\theta \cos \eta & -\sin 2\theta \\ \sin 2\theta \sin \eta & \sin 2\theta \cos \eta & \cos 2\theta \end{bmatrix} \quad (3.20)$$

Only the xy -components are selected due to XBI using an experimental coordinate system which has the z -axis as the propagation direction of the incident X-ray beam and light is a transverse wave. Thus giving the final transmittance matrix as:

$$A_p = \begin{bmatrix} \cos \eta & -\sin \eta \\ \cos 2\theta \sin \eta & \cos 2\theta \cos \eta \end{bmatrix} \quad (3.21)$$

3.4 XBI calculation

In the XBI calculations, the density matrix formalism⁴⁵ has been adapted to describe the changes the beam polarization experiences in the XBI set-up, as it interacts with multiple components which are polarization sensitive. The ratio of intensity recorded at the detector to incident intensity can be determined by the trace (Tr, sum of the diagonal elements) of the matrix μ (polarization state of incident beam), operated on either side by matrices that represent the interaction with the polarization analyzer (A_p), and transmission through the sample (A), where \dagger denotes the transpose of the complex conjugate.

$$\frac{I_1}{I_0} = \text{Tr}(A_p A \mu A^\dagger A_p^\dagger) \quad (3.22)$$

3.5 Theoretical XBI Calculations for 1-bromoadamantane/thiourea

For illustrative purposes, we consider the crystal structure of 1-bromoadamantane/thiourea and determine the predicted XBI behaviour at the bromine K-edge. The crystal structure of 1-bromoadamantane/thiourea is trigonal ($P321$), and is shown in Figure 3.1. The C-Br bond direction, which represents the X-ray optic axis, is parallel to the c -axis, which corresponds to the long needle axis of the crystal morphology.

We recall that XBI is “parity even”, so C-Br bond vectors in anti-parallel orientations exhibit identical behaviour with regard to XBI. This is important with respect to 1-bromoadamantane/thiourea as the orientation of C-Br within different tunnels are likely to be in anti-parallel orientations.

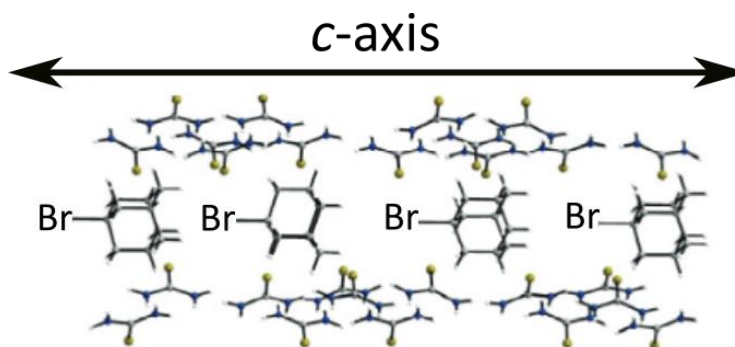


Figure 3.1 Crystal structure of 1-bromoadamantane/thiourea. The C-Br bond direction is parallel to the tunnel axis (c-axis).

The atom coordinates for the carbon and bromine atoms making up the C-Br bonds within the unit cell of 1-bromoadamantane/thiourea are shown in Table 3.1.

Atom Coordinates					
Carbon			Bromine		
x	y	z	x	y	z
1.0	1.0	0.3765	1.0	1.0	0.4544
1.0	1.0	0.3055	1.0	1.0	0.2275
1.0	1.0	0.0463	1.0	1.0	0.1242
2/3	1/3	0.0705	2/3	1/3	-0.0070
2/3	1/3	0.1276	2/3	1/3	0.2052
2/3	1/3	0.3780	2/3	1/3	0.2989
2/3	1/3	0.4696	2/3	1/3	0.5474
2/3	1/3	0.7368	2/3	1/3	0.6584
2/3	1/3	0.8229	2/3	1/3	0.9008

Table 3.1 Atom coordinates of the carbon and bromine atoms making up the C-Br bonds in the unit cell of 1-bromoadamantane/thiourea (200 K).¹⁷ Atom coordinates are in the fractional coordinate system.

The vectors corresponding to each C-Br bond are determined using Equation 3.7 and converted from fractional coordinates into a Cartesian coordinate system using Equation 3.6 (Table 3.2).

Vector Coordinates					
Fractional			Cartesian		
x	y	z	x	y	z
0.0	0.0	-0.0779	0.0	0.0	-1.9283
0.0	0.0	0.0780	0.0	0.0	1.9308
0.0	0.0	-0.0779	0.0	0.0	-1.9283
0.0	0.0	0.0775	0.0	0.0	1.9184
0.0	0.0	-0.0776	0.0	0.0	-1.9209
0.0	0.0	0.0791	0.0	0.0	1.9580
0.0	0.0	-0.0780	0.0	0.0	-1.9258
0.0	0.0	0.0784	0.0	0.0	1.9407
0.0	0.0	-0.0779	0.0	0.0	-1.9283

Table 3.2 Vectors of the C-Br bonds in 1-bromoadamantane/thiourea converted from fractional to Cartesian coordinates using Equation 3.6.

These vectors are used in the tensor (T_{ij}) calculation (Equation 3.5), to give a tensor of:

$$T_{ij} = \begin{bmatrix} -0.333 & 0 & 0 \\ 0 & -0.333 & 0 \\ 0 & 0 & 3.396 \end{bmatrix}$$

The tensor is currently in a Cartesian coordinate system but not the experimental coordinate system. The tensor needs to be rotated to the orientation where the crystal is at $\chi = 0^\circ$ and $\varphi = 0^\circ$, using the rotation matrix U (Equation 3.9). To find the tensor orientation at $\chi = 0^\circ$ and $\varphi = 0^\circ$, the orientation of the crystal structure in the experimental coordinate system must be known.

The crystallographic c -axis (long needle axis, reference axis) is parallel to the x -axis in the experimental system when $\chi = 0^\circ$, in the current Cartesian coordinate system the crystallographic c -axis is parallel to the z -axis in the experimental coordinate system. Therefore the rotation for 1-bromoadamantane/thiourea is quite simple requiring a rotation matrix which will rotate the crystal long-axis from parallel to the z -axis to parallel to the x -axis. The orientation of the sample when $\varphi = 0^\circ$ is unknown. However, as the C-Br bond direction is parallel to the reference axis there should be no change in the tensor as a function of φ . Thus, the U rotation matrix used is:

$$U = \begin{bmatrix} 0 & 0 & -1 \\ 0 & 1 & 0 \\ 1 & 0 & 0 \end{bmatrix}$$

The rotated tensor at $\chi = 0^\circ$ and $\varphi = 0^\circ$ is shown in Figure 3.2. The tensor is clearly elongated along the x -axis as expected from the fact that the C-Br bonds are aligned parallel to the x -axis in this orientation. Furthermore, viewing the tensor along the x -axis (Figure 3.2 (c)) shows the tensor is isotropic about the reference axis, thus confirming that no change in X-ray birefringence should be observed with φ rotation.

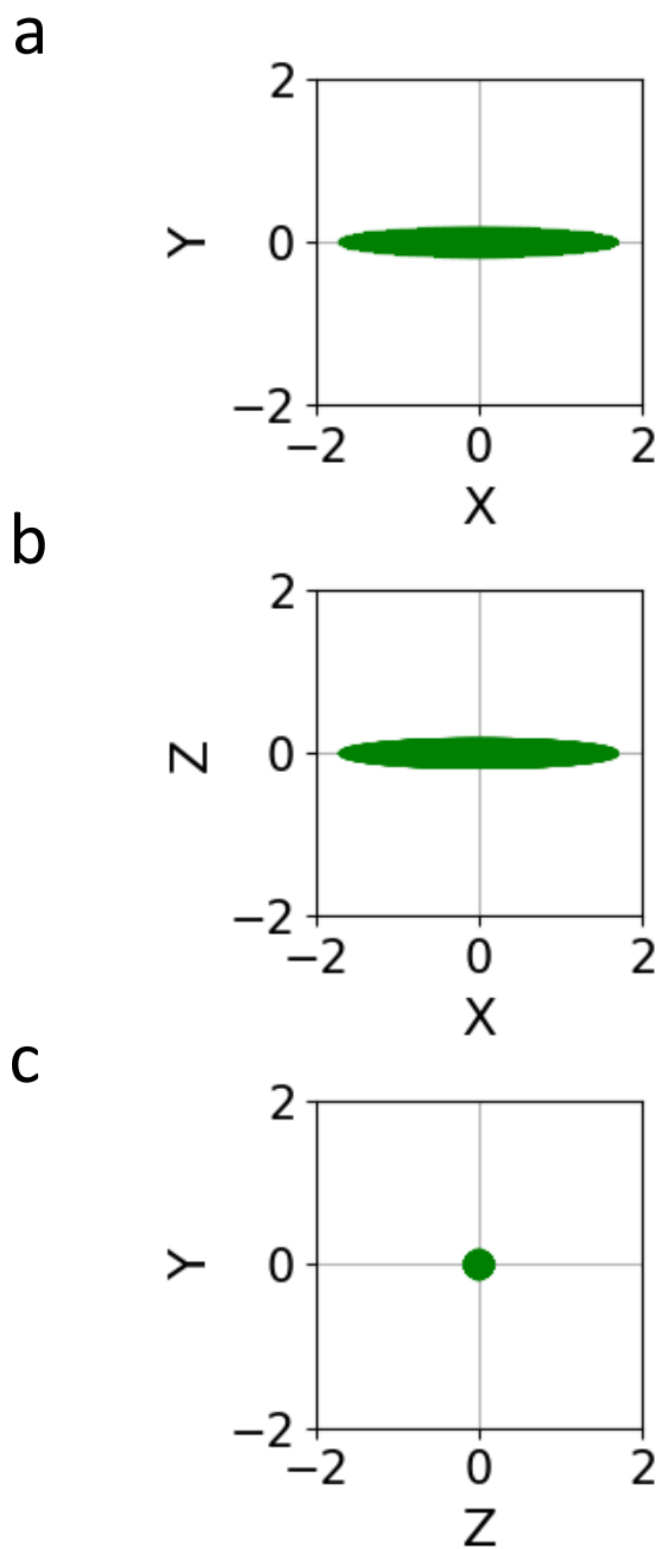


Figure 3.2 Tensor produced from the C-Br bond vectors in the crystal structure of 1-bromoadamantane/thiourea, viewed along (a) the z-axis, (b) the y-axis and (c) the x-axis. The tensor orientation corresponds to the crystal orientation in the XBI set-up at $\chi = 0^\circ$ and $\varphi = 0^\circ$.

As the incident X-ray beam is a transverse wave propagating along the z-axis, the z-component of the complex absorption coefficient ($\underline{\gamma}$) can be ignored, and instead we consider the 2×2 matrix shown in (Equation 3.10). We assume that 1-bromoadamantane/thiourea exhibits strong dichroism and has optimum thickness; thus, the isotropic ($a(E)$) and anisotropic ($b(E)$) absorption coefficients can be assumed to equal one. Therefore, the absorption coefficient matrix Γ can be determined using the rotated tensor and the isotropic and anisotropic absorption coefficient (Equation 3.4).

$$\Gamma = \begin{bmatrix} 4.396 + 3.396i & 0 \\ 0 & 0.666 - 0.333i \end{bmatrix}$$

The matrix Γ can then be used to determine the transmittance matrix (A) (Equation 3.14), required to establish the amplitude and polarization of the X-rays transmitted through the crystal of 1-bromoadamantane/thiourea. When the sample is oriented at $\chi = 0^\circ$ and $\phi = 0^\circ$, the transmittance matrix is:

$$A = \begin{bmatrix} -1.41 \times 10^{-2} - 1.10 \times 10^{-1}i & 0 \\ 0 & 7.07 \times 10^{-1} + 1.19 \times 10^{-1}i \end{bmatrix}$$

For these theoretical calculations, we assume perfect linear polarization for the incident X-ray beam along the x -axis. Thus, using Equation 3.17:

$$\mu = \begin{bmatrix} 1 & 0 \\ 0 & 0 \end{bmatrix}$$

To complete the calculations, we need to decide on a polarization analyzer. For the Br K-edge energy, both the Si (555) reflection and Ge (555) reflection are suitable. The Ge (555) reflection is, however, closer to the ideal 2θ value of 90° , therefore this reflection was selected and $2\theta = 89.536^\circ$ was used for Equation 3.21 to determine the transmittance matrix (A_p) for the polarization analyzer, giving:

$$A_p = \begin{bmatrix} 0 & -1 \\ 8.10 \times 10^{-3} & 0 \end{bmatrix}$$

Finally, with all components affecting the X-rays taken into account (Equation 3.22), the X-ray birefringence intensity as a function of the crystal orientation angles χ and ϕ can be determined (Figure 3.3).

The XBI intensity as a function of χ and φ is shown in Figure 3.3, in excellent agreement with the experimental XBI intensity for a sample with a single C-Br orientation aligned parallel to the reference axis (Figure 2.15). There are maxima in intensity at $\chi = 135^\circ$ and 45° and no variation in intensity as a function of φ . The similarities between the experimental data and calculated data thus indicate a good understanding of the theoretical background underlying the calculation of XBI data.

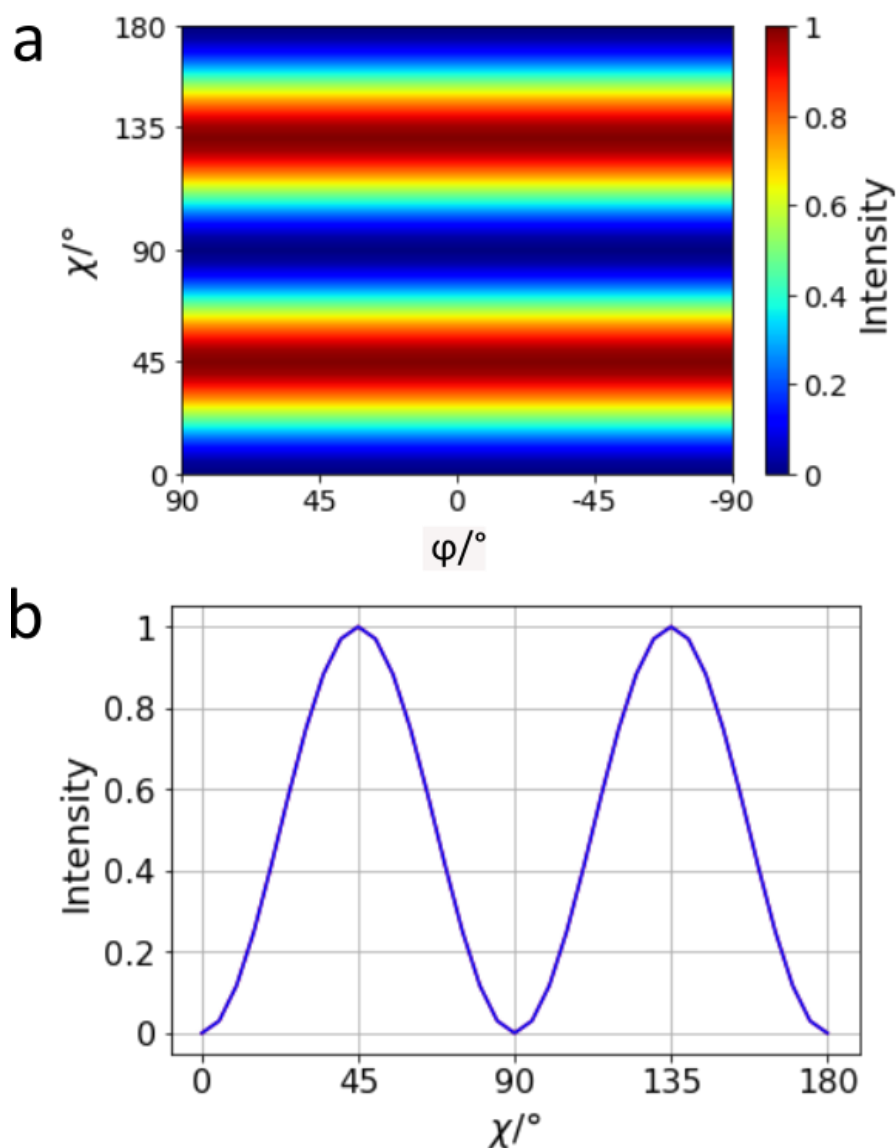


Figure 3.3 (a) Calculated XBI intensity as a function of χ and φ for 1-bromoadamantane/thiourea. (b) Calculated XBI intensity as a function of χ at $\varphi = 0^\circ$.

4 XBI Studies of Mechanically Deformable Crystals

4.1 Introduction

Traditionally, crystals are described as hard and rigid this is in part due to their crystal structure: a regular arrangement of atoms repeating in three dimensions.⁴⁶ Under application of mechanical stress, crystals experience a disruption of this ordered structure at the molecular level. In certain cases, crystals are capable of bending rather than the expected breaking.⁴⁷⁻⁵⁷ Bending crystals are of much interest as bending affects the physical and chemical⁵⁸ properties of the material, which is of particular importance in processing. These materials also have potential as actuators or molecular machines.^{49,50,54,59-70}

Determining which crystals exhibit bending rather than breaking can be related to the internal crystal structure and the intermolecular interactions. An analysis of the bending mechanism at the molecular level has been reported by the C. Malla Reddy group.^{47,59,71} When the intermolecular interactions are strong, the crystal will break; if intermolecular interactions are weak and there is an opportunity for the exchange of weak intermolecular interactions in the process, then the application of mechanical stress can change the shape of the crystal while retaining the macroscopic integrity.

Organic bending crystals can be classified into two types: plastic bending and elastic bending.^{60,72-74} Plastically bent crystals retain their bent shape when the external force causing the deformation is removed and have certain characteristic structural properties, specifically strong interactions (π -stacking, ionic interactions) between molecules within a given stack and weak interactions (Van der Waals, halogen bonding etc.) between molecules in adjacent stacks. When exposed to external pressure, the weaker cohesive forces between stacks is readily broken and the stacks slide along each other, with the weak interactions being broken and reformed during the sliding movement (Figure 4.1 (a)).^{47,74} The volume and inner (l_{in}) and outer (l_{out}) arcs of the crystal remain the same, but there is a large change in the interfacial angles (θ) to compensate for this (Figure 4.1 (b)).⁷¹

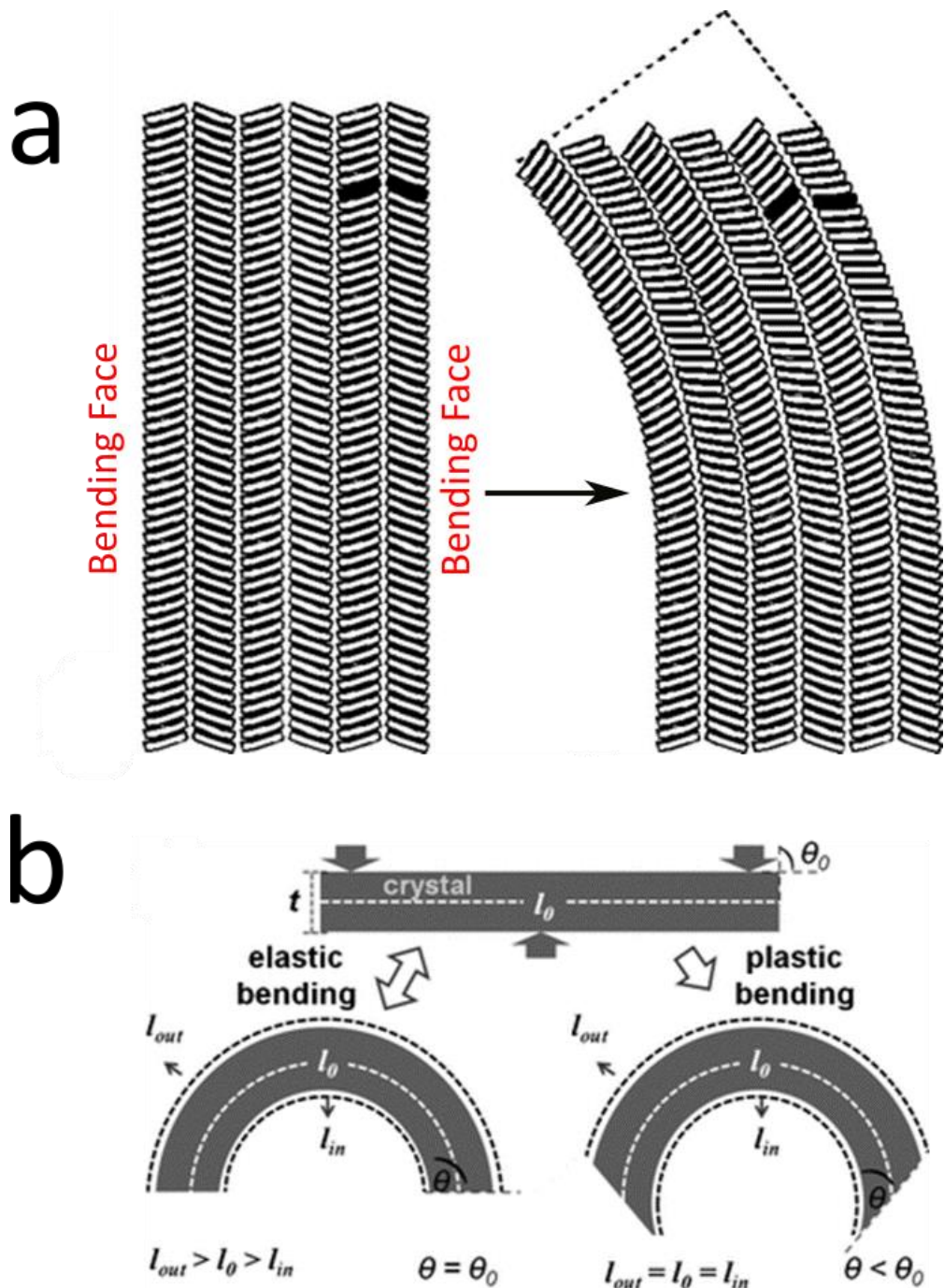


Figure 4.1 (a) Illustration of plastic bending of a crystal structure comprising stacks of planar molecules. The stacks slide relative to each other and there is a large change in the interfacial angles (θ) on the bent crystal. (b) Differences between plastic and elastic bending. Plastic bending shows no change in the outer (l_{out}) and inner (l_{in}) arcs and thus shows a drastic change in the interfacial angle ($\theta < \theta_0$). Elastic bending however shows a compression in l_{in} and extension in l_{out} and no change in the interfacial angle ($\theta = \theta_0$). Adapted from References 47 and 60.^{47,60}

Elastically bent crystals return to their original morphology after the external force causing the deformation is removed they also may bend along any axis perpendicular to the stacking axis. The interfacial angle (θ) does not change, instead, the inner (l_{in}) arc of the crystal is compressed, while the outer arc (l_{out}) is expanded (Figure 4.1 (b)).^{60,73–76}

To appreciate why these crystals bend and therefore to be able to engineer new crystals with similar properties relies on a comprehensive understanding of molecular structure, interactions and their interrelation to the physical properties exhibited by the crystal. Understanding the crystal structure around the bend of the crystal is challenging and not easily determined by diffraction. In this regard, we are interested to explore the opportunity to use XBI to establish the effect of bending on the crystal structure, to image the formation of any possible domains, to determine whether there is a gradual or abrupt change in orientation of molecules along the bent crystal, and to explore if the bending leads to any defects in the crystal.

This chapter focuses on two different bending crystals, copper (II) acetyl acetonate (CuAcAc) and hexabromobenzene (HBB). XBI has already been demonstrated to be effective in the study of bending crystals in the case of 1,4-dibromo-2,3,5,6-tetramethylbenzene.⁷⁷ The bending apparatus shown in Figure 4.2 was developed as part of the present project and allows for in situ measurements of the bending process. A dynamic analysis of the bending of HBB as a function of temperature is important due to the changes in the interactions and physical properties that HBB experiences at high temperature.

The bending apparatus developed in this project consists of a three-point system with the initial straight (unbent) crystal held horizontally on a metal sample holder with two grooves cut out of the holder perpendicular to each other (Figure 4.2). One groove is much deeper and wider to provide room for the crystal to bend. The other perpendicular groove holds the crystal on the sample holder during the bending process. A blunt needle is moved vertically downwards by a remotely controlled drive to bend the crystal. Due to the size of the bending apparatus, the sample assembly cannot be rotated or moved during the XBI measurement, as it is likely to crash with the diffractometer.

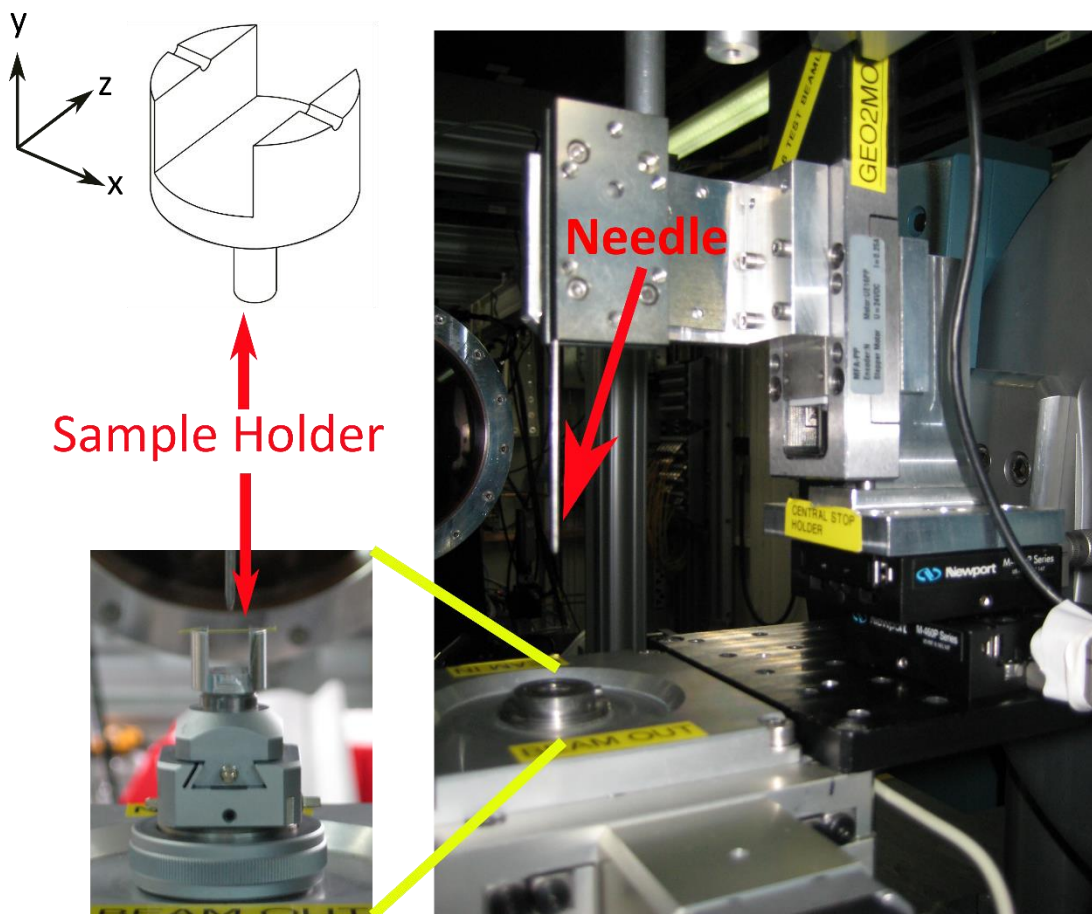


Figure 4.2 Apparatus for *in situ* bending in XBI experiments. The drive and needle used to bend the crystal are shown as well as the sample holder with a single crystal of 9, 10-dibromoanthracene held horizontally on the sample holder.

4.2 Copper (II) acetyl acetonate

The first bending crystal of interest is copper (II) acetyl acetonate (CuAcAc). The molecular structure (Figure 4.3) of CuAcAc is square planar, with the copper atom connected to four oxygen atoms. Such a bonding environment has not previously been studied using XBI. Previous work has already established the bending properties (when opposite forces are exerted on the 101 and $\bar{1}0\bar{1}$ faces) of single crystals of CuAcAc, showing elastic bending at small deformations but changing to plastic bending at larger deformations.⁷⁸

CuAcAc is monoclinic ($P2_1/n$) and the molecules form stacks along the crystallographic b -axis. The plane of the molecules in a stack are parallel with respect to each other and are tilted at an angle of 48.7° with respect to the crystallographic b -axis. The tilt angle for adjacent stacks varies from positive to negative if the b -axis is taken as 0° . During the bending process, the molecules on the inside rotate towards an orientation parallel to the (010) face due to compression. On the outside of the bend, the molecules rotate in the opposite direction, caused by elongation of the crystal.⁷⁸

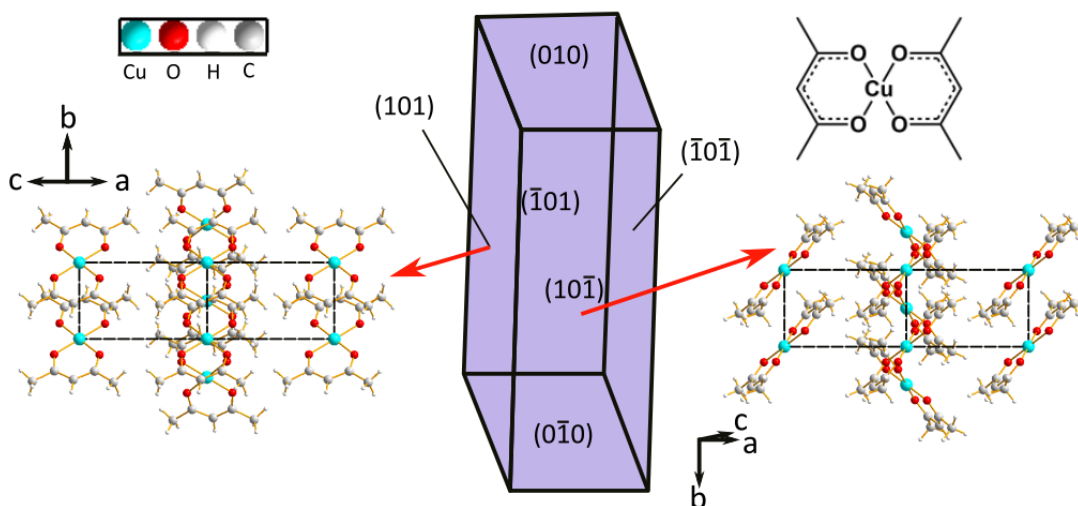


Figure 4.3 CuAcAc molecular structure and crystal structure with face indexing. Crystal structure is viewed along the $[101]$ axis (left) and the $[10\bar{1}]$ axis (right).⁷⁸

4.2.1 Results and Discussion

CuAcAc was obtained from Sigma Aldrich and recrystallized from chloroform as reported previously.⁷⁸ For XBI experiments, the incident X-ray energy was 8.979 keV, corresponding to the Cu K-edge, determined from X-ray dichroism measurements. Data were also recorded above the K-edge at 9.050 keV. Full details of the experiments on CuAcAc crystals discussed in this Chapter can be found in Table 4.1.

CuAcAc Crystal	Scan	Range	Orientation	T/K	Figure No.
1	X-ray absorption	E = 8.945 to 9.080 keV in 0.0005 keV steps	$\chi = 90^\circ, 180^\circ$ $\varphi = 60^\circ, -30^\circ$	Amb	4.4
	XBI χ	$\chi = 0^\circ$ to 180° in 5° steps	$\varphi = -135^\circ$	Amb	4.5 (b)
	XBI φ	$\varphi = -140^\circ$ to 130° in 5° steps	$\chi = 135^\circ$	Amb	4.5 (c)
	XBI χ - φ	$\chi = 0^\circ$ to 180° in 5° steps $\varphi = -140^\circ$ to 130° in 5° steps	N/A	Amb	4.5 (d)
	XBI φ E = 9.050 keV	$\varphi = -140^\circ$ to 130° in 5° steps	$\chi = 90^\circ$	Amb	4.6
2	Bending	Needle moved in and then out once.	N/A	Amb	4.7 (a) Movie S1
3	Bending	Needle moved in and out three times, with progressively larger movements.	N/A	Amb	4.7 (b) Movie S2

Table 4.1 Summary of experiments on CuAcAc crystals discussed in this Chapter. Amb denotes ambient temperature (ranges between 291-301 K).

In this work, the beam dimensions were defined by slits of 4 mm (vertical) and 4 mm (horizontal), and the polarization analyzer used the Si (440) reflection. The detector was the Medipix Merlin hybrid pixel detector. The single crystal of CuAcAc is oriented relative to the XBI set-up so that the crystallographic b -axis (long axis of crystal morphology) is in the xy -plane. Rotation of the b -axis around the z -axis (incident beam direction) is referred to as the χ -rotation, where the crystallographic b -axis is parallel to the x -axis when $\chi = 0^\circ$. The φ rotation refers to rotation of the crystal around the b -axis.

4.2.1.1 XBI studies of Single Crystal of CuAcAc

Before setting up the XBI experiment at the copper K-edge, X-ray absorption measurements were recorded for different orientations of a single crystal of CuAcAc used to calculate the X-ray birefringence spectrum. Two sets of X-ray absorption spectra were taken at $\varphi = 60^\circ$ and $\varphi = -30^\circ$, corresponding roughly to the [101] and $[10\bar{1}]$ axes of CuAcAc parallel to the z -axis (incident beam direction) respectively. The recorded intensity values for the recorded X-ray absorption spectra are first normalized using Equation 4.1. I_0 is the incident X-ray beam intensity before encountering the sample and I_F is the final intensity from the detector.

$$I = -\ln\left(\frac{I_F}{I_0}\right) \quad (4.1)$$

The X-ray absorption spectra were normalized to the intensity (I) at 9.080 keV and 8.945 keV, using Equation 4.2. These intensities are above and below the K-edge, respectively, at which the sample orientation should have no effect on the X-ray absorption.

$$I_N = \frac{(I - I_{8.945})}{(I_{9.080} - I_{8.945})} \quad (4.2)$$

Therefore, different sample orientations should give the same intensity at a given X-ray energy. Each set of spectra consisted of one spectrum with the CuAcAc, needle horizontal ($\chi = 180^\circ$) and one vertical ($\chi = 90^\circ$). This 90° difference means that the X-ray dichroism spectrum can be calculated from the difference between the two X-ray absorption spectra. At $\varphi = -30^\circ$ the X-ray dichroism proved to be negligible with the X-ray absorption spectra for $\chi = 90^\circ$ and $\chi = 180^\circ$ almost identical (Figure 4.4 (a)). As the spectra at $\varphi = -30^\circ$ were so similar, neither the X-ray dichroism nor the X-ray birefringence were calculated.

The X-ray dichroism measurement at $\varphi = 60^\circ$ showed a large difference between the X-ray absorption spectra recorded at different χ values (Figure 4.4 (b)). The difference between the spectra recorded at $\chi = 90^\circ$ and $\chi = 180^\circ$ was calculated to determine the X-ray dichroism spectrum shown in Figure 4.4 (c). The X-ray birefringence was calculated from the X-ray dichroism spectrum using the Kramers-Kronig transform (Equation 1.8), shown overlaid with the X-ray dichroism spectrum in Figure 4.4 (c). Significant X-ray birefringence is observed, ranging from roughly -0.2 to $+0.6$. While the X-ray birefringence is not as strong as that observed for 1-bromoadamantane/thiourea (Figure 2.14) XBI measurements continued as planned.

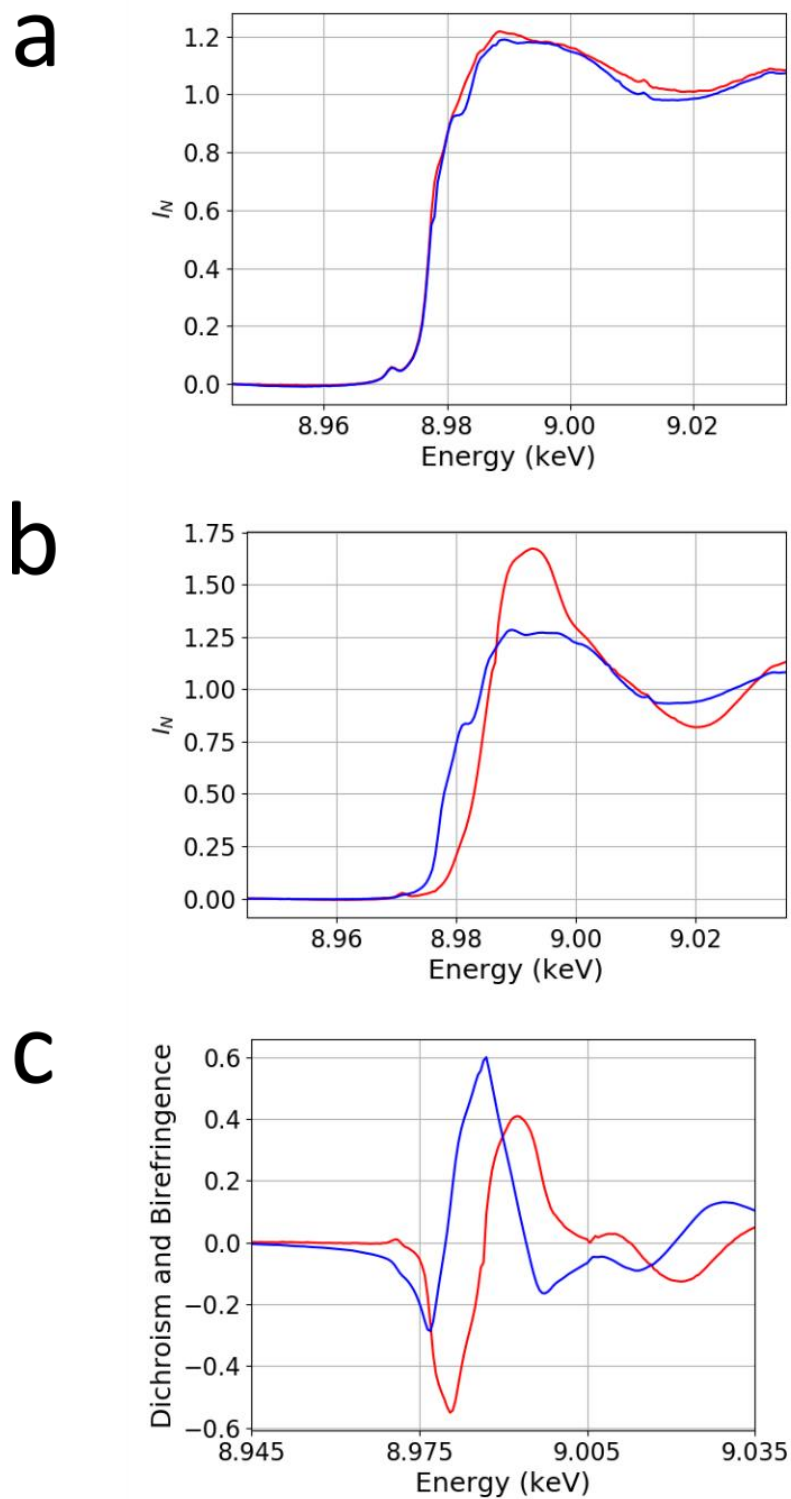


Figure 4.4 X-ray absorption spectra of a single crystal of CuAcAc oriented at $\chi = 90^\circ$ (red) and $\chi = 180^\circ$ (blue) for fixed value of ϕ : (a) $\phi = -30^\circ$ and (b) $\phi = 60^\circ$. (c) X-ray dichroism spectrum (red) calculated from the difference between X-ray absorption spectra in (b) and the calculated X-ray birefringence spectrum (blue).

Figure 4.5 (a) shows XBI images for different orientations (specified by χ and φ) of a single crystal of CuAcAc. With φ fixed at $\varphi = 60^\circ$, the χ dependence can be seen clearly in the changes of intensity on the images. In particular, the crystal orientations $\chi = 45^\circ$ and 135° show up much brighter than when the crystal is oriented at $\chi = 90^\circ$. It should be noted that $\chi = 135^\circ$ is brighter than $\chi = 45^\circ$, which is seen more clearly in Figure 4.5 (b). In this case, the data refer to the mean intensity calculated from a region of interest in the XBI image plotted as a function of χ (crystal is fixed at $\varphi = -135^\circ$). The sinusoidal curve expected from birefringent materials is slightly unsymmetrical; the unequal intensities of the two maxima is due to the presence of a small component of elliptical polarization in the incident beam rather than perfect linear polarization.

Figure 4.5 (a) also shows selected XBI images from the χ rotation with φ fixed at $\varphi = -30^\circ$; in this case, no change in intensity is observed as a function of χ , with the crystal appearing uniformly dark. This is to be expected from the X-ray absorption spectra in Figure 4.4 (a) as no X-ray dichroism/birefringence is seen for this orientation of the crystal.

Figure 4.5 (c) shows the mean intensity as a function of φ , with χ fixed at 135° . From the X-ray absorption spectra (Figure 4.4) we have already determined the X-ray dichroism and hence the X-ray birefringence depend on the orientation of the crystal with respect to rotation around the b -axis (as specified by the value of φ). Indeed, a change in intensity is clearly observed with maxima at $\varphi = 60^\circ$ and -120° , and a rather extended minimum at $\varphi = -30^\circ$.

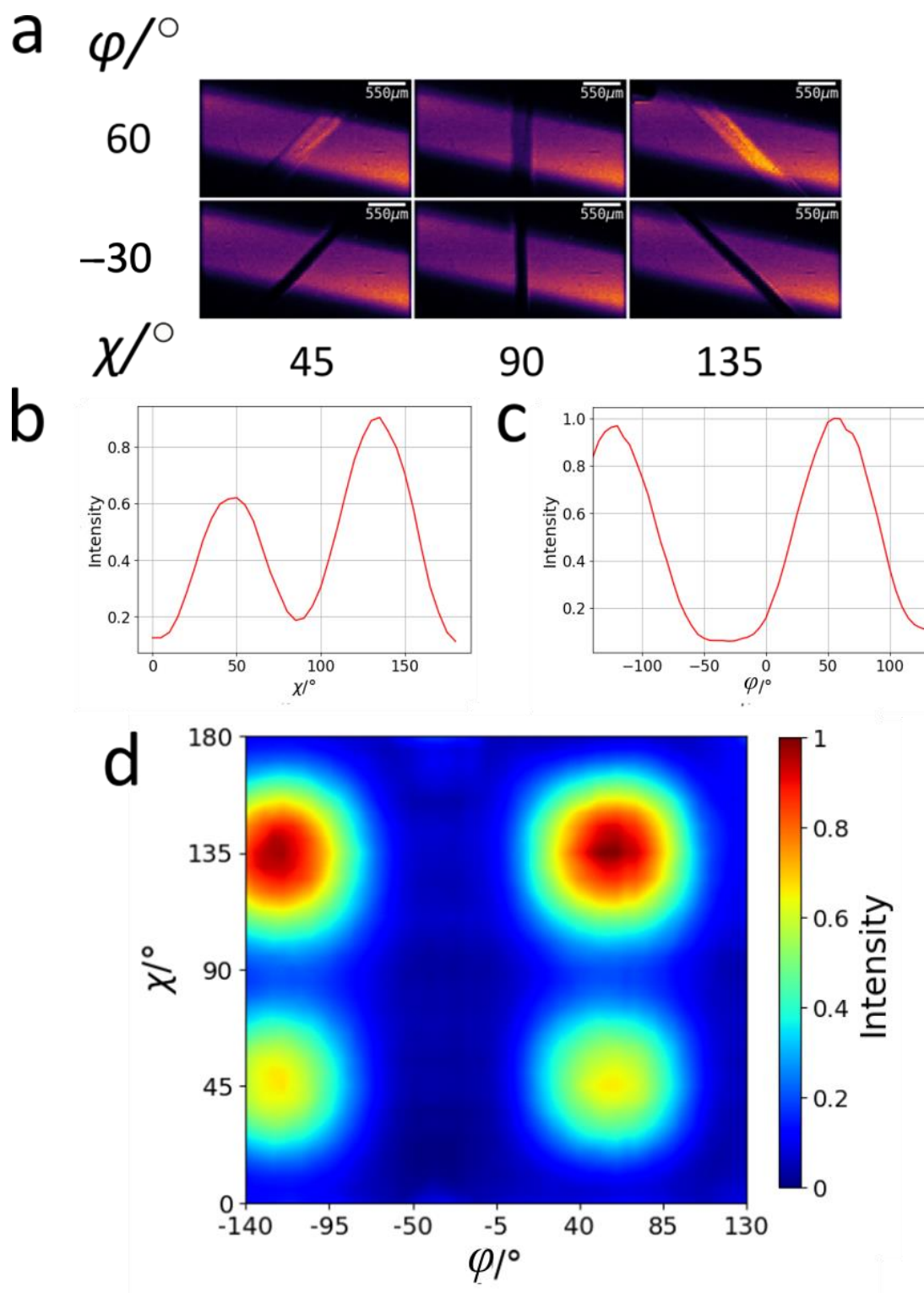


Figure 4.5 (a) XBI images of CuAcAc collected at the copper K-edge (9.028 keV) at $\chi = 45^\circ, 90^\circ, 135^\circ$ and at $\varphi = 60^\circ$ and -30° . (b) χ scan at $\varphi = -135^\circ$. (c) φ scan at $\chi = 135^\circ$. (d) Contour plot showing the intensity of a selected region of the CuAcAc crystal in the XBI image as a function of χ and φ .

The full change in XBI intensity for a single crystal of CuAcAc with χ and φ rotation can be seen more clearly in the intensity contour plot in Figure 4.5 (d). The presence of elliptical polarization is obvious, with the intensity lower by about 40% at $\chi = 45^\circ$ compared to $\chi = 135^\circ$. The intensity change with φ is also clearly seen to be similar at all values of χ . While some of this change in intensity can be attributed to X-ray birefringence, the morphology of the crystal is also important with regard to the φ -dependence of transmitted X-ray intensity. The greater the path length of X-rays through the crystal, the greater the X-ray absorption. The crystal has been observed to have a roughly rectangular cross section (perpendicular to the long axis (*b*-axis) of the morphology).

Equation 3.2 shows that the experimentally recorded intensity in XBI data is dependent on the thickness (*t*) of the sample. For materials with an anisotropic cross sectional morphology, this dependence should be considered when interpreting the XBI results as a function of φ angle. The path length of the beam through the crystal as a function of φ can be estimated by measuring the transmitted X-ray intensity far from the K-edge, where anisotropy is low (with no significant X-ray birefringence).

In this experiment, the intensity from the φ scan can be assumed to relate to the path of the beam through the crystal as a function of φ , and a plot showing the morphology of the crystal can be calculated (Figure 4.6). To determine the morphology, the natural log of the recorded intensity divided by the incident beam intensity (taken as an average background intensity from the beam centre on the images) is used. This gives a representation of the cross section of the sample and the thickness can be more accurately determined.

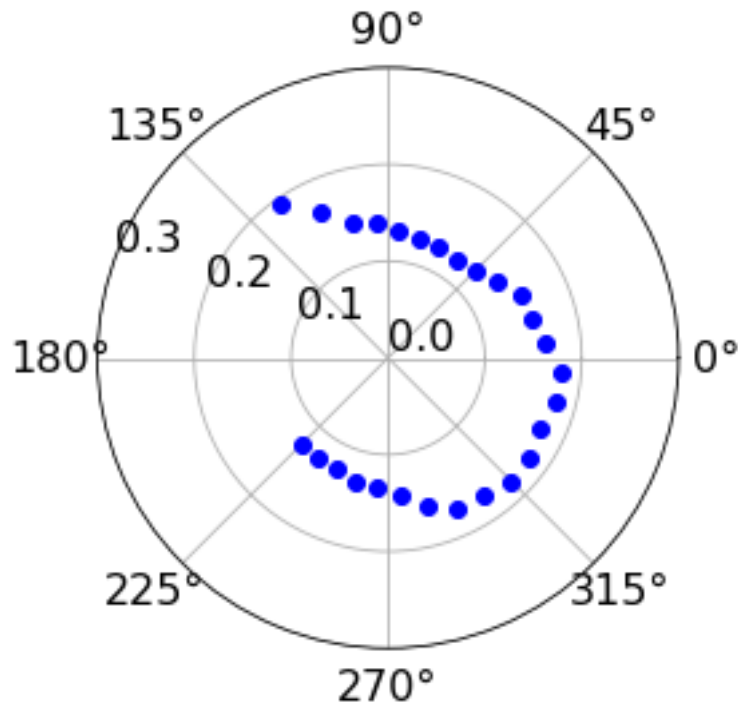


Figure 4.6 Polar plot of $\ln(\text{transmitted intensity}/\text{incident intensity})$ vs. ϕ for a single crystal of CuAcAc using an incident X-ray beam of energy 9.050 keV (blue). Data has been normalized to be within a maximum and minimum thickness of 0.390 and 0.247 cm respectively. These extremes of thickness were determined from experimental XBI images for this sample.

Figure 4.6 clearly demonstrates that the CuAcAc crystal has a roughly rectangular cross section, in line with the face-indexing shown in Figure 4.3. This dependence of intensity on the thickness of the sample is important when analyzing the XBI data and has the potential to be used in theoretical calculations. To turn the intensity measured as a function of ϕ above the Cu K-edge to values for the thickness of the sample, the scatter was normalized between a maximum of 0.390 cm and a minimum of 0.247 cm, corresponding to the variation in thickness of the sample determined from the XBI images. The thickness of the sample can be incorporated into the theoretical calculations in section 4.2.2 but work is still ongoing to include this accurately.

Finally, the lack of X-ray birefringence at $\phi = -30^\circ$ ($10\bar{1}$ face perpendicular to beam direction) can be rationalized on the basis of the right-hand crystal structure shown in Figure 4.3, rather than being purely morphology dependent.

We have assumed that the X-ray optic axis for each molecule of CuAcAc is perpendicular to the Cu-O bonds (section 4.2.2), which effectively gives two optic axes at roughly $\pm 45^\circ$ with respect to the *b*-axis (difference of 90° between optic axes). Previous work where two crystals of 1-bromoadamantane/thiourea (one optic axis aligned to the long needle axis) were joined with a 90° orientation between their optic axes, no X-ray birefringence was observed.⁷⁷ Thus, we can assume that there is no resultant X-ray optic axis at this orientation of φ .

4.2.1.2 XBI studies of the bending of CuAcAc

There are some rather unfortunate implications of the lack of X-ray birefringence observed at $\varphi = -30^\circ$. In this orientation of the crystal, the incident X-ray beam is parallel to the optimal direction to allow the bending to be observed on the XBI images. Figure 4.7 (a) shows a single crystal of CuAcAc subjected to bending in situ during the XBI experiment (bending apparatus is also seen). The single crystal, while clearly bent, shows no noticeable change in intensity around the curved regions of the crystal. Figure 4.7 (b) shows a crystal that has been partially twisted during the bending process so that the 101 face is now facing the incident beam. Therefore, as the crystal is oriented at an angle ca. 45° in the leftmost region, the crystal is bright and X-ray birefringence is observed. The region of the crystal to the right has not been twisted and thus no change in intensity is observed across this region of the crystal. Thus, while the crystal is clearly plastically bent, it is not possible to gain insights into the molecular orientations in the bent regions of the crystal using X-ray birefringence.

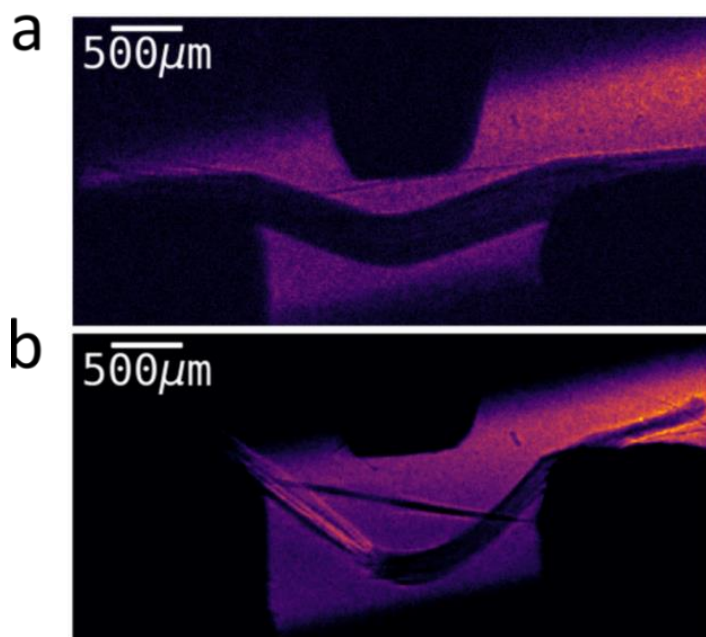


Figure 4.7 Bent single crystals of CuAcAc. (a) No X-ray birefringence is seen as the incident X-ray beam is perpendicular to the $(10\bar{1})$ plane of the crystal. The bending process can be viewed in Movie S1. (b) Bending the crystal has twisted it slightly so that the left hand region of the crystal is oriented such that the (101) face is perpendicular to incident X-ray beam, giving rise to brighter intensity, as the crystal is bent at an angle of roughly 45° . The bending process can be viewed in Movie S2.

4.2.2 Theoretical XBI intensity of a single crystal of CuAcAc

From knowledge of the crystal structure of a material, the theoretical XBI intensity can be calculated as a function of orientation, allowing comparison to the experimental results. Theoretical calculations for XBI have been described in detail in previous work²³ and Chapter 3. However, the bonding in CuAcAc is sufficiently different from previous systems, necessitating an expansion of the previous theoretical calculations. To start the calculations, the anisotropy of the absorption coefficient ($\underline{\gamma}$) of the sample must be accurately determined from the crystal structure.

4.2.2.1 Tensor calculation

CuAcAc is monoclinic ($P2_1/n$), and the molecular structure is shown in Figure 4.3, illustrating that the copper atom is bonded to four separate oxygens. Figure 4.8 shows four unit cells of CuAcAc with only the copper and oxygen atoms present.

Thus, it is apparent that we need to consider two Cu-O bond vectors for each CuAcAc molecule (remember XBI can be described as “parity even”, so Cu-O bond vectors in anti-parallel orientations behave as identical with regard to XBI). Within the unit cell, there are two molecules with different orientations, effectively creating four vectors representing Cu-O bonds.

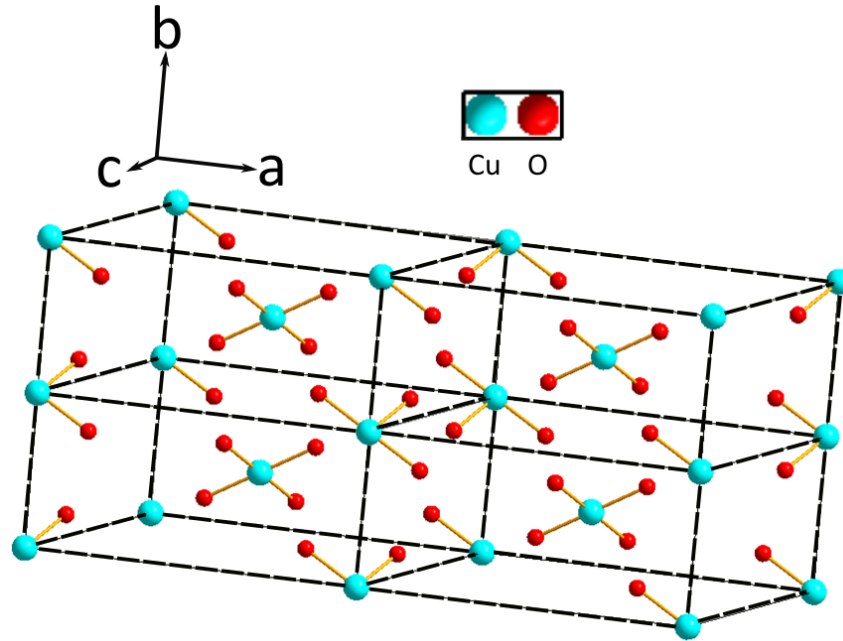


Figure 4.8 Four unit cells of CuAcAc, showing only copper and oxygen atoms. The unit cell is doubled along the *a* and *b* axes.⁷⁸

The tensor calculations proceed by making the simplifying assumption that the approximately square planar coordination is exactly square and so the X-ray absorption at each Cu site is described by a uniaxial tensor with axis perpendicular to the square plane, which also reduces the number of copper-oxygen bond vectors that need to be considered from four to two.

The orientation of each square is determined by finding the vectors that correspond to the two copper-oxygen bonds and then taking the cross product of these vectors, which gives a resultant vector normal to the plane of the square. From these vectors, the tensor can be calculated. Vectors for each copper-oxygen bond are calculated by taking the coordinates of the oxygen atom away from those of the copper atom:

$$V_x, V_y, V_z = Cu_x, Cu_y, Cu_z - O_x, O_y, O_z \quad (4.3)$$

In the unit cell, there are two molecules of CuAcAc, with one molecule having the copper atom centered at the corner of the unit cell.

Atom Coordinates						
	Copper			Oxygen		
	x	y	z	x	y	z
Molecule 1	0.5	0.5	0.5	0.3375	0.2940	0.4944
	0.5	0.5	0.5	0.6625	1.7060	0.5056
	0.5	0.5	0.5	0.5655	0.2988	0.3657
	0.5	0.5	0.5	0.4345	0.7012	0.6343
Molecule 2	0.0	0.0	0.0	0.0655	0.2012	-0.1343
	0.0	0.0	0.0	-0.1625	0.2060	-0.0056
	0.0	0.0	0.0	-0.0655	-0.2012	0.1343
	0.0	0.0	0.0	0.1625	-0.2060	0.0056

Table 4.2 Atom coordinates of copper and oxygen making up the Cu-O bonds in CuAcAc for the two molecular orientations.

The transform mentioned in Chapter 3 (Equation 3.6) is used to convert the crystal coordinates to a suitable Cartesian coordinate system. We note that as XBI is “parity even” there are only two unique vectors per molecule.

	Vector Coordinates					
	Fractional			Cartesian		
	x	y	z	x	y	z
Molecule 1	0.1625	0.206	0.0056	1.6671	0.9564	0.0629
	-0.0655	0.2012	0.1343	-0.7386	0.934	1.5146
Molecule 2	-0.1625	0.206	-0.0056	-1.6671	0.9564	-0.0629
	0.0655	0.2012	-0.1343	0.7386	0.934	-1.5146

Table 4.3 Vectors of the unique Cu-O bonds in CuAcAc converted from fractional to Cartesian coordinates.

The cross product of the two vectors in the molecule is then taken. This final vector is used in the tensor calculation (Chapter 3, Equation 3.5):

$$T_{ij} \text{ Molecule 1} = \begin{bmatrix} 1.6 & -3.6 & 3.1 \\ -3.6 & 6.3 & -5.8 \\ 3.1 & -5.8 & 4.8 \end{bmatrix}$$

$$T_{ij} \text{ Molecule 2} = \begin{bmatrix} 1.6 & 3.6 & 3.1 \\ 3.6 & 6.3 & 5.8 \\ 3.1 & 5.8 & 4.8 \end{bmatrix}$$

The resultant tensor for the unit cell is the sum of the tensors for each molecule.

$$T_{ij} = \begin{bmatrix} 3.2 & 0 & 6.2 \\ 0 & 12.6 & 0 \\ 6.2 & 0 & 9.6 \end{bmatrix}$$

A useful check for our calculations so far relies on Neumann's principle, which states that:

'the symmetry elements of any physical property of a crystal must include the symmetry elements of the point group of the crystal'

As our tensor $\underline{\gamma}$ is a physical property of the crystal, if the calculations are done correctly, it should match with the symmetry properties of our sample. For a monoclinic system the symmetry properties of our sample can be described as:

$$\begin{bmatrix} T_{11} & 0 & T_{13} \\ 0 & T_{22} & 0 \\ T_{31} & 0 & T_{33} \end{bmatrix}$$

The sum of the two tensors is consistent with the monoclinic crystal symmetry of the sample. The values of T_{12} , T_{21} , T_{23} , and T_{32} in our "final tensor" are equal to 0 and $T_{31} = T_{13}$.

As mentioned in Chapter 3, the tensor is currently not in the experimental frame. The tensor needs to be rotated to the orientation where the crystal is at $\chi = 0^\circ$ and $\varphi = 0^\circ$, using the rotation matrix U (Equation 3.9). To find the tensor orientation at $\chi = 0^\circ$ and $\varphi = 0^\circ$, the orientation of the crystal structure in the experimental coordinate system must be known.

The crystallographic b -axis (long needle axis) is parallel to the x -axis in the experimental system when $\chi = 0^\circ$. However, the crystallographic face perpendicular to the beam direction (z -axis) when $\varphi = 0^\circ$ is unknown. Therefore, the U rotation matrix was determined for the rest of the calculations by first rotating the tensor so that the b -axis was parallel to the x -axis:

$$U = \begin{bmatrix} 0 & 1 & 0 \\ -1 & 0 & 0 \\ 0 & 0 & 1 \end{bmatrix}$$

The final tensor was determined by trial and error was through further rotation about the x -axis, by comparing the final theoretical contour plot to the experimental data (Figure 4.5 (d)). The U rotation matrix used is:

$$U = \begin{bmatrix} 0 & 1 & 0 \\ -0.104 & 0 & -0.995 \\ -0.995 & 0 & 0.104 \end{bmatrix}$$

4.2.2.2 Isotropic ($a(E)$) and anisotropic ($b(E)$) absorption coefficients

In Chapter 3, the absorption coefficient ($\underline{\gamma}$) was described using a tensor as it is a physical property in three dimensions.

$$\underline{\gamma} = a(E) + b(E)\hat{T}_{ij} = \begin{bmatrix} a(E) + b(E)T_{11} & b(E)T_{12} & b(E)T_{13} \\ b(E)T_{21} & a(E) + b(E)T_{22} & b(E)T_{23} \\ b(E)T_{31} & b(E)T_{32} & a(E) + b(E)T_{33} \end{bmatrix} \quad (4.4)$$

While, in previous cases, we have assumed that the isotropic ($a(E)$) and anisotropic ($b(E)$) absorption coefficients are close to one, this assumption is not valid for the current calculations due to the unusual bonding in CuAcAc. The calculation of the isotropic ($a(E)$) and anisotropic ($b(E)$) absorption coefficients relies on the use of experimental X-ray absorption spectra taken along different directions of the anisotropic crystal structure (different orientations of the sample), as well as a tensor derived from the bonds of interest in the crystal structure.

For an exact calculation of the transmitted intensity from the sample, we use Equations 4.7, 4.11, where Γ represents the first four components of $\underline{\gamma}$ (γ_{xx} , γ_{xy} , γ_{yx} , γ_{yy}). However, a useful simplification, valid when the anisotropy or thickness is not too large, is to have γ equal to the first tensor component:

$$\gamma = a(E) + T_{11}b(E) \quad (4.5)$$

The γ values at different energies and orientations of the sample can be determined experimentally from X-ray absorption spectra. Matching this information with the tensor T_{ij} orientation, simultaneous equations of Equation 4.5 can be established and solved to determine $a(E)$ and $b(E)$. Equation 4.5 is repeated for all the energy values in the scan, as $a(E)$ and $b(E)$ differ with energy. Furthermore, $a(E)$ and $b(E)$ can be checked by calculating γ using the $a(E)$ and $b(E)$ values calculated from the first two X-ray absorption spectra and comparing to other experimentally recorded X-ray absorption measurements at different orientations (Figure 4.9).

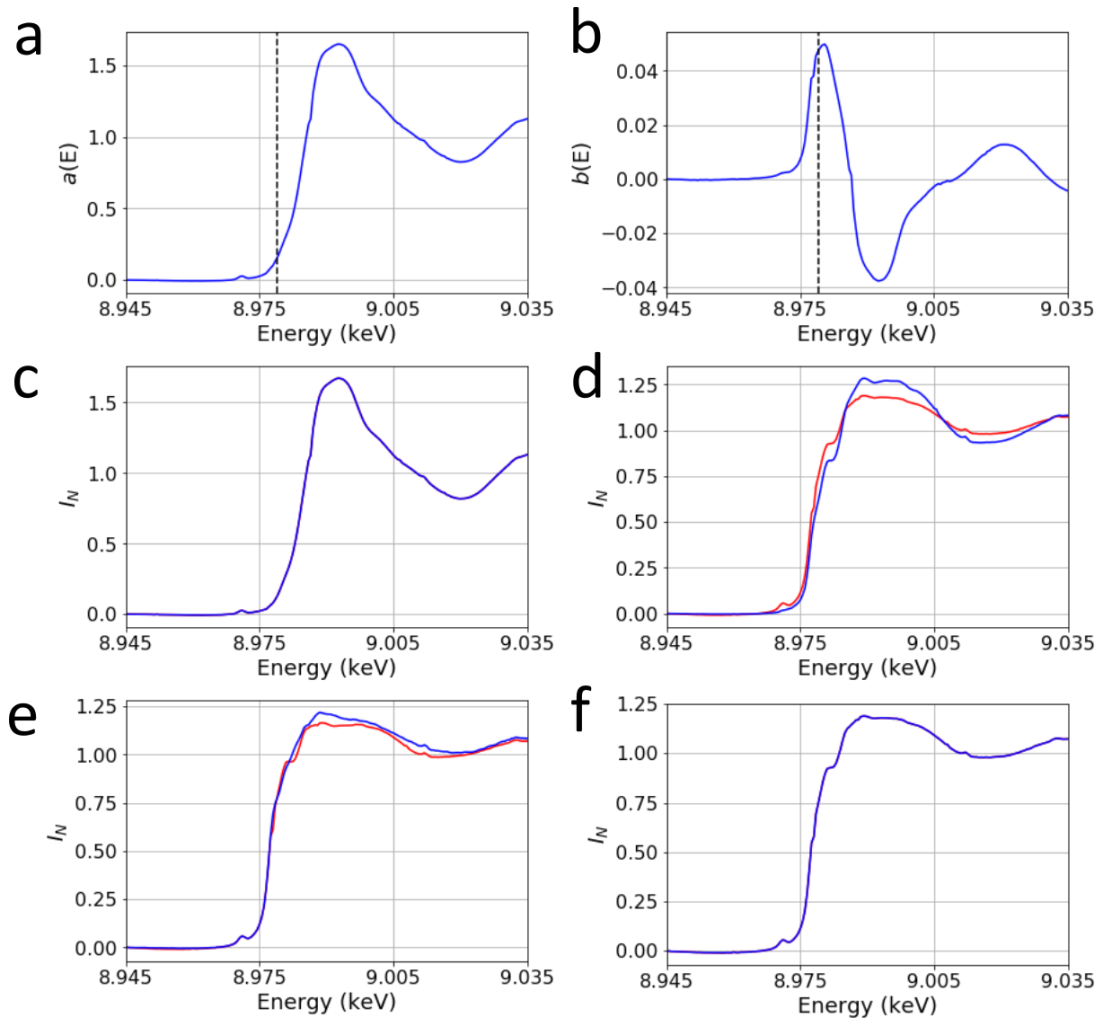


Figure 4.9 The absorption coefficients $a(E)$ (isotropic) and $b(E)$ (anisotropic) are shown in (a) and (b) respectively, dashed lines indicate an energy of 8.979 keV. In (c) to (f), experimental X-ray absorption spectra are shown in blue with the theoretical calculations shown in red. Single crystal of CuAcAc oriented at (c) $\chi = 90^\circ$, $\varphi = 60^\circ$, (d) $\chi = 180^\circ$, $\varphi = 60^\circ$, (e) $\chi = 90^\circ$, $\varphi = -30^\circ$ and (f) $\chi = 180^\circ$, $\varphi = -30^\circ$. Spectra (c) and (f) were used to calculate the absorption coefficients ($a(E)$ and $b(E)$), which were then used to calculate the spectra shown in (e) and (d), allowing an assessment of the quality of $a(E)$ and $b(E)$ values.

The spectra shown in Figure 4.9 (c) and (f) ($\chi = 90^\circ$, $\varphi = 60^\circ$ and $\chi = 180^\circ$, $\varphi = -30^\circ$ respectively) are used to calculate the $a(E)$ and $b(E)$ values. Figure 4.9 (d) and (e) show a comparison between calculated and recorded X-ray absorption measurements for other values of χ and φ using the values of $a(E)$ and $b(E)$ determined from analysis of (c) and (f).

A good fit is observed between the experimental and calculated X-ray absorption spectra, although there does appear to be some small differences in overall intensity. The differences observed are likely due to the morphology of the single crystal.

From these results the real component of $a(E)$ and $b(E)$ can be determined at 8.979 keV, which is the experimental energy close to the Cu K-edge used to record the XBI data for CuAcAc. Now we must remember that $b(E)$ is complex and consists of real and imaginary parts, but we can calculate the imaginary part using the Kramers-Kronig transform.

$$\Delta\gamma''(E) = \frac{2}{\pi} P \int_0^{\infty} \frac{E' \Delta\gamma'(E')}{(E'^2 - E^2)} dE' \quad (4.6)$$

where $\Delta\gamma'(E')$ are our calculated $b(E)$ values and E corresponds to the energy. Performing the calculation for each energy provides the imaginary part of the anisotropic absorption coefficient ($b(E)i$), shown in Figure 4.10.

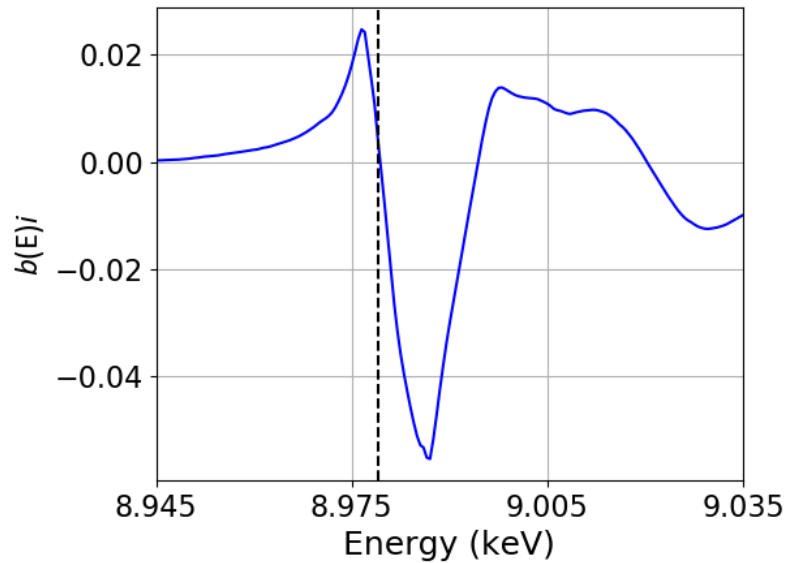


Figure 4.10 Imaginary part of the anisotropic absorption coefficient ($b(E)i$) calculated using the Kramers-Kronig transform. Dashed line indicates an energy of 8.979 keV.

We now know $a(E)$ (0.1570) and $b(E)$ ($0.0470+0.0044i$) at the energy of the copper K-edge (8.979 keV), which can then be used in theoretical calculations of XBI behaviour.

4.2.2.3 X-ray Birefringence Calculation

Finally, we can go back to the full tensor $\underline{\gamma}$ to calculate the X-ray birefringence signal. From here on, the calculations match the description in Chapter 3. We can write the complex absorption coefficient ($\underline{\gamma}$) as a four-component matrix. The respective components of the matrix can be calculated from the tensor determined in Section 4.2.2.1 and the isotropic and anisotropic absorption coefficients determined in Section 4.2.2.2.

$$\Gamma = \begin{bmatrix} \gamma_{xx} & \gamma_{xy} \\ \gamma_{yx} & \gamma_{yy} \end{bmatrix} \quad (4.7)$$

$$\gamma_{xx} = a + bT_{11} \quad (4.8)$$

$$\gamma_{yy} = a + bT_{22} \quad (4.9)$$

$$\gamma_{xy} = \gamma_{yx} = bT_{12} = bT_{21} \quad (4.10)$$

The transmittance matrix A, incorporating the complex absorption coefficient, is used to describe the amplitude and polarization of X-rays as they propagate through the CuAcAc crystal. As a description of the thickness of the crystal as a function of the ϕ rotation has not yet been incorporated, the thickness (t) is defined as equal to one for these calculations.

$$A = e^{-(\gamma_{xx} + \gamma_{yy})t/4} \begin{bmatrix} \cosh\phi - \frac{(\gamma_{xx} - \gamma_{yy})t \sinh\phi}{4\phi} & \frac{\gamma_{xy}t \sinh\phi}{2\phi} \\ -\frac{\gamma_{xy}t \sinh\phi}{2\phi} & \cosh\phi + \frac{(\gamma_{xx} - \gamma_{yy})t \sinh\phi}{4\phi} \end{bmatrix} \quad (4.11)$$

$$\Phi = \frac{t}{4} \sqrt{(\gamma_{xx} - \gamma_{yy})^2 + 4\gamma_{xy}\gamma_{yx}} \quad (4.12)$$

When $\chi = 0^\circ$ and $\phi = 0^\circ$ the transmittance matrix A is:

$$A = \begin{bmatrix} 0.6879 - 0.0190i & 0 \\ 0 & 0.7168 - 0.0171i \end{bmatrix}$$

Elliptical polarization was clearly observed in the experimental results for the single crystal of CuAcAc, thus, this must be incorporated into the state of polarization of the incident beam using the polarization density matrix μ (Equation 4.13). More specifically using the Stokes parameter denoted P_2 , which describes circular polarization.

$$\mu = \frac{1}{2} \begin{bmatrix} 1 + P_3 & P_1 - iP_2 \\ P_1 + iP_2 & 1 - P_3 \end{bmatrix} \quad (4.13)$$

To determine the value of P_2 to accurately model the XBI experimental results, generated theoretical contour plots were compared to the experimental contour plots using the mean squared error. Thus, a value of $P_2 = 0.22$ was determined to give the best match between experimental and calculated XBI data. Thus, the matrix used to describe incident beam polarization is:

$$\mu = \begin{bmatrix} 1 & -0.11i \\ 0.11i & 0 \end{bmatrix}$$

A transmittance matrix (A_p) is used to describe the effect of the polarization analyzer on the X-rays, where 2θ is the scattering angle and η the rotation about the beam direction (90°).

$$A_p = \begin{bmatrix} \cos \eta & -\sin \eta \\ \cos 2\theta \sin \eta & \cos 2\theta \cos \eta \end{bmatrix} \quad (4.14)$$

For the Si (440) reflection at 8.979 keV, 2θ is equal to 91.972° .

$$A_p = \begin{bmatrix} 0 & -1 \\ -3.44 \times 10^{-2} & 0 \end{bmatrix}$$

The ratio of transmitted intensity (I_F) to incident intensity (I_0) was determined using an adaption of the density matrix formalism, which incorporates the polarization state of the incident beam from (μ), operated on either side by matrices that represent scattering from (A_p), and transmission through (A), optical components and samples, where \dagger denotes the transpose of the complex conjugate and Tr is the trace (sum of the diagonal elements).

$$\frac{I_1}{I_0} = \text{Tr.}(A_p A \mu A^\dagger A_p^\dagger) \quad (4.15)$$

Using the above equations for all values of χ and ϕ considered in our experimental measurements, the calculated intensity contour plot as a function of χ and ϕ is shown in Figure 4.11. This contour plot is comparable to the experimental contour plot for CuAcAc shown in Figure 4.5 (d). There are maxima in intensity at χ values of 135° and 45° , with the difference in the values of intensity at these taken into account by elliptical polarization. The variation in intensity as a function of ϕ in the calculated data also agrees well with the experimental data even without introducing the thickness dependence of the sample as a function of ϕ in the calculation. The maxima seem slightly wider in ϕ for the calculated data than the experimental data which could be related to the effects of sample thickness over the experimental data (Figure 4.6). The similarities between the experimental and calculated plots thus indicate a good understanding of the theoretical background underlying the calculation of XBI data.

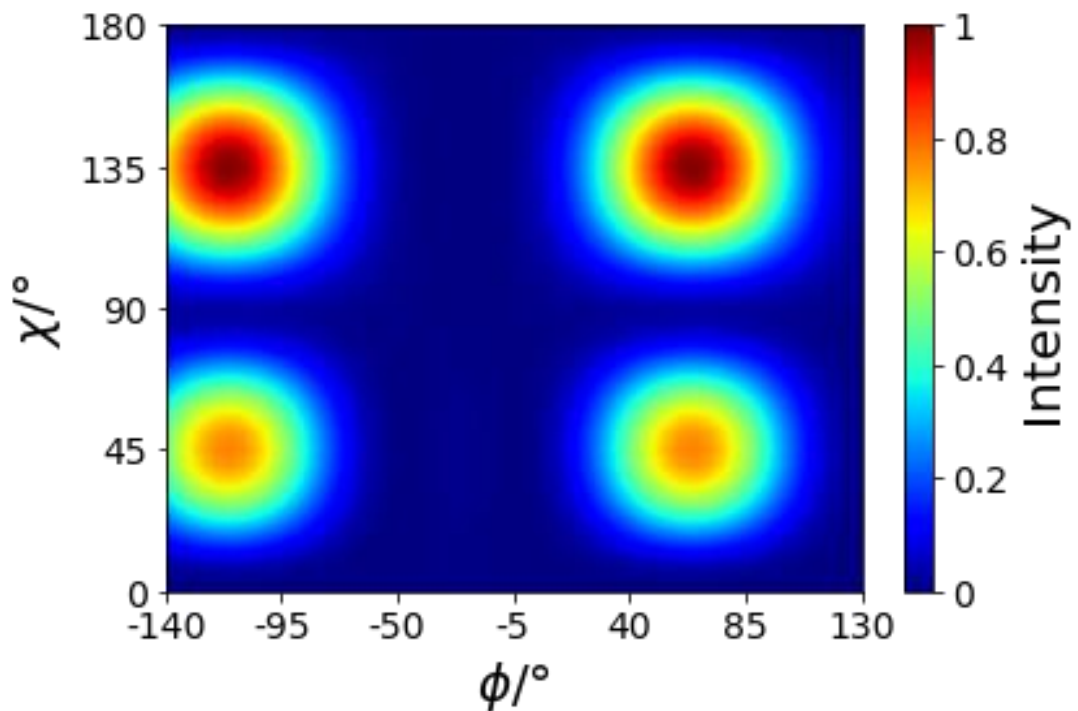


Figure 4.11 Calculated XBI intensity at the copper K-edge, as a function of χ and ϕ for CuAcAc.

4.3 Hexabromobenzene

Although hexabromobenzene (HBB) and hexachlorobenzene (HCB) have isomorphous crystal structures at room temperature, they are found to exhibit disparate behaviour with regard to crystal bending. HCB at room temperature exhibits plastic bending when stress is applied to the (001) face (the bending face). In contrast, HBB is brittle at ambient temperature and breaks under mechanical pressure. At high temperature, HBB is more malleable, showing the same plastic bending behaviour as HCB.^{47,71,72}

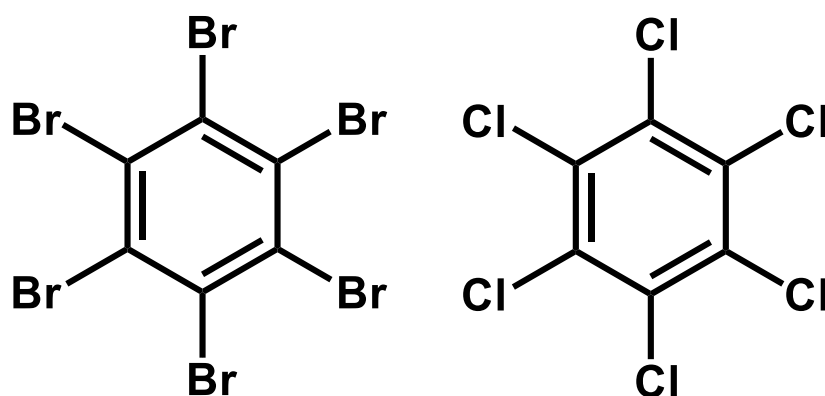


Figure 4.12 Molecular structure of HBB (left) and HCB (right).

The different bending behaviour of HCB and HBB can be explained by the differing properties of their respective halogen bonding. Certain geometries of halogen bonding are favoured, including the Hal₃ synthons (Figure 4.13) present in HCB and HBB. Hal₃ synthons and single halogen interactions form between stacks in the crystal structure of HCB and HBB, while stronger π - π interactions are formed between molecules in each stack, representing the strong and weak interactions perpendicular to each other, which is characteristic of bending crystals (Figure 4.1 (a)).⁷⁹

Hal₃ synthons exist between stacks in both HBB and HCB but the halogen bonding in HCB is weaker than that in HBB. Therefore, breaking the intermolecular halogen bonds is easier for HCB at ambient temperature, so the crystal is able to bend. Breaking the intermolecular halogen bonds for HBB requires a higher temperature, which is why the crystal does not bend at ambient or low temperature.

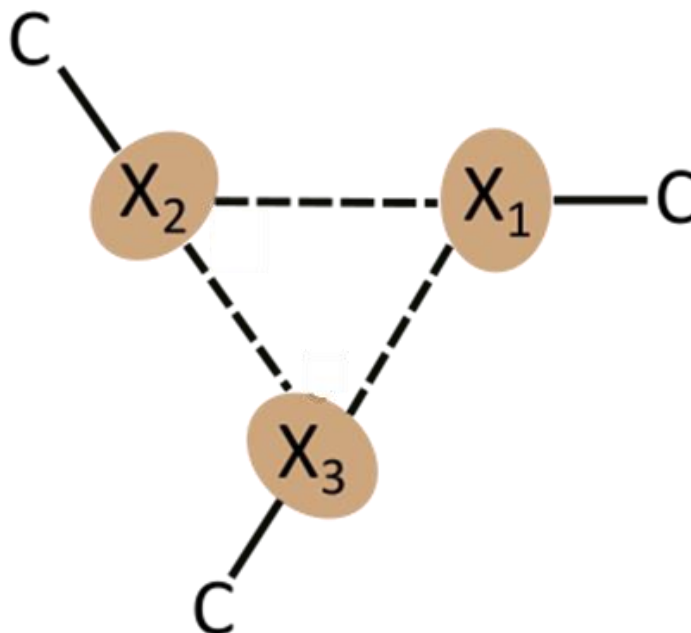


Figure 4.13 The Hal_3 synthon, involving halogen bonding (denoted by dashed lines) between three halogen atoms (X). Adapted from Reference 80.⁸⁰

HBB (and HCB) is monoclinic with $P2_1/n$ symmetry, with the planar molecules stacking along the b -axis (long axis of the crystal). While bending has been observed at high temperature (403 K)⁸⁰ there is no reported phase transition at high temperature.

Crystal System		Monoclinic
Space Group		$P2_1/n$
Cell Parameters	a (Å)	15.357
	b (Å)	4.007
	c (Å)	8.364
	β (°)	92.65
Intra-stack distance (Å)		4.007

Table 4.4 Crystal structure data for HBB at ambient temperature.⁸¹

At ambient temperature, HBB forms two types of stack along the b -axis, within a stack the molecules remain in the same plane at a distance equal to the length of the b -axis (4.007 Å). Adjacent stacks are shifted relative to each other along the b -axis to minimize steric interactions. The planar HBB rings are tilted ca. 65° relative to the stack direction (Figure 4.14).⁸¹

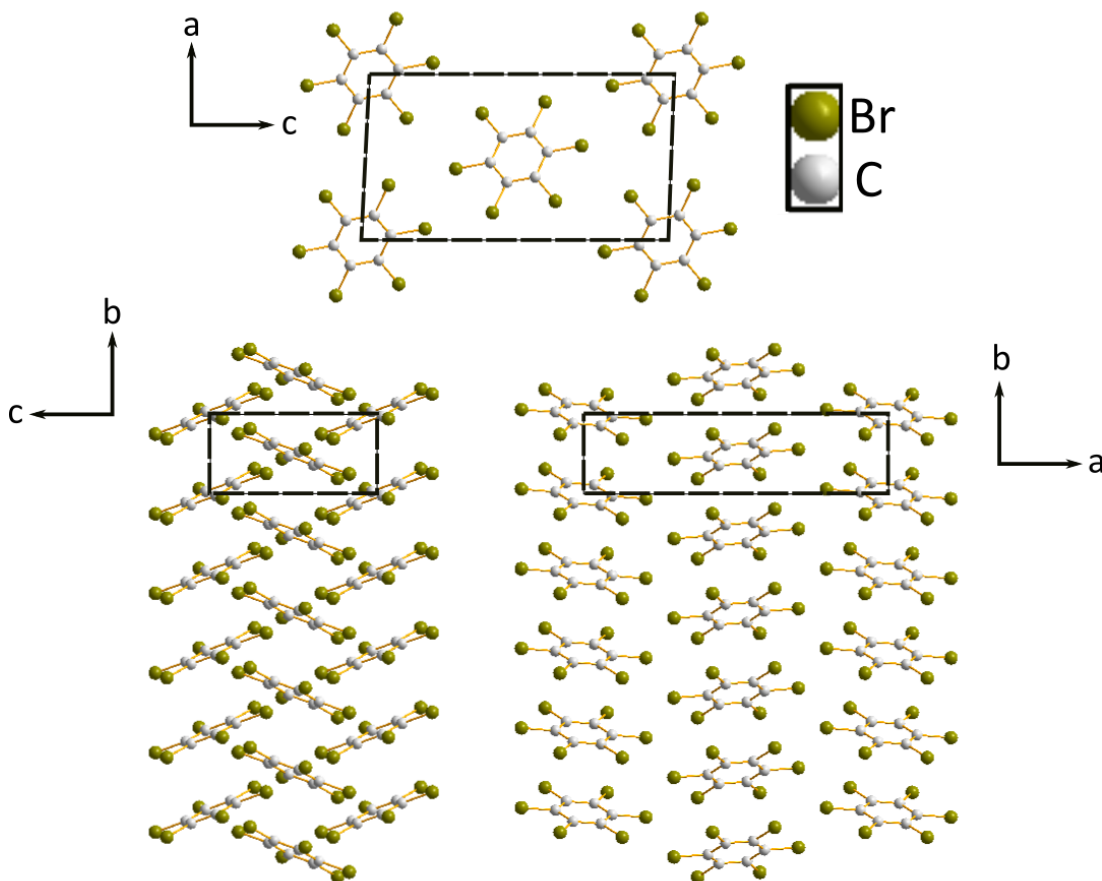


Figure 4.14 Crystal structure of HBB at 300 K viewed along the three unit cell axes. Crystal structure along the *b*-axis has been extended beyond the unit cell to illustrate the stacks made up of individual HBB molecules.⁸¹

4.3.1 Results and Discussion

HBB was obtained from Sigma Aldrich and recrystallized from methanol, to form needle-like crystals. Rather than forming single crystals, HBB often formed crystalline groupings with multiple single crystals aligned together. Full details of the experiments on HBB crystals discussed in this Chapter can be found in Table 4.5.

HBB Crystal	Scan	Range	Orientation	T/K	Figure No.
1	XBI image	N/A	$\chi = 45^\circ$, $\varphi = 90^\circ$	Amb	4.15 (a)
	XBI χ - φ	$\chi = 0^\circ$ to 180° in 5° steps $\varphi = 90^\circ$ to -90° in 5° steps	N/A	105	4.16
	Temperature	T = 295 to 105 K in 5 K steps	$\chi = 45^\circ$, $\varphi = 45^\circ$	N/A	4.17 (a), 4.17 (b) Movie S3
	XBI image	N/A	$\chi = 45^\circ$, $\varphi = 90^\circ$	395	4.17 (d)
	XBI χ - φ	$\chi = 0^\circ$ to 180° in 5° steps $\varphi = 90^\circ$ to -90° in 5° steps	N/A	395	4.18
2	XBI image	N/A	$\chi = 45^\circ$, $\varphi = 90^\circ$	Amb	4.15 (b)
	XBI χ - φ	$\chi = 0^\circ$ to 190° in 5° steps $\varphi = 95^\circ$ to -95° in 5° steps	N/A	Amb	4.17 (c)
3	Bending	Needle moved in and out once.	N/A	400	4.19 Movie S4

Table 4.5 Summary of experiments on HBB crystals discussed in this Chapter. Amb denotes ambient temperature (ranges between 291-301 K).

XBI experiments were carried out using an incident X-ray energy of 13.474 keV, corresponding to the Br K-edge. In this work, the beam dimensions were defined by slits of 4 mm (vertical) and 4 mm (horizontal), and the polarization analyzer used the Ge (555) reflection. The detector used was the “X-ray eye” detector (12 bit **CCD** miniFDI camera from Photonic Science Ltd.; 6.5 μm pixel size; 1392×1040 pixels in the field of view).

The crystals of HBB are oriented relative to the XBI set-up so that the crystallographic b -axis (long axis of crystal morphology) is in the xy -plane. Rotation of the b -axis around the z -axis (incident beam direction) is referred to as the χ -rotation, where the crystallographic b -axis is parallel to the x -axis when $\chi = 0^\circ$. The ϕ rotation refers to rotation of the crystal around the b -axis.

4.3.1.1 XBI studies of a Single Crystal of HBB

Before assessing the XBI behaviour of bent crystals of HBB, a straight crystal of HBB was studied. Finding a suitable single crystal of HBB proved difficult, as most crystals were made up of multiple joined crystals (Figure 4.15 (a, b)). Previous work has already established that HBB commonly forms multiple crystals.⁸¹ We have made the assumption that the individual crystals of HBB have parallel b -axes when making up the larger joined crystals, thus, allowing for an interpretation of the XBI results.

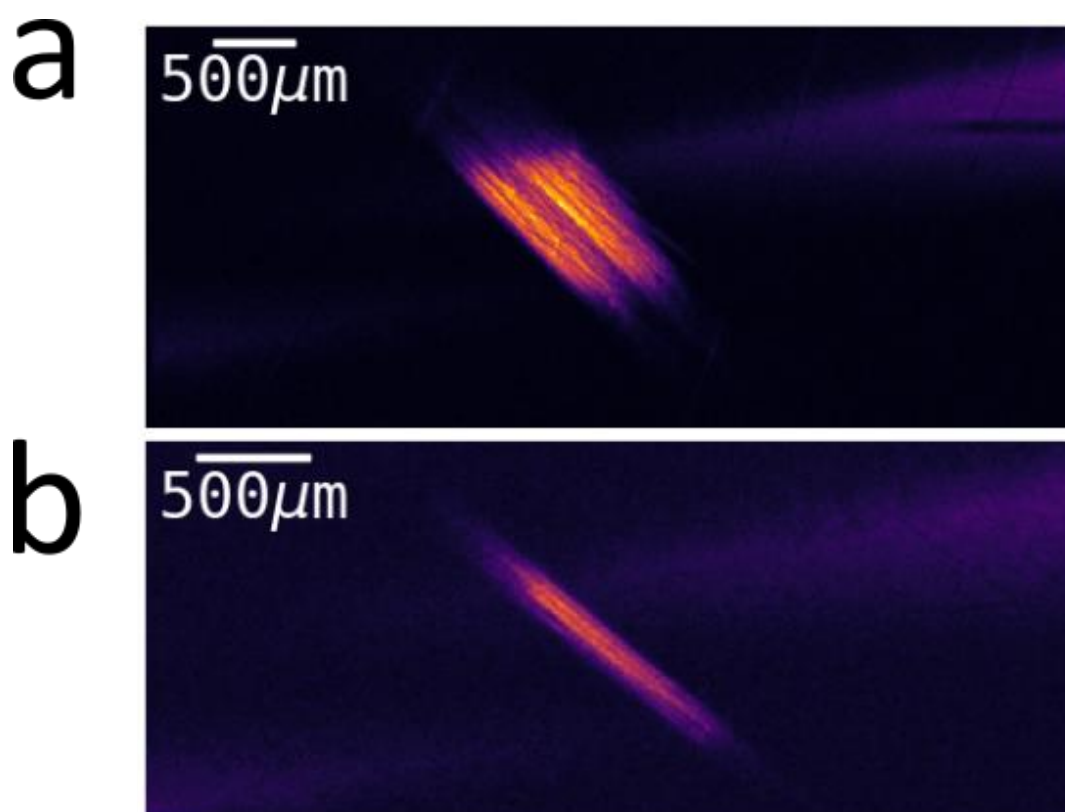


Figure 4.15 XBI images of crystals of HBB at $\chi = 45^\circ$ and $\phi = 90^\circ$. (a) Crystal used for measurements at 105 K, 395 K and temperature scan from 105 K to ambient temperature ($E = 13.474$ keV). (b) Crystal used for measurements at ambient temperature ($E = 13.476$ keV).

At 105 K, the XBI behaviour of HBB is fairly simple to understand, showing the classic sinusoidal curve as a function of χ . Peaks in intensity are seen at $\chi = 45^\circ$ and 135° and the crystal remains bright at these values of χ as the value of φ is varied (Figure 4.16 (b)), apart from a dip in intensity around $\varphi = -30^\circ$. The images at $\varphi = -30^\circ$ show a central dark region parallel to the long axis, while the outer edges of the crystal are brighter (Figure 4.16 (a)).

This φ dependent XBI behaviour is similar to the behaviour exhibited by 1-bromoadamantane/thiourea (Figure 2.15), which shows no change in intensity with φ as the C-Br bond direction is aligned parallel to the φ rotation axis. However, the minimum observed at $\varphi = -30^\circ$ for HBB cannot be explained by an X-ray optic axis aligned parallel to the φ rotation axis. It is possible that the minimum observed at $\varphi = -30^\circ$ is due to some sort of thickness effect or the presence of multiple crystals. This would be consistent with the dark region in the crystal banded by two lighter regions observed in Figure 4.16 (a), when the crystal is oriented at $\varphi = -30^\circ$.

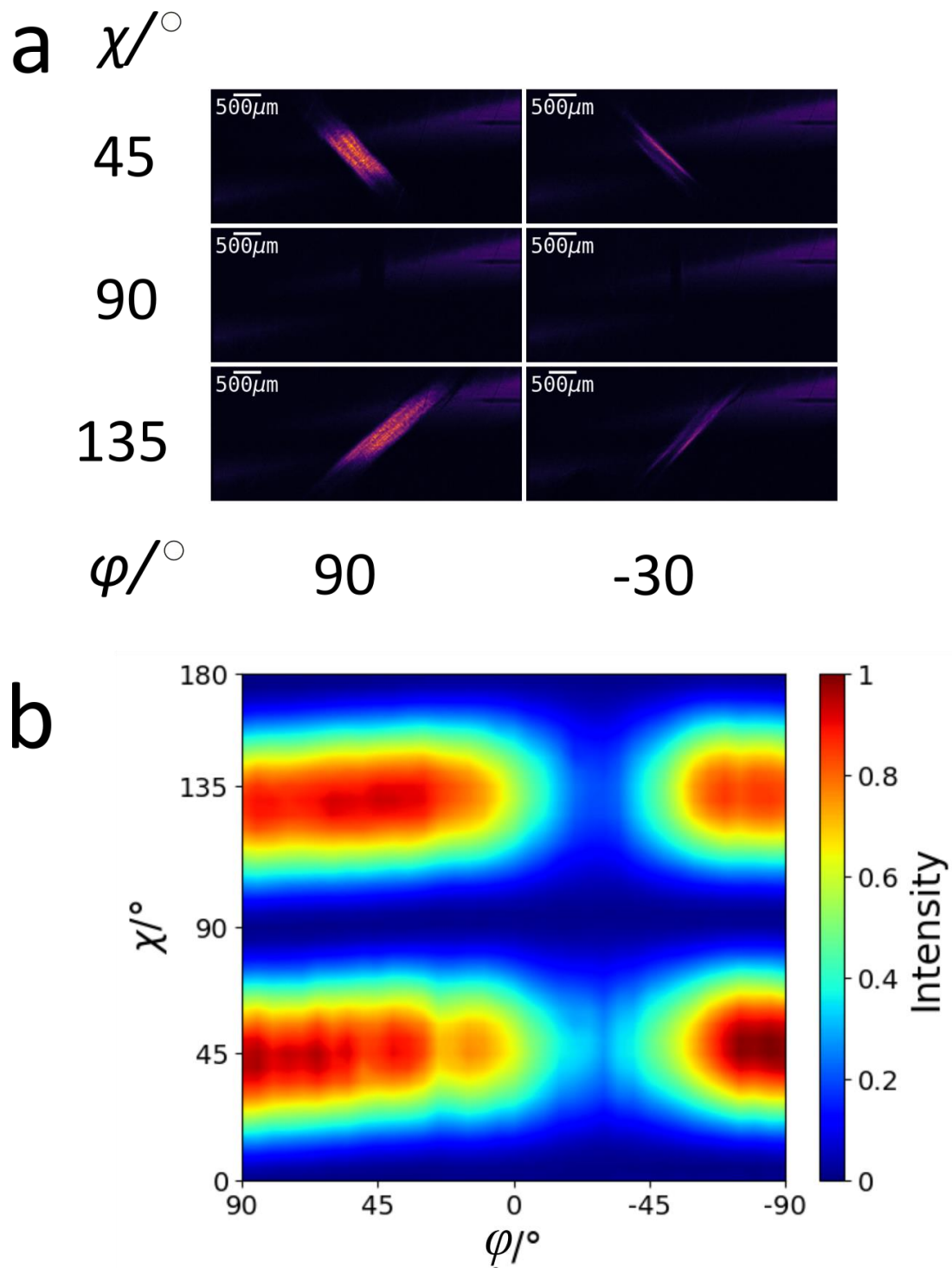


Figure 4.16 (a) XBI images of HBB at 105 K collected at the bromine K-edge (13.474 keV) at $\chi = 45^\circ, 90^\circ, 135^\circ$ and $\varphi = 90^\circ, -30^\circ$. (b) Intensity contour plot showing the intensity as a function of χ and φ at 105 K.

Cooling a single crystal of HBB from 295 K to 105 K with crystal orientation fixed at $\chi = 45^\circ$ and $\varphi = 0^\circ$ showed no noticeable change in intensity (Figure 4.17 (b)). However, the images of the crystal during cooling clearly show some change in the uniformity of the crystal (Figure 4.17 (a)). Dark regions (possibly cracks) perpendicular to the long axis of the crystal start to form at about 220-180 K, and the decrease of intensity in these regions suggests that X-ray birefringence is lost, which could mean a loss of crystallinity of the sample in these regions. Furthermore, the existence of these “cracks” appears to be reversible (Figure 4.17 (d)), as they disappear in an XBI image of the crystal after it was heated back to 395 K.

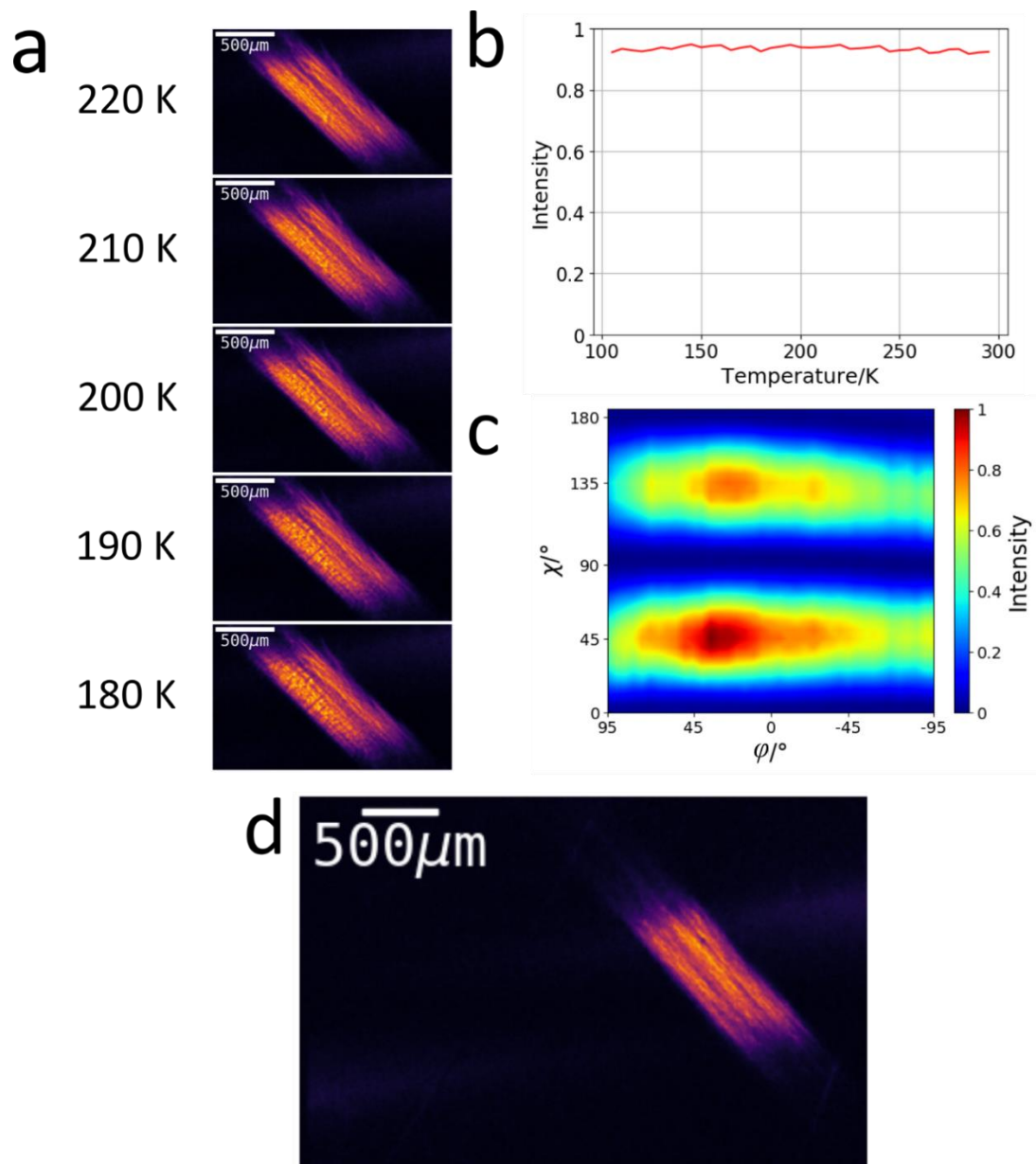


Figure 4.17 (a) Selected XBI images recorded on cooling a single crystal of HBB (with an XBI image recorded every 10 K between 220 K and 180 K). (b) Plot of intensity for a single crystal of HBB recorded on cooling from 295 K to 105 K in steps of 5 K (data from the same experiment shown in (a)). The XBI intensity data has been normalized using the maximum and minimum values of an ambient temperature χ scan ($\phi = 90^\circ$). The XBI images corresponding to this temperature scan can be viewed in Movie S3. (c) Intensity contour plot from XBI data recorded at ambient temperature for a single crystal of HBB as a function of χ and ϕ (different crystal to rest of straight crystal measurements). (d) XBI image of crystal recorded at 395 K after cooling to 105 K, oriented at $\chi = 45^\circ$ and $\phi = 90^\circ$ (same crystal as used for (a) and (b)).

The intensity contour plot as a function of χ and φ (Figure 4.17 (c)) at ambient temperature was recorded using a different HBB crystal than that studied as a function of temperature (Figure 4.16, Figure 4.17 (a), (b), and (d) and Figure 4.18). It shows the same XBI behaviour as a function of χ , with intensity maxima at $\chi = 135^\circ$ and $\chi = 45^\circ$ for each value of φ . We note there is no minimum at $\varphi = -30^\circ$ when $\chi = 45^\circ$ or $\chi = 135^\circ$, suggesting that the minimum observed at $\varphi = -30^\circ$ for the previous sample does not represent intrinsic behaviour.

A full 2D XBI measurement at 395 K for HBB (Figure 4.18 (b)) was completed using the same crystal as for the low temperature study. Overall, the contour plot at 105 K (Figure 4.16 (b)) and 395 K (Figure 4.18 (b)) are quite similar, as are the recorded XBI images. The φ behaviour, which shows a minimum around $\varphi = -30^\circ$, remains unchanged. At 395 K the intensity maxima at $\chi = 45^\circ$ and 135° observed at 105 K appear to occur at a slightly lower χ value at $\varphi = 90^\circ$, but occur at $\chi = 45^\circ$ and 135° at $\varphi = -90^\circ$. It is possible that during heating or rotation the crystal has shifted slightly so the b -axis is no longer parallel to the x -axis at $\chi = 0^\circ$, but an explanation for this shift in intensity maxima for the χ rotation is still unclear.

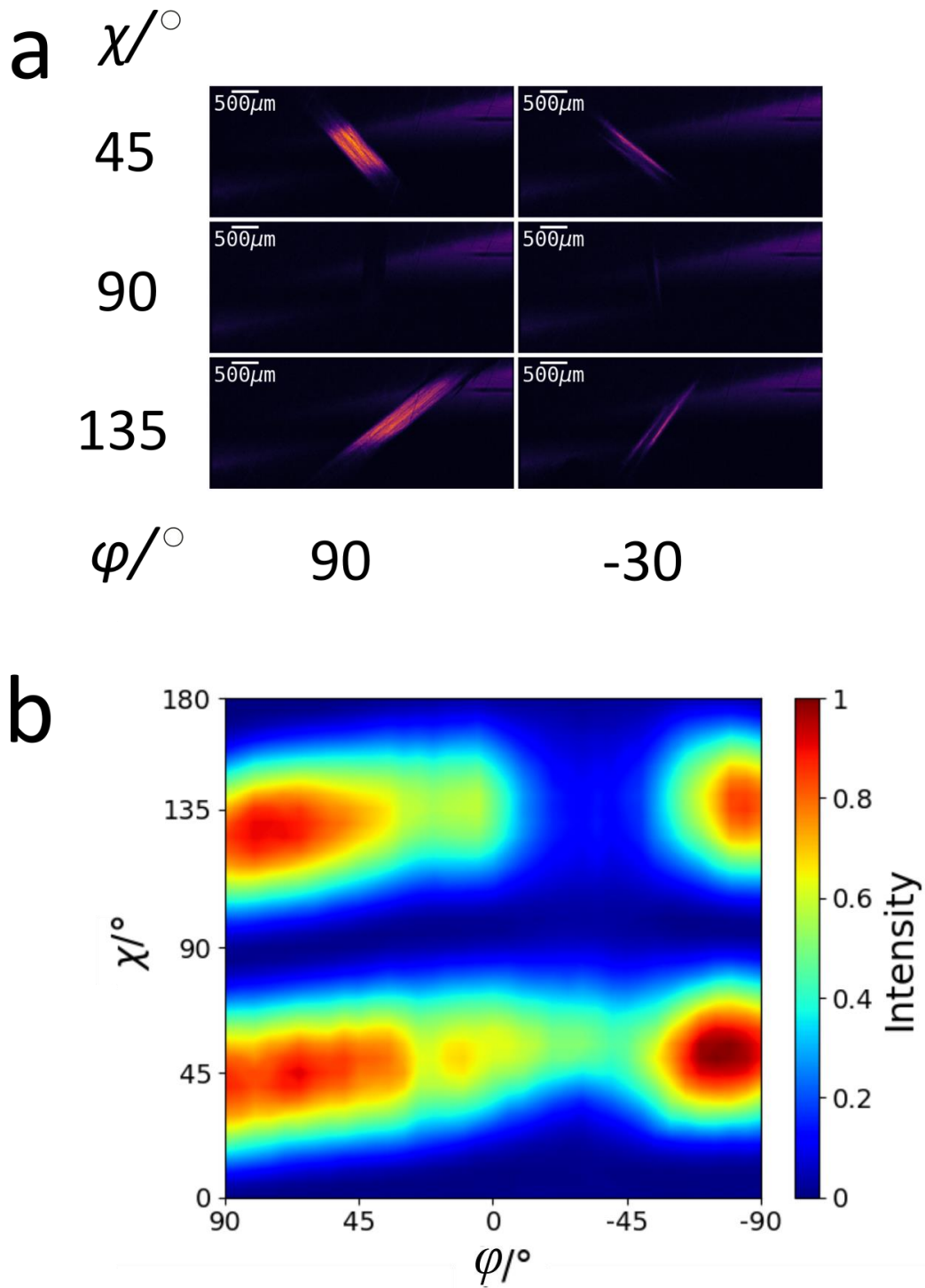


Figure 4.18 (a) XBI images of a crystal of HBB at 395 K recorded at the bromine K-edge (13.474 keV) at $\chi = 45^\circ, 90^\circ, 135^\circ$ and $\varphi = 90^\circ, -30^\circ$. (b) Contour plot showing intensity as a function of χ and φ at 395 K for a crystal of HBB.

4.3.1.2 XBI studies of Bending of HBB Crystals

As mentioned in section 4.1, single crystals of HBB have already been reported to bend at high temperature. In situ XBI studies of a single crystal of HBB were carried out at 400 K using the bending apparatus described in Figure 4.2. The single crystal bent as expected but, interestingly, showed signs of elastic bending (Figure 4.19 (a)).

Five images are shown. The XBI image at the left show the needle of the bending setup pushed downwards onto the crystal, which is horizontal. The XBI images to the right show the upwards journey of the needle, decreasing the force applied to the crystal. Clearly, upon removal of the force exerted by the needle, the HBB crystal returns to its original shape, thus demonstrating elastic bending.

To illustrate the elastic bending, a profile plot of the intensity along the HBB crystal was measured at three stages during the bending process corresponding to Images 1, 2 and 3 (Figure 4.19 (b)). The intensity plots from Images 1 and 3 very closely match, corresponding to the bent HBB crystal before and after the maximum deformation. Image 2, which shows the greatest degree of bending of the HBB crystal during this experiment, shows higher intensity than Images 1 and 3. The maximum in intensity is due to the HBB crystal at this point now being more closely aligned to an angle of $\chi = 45^\circ$ or 135° relative to the direction of incident polarization.

Observing the XBI behaviour of the crystal during the full bending process (involving deformations greater than that shown in Figure 4.19) is difficult due to limitations caused by the height of the beam. Unequal intensities are observed in Figure 4.19 where the intensity to the left side appears consistently higher than the intensity to the right side. This is due to the beam not being perfectly centered at which point perfect linear polarization is not achieved and the incident beam contains slight elliptical polarization. Assuming that the crystal to either side of the needle is bent to roughly the same angle, the same XBI intensity should be observed.

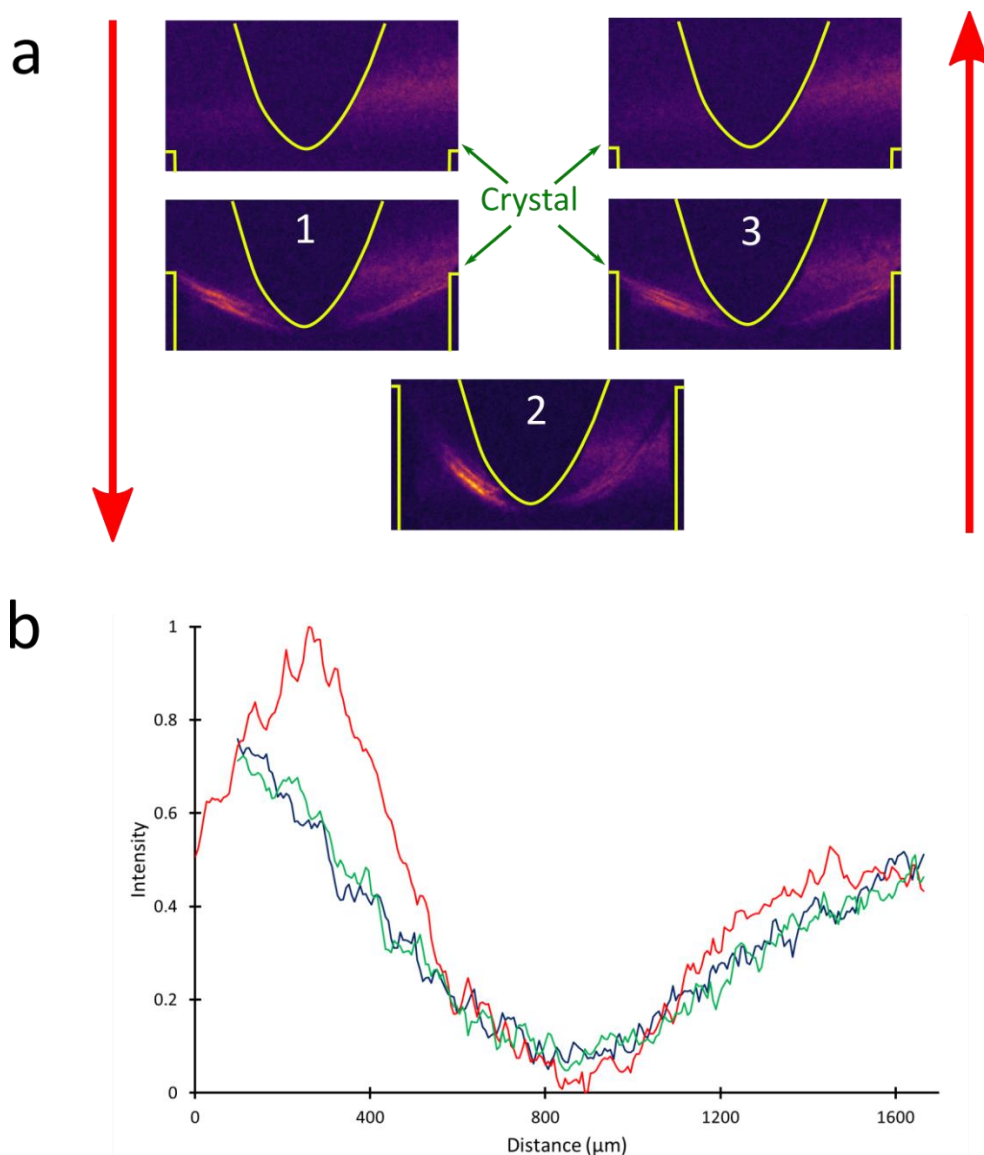


Figure 4.19 (a) XBI images recorded for a single crystal of HBB at 400 K during the bending process. The bending process can be viewed in Movie S4. (b) Intensity recorded along the bent crystals in Image 1 (blue), Image 2 (red) and Image 3 (green).

4.4 Conclusions

This Chapter focused on samples which are mechanically deformable. Unfortunately, we were not able to observe changes in XBI behaviour as a function of deformation on bending a crystal of CuAcAc. The XBI behaviour of the straight crystal determined that no X-ray birefringence is seen when the known bending axis is parallel to the beam direction and the in situ setup for bending means that XBI measurements can only be recorded in this orientation.

However, CuAcAc still proved to be an interesting sample to study. The theoretical calculations on the XBI behaviour of the straight (unbent) crystal have been expanded to incorporate calculations for the isotropic ($a(E)$) and anisotropic ($b(E)$) absorption coefficients. In addition, it was the first instance of theoretical calculations for which the bonding environment of the X-ray absorbing element was more complicated than a single bond. The CuAcAc crystal showed an unusual cross sectional morphology (rectangular) which could affect the XBI behaviour during a φ rotation, due to the differing X-ray path lengths experienced. While the cross section of the sample has been determined in relation to the φ rotation, future work will involve incorporating this thickness dependence into the theoretical calculations to produce a more accurate simulated XBI intensity for CuAcAc.

XBI studies of HBB show a strong change in intensity with χ rotation, for most values of φ . Therefore, the in situ bending for HBB did not encounter the same problems as for CuAcAc. However, unexpected behaviour at specific values of φ does need to be investigated further; at this point, it is unclear whether the minimum observed is due to sample morphology, crystal microstructural defects, or a multiple crystal. Theoretical calculations are ongoing and with further XBI measurements of single crystals would help with understanding this phenomenon.

Elastic bending of HBB was observed at high temperature rather than the expected plastic bending. Possible reasons that elastic bending is observed could be a dependence on the thickness of the crystal or the extent by which the crystal is bent. CuAcAc has been observed to bend elastically before plastic bending is observed, as long as the deformation of the crystal is sufficiently low.⁷⁸ Clearly, understanding the bending behaviour of HBB in more detail requires further work.

In addition, a number of halogenated benzenes have been observed to exhibit unusual properties such as phase transitions, bending and shearing.^{71,80} A review of the literature is needed to identify brominated benzenes, which have the potential to show interesting XBI behaviour upon application of a physical stimulus.

5 XBI Studies of 1,2,4,5-Tetrabromobenzene

5.1 Introduction

The compound 1,2,4,5-tetrabromobenzene (TBB, Figure 5.1) proved to be an exceedingly interesting sample to study using XBI. Upon heating to 318.15 K, TBB undergoes a reversible phase transition from the β form to the γ form, which is accompanied by the crystal jumping or breaking. Materials which respond to external stimuli via mechanical motion are particularly important to materials science due to their potential use as actuators.^{49,50,54,59–70} Particularly exciting are materials which have controllable and reversible motion at fast time scales. However, using single-crystals as actuators encounters problems due to often non-repeatable motions, as the crystal may start to break down over repeated usage.

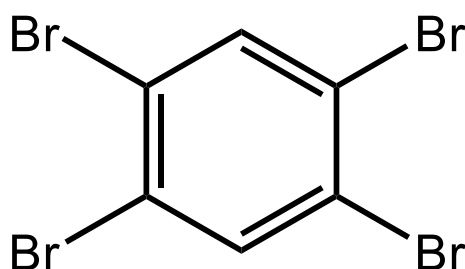


Figure 5.1 Molecular structure of 1,2,4,5-tetrabromobenzene (TBB).

TBB very commonly forms contact twins upon crystallization, which means that it can be observed to act as an analogue of a bimetallic strip. Bimetallic strips are formed of different metals joined lengthwise; upon heating, the strip will bend due to the two metals expanding at different rates. Twinned crystals of TBB for which only one of the crystals is heated to transition (318.15 K) exhibit a reversible motion in the crystal similar to the bimetallic strip. The crystal integrity does not deteriorate as long as the temperature variation to produce the crystal motion is kept close to 318.15 K. Increasing the temperature leads to a point at which the crystal splits along the twin axis. A further increase in temperature causes the two ends of the twins to oscillate away and together (if still joined at one end). The motion exhibited by the crystals at the phase transition has been observed by the polarizing optical microscope, indicating that XBI may be a useful tool to study these crystals.^{67,82}

We note that the transition temperature for twinned crystals and single crystals of TBB has been observed to differ (318.65 K and 318.15 K, respectively), and the reverse transition occurs on cooling at 305.85 K.^{82,83} The crystal structures of the β and γ are actually very similar, belonging to the monoclinic crystal system and the $P2_1/n$ space group.⁸⁴⁻⁸⁷

	Temperature (K)	a (Å)	b (Å)	c (Å)	β (°)	V (Å ³)
β	293	4.0172	10.6917	10.2615	100.175	433.807
γ	323	4.0618	11.1039	9.8533	100.618	436.793

Table 5.1 Crystal structure data for the β (at ambient temperature) and γ (at 323 K) polymorphic forms of TBB.⁸⁷

The long axis of the needle morphology corresponds to the a -axis [100], along which the molecules are stacked. Each stack is surrounded by four other stacks which are offset from the central stack along the [100] axis (Figure 5.2). The molecules within a stack can be viewed perpendicularly to the molecular plane along the $[\bar{1}02]$ axis in the β phase, upon transition to the γ phase the TBB molecular planes shift slightly. There is an angle between stacks of roughly 167° for β and 172° for γ . The interplanar distances between molecules in the stacks are 4.017 Å for β and 4.0618 Å for γ .^{85,87}

The violent transition observed in TBB can be assigned to the anisotropic change observed in the unit cell. The unit cell expands along the b -axis and contracts along the c -axis. This anisotropic change is, however, small and other factors may be involved in the rather explosive phase transition. A study of TBB using Brillouin light scattering was used to establish that the relatively violent nature of the crystal at the phase transition is caused by elastic instability. A side effect of this study confirmed that a single crystal of TBB exhibits birefringence at certain orientations.⁸⁸

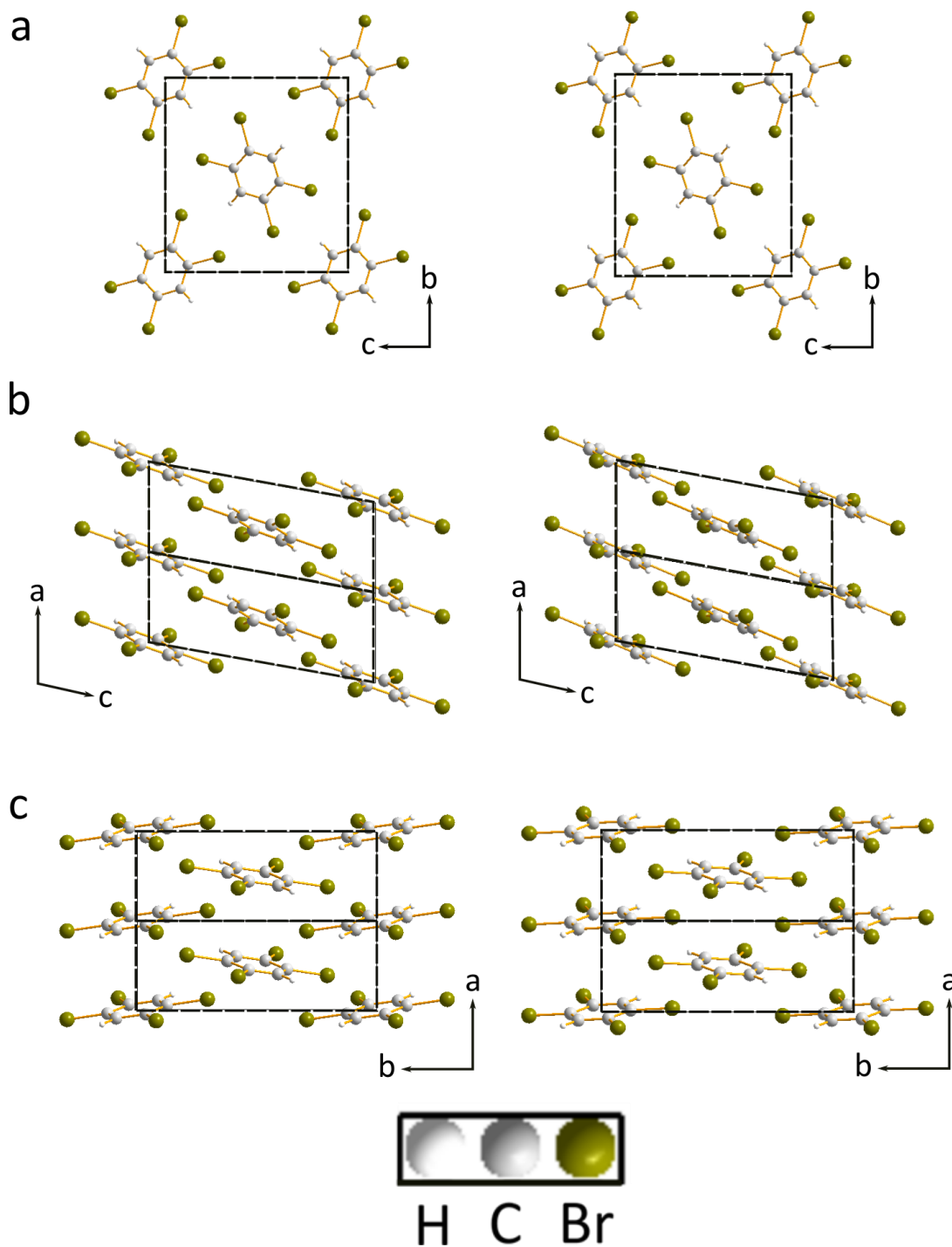


Figure 5.2 Crystal structure of TBB in the β phase (at ambient temperature) left, and the γ phase (at 323 K) right, viewed along the (a) a-axis, (b) b-axis and (c) c-axis.⁸⁷

Face-indexing of a single crystal of the β phase of TBB has established that the side faces are $(0\bar{1}1)$ and $(0\bar{1}\bar{1})$ (Figure 5.3).⁸⁹ The faces at the top and bottom of the crystal are of little concern for XBI as we cannot image from this direction and we have already established the long needle axis as the $[100]$ axis in both β and γ phases.

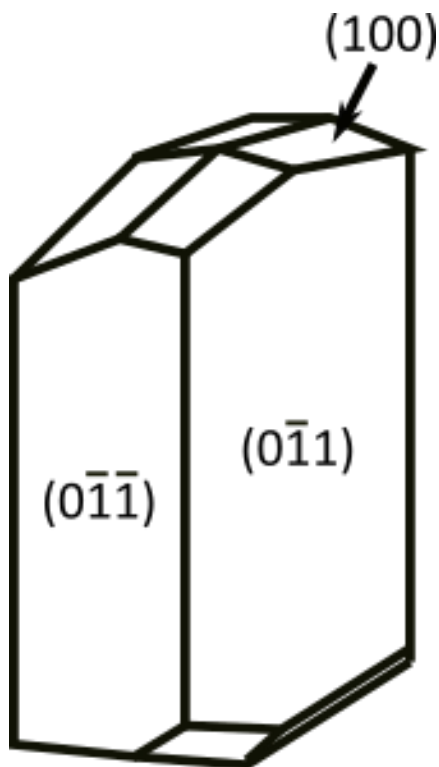


Figure 5.3 Face-indexing of a single crystal of TBB in the β phase. Adapted from Reference 89.⁸⁹

Theory predicts that the intermolecular interactions, which stabilize the β and γ polymorphs, also stabilize the twin interface. This also helps to explain the difference in phase-transition temperature between single crystals and twinned crystals as there is believed to be a slight stabilization from the twin plane intermolecular interactions.⁸³ Lattice energy calculations have predicted that the twinned crystals are displaced by $a/2$.⁹⁰ Twinned crystals have parallel or antiparallel $[100]$ axes and the twin boundary is the (011) plane. The twinned crystals rarely consist of twins of the same thickness. There is an angle of 49° between molecular planes across the twin plane, and it is suggested that the $\text{Br}\cdots\text{Br}$ halogen bonds and $\text{C-H}\cdots\text{Br}$ hydrogen bonds may be formed across the twin boundary. This twin interface has been visualized by H. F. Lieberman, R. J. Davey, and D. M. T. Newsham,⁸³ utilizing the molecular modelling software CERIOUS (Figure 5.4).

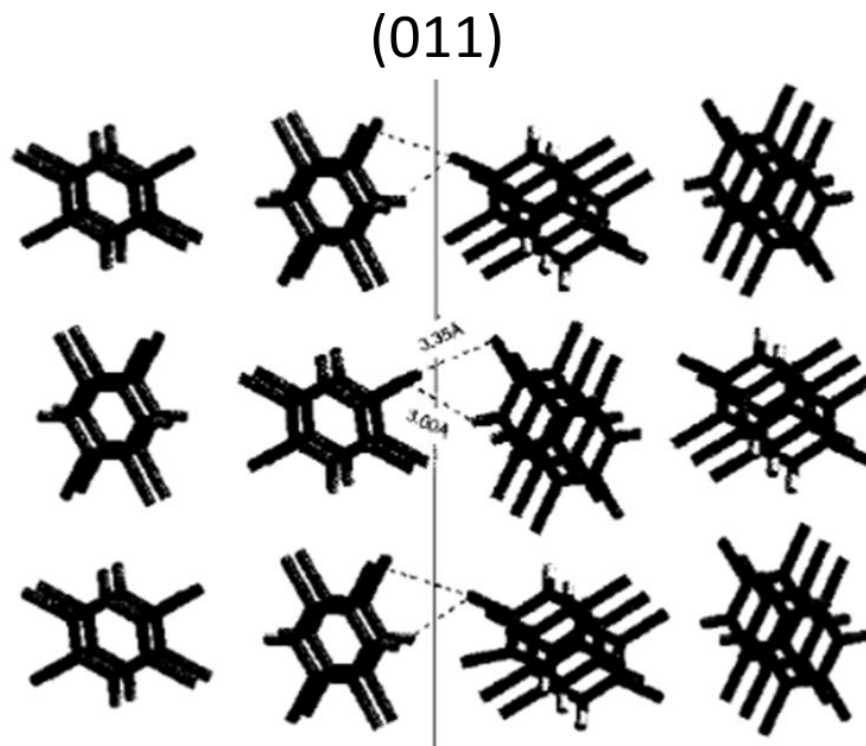


Figure 5.4 Twin interface at the (011) face visualized by H. F. Lieberman et al. Bromine-bromine and bromine-hydrogen contacts across the interface are shown. Adapted from Reference 83.⁸³

5.2 Results and Discussion

TBB was recrystallized from toluene by slow cooling. For the XBI experiments, the incident X-ray energy was 13.474 keV, corresponding to the Br K-edge. In this work, the beam dimensions were defined by slits of 4 mm (vertical) and 4 mm (horizontal), and the polarization analyzer was Si (555). The detectors used for XBI were the Medipix Merlin hybrid pixel detector and “X-ray eye” detector (12 bit CCD miniFDI camera from Photonic Science Ltd).

The discussion of the experimental XBI data of TBB crystals is separated into single crystal, twinned crystal and ‘hourglass’ samples. Hourglass discusses results concerning a single crystal of TBB with XBI behaviour differing from that of typical single or twinned crystals. All the crystals have a similar cross-sectional morphology, resembling a rectangle, as expected from the face indexing in Figure 5.3. Full details of the experiments on TBB crystals discussed in this Chapter can be found in Table 5.2.

TBB Crystal		Scan	Range	Orientation	T/K	Figure No.
Single	1	X-ray absorption	E = 13.4 to 13.5 keV in 0.001 keV steps	$\chi = 90^\circ, 180^\circ$ $\varphi = 90^\circ, -90^\circ$	Amb	5.5
		XBI χ - φ	$\chi = 10^\circ$ to 205° in 5° steps $\varphi = 90^\circ$ to -90° in 5° steps	N/A	Amb	5.6
	2	Temperature	T = 315 K to 328 K in 0.1 K steps	$\chi = 135^\circ, \varphi = 0^\circ$	N/A	5.7
		XBI χ	$\chi = 20^\circ$ to 200° in 5° steps	$\varphi = 0^\circ$	328	5.8
Twinned	1	XBI χ	$\chi = 20^\circ$ to 195° in 5° steps	$\varphi = 0^\circ$	Amb	5.15 Movie S5
	2	XBI χ	$\chi = 10^\circ$ to 210° in 5° steps	$\varphi = 90^\circ, -90^\circ$	Amb	5.16, 5.17
	3	Temperature	T = 293 K to 328 K in 0.1 K steps	$\chi = 120^\circ, \varphi = 90^\circ$	N/A	5.19, 5.20 Movie S6
'Hourglass'	1	XBI χ	$\chi = 20^\circ$ to 205° in 5° steps	$\varphi = 0^\circ$	Amb	5.22 Movie S7
		XBI χ	$\chi = 180^\circ$ to 40° in 5° steps	$\varphi = 0^\circ$	328	5.23 (a)
	2	Time	t = 1 s to 1092 s every 2 s	$\chi = 145^\circ, \varphi = 0^\circ$	333	5.23 (b) Movie S8
		XBI χ	$\chi = 40^\circ$ to 180° in 5° steps	$\varphi = 0^\circ$	293	5.24
		XBI χ	$\chi = 180^\circ$ to 40° in 5° steps	$\varphi = 0^\circ$	333	5.24

Table 5.2 Summary of experiments on TBB crystals discussed in this Chapter. Amb denotes ambient temperature (ranges between 291-301 K).

Single, twinned and ‘hourglass’ crystals were identified using optical microscopy. Single crystals are long and translucent, twinned crystals can be identified by a line in the centre of a crystal face running parallel to the long axis of the crystal, denoting the twin interface. The ‘hourglass’ crystals are easily identified by opaque regions in the crystal in an ‘hourglass’ shape. The crystals of TBB are oriented relative to the XBI set-up so that the crystallographic a -axis (long axis of crystal morphology) is in the xy -plane. Rotation of the a -axis around the z -axis (incident beam direction) is referred to as the χ -rotation, with $\chi = 0^\circ$ defined as the orientation with the crystallographic a -axis parallel to the x -axis (horizontal). The ϕ rotation refers to rotation of the crystal around the a -axis.

5.2.1 XBI Studies of a Single crystal of TBB

Initially, X-ray absorption spectra were recorded for four orientations of a single crystal of TBB (Figure 5.5). The recorded intensity values for the recorded X-ray absorption spectra are first normalized using Equation 5.1. I_0 is the incident X-ray beam intensity before encountering the sample and I_F is the final intensity from the detector.

$$I = -\ln\left(\frac{I_F}{I_0}\right) \quad (5.1)$$

The X-ray absorption spectra were normalized to the intensity (I) at 13.500 keV and 13.400 keV, using Equation 5.2. These intensities are above and below the K-edge, respectively, at which the sample orientation should have no effect on the X-ray absorption.

$$I_N = \frac{(I - I_{13.400})}{(I_{13.500} - I_{13.400})} \quad (5.2)$$

Therefore, different sample orientations should give the same intensity at a given X-ray energy.

Figure 5.5 (a) shows X-ray absorption spectra recorded for a single crystal of TBB at $\chi = 90^\circ$ and 180° , with $\varphi = 90^\circ$ in each case. Figure 5.5 (b) shows the X-ray absorption spectra for a single crystal of TBB oriented at $\chi = 90^\circ$ and 180° , with $\varphi = -90^\circ$ in each case. These two orientations in φ correspond to the large faces of the crystal perpendicular to the incident X-ray beam (z -axis). X-ray absorption spectra recorded at $\varphi = 0^\circ$ are very clearly of a much lower quality, probably due to the cross-sectional morphology of the TBB crystal, as at $\varphi = 0^\circ$ the path length of the X-ray beam through the crystal is much larger.

At $\varphi = 90^\circ$ and $\varphi = -90^\circ$, there is a clear difference between the X-ray absorption spectra recorded for $\chi = 90^\circ$ and $\chi = 180^\circ$. Thus, the X-ray dichroism spectra were determined for both $\varphi = 90^\circ$ and $\varphi = -90^\circ$ and the calculated X-ray birefringence is shown in Figure 5.5 (c). X-ray birefringence is clearly observed for both $\varphi = 90^\circ$ and $\varphi = -90^\circ$ with an X-ray birefringence difference of roughly 0.65 at each value of φ .

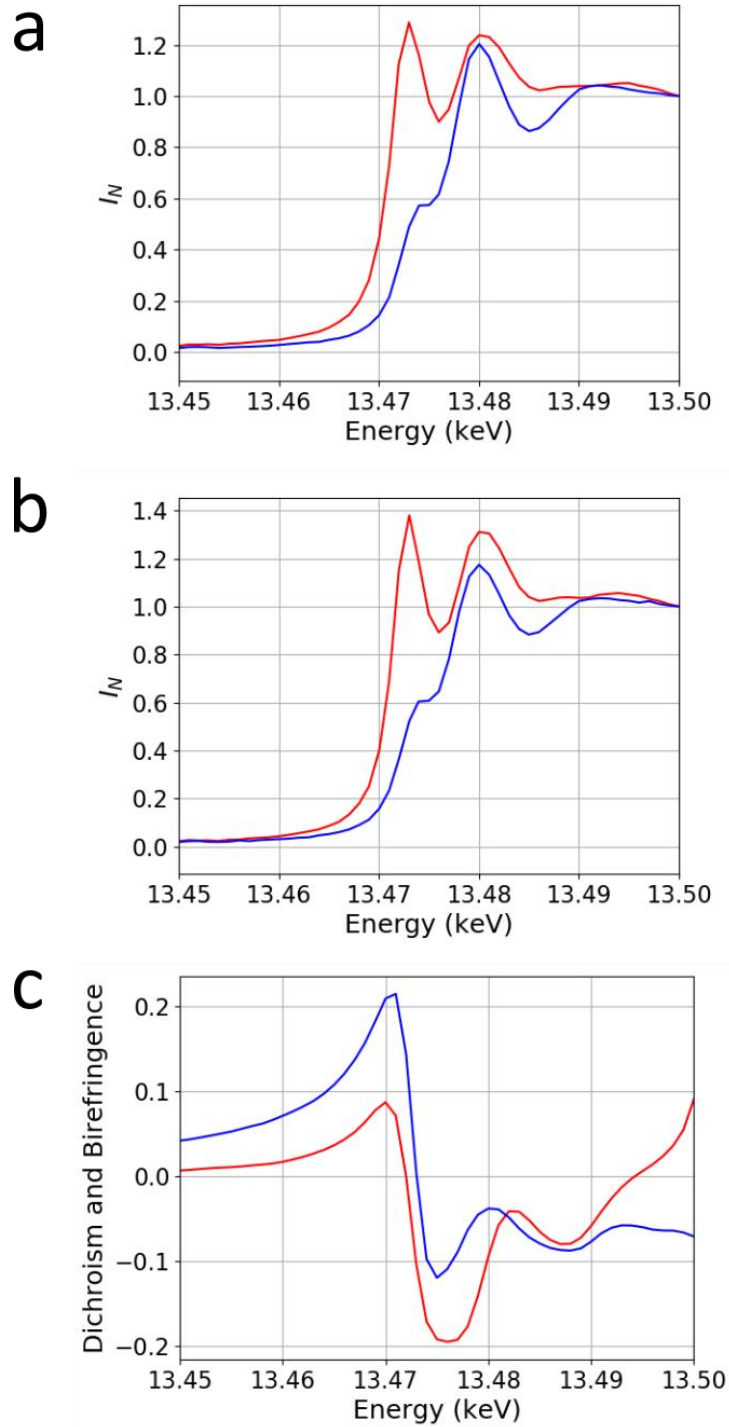


Figure 5.5 X-ray absorption spectra recorded for a single crystal of TBB at four different orientations, normalized using Equations 5.1 and 5.2. (a) Crystal oriented at $\chi = 90^\circ$ and $\phi = 90^\circ$ (red) and crystal oriented at $\chi = 180^\circ$ and $\phi = 90^\circ$ (blue). (b) Crystal oriented at $\chi = 90^\circ$ and $\phi = -90^\circ$ (red) and crystal oriented at $\chi = 180^\circ$ and $\phi = -90^\circ$ (blue). (c) X-ray birefringence calculated from the X-ray absorption data in (a) (red) and (b) (blue).

XBI images were recorded for the single crystal of TBB at 293 K (Figure 5.6 (a)). The two orientations of the crystal with the large flat faces perpendicular to the incident X-ray beam (corresponding to $\varphi = 90^\circ$ and -90°) show almost opposite XBI behaviour as a function of χ . Recorded χ scans (Figure 5.6 (b)) indicate that when the crystal is oriented at $\varphi = 90^\circ$, there are intensity maxima at $\chi = 65^\circ$ and 155° , with minima at $\chi = 20^\circ$, 110° and 200° . When the crystal is rotated by $\Delta\varphi = 180^\circ$ to $\varphi = -90^\circ$, the intensity maxima are now at $\chi = 25^\circ$, 115° and 205° , with minima at $\chi = 70^\circ$ and 160° . These observations suggest that, by rotating the crystal by $\Delta\varphi = 180^\circ$ the XBI behaviour shifts by 40° in χ . The XBI behaviour is clearly very similar to the XBI behaviour exhibited by CuBr_2 , as discussed in Chapter 6. The minimum at $\varphi = -90^\circ$ and $\chi = 160^\circ$ is not as deep as the other minimum in the χ scan at $\varphi = -90^\circ$, although it is currently unclear whether this is a feature of the crystal structure or an artefact in the XBI measurement.

The intensity contour plot for a χ - φ scan shown in Figure 5.6 (c) illustrates a gradual shift in the value of χ corresponding to intensity maxima with φ rotation. The cross-sectional shape of the TBB crystal clearly has an effect on the intensity observed at different values of φ . The greater path length of the beam through the crystal at close to $\varphi = 0^\circ$ causes a loss in intensity, while directly along $\varphi = 0^\circ$ there is a slightly larger intensity at all values of χ . If the selected region of the XBI image used to measure the mean intensity is too large, then some intensity from the background could interfere (the smallest face is perpendicular to the beam direction at $\varphi = 0^\circ$).

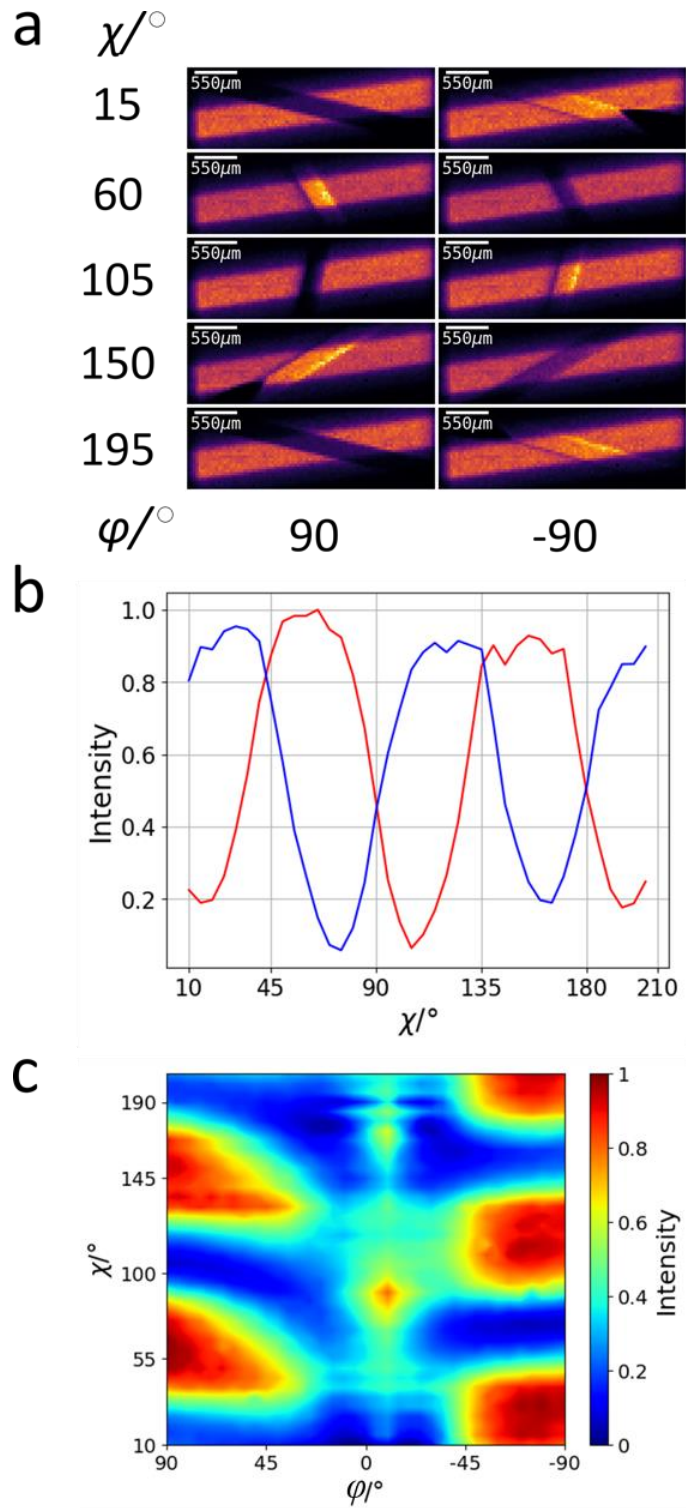


Figure 5.6 (a) Selected XBI images for a single crystal of TBB at 293 K, with the crystal oriented at $\chi = 15^\circ, 60^\circ, 105^\circ, 150^\circ, 195^\circ$ for both $\varphi = 90^\circ$ and -90° . (b) Intensity as a function of χ for a single crystal of TBB at $\varphi = 90^\circ$ (red) and $\varphi = -90^\circ$ (blue). (c) Intensity contour plot for XBI images of single crystal of TBB recorded as a function of χ and φ .

A temperature scan of a different single crystal of TBB recorded from 315 K to 328 K (with fixed crystal orientation at $\chi = 135^\circ$, $\varphi = 0^\circ$) shows a clear change in the recorded intensity at around 318.5 K (Figure 5.7). It is logical to conclude that this change in intensity corresponds to the phase transition in TBB. The change in intensity corresponds to a drop of roughly 7%. Considering the very small changes in crystal structure of TBB associated with the phase transition, the fact that any change in intensity is observed at all is exciting. In the XBI images, there is no detectable change in the dimensions of the single crystal at the transition.

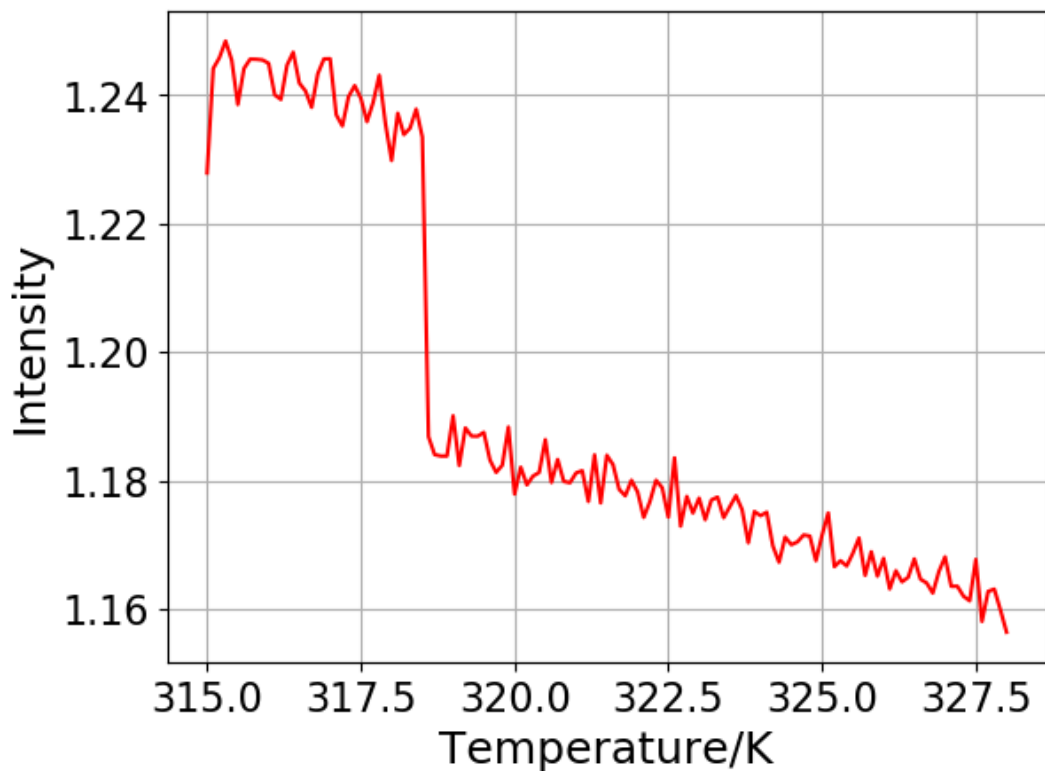


Figure 5.7 Temperature scan from 315 K to 328 K in 0.1 K steps, for a crystal fixed at $\chi = 135^\circ$ and $\varphi = 0^\circ$ (large face of TBB crystal perpendicular to incident X-ray beam direction). A clear decrease in intensity is observed at around 318.5 K. The temperature scan is normalized to the maximum and minimum values of intensity observed in the χ scan (for the same crystal) in Figure 5.8.

A χ scan (at 328 K) for a single crystal of TBB in the γ phase (the same single crystal used in the temperature scan shown in Figure 5.8) shows sinusoidal behaviour (as often observed for XBI imaging), with maxima at $\chi = 40^\circ$ and $\chi = 130^\circ$, and minima at $\chi = 85^\circ$ and $\chi = 175^\circ$. Unfortunately, a χ scan was not recorded for the same crystal in the β phase, so determining if there is any change in the χ scan at the phase transition is not possible with the current data.

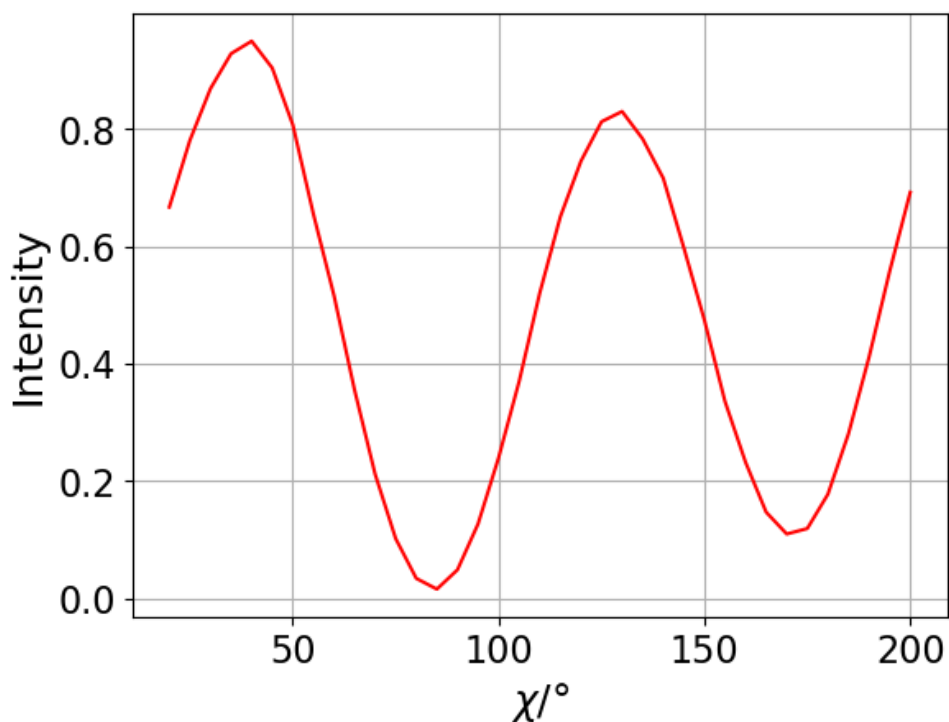


Figure 5.8 Plot of intensity vs. χ of a single crystal of TBB recorded at 328 K. Crystal is oriented at $\varphi = 0^\circ$ (corresponds to the large face $(0\bar{1}1)$ perpendicular to the incident beam direction).

5.2.1.1 Theoretical Calculations of XBI behaviour for a single crystal of TBB

To start the theoretical calculations the atom coordinates of the carbon and bromine atoms making up the C-Br bonds within the unit cell are used to determine the C-Br bond vectors (for the β phase).

Atom Coordinates					
Carbon			Bromine		
x	y	z	x	y	z
0.0464	0.8762	0.0397	0.1152	0.7072	0.0892
0.9469	0.9647	0.1247	0.8715	0.9211	0.2952
0.5531	0.4647	0.3753	0.6285	0.4211	0.2048
0.4536	0.3762	0.4603	0.3847	0.2072	0.4108
0.5464	0.6238	0.5397	0.6152	0.7929	0.5892
0.4469	0.5353	0.6247	0.3715	0.5787	0.7952
0.0531	0.0353	0.8753	0.1285	0.0789	0.7048
0.9536	0.1238	0.9603	0.8848	0.2929	0.9108

Table 5.2 Atom coordinates of the carbon and bromine atoms making up the C-Br bonds within the unit cell of the β phase of TBB (293 K).⁸⁷ Atom coordinates are in the fractional coordinate system.

The C-Br bond vectors are calculated by subtracting the atom coordinates of the bromine atom from the atom coordinates of the corresponding carbon. The vector coordinates are then converted from the fractional coordinate system into a Cartesian coordinate system using Equation 3.6.

Vector Coordinates					
Fractional			Cartesian		
x	y	z	x	y	z
-0.0688	0.1691	-0.0495	-0.1868	1.8076	-0.5003
0.0754	0.0436	-0.1705	0.6119	0.4659	-1.7220
-0.0754	0.0436	0.1705	-0.6119	0.4659	1.7220
0.0688	0.1691	0.0495	0.1868	1.8076	0.5003
-0.0688	-0.1691	-0.0495	-0.1868	-1.8076	-0.5003
0.0754	-0.0436	-0.1705	0.6119	-0.4659	-1.7220
-0.0754	-0.0436	0.1705	-0.6119	-0.4659	1.7220
0.0688	-0.1691	0.0495	0.1868	-1.8076	0.5003

Table 5.3 Vectors of the C-Br bonds within the unit cell of the β phase of TBB (293 K) expressed as fractional and Cartesian coordinates. Cartesian coordinates calculated from the fractional coordinates using Equation 3.6.

The vectors are input into Equation 3.5 to give the following tensor:

$$T_{ij} = \begin{bmatrix} -0.129 & 0 & -0.480 \\ 0 & 1.409 & 0 \\ -0.480 & 0 & 1.274 \end{bmatrix}$$

The tensor as a physical property should match the symmetry properties of the crystal according to Neumann's principle. For a monoclinic system, the symmetry property is:

$$\begin{bmatrix} T_{11} & 0 & T_{13} \\ 0 & T_{22} & 0 \\ T_{31} & 0 & T_{33} \end{bmatrix}$$

Thus, this tensor can be considered correct but is in a Cartesian frame not aligned with the experimental frame. Consequently, the rotation matrix U is required to bring the crystal and experimental frames into coincidence when $\chi = 0^\circ$ and $\varphi = 0^\circ$ (Equation 3.9).

The crystallographic a -axis is parallel to the long-axis of the crystal, thus, the long-axis of the crystal is already parallel to the x -axis of the experimental coordinate system when $\chi = 0^\circ$ after conversion from fractional coordinates to the Cartesian coordinate system using Equation 3.6. Therefore, the U rotation matrix only needs to rotate about the x -axis in order to bring the crystal and experimental frames into coincidence. Thus, an approximate value for U was determined through trial and error by rotating about the x -axis until the theoretical results matched with the experimental.

$$U = \begin{bmatrix} 1 & 0 & 0 \\ 0 & 0.989 & -0.146 \\ 0 & 0.146 & 0.989 \end{bmatrix}$$

The tensor at $\chi = \phi = 0^\circ$ is viewed in Figure 5.9. The z -axis corresponds to the incident beam direction. When viewed along the z -axis (Figure 5.9 (a)), the tensor is clearly anisotropic. The long-axis of the tensor is slightly tilted away from the y -axis, tilting into negative along the x -axis as y becomes more positive. Viewing the tensor along the y -axis (Figure 5.9 (b)), it is slightly tilted from having its long axis parallel to the z -axis. Interestingly, when viewed along the x -axis (along the long axis of the crystal morphology), the tensor appears almost isotropic, although the tensor is tilted so that it is further away in x with a more positive z .

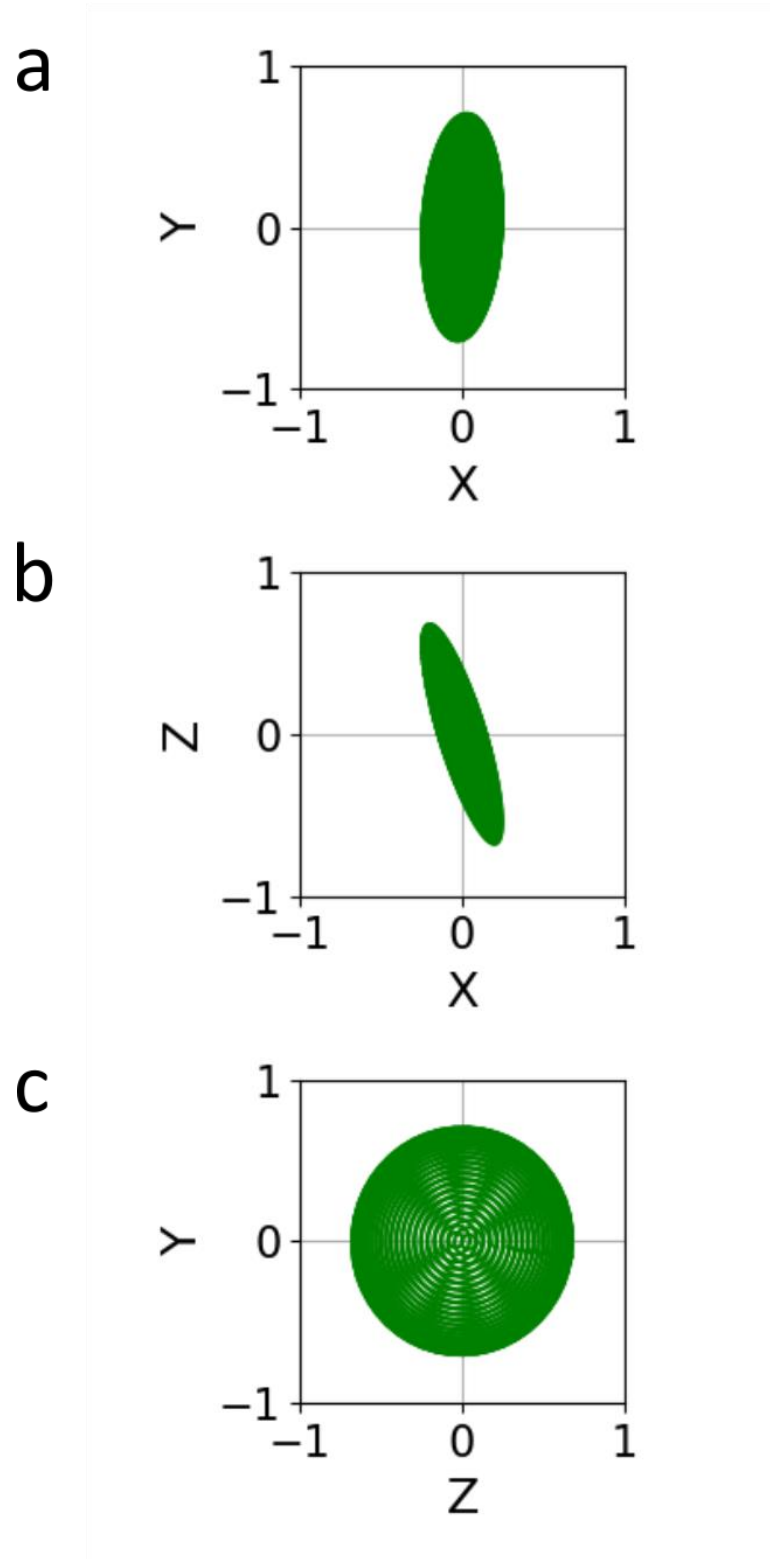


Figure 5.9 Tensor for a single crystal of TBB oriented at $\chi = \varphi = 0^\circ$ viewed along (a) the z-axis, (b) the y-axis and (c) the x-axis. Experimental coordinate system is used with z-axis as incident beam direction and the x-axis as the direction of linear polarization.

Next, the isotropic ($a(E)$) and anisotropic ($b(E)$) absorption coefficients can be determined from the experimental X-ray absorption spectra recorded at different orientations of the crystal discussed earlier. A simplification of the transmitted intensity is to only consider the polarization along \hat{x} , where the absorption coefficient (γ) is equal to the first tensor component:

$$\gamma = a + T_{11}b \quad (5.3)$$

Recording X-ray absorption measurements at different sample orientations gives the absorption coefficient γ at different orientations. Thus, using these measurements with the corresponding tensor T_{ij} orientations, $a(E)$ and $b(E)$ can be calculated using Equation 5.3 as simultaneous equations for all energies in the spectra. Once the $a(E)$ and $b(E)$ values have been determined, they can be used to calculate X-ray absorption spectra at any other orientation, which provides a check against other experimental X-ray absorption measurements at different orientations (Figure 5.10).

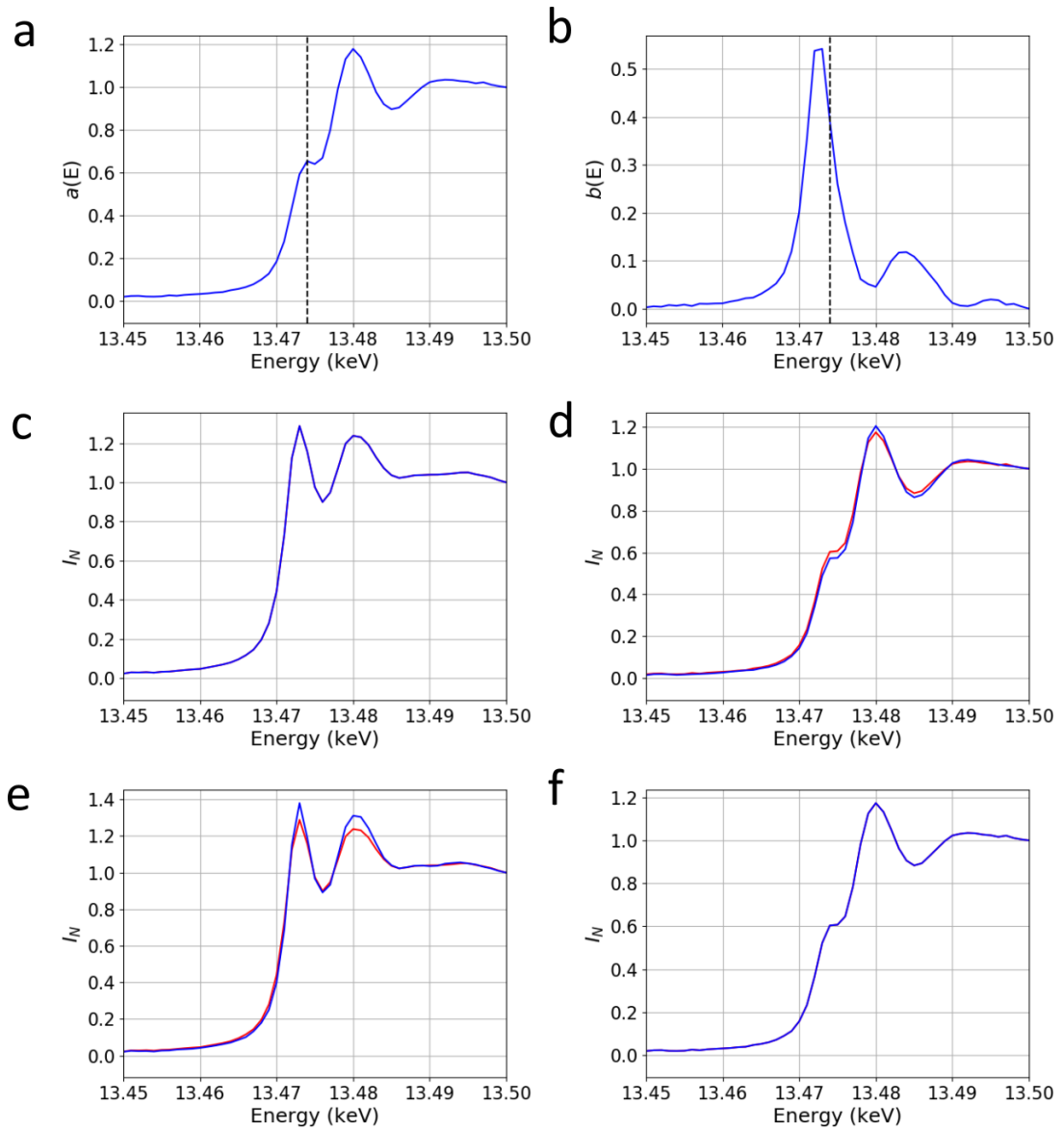


Figure 5.10 The absorption coefficients $a(E)$ (isotropic) and $b(E)$ (anisotropic) are shown as a function of X-ray energy in (a) and (b) respectively; dashed lines indicate the energy (13.474 keV) used in our XBI studies. X-ray absorption spectra for a single crystal of TBB oriented at (c) $\chi = 90^\circ$, $\varphi = 90^\circ$, (d) $\chi = 180^\circ$, $\varphi = 90^\circ$, (e) $\chi = 90^\circ$, $\varphi = -90^\circ$ and (f) $\chi = 180^\circ$, $\varphi = -90^\circ$. The experimental spectra shown in (c) and (f) were used to calculate the absorption coefficients ($a(E)$ and $b(E)$) shown in (a) and (b). The absorption coefficients were then used to simulate spectra to assess the quality of values of $a(E)$ and $b(E)$ as shown in (d) and (e), in which the experimental spectra are in blue and the simulated spectra are in red.

Figure 5.10 (c) and (f) show the experimental X-ray absorption spectra at $\chi = 90^\circ$, $\phi = 90^\circ$ and $\chi = 180^\circ$, $\phi = -90^\circ$, which were used to calculate the $a(E)$ and $b(E)$ values (Figure 5.10 (a) and (b)). The calculated absorption coefficients were then used to calculate simulated X-ray absorption spectra at other crystal orientations shown in Figure 5.10 (d) and (e). The experimental and calculated spectra in Figure 5.10 (d) and (e) are very similar to the experimental spectra indicating a good fit for the real component of the calculated $a(E)$ and $b(E)$ (as expected as there are only two independent orientations). The anisotropic absorption coefficient ($b(E)$) also has an imaginary component, which can be calculated using the Kramers-Kronig transform (Equation 1.8, Figure 5.11).

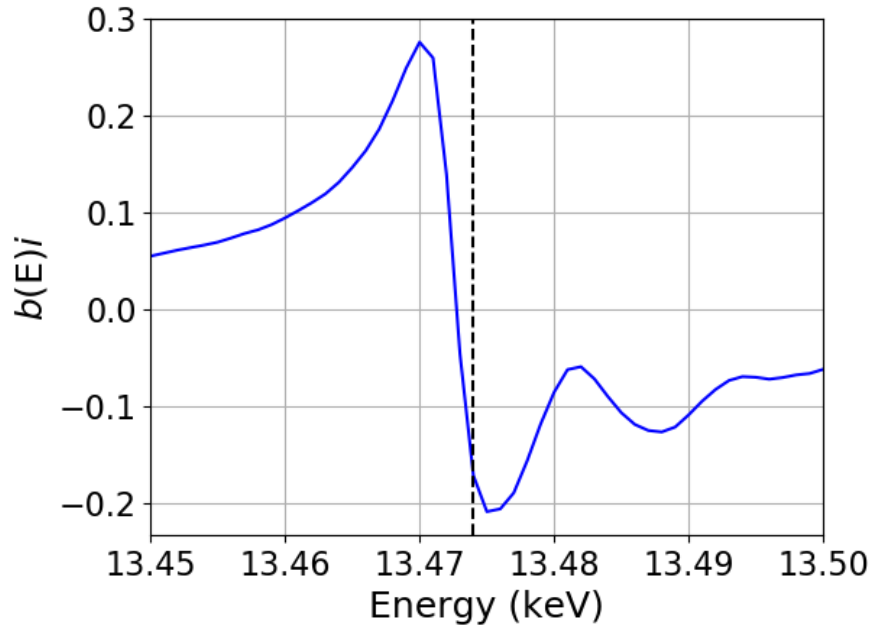


Figure 5.11 Imaginary part of the anisotropic absorption coefficient ($b(E)$) calculated using the Kramers-Kronig transform for a single crystal of TBB. The dashed line corresponds to the energy (13.474 keV) used in our XBI measurements.

Thus, we have determined the isotropic (0.6542) and anisotropic ($0.3930-0.1720i$) absorption coefficients at the bromine K-edge (13.474 keV), allowing the X-ray birefringence to be calculated using the full tensor $\underline{\gamma}$ written as a four-component matrix.

$$\Gamma = \begin{bmatrix} \gamma_{xx} & \gamma_{xy} \\ \gamma_{yx} & \gamma_{yy} \end{bmatrix} \quad (5.4)$$

The transmittance matrix A is used to describe the amplitude and polarization of the X-rays as they propagate through the sample.

$$A = e^{-\frac{(\gamma_{xx} + \gamma_{yy})t}{4}} \begin{bmatrix} \cosh\Phi - \frac{(\gamma_{xx} - \gamma_{yy})t \sinh\Phi}{\Phi} & \frac{\gamma_{xy} t \sinh\Phi}{\Phi} \\ \frac{\gamma_{xy} t \sinh\Phi}{\Phi} & \cosh\Phi + \frac{(\gamma_{xx} - \gamma_{yy})t \sinh\Phi}{\Phi} \end{bmatrix} \quad (5.5)$$

$$\Phi = \frac{t}{4} \sqrt{(\gamma_{xx} - \gamma_{yy})^2 + 4\gamma_{xy}\gamma_{yx}} \quad (5.6)$$

Thus, using the tensor calculated from the C-Br bond vectors and the calculated isotropic ($a(E)$) and anisotropic absorption coefficients ($b(E)$) transmittance matrix A at $\chi = 0^\circ$ and $\varphi = 0^\circ$ is:

$$A = \begin{bmatrix} 0.7383 - 0.0083i & -0.0125 + 0.0073i \\ -0.0125 + 0.0073i & 0.6007 + 0.0723i \end{bmatrix}$$

The matrix μ describing the polarization of the incident beam is expressed in Stokes parameters, where P_3 is linear polarization along x , P_2 is the circular polarization and P_1 is the linear polarization at 45° from x in the xy plane. With almost perfect linear polarization $P_1 = P_2 = 0$ and $P_3 = 1$. In our experimental data, no significant elliptical polarization is observed, so we may assume almost perfect linear polarization:

$$\mu = \frac{1}{2} \begin{bmatrix} 1 + P_3 & P_1 - iP_2 \\ P_1 + iP_2 & 1 - P_3 \end{bmatrix} = \begin{bmatrix} 1 & 0 \\ 0 & 0 \end{bmatrix} \quad (5.7)$$

A_p is the transmittance matrix of the polarization analyzer, where 2θ is the scattering angle and η is the rotation about the beam direction (90°). For the Si (555) reflection at 13.474 keV, 2θ is equal to 94.386° , and hence:

$$A_p = \begin{bmatrix} \cos \eta & -\sin \eta \\ \cos 2\theta \sin \eta & \cos 2\theta \cos \eta \end{bmatrix} = \begin{bmatrix} 0.000 & -1.000 \\ -0.076 & 0.000 \end{bmatrix} \quad (5.8)$$

The ratio of transmitted intensity to incident intensity is determined from the trace of the matrix μ , operated on either side by matrices that represent scattering from (A_p), and transmission through (A), optical components and the sample, where † is the transpose of the complex conjugate.

$$\frac{I_1}{I_0} = \text{Tr.} (A_p A \mu A^\dagger A_p^\dagger) \quad (5.9)$$

Figure 5.12 (a) shows calculated intensity as a function of χ at $\varphi = 90^\circ$ and $\varphi = -90^\circ$, which are clearly in good agreement with the experimental data shown in Figure 5.6 (b). At $\varphi = 90^\circ$, maxima occur in the calculated data at $\chi = 65^\circ$ and 155° , with minima at $\chi = 20^\circ$, 110° and 200° . At $\varphi = -90^\circ$, maxima are observed in the calculated data at $\chi = 25^\circ$, 115° and 205° the minima at $\chi = 70^\circ$ and 160° . The calculated χ scans therefore show the same behaviour as the experimental data, even showing a higher intensity for the minima at $\chi = 160^\circ$, $\varphi = -90^\circ$ and $\chi = 200^\circ$, $\varphi = 90^\circ$ for both experimental and calculated χ scans.

The calculated intensity contour plot (Figure 5.6 (b)) shows the gradual shift of the maxima in χ as the angle φ is varied, leading to an “undulating pattern”. The “undulating pattern” starts with a maximum at $\chi = 155^\circ$ and $\varphi = 90^\circ$, which shifts to a maximum of $\chi = 115^\circ$ when φ is rotated to -90° representing a change of 40° in χ . Rotating further in φ would give rise to the reverse shift in χ . The intensity maxima within the “undulating pattern” are observed at the highest and lowest values of χ as φ is varied. Furthermore, the intensity minimum at roughly $\chi = 110^\circ$, $\varphi = 90^\circ$ is noticeably deeper than the other minima observed at $\varphi = 90^\circ$, matching the experimental data.

However, the calculated intensity contour plot (Figure 5.12 (b)) does not match up with the experimental intensity contour plot (Figure 5.6 (c)) in the region close to $\varphi = 0^\circ$. As discussed above, the path length of the beam through the sample is significantly increased around $\varphi = 0^\circ$ as a consequence of the crystal morphology used to record the experimental XBI data, but this effect was not incorporated into the theoretical analysis (i.e., the parameter t in Equation 5.5 and Equation 5.6 was assumed to be independent of sample orientation and given a value of 1). If a thickness dependence were included it would likely cause a decrease in intensity around $\varphi = 0^\circ$ in the calculated data, similar to that observed in the experimental data.

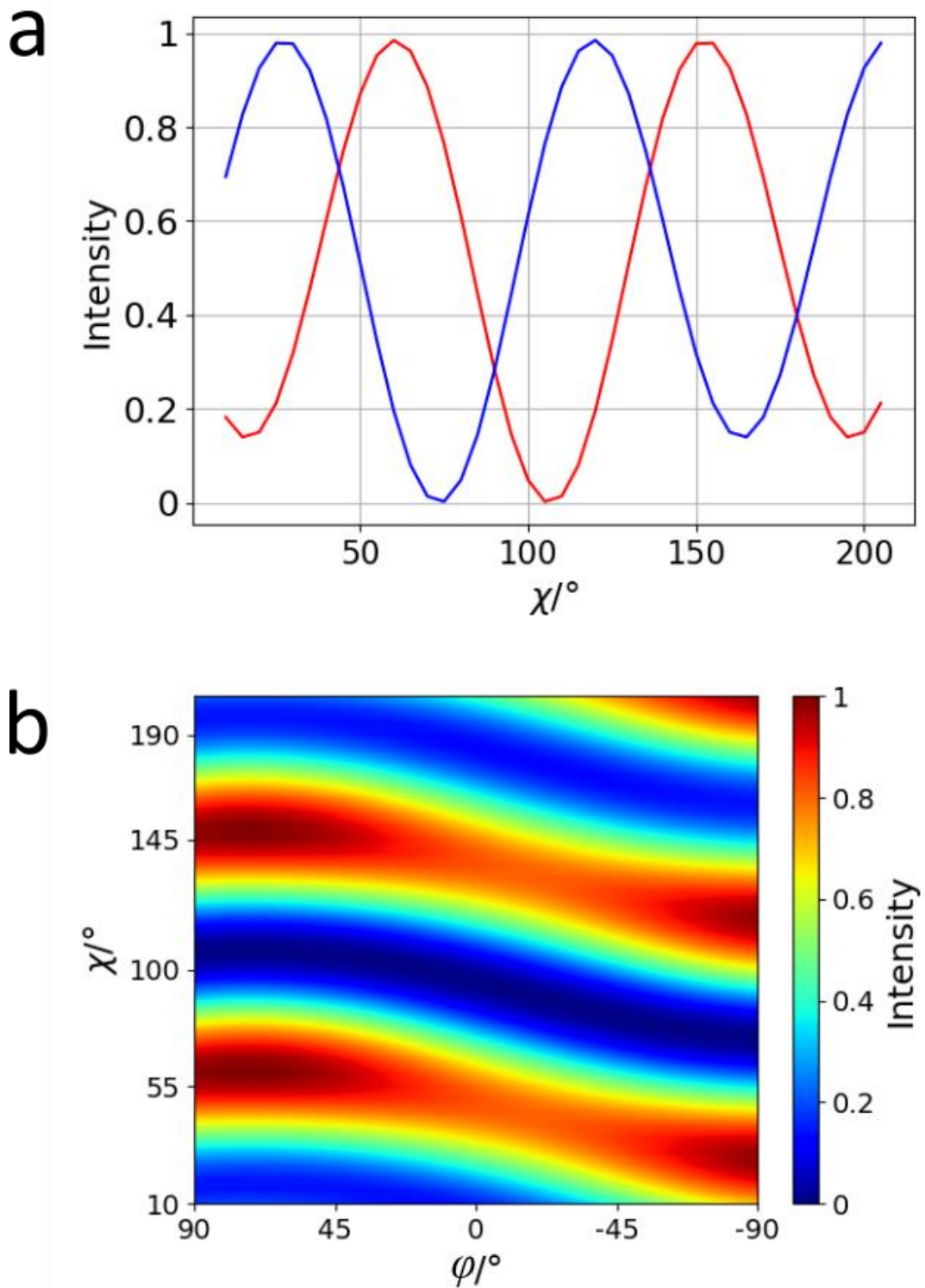


Figure 5.12 Results of simulated XBI data for: (a) χ scans at $\varphi = 90^\circ$ (red) and $\varphi = -90^\circ$ blue. (b) Intensity contour plot of XBI data as a function of χ and φ . Calculated from the crystal structure of TBB at ambient temperature (β phase).

The theoretical calculations were also performed for the γ phase of TBB. First the atom coordinates for the C-Br bonds in the unit cell of the γ phase are needed (Table 5.4).

Atom Coordinates					
Carbon			Bromine		
x	y	z	x	y	z
0.0192	0.8811	0.0426	0.0413	0.7175	0.0949
0.9270	0.9699	0.1280	0.8272	0.9324	0.3023
0.5730	0.4699	0.3720	0.6729	0.4324	0.1977
0.4808	0.3811	0.4574	0.4587	0.2175	0.4051
0.5192	0.6189	0.5426	0.5413	0.7825	0.5949
0.4270	0.5301	0.6280	0.3272	0.5676	0.8023
0.0730	0.0301	0.8720	0.1729	0.0676	0.6977
0.9808	0.1189	0.9574	0.9587	0.2825	0.9051

Table 5.4 Atom coordinates of the carbon and bromine atoms making up the C-Br bonds within the unit cell of the γ phase of TBB (323 K).⁸⁷ Atom coordinates are in the fractional coordinate system.

The C-Br bond vectors are calculated by subtracting the atom coordinates of the bromine atom from the atom coordinates of the corresponding carbon. The vector coordinates are then converted from the fractional coordinate system into a Cartesian coordinate system using Equation 3.6.

Vector Coordinates					
Fractional			Cartesian		
x	y	z	x	y	z
-0.0220	0.1636	-0.0523	0.0055	1.8169	-0.5064
0.0999	0.0375	-0.1743	0.7220	0.4162	-1.6877
-0.0999	0.0375	0.1743	-0.7220	0.4162	1.6877
0.0220	0.1636	0.0523	-0.0055	1.8169	0.5064
-0.0220	-0.1636	-0.0523	0.0055	-1.8169	-0.5064
0.0999	-0.0375	-0.1743	0.7220	-0.4162	-1.6877
-0.0999	-0.0375	0.1743	-0.7220	-0.4162	1.6877
0.0220	-0.1636	0.0523	-0.0055	-1.8169	0.5064

Table 5.5 Vectors of the C-Br bonds within the unit cell of the γ phase of TBB (323 K) expressed as fractional and Cartesian coordinates. Cartesian coordinates calculated from the fractional coordinates using Equation 3.6.

Using Equation 3.5 the tensor for the γ phase of TBB is:

$$T_{ij} = \begin{bmatrix} -0.073 & 0 & -0.611 \\ 0 & 1.404 & 0 \\ -0.611 & 0 & 1.219 \end{bmatrix}$$

The U rotation matrix to convert the Cartesian frame into the experimental frame is the same as used for the β phase to more easily compare the difference in calculated XBI intensity between the two phases.

$$U = \begin{bmatrix} 1 & 0 & 0 \\ 0 & 0.989 & -0.146 \\ 0 & 0.146 & 0.989 \end{bmatrix}$$

The tensor for the γ phase at $\chi = \varphi = 0^\circ$ is shown in Figure 5.13. The γ phase tensor (Figure 5.13) is very similar to the β phase tensor (Figure 5.9). There is a slight difference as the γ phase tensor is slightly rotated about the y-axis so that the tensor appears larger when viewed along the z-axis and smaller when viewed along the x-axis when compared to the β phase tensor.

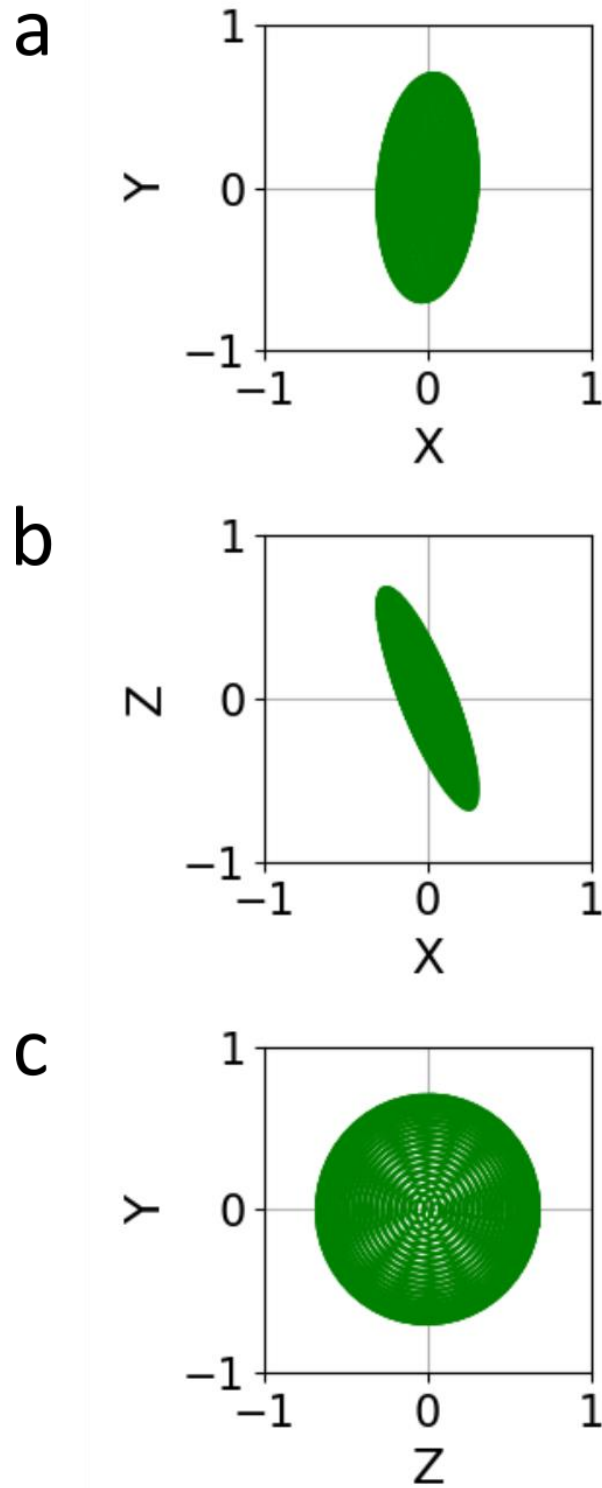


Figure 5.13 Tensor for a single crystal of TBB oriented at $\chi = \varphi = 0^\circ$ viewed along (a) the z-axis, (b) the y-axis and (c) the x-axis. Experimental coordinate system is used with z-axis as incident beam direction and the x-axis as the direction of linear polarization.

The theoretical calculations for this phase are limited due to a lack of experimental data, specifically a lack of X-ray absorption measurements. Thus the isotropic ($a(E)$) and anisotropic ($b(E)$) absorption coefficient values used were taken from the theoretical calculations for the β phase. Therefore the calculations can move straight to the calculations of the transmittance matrix (A) at $\chi = 0^\circ$ and $\varphi = 0^\circ$:

$$A = \begin{bmatrix} 0.7317 - 0.0049i & -0.0225 + 0.0085i \\ -0.0225 + 0.0085i & 0.5455 + 0.0650i \end{bmatrix}$$

We are assuming linear polarization of the incident beam so matrix μ describing the polarization of the incident beam is the same as the β phase (Equation 5.7). Similarly we are assuming the use of the same polarization analyzer so the transmittance matrix (Equation 5.8) from the β phase is unchanged. Thus, the ratio of transmitted intensity to incident intensity for the γ phase is determined using Equation 5.9.

The calculated intensity contour plot (Figure 5.14 (a)) shows a similar XBI behaviour to the β phase with a gradual shift of the maxima in χ as the angle φ is varied. The “undulating pattern” starts with a maximum at $\chi = 155^\circ$ and $\varphi = 90^\circ$, which shifts to a maximum of $\chi = 115^\circ$ when φ is rotated to -90° representing a change of 40° in χ , the same as observed in the β phase. The intensity maxima within the “undulating pattern” show the difference between the β and γ phases. The χ maxima at $\varphi = 0^\circ$ are much less intense than the χ maxima at $\varphi = 90^\circ$ and $\varphi = -90^\circ$ for the γ phase when compared to the β phase.

A comparison of the χ scan at $\varphi = 90^\circ$ for the β and γ phases is shown in Figure 5.14 (b). The two χ scans are similar although upon transition to the γ phase there appears to be a slight shift in χ and the XBI intensity is noticeably greater.

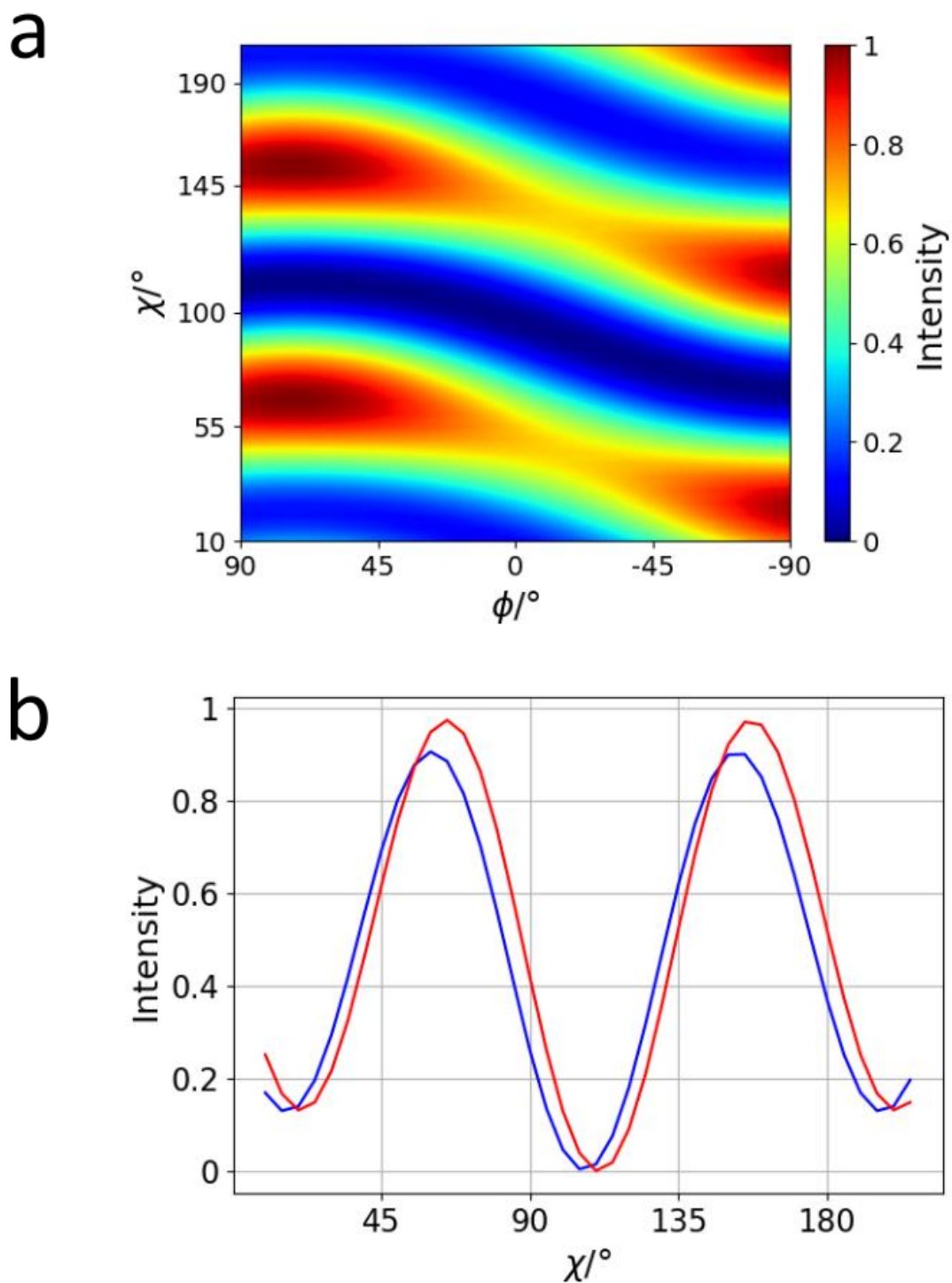


Figure 5.14 Results of simulated XBI data for: (a) Intensity contour plot of XBI data as a function of χ and ϕ . Calculated from the crystal structure of TBB at 323 K (γ phase). (b) χ scans at $\phi = 90^\circ$ for the β phase (blue) and the γ phase (red).

5.2.2 XBI Studies of Twinned crystals of TBB

TBB has already been established as commonly forming twinned crystals. XBI images of such twinned crystals show distinct XBI behaviour between the two twin components (Figure 5.15), which shows XBI images recorded as a function of χ for fixed ϕ . In Figure 5.15, intensity maxima for the left crystal are observed at $\chi = 60^\circ$ and 150° , with minima at $\chi = 105^\circ$ and 195° , whereas the crystal at the right has intensity maxima at $\chi = 35^\circ$ and 125° , with minima at $\chi = 80^\circ$ and 170° . Thus, the XBI behaviour for each twin component is shifted by $\Delta\chi = 25^\circ$. For the right crystal, the intensity minimum at $\chi = 80^\circ$ is noticeably not as deep as the other minimum. Furthermore, the right crystal has a markedly greater range in intensity than the left crystal. Twinned crystals often have dissimilar sizes, which could explain the different range in intensities.

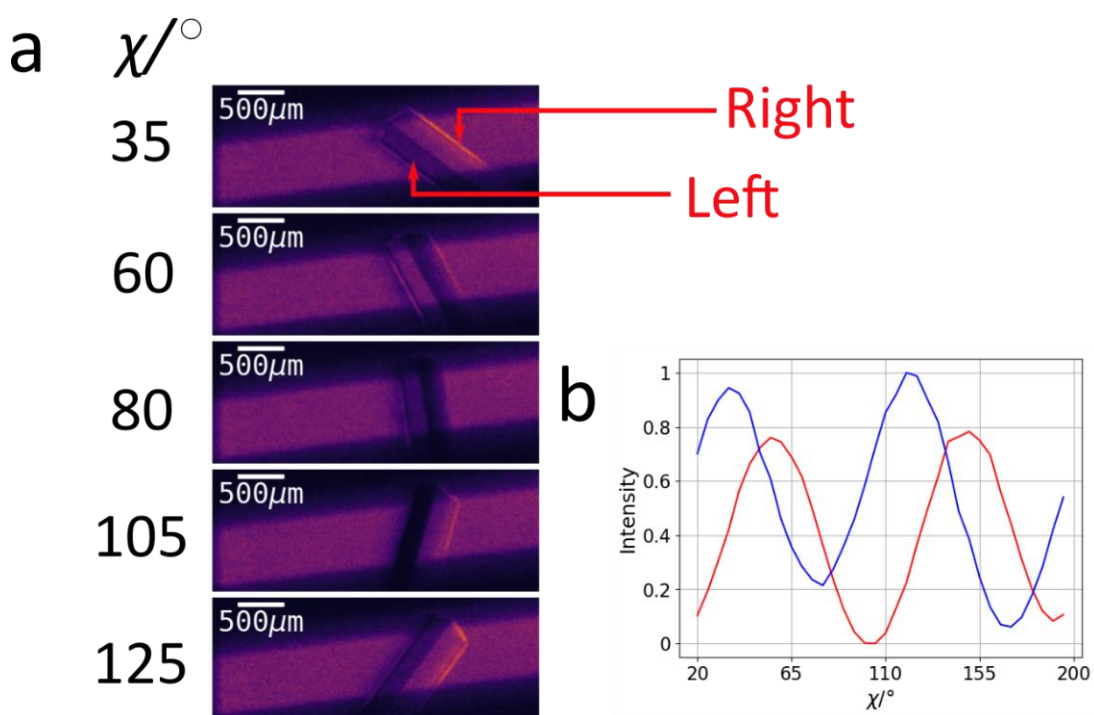


Figure 5.15 XBI data for a twinned crystal of TBB at ambient temperature, recorded as a function of χ at $\phi = 0^\circ$ (large face of crystal morphology perpendicular to beam direction). The XBI images corresponding to this χ scan can be viewed in Movie S5. (a) Selected images at different values of χ ($\chi = 35^\circ, 60^\circ, 80^\circ, 105^\circ$ and 125°) from a χ scan. In the top image, the left and right regions of the crystal are highlighted. (b) Normalized intensity for the left region (red) and right region (blue) as a function of χ .

Further work on another twinned crystal aimed to establish if the XBI behaviour as a function of φ rotation is similar to the single crystal of TBB examined earlier. As the crystal is rotated in φ by 180° , the left twin will become the right twin and the right twin will become the left twin. To remove confusion, the twin components are labelled as 1 (Figure 5.16 (a)) and 2 (Figure 5.17 (a)). We note that for each φ orientation, the shift in χ scans between the two twins is roughly 20° , as observed for the crystal in Figure 5.15, indicating that the orientational relation between the twin components is consistent in each case.

In Figure 5.16 twin 1 shows a maximum in intensity at $\chi = 60^\circ$ and minimum at $\chi = 105^\circ$ for $\varphi = 90^\circ$, and shows a maximum at $\chi = 35^\circ$ and minimum at $\chi = 80^\circ$ for $\varphi = -90^\circ$. Therefore, this twin exhibits a shift in the intensity maximum of $\Delta\chi \approx 25^\circ$ with rotation of φ by $\Delta\varphi = 180^\circ$. Another shallow minimum is observed at $\chi = 80^\circ$, $\varphi = -90^\circ$. Furthermore, the χ scans for twin 1 (Figure 5.16 (b)) are notably less intense than twin 2 (Figure 5.17 (b)), with a roughly 50% decrease in intensity. Again, this disparity in intensity for the two twin components, as with the other twinned crystal studied, is most likely due to an inequality in size of the crystals.

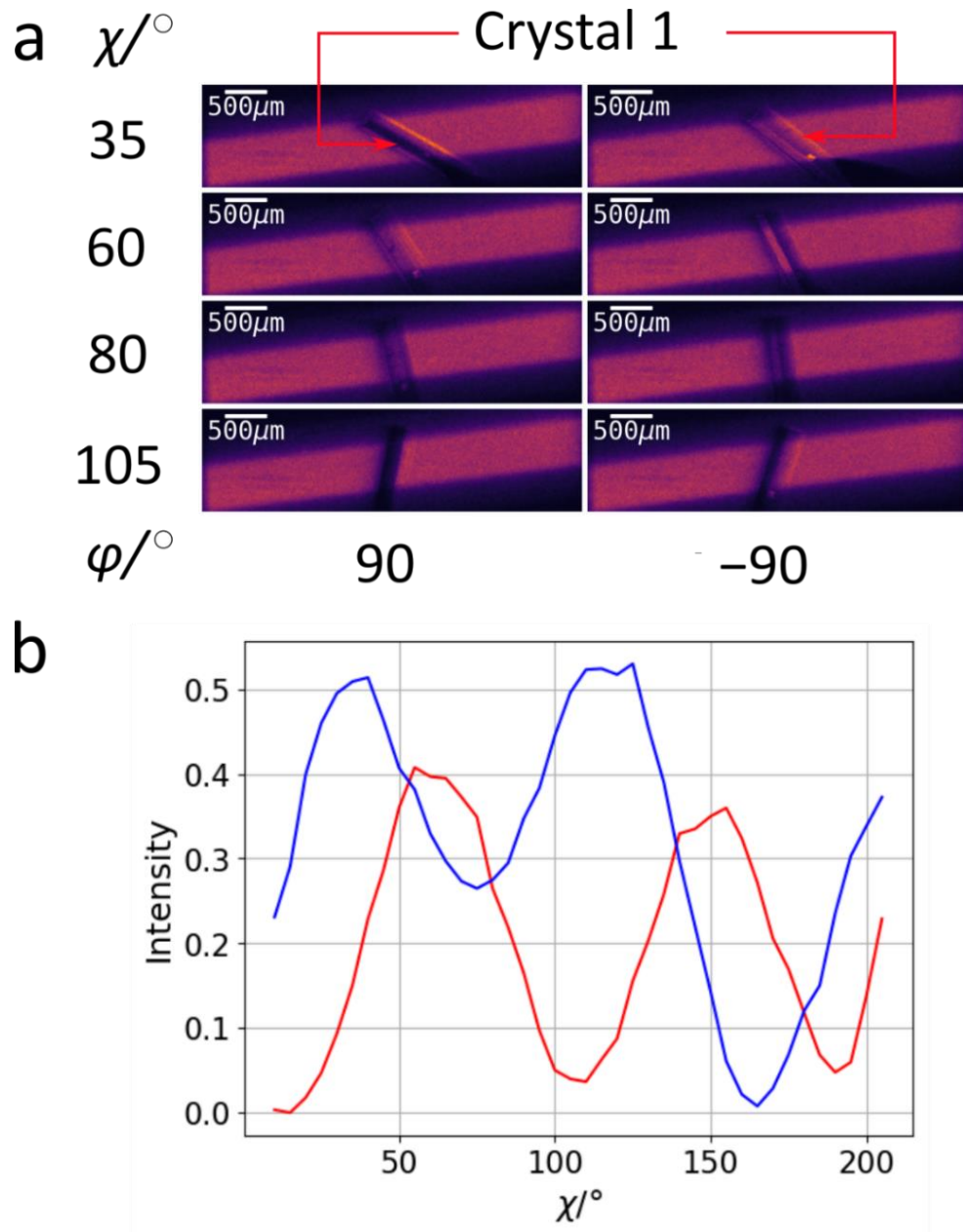


Figure 5.16 (a) Selected XBI images of a twinned crystal of TBB at $\chi = 35^\circ$, 60° , 80° and 105° , for $\varphi = 90^\circ$ and -90° . The red arrows identify twin 1 for each value of φ . (b) Normalized intensity as a function of χ in the χ scans recorded for twin 1 at $\varphi = 90^\circ$ (red) and $\varphi = -90^\circ$ (blue). Recorded at ambient temperature.

For twin 2 at $\varphi = 90^\circ$ (Figure 5.17), a maximum in intensity is observed at $\chi = 40^\circ$ and a minimum is observed at $\chi = 85^\circ$. For twin 2 at $\varphi = -90^\circ$, a maximum is observed $\chi = 55^\circ$ and a minimum at $\chi = 100^\circ$. Thus, this crystal shows a shift in the intensity maximum by $\Delta\chi \approx 15^\circ$ with rotation of φ by $\Delta\varphi = 180^\circ$. Another shallow minima is observed at $\chi = 85^\circ$, $\varphi = 90^\circ$.

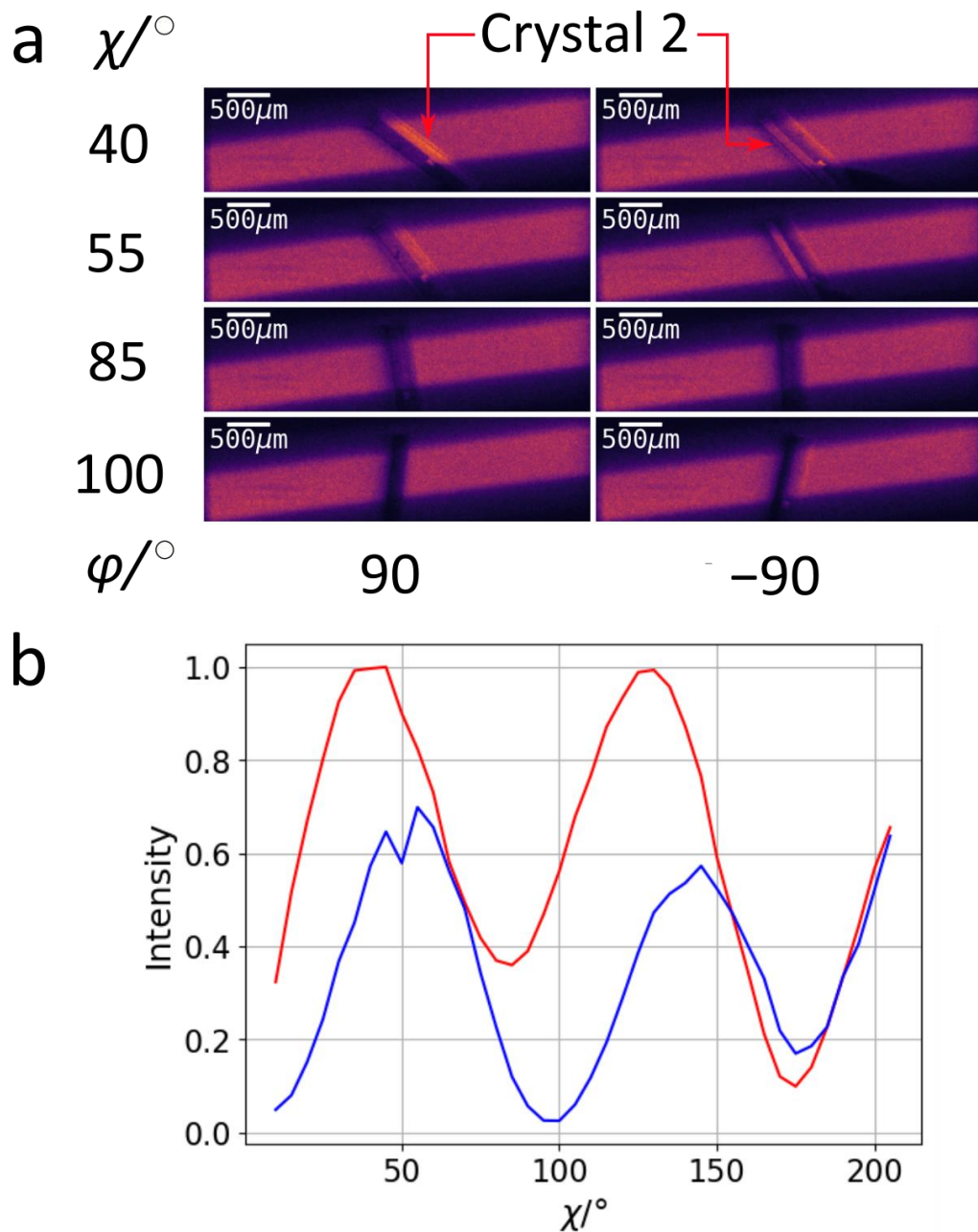


Figure 5.17 (a) Selected XBI images of a twinned crystal of TBB at $\chi = 40^\circ$, 55° , 85° and 100° , for $\varphi = 90^\circ$ and -90° . The red arrows identify twin 2 for each value of φ . (b) Normalized intensity as a function of χ for twin 2 in the χ scans recorded at $\varphi = 90^\circ$ (red) and $\varphi = -90^\circ$ (blue). Recorded at ambient temperature.

The results of our theoretical calculations on the single crystal give a possible explanation of the XBI behaviour of the twinned crystal. The intensity contour plot in Figure 5.12 assumes a U rotation matrix which moves the crystal into the correct orientation when $\chi = \varphi = 0^\circ$.

If the crystal were aligned differently in φ , it would correspond to a different place along the undulation, specifically, if the U rotation matrix corresponds to rotation about the x -axis by $\sim 15^\circ$, the two theoretical χ scans at $\varphi = 90^\circ$ and $\varphi = -90^\circ$ (Figure 5.18 (a)) would match the experimental data for twin 1. We note that the XBI behaviour for twin 1 at $\varphi = 90^\circ$ is very similar to the single crystal (Figure 5.12 (a)), while the shift in χ at $\varphi = -90^\circ$ between the single and twinned crystal is more obvious. For twin 2, rotation about the x -axis by $\sim 115^\circ$ would result a good match between the theoretical χ scans at $\varphi = 90^\circ$ and $\varphi = -90^\circ$ in the experimental data (Figure 5.18 (b)).

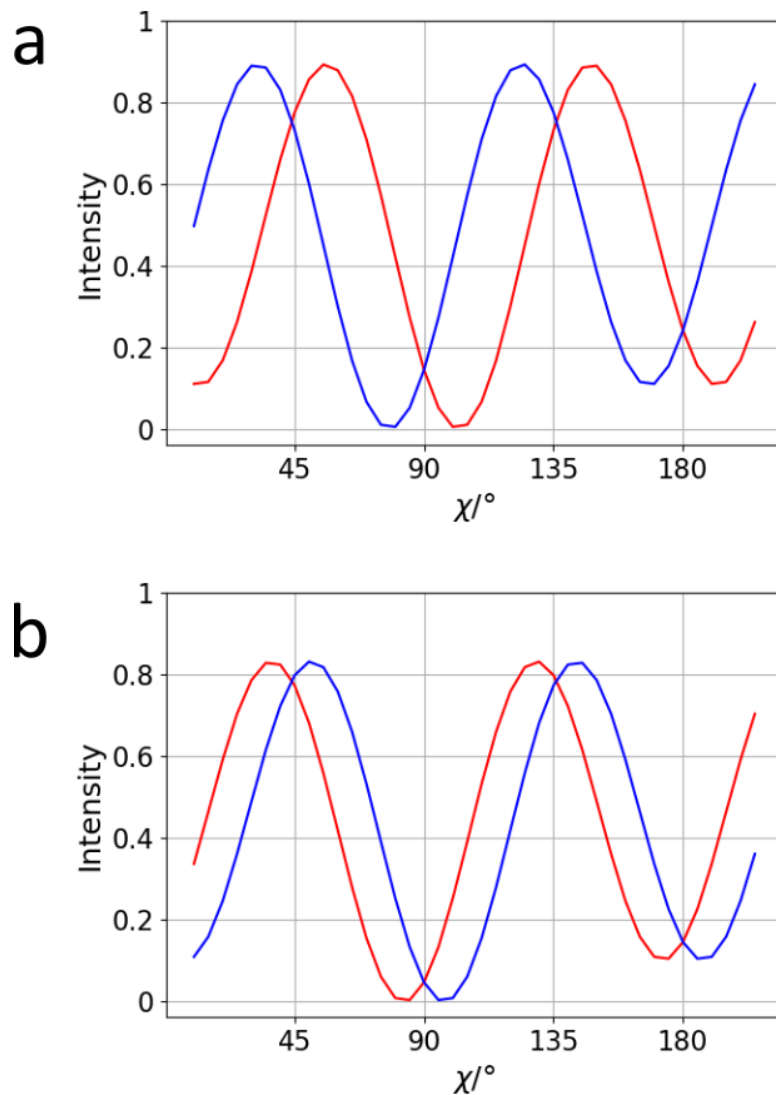


Figure 5.18 Plots of intensity as a function of χ corresponding to the theoretical calculations for a single crystal of TBB at $\varphi = 90^\circ$ (red) and $\varphi = -90^\circ$ (blue), where the crystal has shifted by (a) $\Delta\varphi = 15^\circ$ and (b) $\Delta\varphi = 115^\circ$ compared to Figure 5.12.

Based on these interpretations, the two twin components are deduced to differ in orientation by ca. 100° rotation about the x -axis. However, the fact that the minima at around $\chi = 80^\circ$ are shallow for certain orientations of φ for the twin components is more difficult to explain as, according to the theoretical contour plot in Figure 5.12, the minimum at this position is expected to be deeper. If this shallow minimum is to be explained using the crystal structure, it would indicate that the $[100]$ axis of the crystal is no longer parallel to the x -axis. Other explanations would indicate that these minima are not dependent on the crystal structure and are instead some artefact of the XBI setup or crystal morphology.

A temperature scan on a twinned crystal for fixed orientation shows an abrupt change of intensity between 318.4 K and 320.4 K. Unlike the transition observed for the single crystal, there appears to be a small “ledge” at roughly 319 K (Figure 5.19) within the sharp drop in intensity. This ledge is potentially due to the sample not being a single crystal. The intensity decreases by roughly 7% at the transition, similar to the intensity decrease observed in the single crystal.

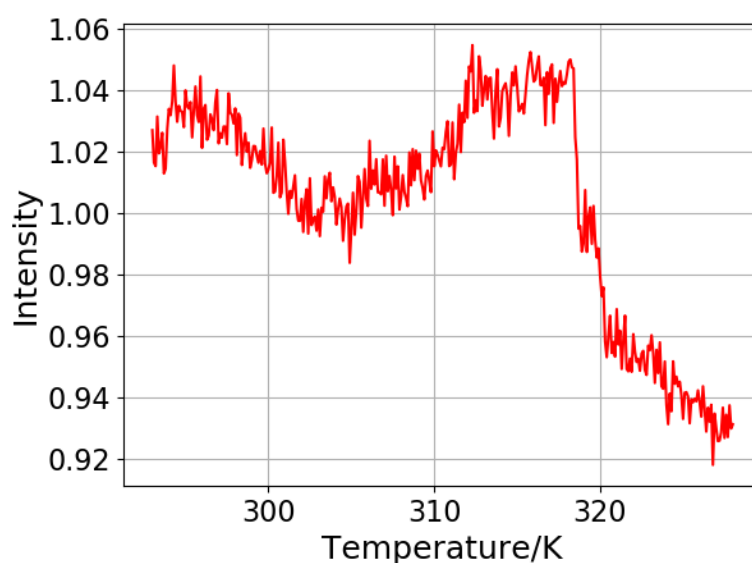


Figure 5.19 Temperature scan (293 K to 328 K in 0.1 K steps) of a twinned crystal of TBB. The crystal was oriented at $\chi = 120^\circ$, $\varphi = 90^\circ$. Intensity was recorded over both twin components. The temperature scan was normalized between maximum and minimum intensity values of the χ scan of a single twin component of the crystal oriented at $\varphi = -20^\circ$. The XBI images corresponding to this temperature scan can be viewed in Movie S6.

Viewing the XBI images across the phase transition shows some movement of the crystal (Figure 5.20). A profile measurement across the crystal below and above the phase transition (Figure 5.20 (b)) shows a clear movement in part of the crystal, with the middle darker region becoming slightly wider and more intense. The other portions of the twinned crystal do not appear to change. Thus, this behaviour could be an indication of only one crystal in the twin undergoing the transition, although this interpretation is not certain. Further work is clearly required to understand the structure of the twinned crystals and its relation to the XBI behaviour observed.

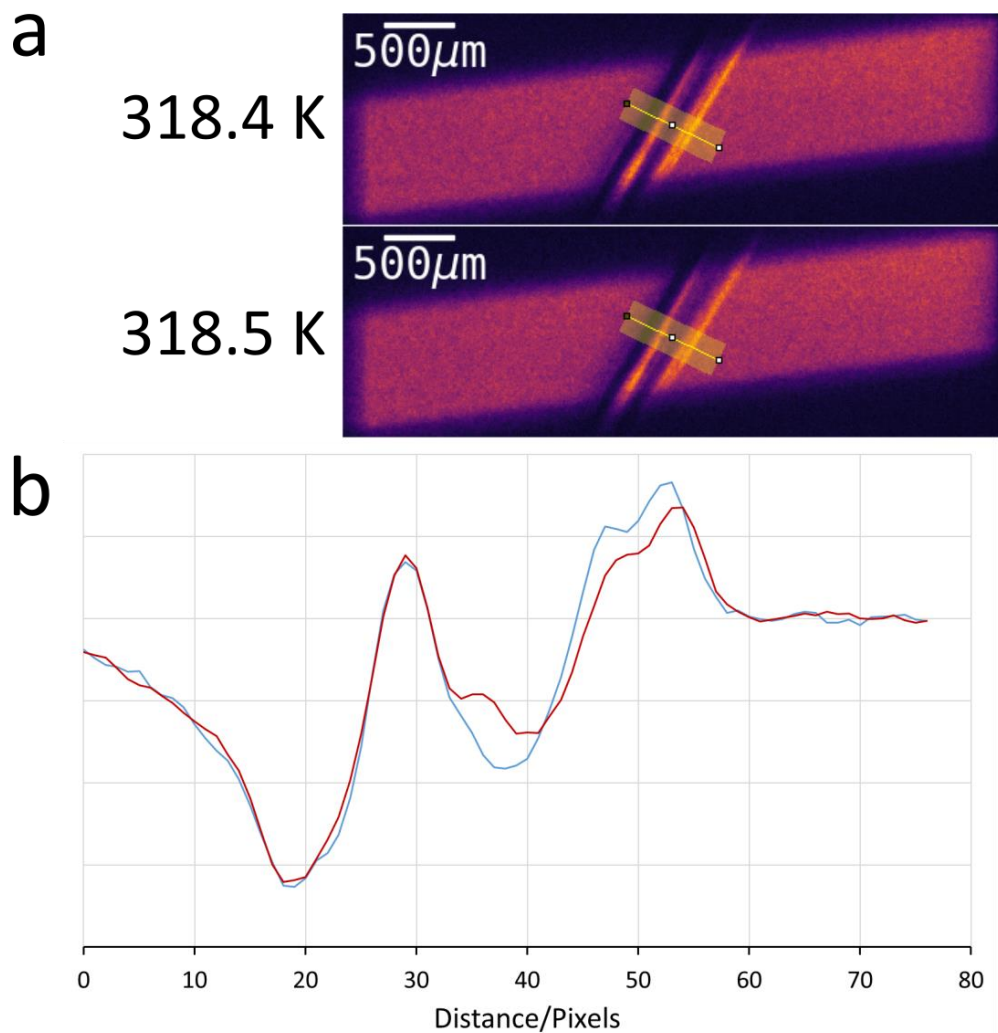


Figure 5.20 (a) XBI images of a crystal of TBB at 318.4 K and 318.5 K ($\chi = 120^\circ$ $\varphi = 90^\circ$). These temperatures were chosen as there is an obvious change in the crystal in the XBI images between these two temperatures. The yellow line on the images indicates measurement positions for the intensity profiles shown in (b) for 318.4 K (blue) and 318.5 K (red).

5.2.3 XBI Studies of ‘Hourglass’ TBB crystals

During our XBI experiments on TBB, while mounting single crystals of TBB to the goniometer using glue, some of the crystals reacted strangely to the glue, changing from the typical flat plate, near transparent crystal to a crystal with an opaque ‘hourglass’ shape when viewed perpendicular to the largest face (Figure 5.19).



Figure 5.21 Image of the ‘hourglass’ shape that appeared on a single crystal of TBB.

XBI experiments on these crystals proved interesting for a number of reasons. Firstly, XBI behaviour is observed for the ‘hourglass’ in a χ scan (Figure 5.22 (c)), with intensity maxima at $\chi = 60^\circ$ and $\chi = 150^\circ$, and minima observed at $\chi = 105^\circ$ and $\chi = 195^\circ$. Furthermore, the region that exhibits X-ray birefringence shows a clear pattern of curved lines radiating out from the centre of the crystal. The two regions to the side of the ‘hourglass’ show no change in intensity as a function of χ in the χ scan. This indicates that, for these regions of the crystal, the incident X-ray beam is parallel to an X-ray optic axis, or that the crystal structure in these regions is isotropic, or that these domains are polycrystalline.

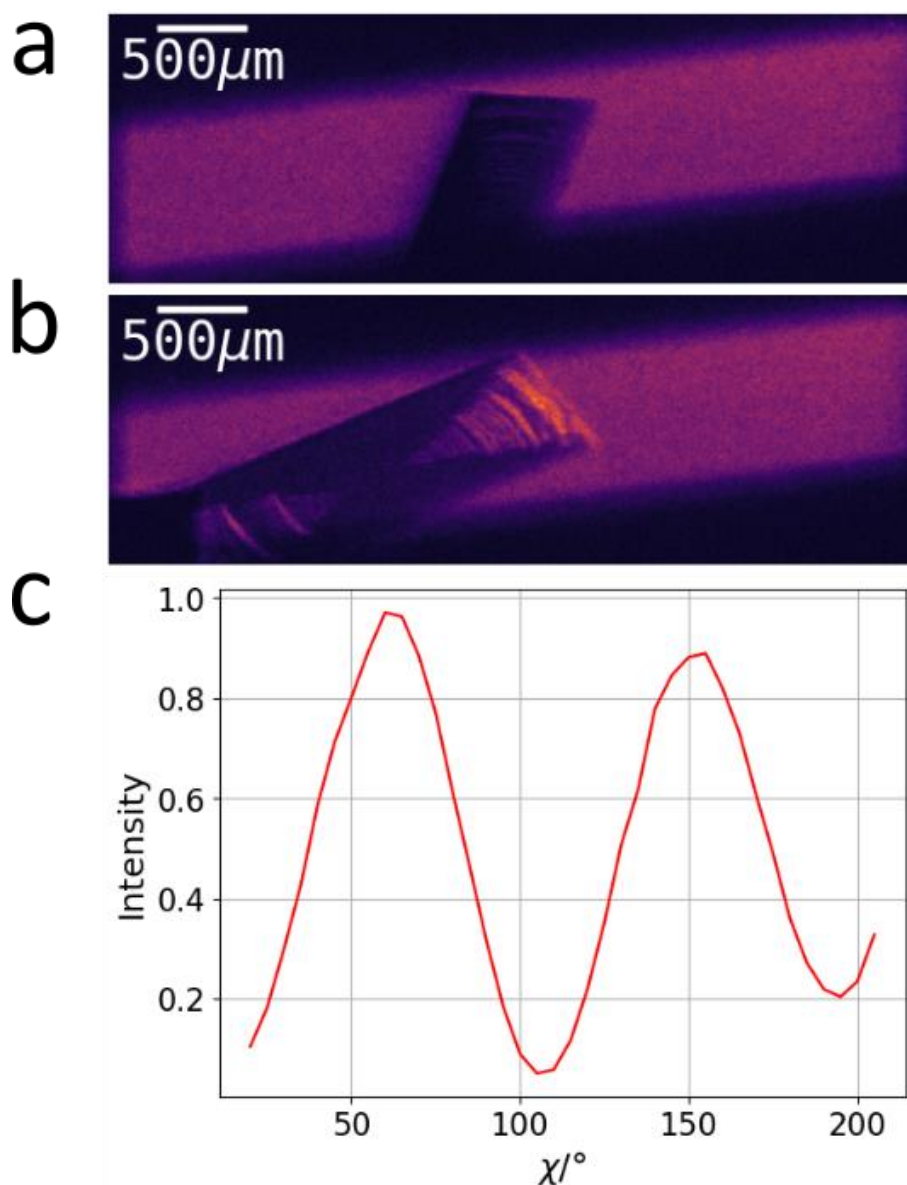


Figure 5.22 XBI images recorded for a single crystal of TBB with ‘hourglass’ features at ambient temperature oriented (a) $\chi = 105^\circ$, and (b) $\chi = 150^\circ$, with $\varphi = 0^\circ$ in each case. (c) Normalized intensity from the χ scan. Intensity taken from region of interest over the central ‘hourglass’ domain. The XBI images corresponding to this χ scan can be viewed in Movie S7.

While most of the TBB crystals exhibiting the ‘hourglass’ were originally normal single crystals that underwent some sort of transition to form the ‘hourglass’, we have also observed the formation of ‘hourglass’ features during crystal growth. Some TBB crystals, which were crystallized from toluene via slow cooling, already had the ‘hourglass’ feature and gave similar XBI behaviour.

Clearly, under certain conditions, the TBB crystal can form domains, with rather drastic differences in crystal structure. Notably, the crystal still undergoes a phase transition, albeit at a higher temperature than that observed for the twinned crystals or single crystals of TBB. In the XBI data, an abrupt change of intensity is observed only at 333 K (Figure 5.23).

In our XBI studies, one ‘hourglass’ crystal was observed to break within the ‘hourglass’ at 328 K on heating (Figure 5.23 (a)). A different crystal showed a small drop in intensity (roughly 8%) at ca. 333 K on heating (Figure 5.23 (b)). This drop in intensity was marked by a small expansion in the crystal. The spikes in intensity at higher temperatures are caused by the crystal contracting and expanding again. Only changes within the ‘hourglass’ were observed using XBI.

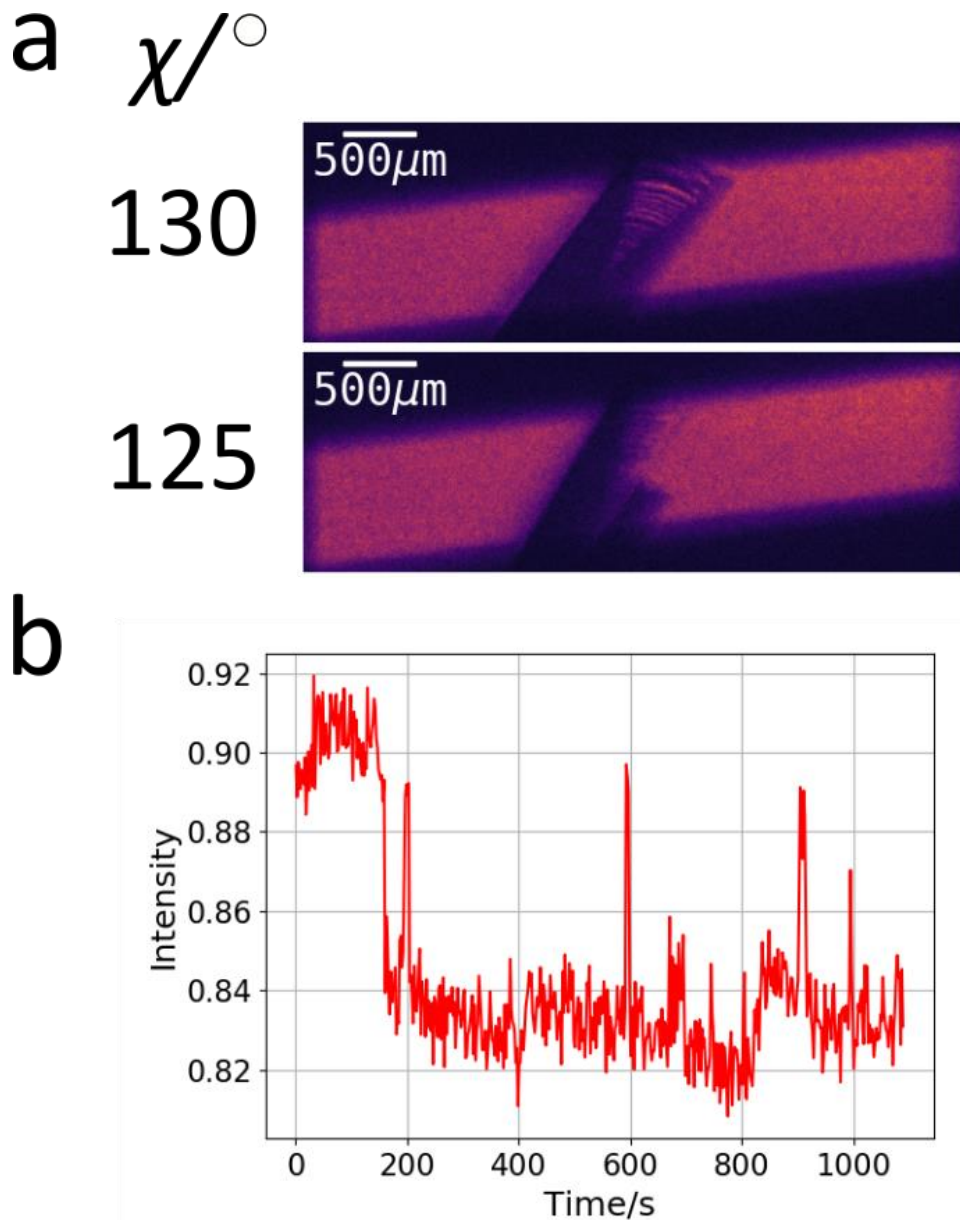


Figure 5.23 (a) XBI images before and after transition of a χ scan at 328 K ($\varphi = 0^\circ$). (b) Time scan of a single crystal of TBB oriented at $\chi = 145^\circ$ and $\varphi = 0^\circ$ after heating to 333 K. Temperature scan is normalized to the maximum and minimum values of the ambient χ scan plotted in Figure 5.24. The XBI images corresponding to this time scan can be viewed in Movie S8.

At ambient temperature and at 333 K, where the crystal appears to have undergone a phase transition, χ scans of an ‘hourglass’ crystal were recorded (Figure 5.24). A small but clear difference is observed, corresponding to a shift in the χ scan to slightly higher χ values, by about $\Delta\chi \approx 5^\circ$.

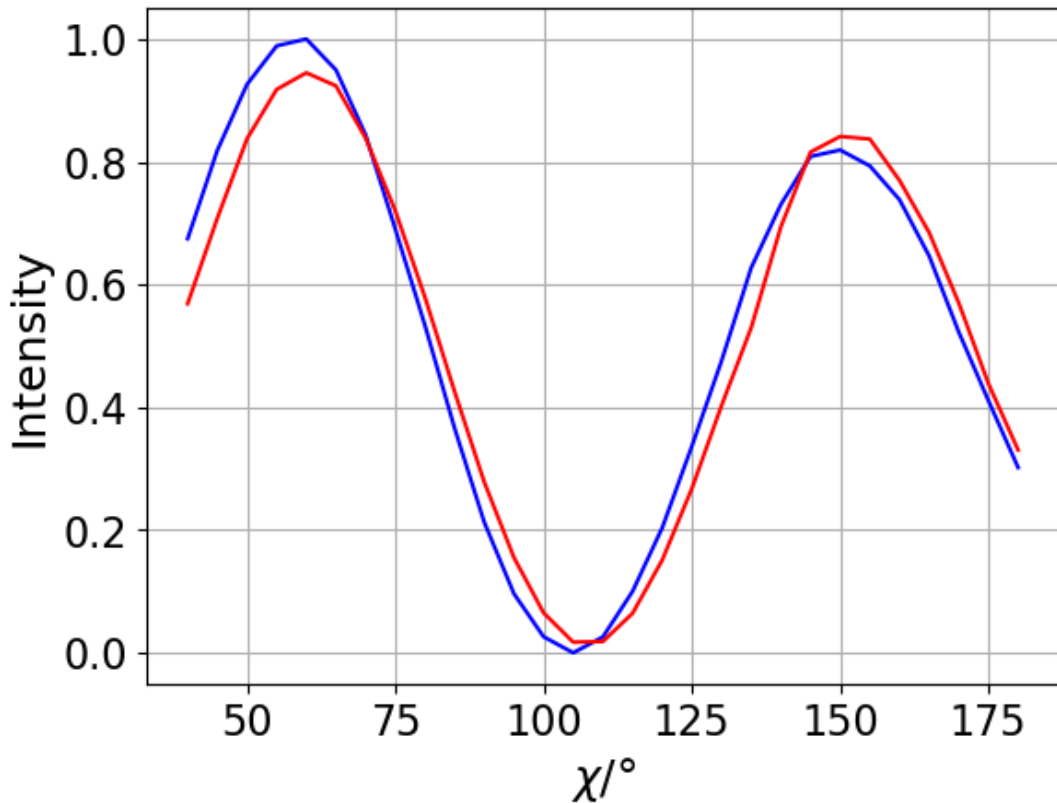


Figure 5.24 Intensity as a function of χ for an 'hourglass' crystal of TBB recorded at ambient temperature (blue) and 333 K (red).

5.3 Conclusions

Single crystals of TBB show clear XBI behaviour not previously observed for other brominated materials, which is successfully explained using current theoretical XBI calculations (further validating the current theoretical work). However, appropriate thickness correspondence needs to be incorporated into the theoretical calculations and more variable temperature experimental work is needed to understand the phase transition behaviour of the single crystal.

Twinned crystals of TBB show XBI behaviour that can be explained on the basis of theoretical results for independent twin components, although a better understanding of the individual crystal structure orientations is needed to interpret the results and to produce appropriate theoretical calculations. In addition, an attempt to image the bimetallic strip behaviour of twinned crystals (mentioned on Page 103) using XBI would be exceedingly interesting.

Furthermore, XBI was used to image some interesting crystals of TBB which had formed four domains in an ‘hourglass’ shape. Two domains (‘hourglass’) show XBI behaviour, while the other two domains did not exhibit XBI behaviour. A clear phase transition is observed at a much higher temperature (333 K) than for the single (318.15 K) or twinned (318.65 K) crystals, although only the domains exhibiting XBI behaviour show any evidence of the phase transition. Further work is needed to establish the structural properties of these ‘hourglass’ crystals to understand the mechanism of their formation, and to establish a more detailed understanding of their XBI behaviour.

6 Extending the Application of the XBI technique to Elements Other than Bromine

6.1 Introduction

Previously, all XBI experimental work not outlined in this thesis has focused on studying materials at the bromine K-edge.^{8,23,24,32,33,43} The focus of early XBI studies on the Br K-edge was driven primarily by the fact that the Br K-edge is readily accessible on beamline B16 at Diamond Light Source (DLS), and by the fact that interpretation of XBI data recorded at the Br K-edge is straightforward, given that X-ray birefringence depends specifically on the orientational properties of C-Br bonds. Expanding the basic capabilities of XBI by utilizing other X-ray absorption edges has the potential to extend the application of the technique to a much wider range of types of material. It also gives the possibility of imaging a sample at multiple absorption edges for a given material, meaning a greater understanding of the local anisotropy.

Figure 6.1 shows the percentage X-ray transmission through 3 m of air as a function of X-ray energy. At lower energies, transmission is quite poor, increasing until a gradual levelling off (~6-9 keV). This has consequences in terms of which X-ray absorption edges are viable for XBI on B16, as at lower energies the attenuation of X-rays before reaching the detector increases. The lower limit of observable X-ray absorption is dependent on the beamline setup, i.e., the medium the X-ray beam must travel through before reaching the detector (air path, vacuum windows, monochromator, etc.). Of course, the X-ray absorption is also sample dependent and controlling the thickness of the sample is also a vital factor in XBI experiments at lower energies.

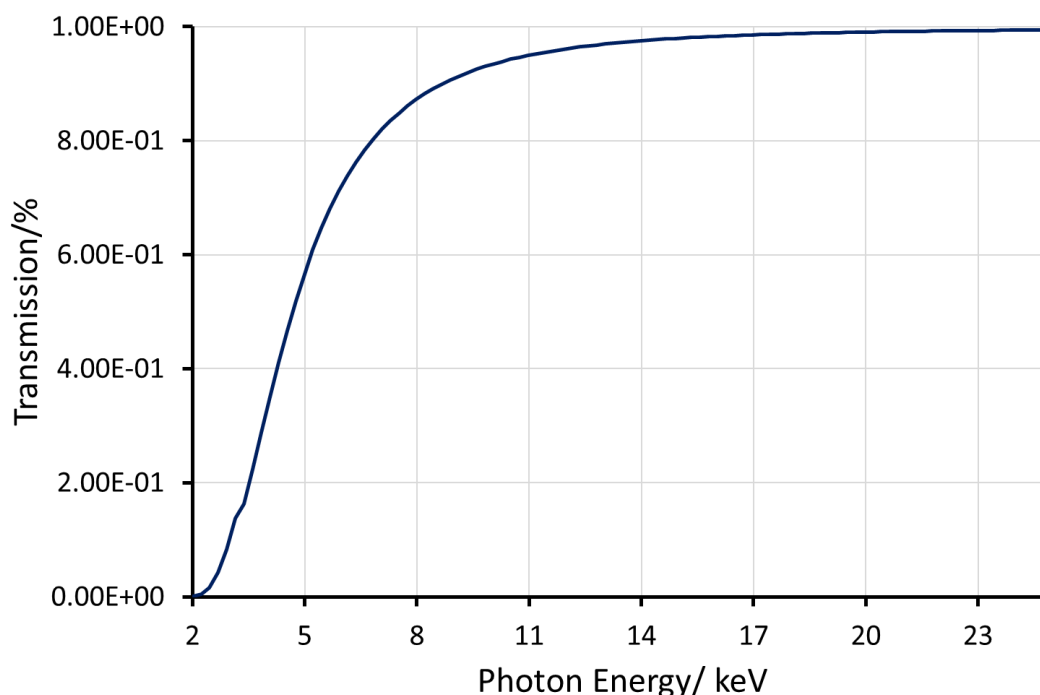


Figure 6.1 A graph of % X-ray transmission vs. X-ray energy (2 to 25 keV which is the photon energy range for B16) for a path length of 3 m in air.⁹¹

To establish the lower limit for XBI measurements on beamline B16, samples containing chromium (K-edge energy, 5.99 keV), iron (7.11 keV) and copper (8.98 keV) were selected. The chromium, iron and copper K-edge energies are all significantly lower than the bromine K-edge (13.47 keV), and encompass an X-ray energy range of roughly 3 keV, thus, providing a good range of absorption edges to determine a lower energy limit for XBI studies on B16.

The sulphur K-edge at 2.47 keV is too low to reach on B16 but the X-ray dichroism at the sulphur K-edge was studied for a thiourea crystal on beamline I16 at DLS. I16 has higher flux (as I16 has an undulator as opposed to the bending magnet on B16), and lower energies can be reached, mainly because fewer parts of the setup (and air) absorb the low energy beam. Recording the X-ray dichroism means the X-ray birefringence of the same sample can be calculated using the Kramers-Kronig transform. Therefore, X-ray dichroism measurements can be used to assess potential samples for future XBI studies.

The chromium and iron containing materials selected for study are thiourea inclusion compounds, containing the following organometallic complexes as the guest component:

1. $(\eta^6\text{-benzene})\text{Cr}(\text{CO})_3$
2. $\text{Fe}(\text{C}_5\text{H}_5)_2$
3. $(\eta^4\text{-1,3-cyclohexadiene})\text{Fe}(\text{CO})_3$
4. $(\eta^4\text{-trimethylene methane})\text{Fe}(\text{CO})_3$

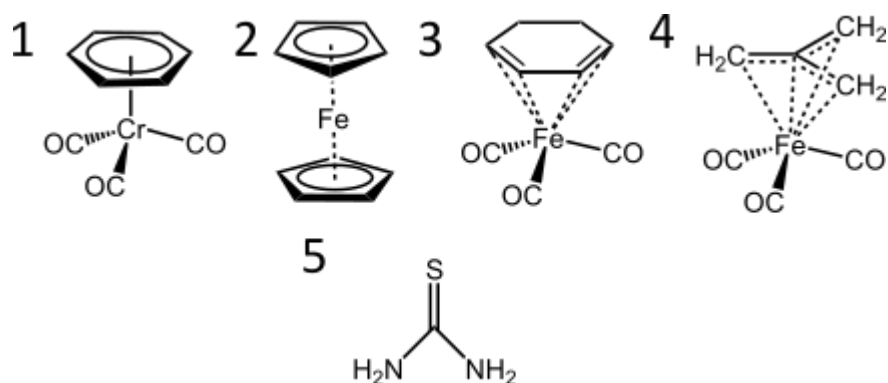


Figure 6.2 Molecular structures of (1) $(\eta^6\text{-benzene})\text{Cr}(\text{CO})_3$, (2) $\text{Fe}(\eta^5\text{-C}_5\text{H}_5)_2$, (3) $(\eta^4\text{-1,3-cyclohexadiene})\text{Fe}(\text{CO})_3$, (4) $(\eta^4\text{-trimethylene methane})\text{Fe}(\text{CO})_3$, and (5) thiourea.

Inclusion compounds consist of one species acting as a host and another species acting as a guest within the host. Thiourea inclusion compounds are crystalline materials in which a hydrogen-bonded arrangement of thiourea molecules form a host tunnel structure, which contains appropriate guest molecules.⁹²⁻⁹⁵ Without the presence of guest molecules thiourea does not form the tunnel structure.

Rather than forming cylindrical tunnels, the thiourea tunnel structure has a series of bulges (7.1 Å) and constrictions (5.8 Å) along the tunnel axis and is more aptly described as a cage-type inclusion compound (Figure 6.3).⁹⁶ Thus, thiourea prefers quite a bulky guest, which can fit comfortably inside a single “cage” within the tunnel.⁹⁷ The organometallic compounds mentioned earlier are ideal in this regard. Enclosing the guest molecules within the thiourea tunnels can lead to an orientational ordering of the molecules with respect to the long axis of the tunnel, thus, making X-ray birefringence more likely and facilitating the interpretation of XB results.

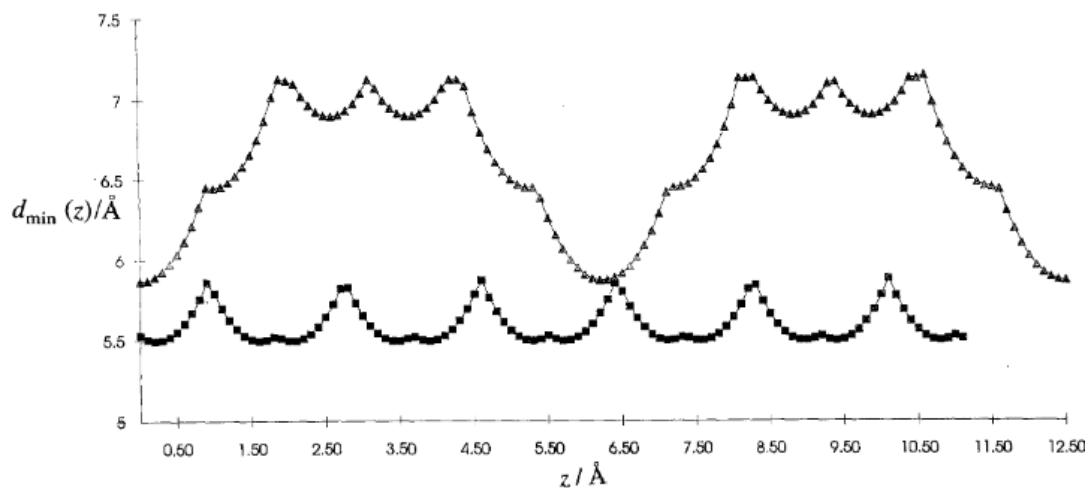


Figure 6.3 A plot of the minimum tunnel diameter ($d_{\min}(z)/\text{\AA}$) vs. $z/\text{\AA}$ (tunnel length) for chlorocyclohexadecane/thiourea inclusion compound (\blacktriangle , cage-type inclusion compound) and hexadecane/urea inclusion compound (\blacksquare , tunnel-type inclusion compound). The z range measures along the tunnel axis and corresponds to roughly one lattice period of the host structure.⁹⁶

Thiourea inclusion compounds typically have monoclinic or rhombohedral crystal structures (Figure 6.4). Typically, the ambient temperature structure is rhombohedral and transforms to monoclinic at low temperature. However, the properties of the thiourea inclusion compound, such as crystal structure, depend on the identity of the guest. A guest molecule with an isotropic shape will typically form a thiourea inclusion compound with rhombohedral structure at ambient temperature and the guest is orientationally disordered. If the guest molecule is more planar, a monoclinic structure is favoured at ambient temperature, and the guest is typically more orientationally ordered within the tunnels.⁹⁸

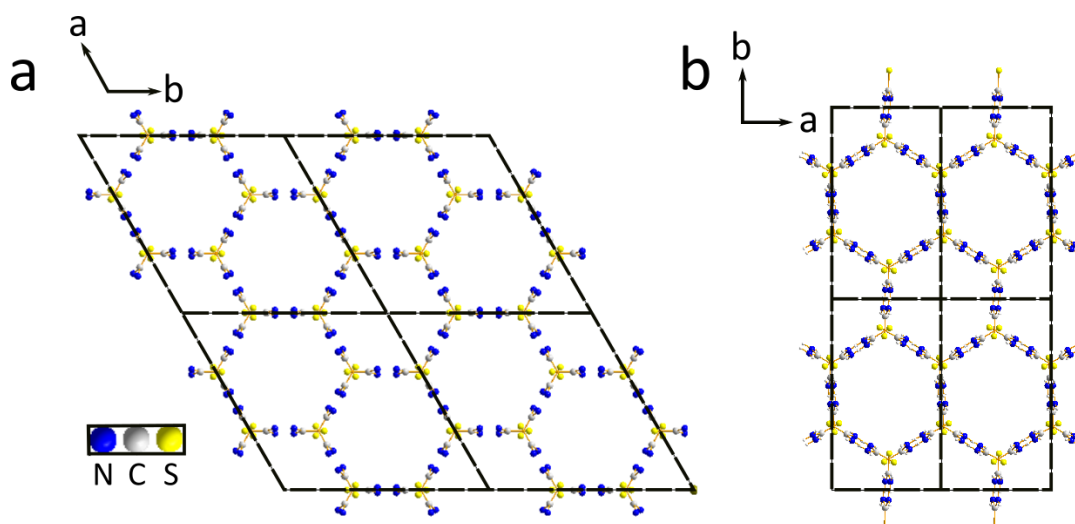


Figure 6.4 Crystal structure of a thiourea inclusion compound viewed along the *c*-axis, parallel to the tunnel axis (with ferrocene guest molecule removed) (a) rhombohedral at ambient temperature⁹⁹ and (b) monoclinic at 135 K.¹⁰⁰

The thiourea inclusion compounds typically form long needle-shaped crystals with a hexagonal cross section, corresponding to the hexagonal tunnels seen in the crystal structure when viewed parallel to the tunnel direction (Figure 6.4). Thus, the tunnel axis corresponds to the long axis of the crystal but there is no discernible difference in the crystal faces perpendicular to the long axis.

The four guest molecules under study each have different ligands bound to the central metal atom and thus different bonding environments. Understanding the bonding of the metal in these materials is critical for rationalizing the XBI behaviour, in particular to understand the directionality of the orbital occupied by the excited electron. XBI data at the Br K-edge can be readily interpreted, as the relevant orbital is the σ^* corresponding to the C-Br bond, which clearly has strong directionality.^{15,24} For the metallocenes discussed in this section, it is more difficult to predict the XBI behaviour, as the X-ray absorbing atom is bonded to more than one other atom and could exist in a variety of different types of bonding environment. Furthermore, the metallocenes in Figure 6.2 can exhibit different types of bonding between the metal and carbon atoms within the same molecule.

Moreover, the bonding in the metallocenes will be drastically different when compared to Br or S. According to the electric dipole approximation, (Page 17) K-edge transitions occur from the 1s to p-type orbitals. The p states are the most important orbitals for Br and S and are highly directional (e.g. the σ^* orbital of the C-Br bond). For the first row transition metals, the 3d orbitals are more important and the p states are more delocalized. However, the p and d states can hybridize (if the bonding environments are non-centrosymmetric) and these mixed states can be highly directional.^{15,101–103} Brouder made a comprehensive review of linear dichroism at X-ray absorption edges in 1990.¹⁴ Transitions to these hybrid orbitals are narrow (due to the narrowness of 3d states) and their energy is slightly below the main absorption edge energy. Predicting XBI behaviour for the materials studied in this Chapter is therefore vastly more complicated than for the brominated materials studied previously. Thus, measurements and discussion carried out in this Chapter are more qualitative and exploratory.

To facilitate discussion of X-ray birefringence behaviour in this Chapter, tensors which describe the resultant X-ray behaviours of each of the guest molecules have been determined, using the bond vectors which contain the X-ray absorbing elements (Equation 3.5). These tensors are limited in the information they contain, as for a more complete understanding we would require the individual tensors for each bond to be known before averaging. Using the tensors described in this chapter, we can establish the expected magnitude of the X-ray birefringence/dichroism, but the shape information is limited. For example, even if we know by symmetry that the tensor is axial, we cannot tell if it is prolate or oblate (rugby ball or pancake).

A rigorous calculation of the tensor taking into account the bonding environment and molecular orbitals of the materials is beyond the scope of this the present work . For the purposes of discussing X-ray absorption and XBI results in this Chapter we assume that a tensor created from bond vectors involving the X-ray absorbing atom is sufficient to describe the behaviour observed.

In each study described here, the X-ray dichroism for the sample was studied first. The X-ray dichroism can be determined very simply from X-ray absorption spectra, for two different sample orientations differing by 90° in χ . XBI requires very fine alignment to the beam centre and of the polarization analyzer (Chapter 2), thus, setting up XBI measurements for each new X-ray K-edge energy is time-consuming. Therefore, establishing that the material exhibits X-ray dichroism, which we know confirms that the material will exhibit X-ray birefringence, is a more time effective strategy in identifying potential samples.

The recorded intensity values for the X-ray absorption spectra are first normalized using Equation 6.1. I_0 is the incident X-ray beam intensity before encountering the sample and I_F is the final intensity from the detector.

$$I = -\ln\left(\frac{I_F}{I_0}\right) \quad (6.1)$$

The X-ray absorption spectra were normalized to the intensity (I) above (I_A) and below (I_B) the absorption edge, using Equation 6.2. At these energies the sample orientation should have no effect on the X-ray absorption.

$$I_N = \frac{(I - I_B)}{(I_A - I_B)} \quad (6.2)$$

Therefore, different sample orientations should give the same intensity at a given X-ray energy.

6.2 Studies at the Sulphur K-edge

During my PhD, one of the beamlines at DLS, I16, became usable at the sulphur K-edge (2.47 keV). While I16 cannot currently be setup for XBI, it is possible to record X-ray absorption spectra and therefore to study X-ray dichroism and to calculate the X-ray birefringence of a sample. To assess the prospects for XBI studies at the S K-edge, a preliminary study was done on a single crystal of thiourea.

The thiourea tunnel structure in thiourea inclusion compounds is known as a “soft” host. Thus, without the presence of the guest molecules, the thiourea tunnel structure is unstable and a more densely packed structure is observed. “Pure thiourea” has an orthorhombic structure with *Pnma* space group.^{104,105} Previous work has established that cylindrical crystals can be obtained with the long axis corresponding to any of the unit cell axes.¹⁰⁴

The crystal structure of thiourea is shown in Figure 6.5, viewed along each of the unit cell axes. In addition, a tensor is shown describing the C-S bonds along each of the axes, calculated using Equation 3.5. This tensor relies on the assumption that the excited-state orbital directionality corresponds to C-S bond direction. The resultant tensor is described as an prolate spheroid. If viewed along either the *a* or *b* axes (Figure 6.5 (a) and (b)), rotating the crystal about the axis of view will result in an obvious change in the orientation of the tensor; thus, X-ray dichroism will be observed.

However, Figure 6.5 (c) shows the crystal structure and tensor viewed along the *c*-axis. In this view, the tensor is circular. Therefore, rotating the crystal about the *c*-axis will not show much change in the orientation of the tensor. Thus, X-ray dichroism and X-ray birefringence with the incident X-ray beam parallel to this axis will be much weaker. If the *a* or *b*-axis is parallel to the incident X-ray beam, χ -rotation of the sample will change the orientation of the bonds and thus X-ray dichroism/birefringence should be observed.

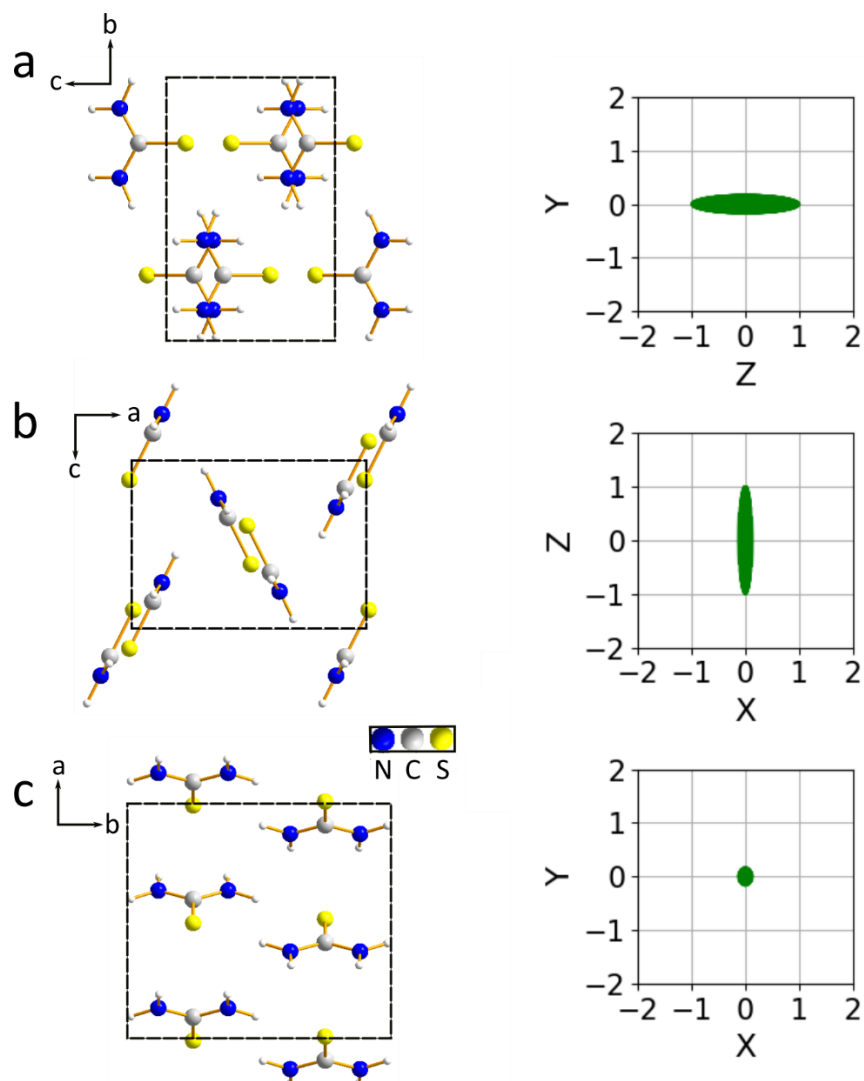


Figure 6.5 Thiourea crystal structure and tensor (green, determined from the C-S bond vectors of the unit cell using Equation 3.5) viewed along (a) the $a(x)$ -axis, (b) the $b(y)$ -axis and (c) the $c(z)$ -axis.¹⁰⁶

Two X-ray absorption spectra were recorded with the needle-like crystal oriented horizontally ($\chi = 0^\circ$) and vertically ($\chi = 90^\circ$), (Figure 6.6 (a)). The two X-ray absorption spectra clearly show a significant difference at 2.47 keV (the sulphur K-edge). The S K-edge occurs at a slightly lower energy when the sample is oriented at $\chi = 90^\circ$. A large negative peak can be seen just above 2.48 keV, which is due to a monochromator multiple scattering glitch (and not due to the sample). From these two X-ray absorption spectra, the X-ray dichroism spectrum (Figure 6.6 (b)) was determined. From the X-ray dichroism spectrum, the X-ray birefringence was calculated using the Kramers-Kronig transform (Figure 6.6 (b)).

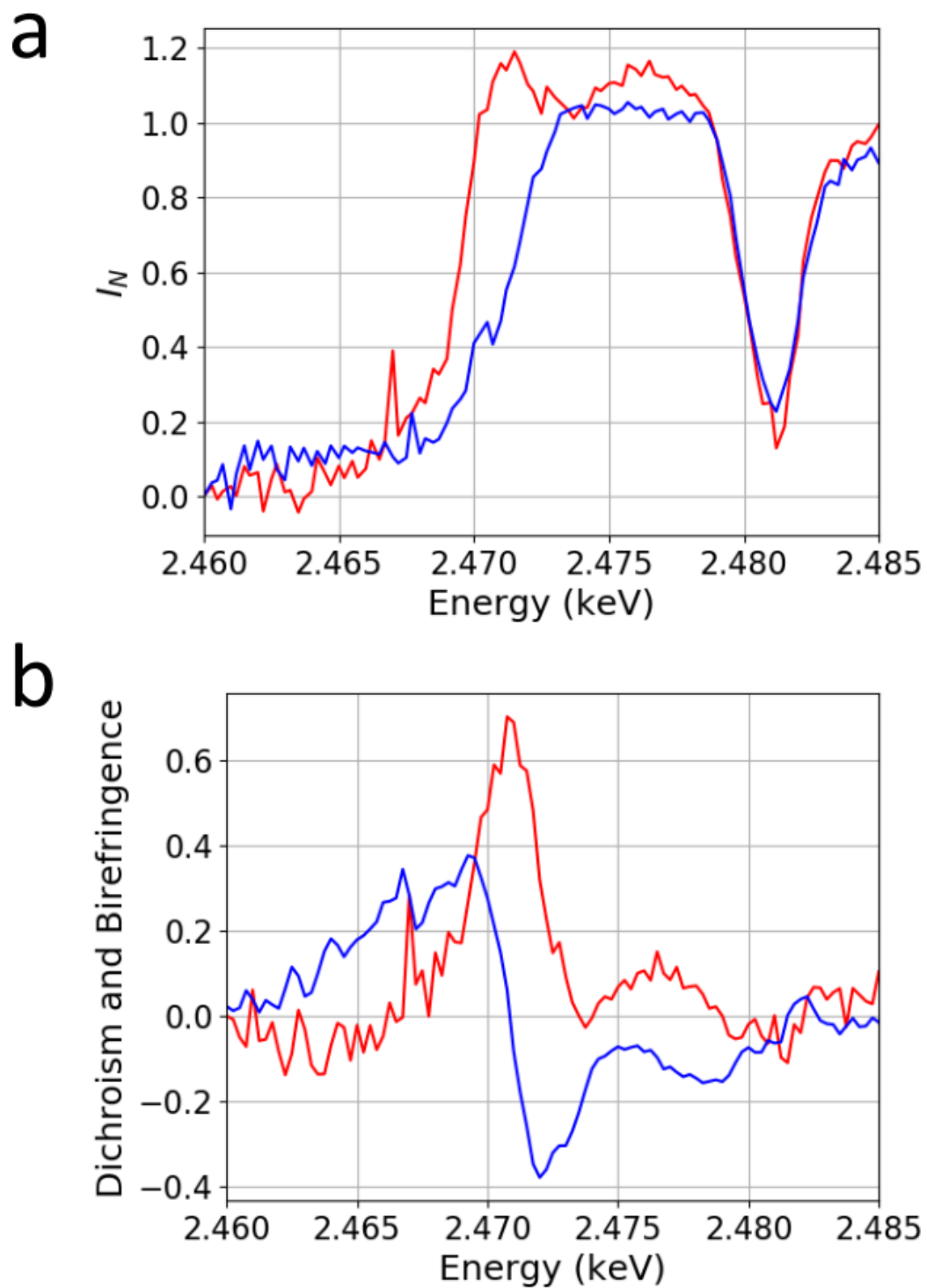


Figure 6.6 (a) X-ray absorption spectra of a single crystal of thiourea with; $\chi = 90^\circ$ (red) and $\chi = 0^\circ$ (blue). The orientation of the crystal was held at $\varphi = 180^\circ$ for both. (b) X-ray dichroism spectrum (red) (difference between spectra in part (a) and calculated X-ray birefringence spectrum (blue). Recorded by Dr Steve Collins on I16, DLS.

The X-ray dichroism and X-ray birefringence for a thiourea single crystal are clearly seen in Figure 6.6 (b), with the X-ray birefringence ranging from 0.4 to -0.4 . The evidence of strong X-ray birefringence calculated from the X-ray dichroism demonstrates that thiourea single crystals would be an excellent choice for XBI imaging, if beamline B16 could be configured for this K-edge, or if I16 could be configured with the XBI experimental setup. Furthermore, we can extrapolate that the crystal is not viewed along the c -axis as X-ray birefringence in this orientation is unlikely according to the discussion of the tensor above. Due to time constraints no further experiments were carried out. If the absence or presence of X-ray birefringence at other positions in ϕ had been confirmed, this would have given us more information about the relationship between the unit cell axes and the morphology of the crystal.

The potential to explore X-ray dichroism and X-ray birefringence at the sulphur K-edge would lead to characterization of the orientational properties of thiolated materials. Thiolated materials are used extensively in the fabrication of devices, e.g., polymers¹⁰⁷ and self-assembled monolayers^{108,109} many of which are partially ordered and thus cannot be structurally analyzed by standard techniques such as X-ray diffraction. Furthermore, these molecules contain a C-S bond comparable to the C-Br bond (used extensively in XBI studies, due in part to the strong directionality of the C-Br bond), thus, X-ray birefringence is predicted to depend strongly on the C-S bond direction.

The possibility to carry out XBI studies of thiourea is of particular interest as a lot of previous XBI work has focused on thiourea inclusion compounds. The crystal structure of thiourea inclusion compounds undoubtedly demonstrates that the crystals will show X-ray birefringence due to all the sulphur bonds being close to perpendicular to the long axis of the crystal (Figure 6.4). The ability to view the host as well as the guest would give a more complete understanding of structural changes in thiourea inclusion compounds associated with, phase transitions, decomposition and the exchange of guest molecules.

6.3 Studies at the Chromium K-edge

The (η^6 -benzene)Cr(CO)₃/thiourea (CrTUIC) crystals were made as reported previously.⁹⁴ Elongated (along the *c*-axis) hexagonal crystals characteristic of thiourea inclusion compounds were formed.

The crystallographic *c*-axis remains in the *xy*-plane, rotation of the *c*-axis around the *z*-axis (incident beam direction) is referred to as the χ -rotation, where the crystallographic *c*-axis is parallel to the *x*-axis when $\chi = 0^\circ$. The φ rotation refers to rotation of the crystal around the *c*-axis. X-ray absorption measurements were recorded on B16 and I16 (at DLS) around the chromium K-edge energy of 5.99 keV. X-ray absorption spectra recorded on B16 and I16 were normalized against intensities recorded on an ionization chamber before encountering the sample.

Interestingly, the original interest in CrTUIC was in the context of second harmonic generation (SHG). As the crystals were designed to have the potential to convert incident light into light of twice the frequency.⁹⁴ (η^6 -benzene)Cr(CO)₃ consists of a chromium atom bonded to three carbonyl groups and to a benzene ring via bonding to each carbon. The tensor shown in Figure 6.7 (a) is based purely on the Cr-C bond vectors as discussed on Page 149.

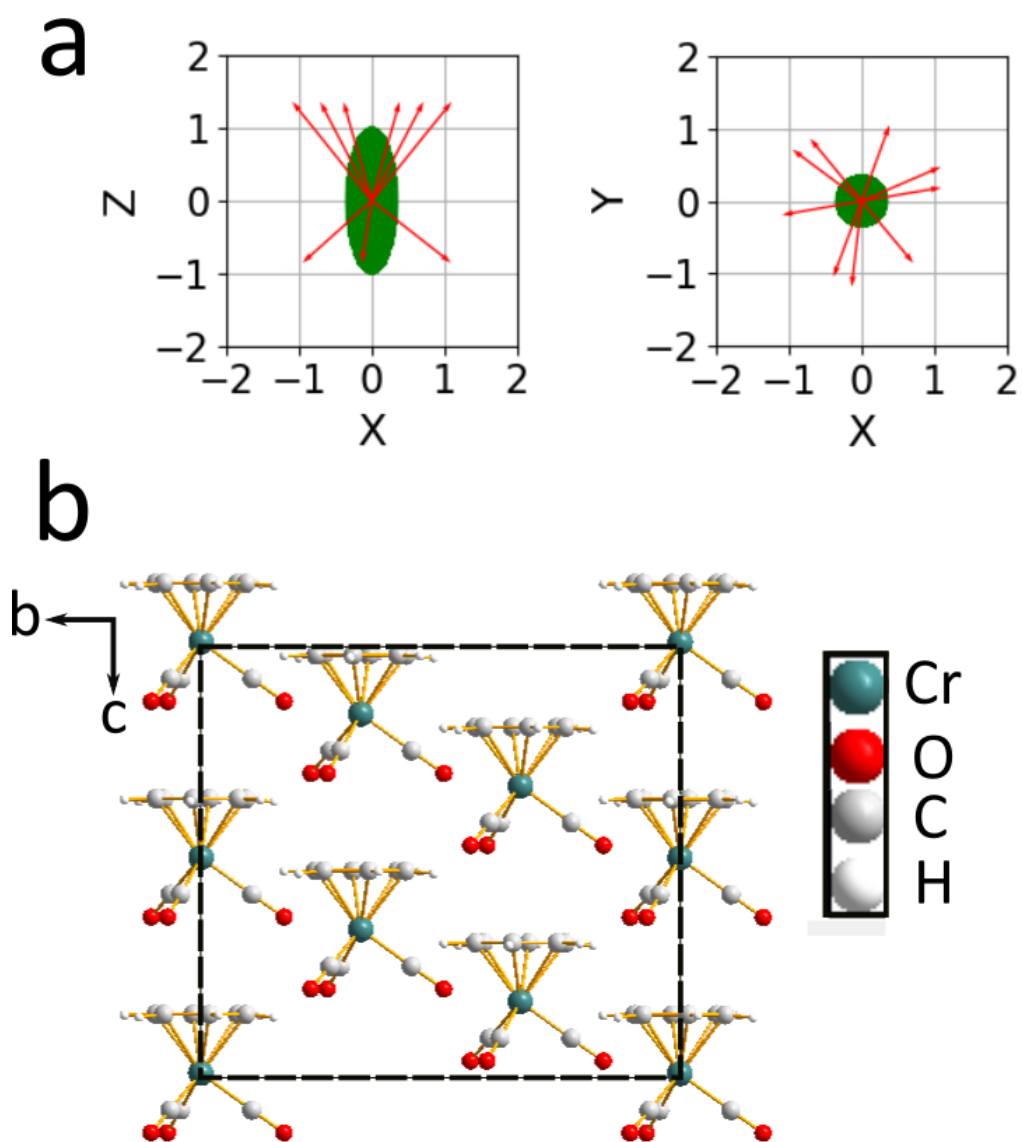


Figure 6.7 (a) Tensor (green) of Cr-C bonds (red) for a single molecule of $(\eta^6\text{-benzene})\text{Cr}(\text{CO})_3$ in two orientations, viewed along the the y-axis (left) and the z-axis (right). (b) Crystal structure of CrTUIIC viewed along the a-axis with the thiourea molecules removed (the thiourea tunnel axis is parallel to the c-axis).⁹⁴

The *c*-axis is parallel to the thiourea tunnels and correspond to the long axis of the crystal. The $(\eta^6\text{-benzene})\text{Cr}(\text{CO})_3$ molecules stack head to tail in the thiourea tunnel. On moving along the tunnel, the orientation of the guest molecule alternates by 13.3° about the *c*-axis (Figure 6.7 (b)).⁹⁴

The tensor for this metallocene is shown in Figure 6.7 (a), viewed from two orientations. The left image has the same orientation as the molecules seen in the crystal structure of Figure 6.7 (b), right is the tensor viewed along the c -axis. This ellipsoid can be described as prolate with the long axis of the tensor parallel to the c -axis and appears isotropic when viewed perpendicular to this direction. As the c -axis is parallel to the long needle direction, rotating the crystal in χ should result in a difference in the bond orientation and therefore produce X-ray birefringence for all ϕ orientations, if our assumed tensor is correct.

Chromium has the lowest K-edge energy of the materials studied by XBI on B16 and is therefore the material most susceptible to X-ray attenuation in the XBI set-up. As seen in Figure 6.1, the transmission is about 75 % for X-rays of energy 5.99 keV travelling through 3 m of air. Transmission will also be further decreased by passing through the sample. Therefore, before studying the sample of CrTCH, the X-ray absorption spectrum was recorded for a chromium foil (Figure 6.8). The small X-ray path length through the chromium foil means that there is a greater chance of observing the chromium K-edge.

However, there was no evidence of a K-edge at the expected energy of 5.99 keV. Indeed, there was no noticeable difference between spectra recorded with the chromium foil in the beam and with no foil in the beam (Figure 6.8). This suggests that the chromium K-edge at just under 6 keV is at too low an energy to record data on B16. Reducing the air path (e.g. using vacuum tubes) and sample thickness may allow chromium containing samples to be studied using XBI on B16 but would need a more complex setup and sample preparation than has been used previously.

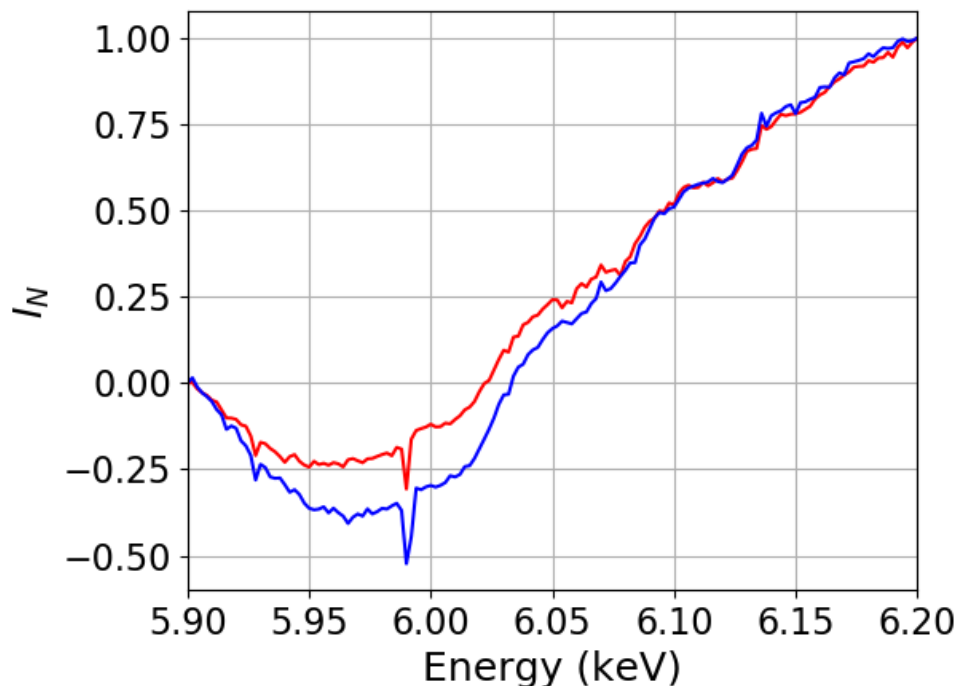


Figure 6.8 X-ray absorption spectra recorded on B16 for Cr foil (red) and with no foil (blue) in the beam path.

While this ruled out the possibility of studying chromium containing samples using the XBI setup on B16, X-ray absorption and therefore X-ray dichroism could be recorded at the Cr K-edge on I16 at DLS. Figure 6.9 (a) and (b) shows the X-ray absorption measurements for a single crystal of CrTCH recorded on I16. The spectrum in Figure 6.9 (a) when $\chi = 90^\circ$, shows evidence of a narrow transition slightly below the K-edge as expected for 3d-p hybridized orbitals. Differences observed in the X-ray absorption spectra above the K-edge are most likely due to systematic errors occurring due to a change in morphology or a problem in the alignment.

Figure 6.9 (b) shows evidence of X-ray dichroism for this material providing proof that there is at least some anisotropy in the local bonding environment around the chromium. X-ray birefringence spectra calculated from the X-ray dichroism data show evidence of X-ray birefringence ranging from roughly 0.1 to -1.5 . Compared to the X-ray birefringence observed for 1-bromoadamantane/thiourea at the Br K-edge (Figure 2.14), which ranges roughly from 1 to -1 , it is unlikely that significant XBI intensity would be observed for CrTCH, although it would be interesting to test this limit.

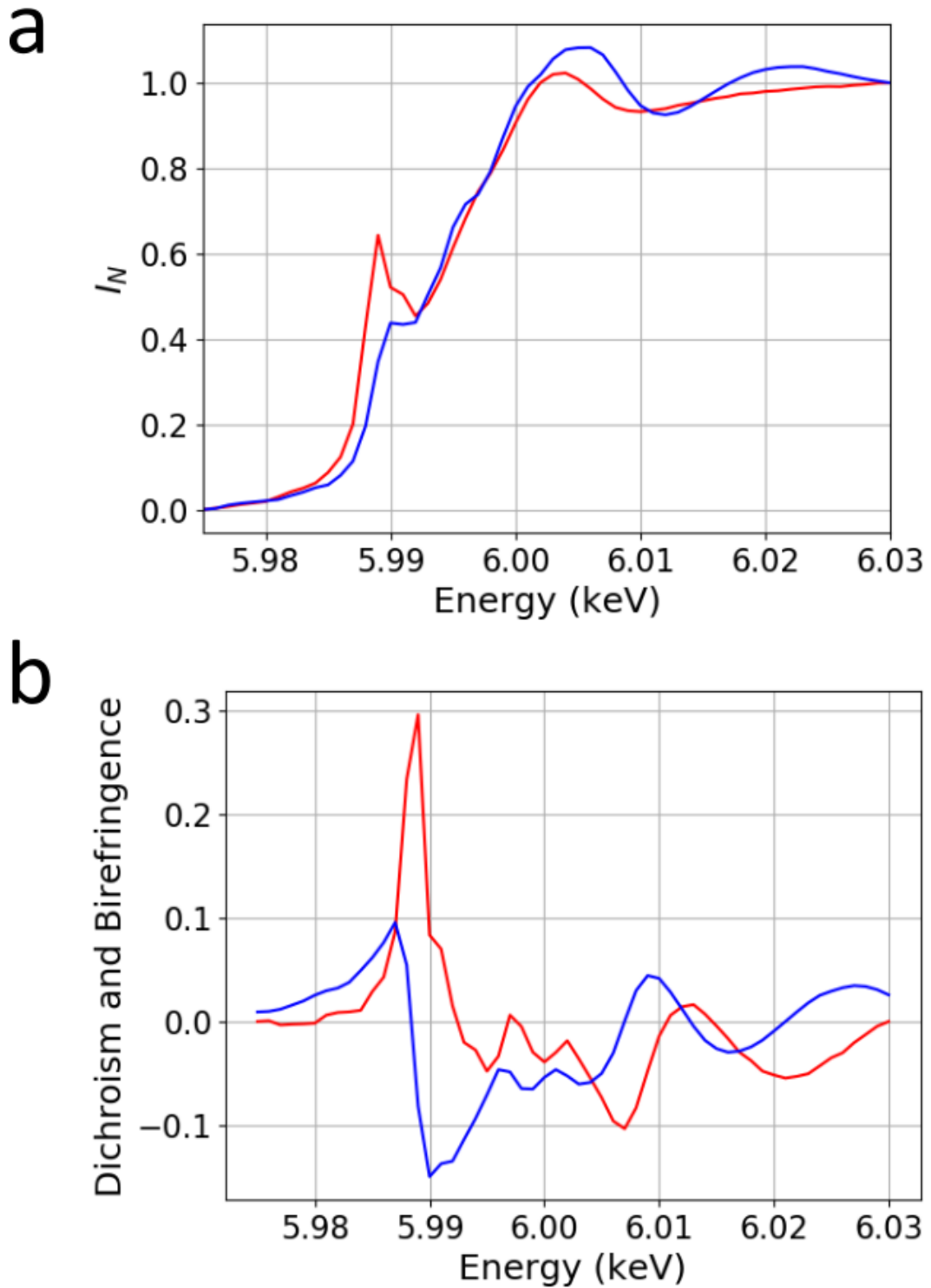


Figure 6.9 (a) X-ray absorption spectra recorded on I16 by Dr Steve Collins for a single crystal of CrTCH at $\chi = 90^\circ$ (red) and $\chi = 0^\circ$ (blue). (b) X-ray dichroism spectrum (red; difference between spectra in part (a)) and calculated X-ray birefringence spectrum (blue).

6.4 Studies at the Iron K-edge

The iron K-edge at 7.11 keV proved more promising than the chromium K-edge on B16, with successful X-ray absorption measurements for three samples. X-ray absorption spectra recorded on B16 were normalized against intensities recorded on an ionization chamber before encountering the sample.

6.4.1 Ferrocene/thiourea

Ferrocene is known as a “sandwich” compound, comprising a central metal atom which is effectively sandwiched between planar ligands. The discovery of ferrocene led to a marked increase in interest in organometallic chemistry. In fact, the Nobel Prize for chemistry in 1973 was awarded to Wilkinson and Fischer for work on “sandwich” compounds.

For FerTUIC crystals the long axis (tunnel axis) of the hexagonal shaped crystals corresponds to the crystallographic c -axis. The χ rotation of the crystal refers to the rotation of the crystallographic c -axis about the incident X-ray beam (z -axis), where the c -axis remains in the xy -plane. When $\chi = 0^\circ$ the crystallographic c -axis is parallel to the x -axis. The ϕ rotation refers to rotation of the crystal around the c -axis. In ferrocene, cyclopentadienyl ligands binds to the metal with each ring perpendicular to the molecular symmetry axis, with the carbon atoms in the ring roughly equidistant to the metal. Staggered cyclopentadienyl rings are expected for solid-state ferrocene, the vapour phase has eclipsed rings.^{110,111} The energy barrier to interconvert between eclipsed and staggered is low, so in thiourea tunnels the confirmation may be variable or may depend on the orientation of the molecules with respect to the tunnel.⁹⁹

The tensor shown in Figure 6.10 is for the staggered state and calculated from the Fe-C bond vectors. The tensor is elongated along the high symmetry axis of ferrocene and appears isotropic when viewed parallel to the high symmetry axis. Thus, if this tensor is assumed to describe the XBI behaviour of individual ferrocene molecules, the ferrocene molecules will exhibit X-ray birefringence when viewed perpendicular to the high symmetry axis. If viewed parallel to the high symmetry axis no X-ray birefringence will be observed.

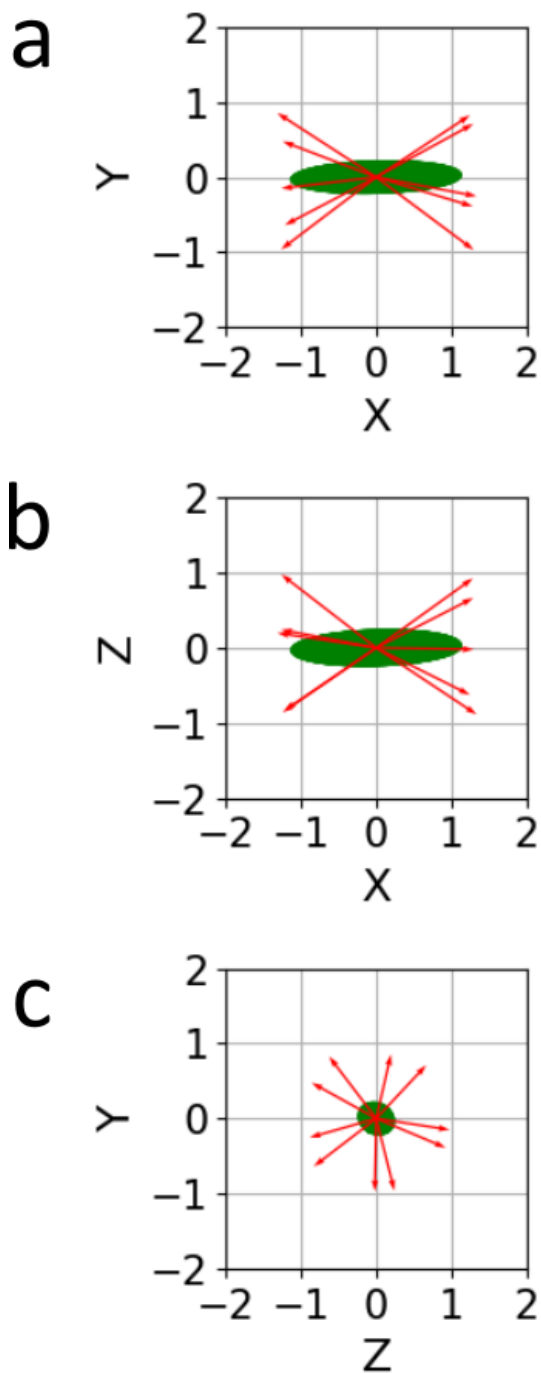


Figure 6.10 Tensor (green) of staggered form of a single molecule of $\text{Fe}(\text{C}_5\text{H}_5)_2$ based on Fe-C bond vectors (red) of FerTUIIC recorded at 135 K.¹⁰⁰ Tensor is viewed from three directions (a) along the z-axis, (b) along the y-axis, and (c) along the x-axis. Note that the axes used in this figure do not correspond to the experimental axis system, as ferrocene is disordered within the thiourea tunnel. The axis system in the figure is simply used to aid in description of the tensor.

The structure and dynamics of FerTUIC has been studied extensively by Mössbauer spectroscopy,¹¹² ¹³C NMR¹¹³ and ²H NMR.¹¹⁴ A first-order reversible phase transition is observed at 162 K, with the crystal structure transforming from rhombohedral (high-temperature phase) to monoclinic (low-temperature phase).^{99,112–117} Evidence of reversible twinning has also been found below 160 K.⁹⁹

The changes in the guest molecule orientations with temperature are more complex. We can consider that there are four possible orientations of the ferrocene molecule relative to the thiourea tunnel structure, one along the *y*-axis (tunnel axis, when $\chi = 90^\circ$) and three in the *xz*-plane (Figure 6.11). The orientation parallel to the *y*-axis does not actually consist of a single orientation exactly parallel to the tunnel but instead three orientations related by the C_3 axis of the tunnel, with the symmetry axis of the molecule tilted by about 17° from *y*.¹¹⁴ For the purposes of XBI, we have chosen to ignore this small tilt angle and instead consider a single orientation parallel to the tunnel. The hexagonal tunnels of thiourea have 3-fold rotational symmetry, suggesting that there are three equivalent orientations in the *xz*-plane related by 120° rotation about the tunnel. The energy minima have the symmetry axis of the ferrocene molecule pointing at the edges of the hexagonal tunnels (Figure 6.11). Other orientations are less favourable due to guest host interactions and ineffective packing of the guest.

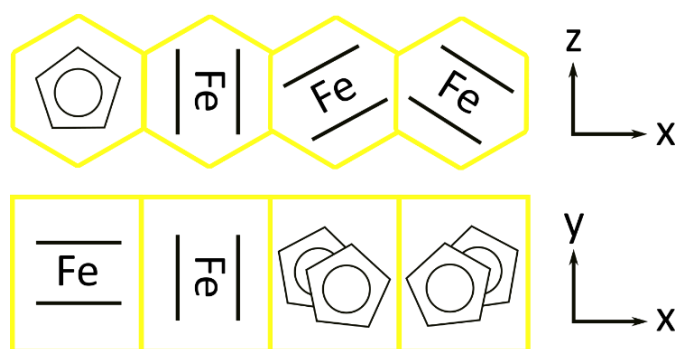


Figure 6.11 Probable orientations of ferrocene within the hexagonal thiourea tunnel viewed along the tunnel axis (top) and perpendicular to the tunnel (bottom). Adapted from Reference 117.¹¹⁷ The Experimental cartesian axis system used in the image indicates that the tunnel axis is vertical ($\chi = 90^\circ$). Left most: ferrocene symmetry axis aligned parallel to the tunnel axis. In the others, the ferrocene symmetry axis is the three orientations related by 120° rotation about the tunnel axis.

At ambient temperature, the ferrocene molecules reorient rapidly between all four orientations. Therefore, at ambient temperature, the orientational properties of the molecule can be considered isotropic. In addition, the ferrocene molecule rotates about its symmetry axis, which has no significant bearing on X-ray dichroism or X-ray birefringence as we have already determined that, viewed along the molecular symmetry axis, the tensor is isotropic. Between 160 K and 200 K, conversion between the orientations parallel to the tunnel and perpendicular to the tunnel is slow, but rotation in the xz -plane occurs, at a much faster timescale.

Below 160 K, the ferrocene molecules become effectively frozen, although there is a change in the proportion of molecules in the parallel and perpendicular orientations with decreasing temperature. At 155 K, around 60% of molecules are perpendicular, while decreasing the temperature lowers this proportion at 140 K to 55% and 52% at 110 K.¹¹⁴ Above 220 K, around 63% of the ferrocene molecules are perpendicular to the tunnel.¹¹³ However, the rate of exchange between the parallel and perpendicular orientations is on the 10^5 s^{-1} timescale, and therefore, the XBI measurements will simply observe an average over these orientations.¹¹⁷

The FerTUIC crystals were made as reported previously.¹¹⁶ A single crystal of good quality was selected and two X-ray absorption spectra at ambient temperature were recorded, with the crystal long axis vertical ($\chi = 90^\circ$) and horizontal ($\chi = 180^\circ$) respectively (Figure 6.12 (a)). The two spectra are essentially identical, except from a small difference at around 7.12 keV.

X-ray absorption measurements at 110 K (Figure 6.12 (b)) (below the phase transition), showed a more pronounced difference between the horizontal and vertical crystal orientations than observed at ambient temperature indicating a small amount of X-ray dichroism. The X-ray absorption spectra recorded at 110 K also show a difference above the K-edge. The differences at higher energy are broader and could be due to anisotropy in the p-orbitals but another possibility is that the differences are due to systematic errors (morphology, alignment etc.). However, these features are clearly not related to the electron excited at the K-edge and therefore, will have no effect on X-ray birefringence.

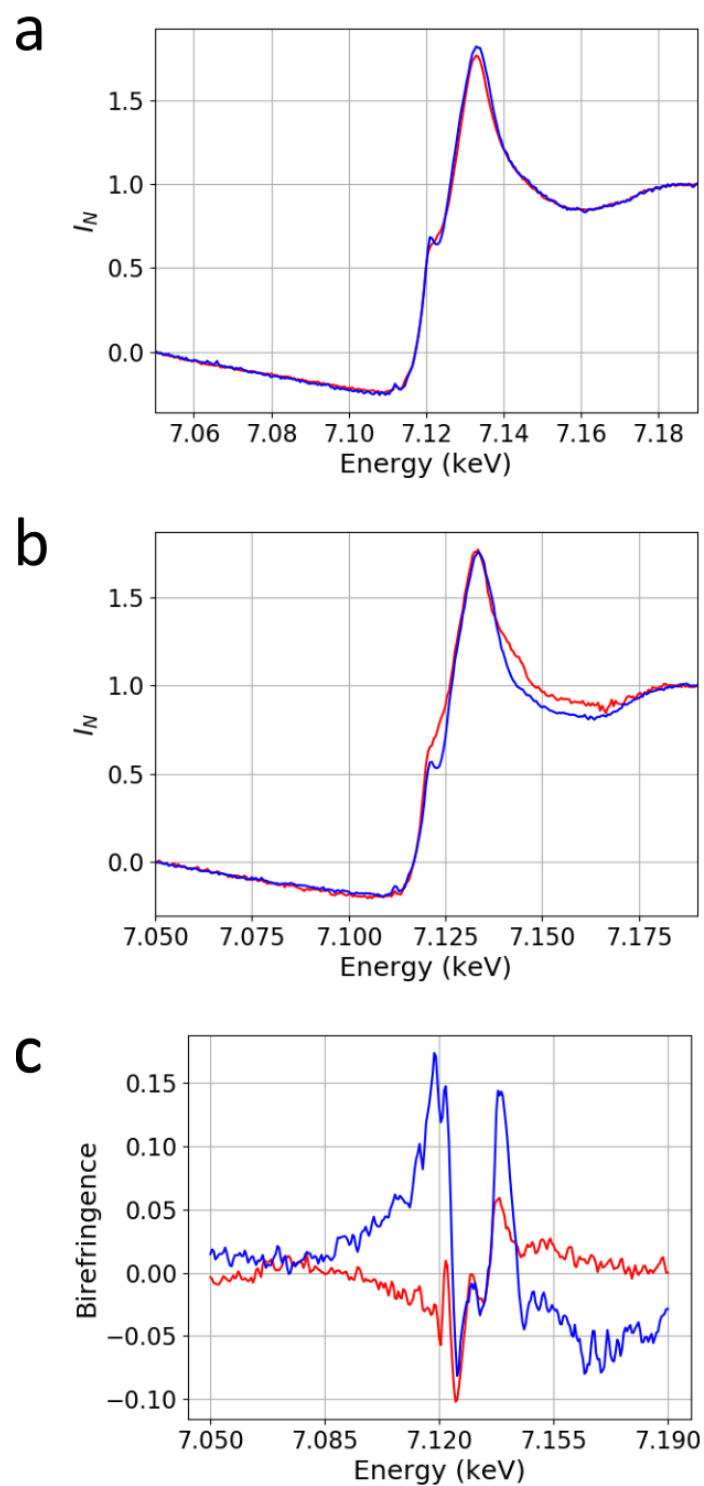


Figure 6.12 X-ray absorption spectra of a single crystal of ferrocene/thiourea inclusion compound (a) $\chi = 90^\circ$ (red) and $\chi = 0^\circ$ (blue) at ambient temperature. (b) $\chi = 90^\circ$ (red) and $\chi = 180^\circ$ (blue) at 110 K. (c) X-ray birefringence spectra at ambient temperature (red) and 110 K (blue) calculated from the X-ray dichroism spectrum (not shown).

From the measured X-ray absorption spectra, the X-ray dichroism spectra were determined at ambient temperature and at 110 K, and the X-ray birefringence spectra were then determined at each temperature using the Kramers-Kronig transform (Figure 6.12 (c)). The X-ray birefringence spectrum at ambient temperature exhibits only weak X-ray birefringence, whereas the X-ray birefringence spectrum at 110 K shows roughly a three-fold increase in X-ray birefringence. However, the X-ray birefringence at 110 K is still very low and it is unlikely that any significant XBI intensity would be observed for this sample.

The difference in predicted X-ray birefringence above and below the phase transition can be related to the dynamics of the ferrocene molecule. The rapid re-orientation of the ferrocene guest molecule above the phase transition means that the average molecular orientation is more isotropic. Below the phase transition at 110K, there are almost equal populations of ferrocene molecules perpendicular (52%) and parallel (48%) to the tunnel,¹¹⁴ so again the average orientational distribution is close to isotropic, consistent with very low X-ray birefringence observed. However, the 4% difference in population gives rise to slight anisotropy in the orientational distribution.

Another factor that may limit the X-ray birefringence is the nature of the bonding between the iron and the carbon in the molecule. Compared to the C-Br bonds studied in previous work, for which the excited σ^* orbital is highly directional, the excited-state orbital for ferrocene (although unknown) is likely to be highly delocalized and therefore unlikely to be strongly directional. Nevertheless, the excited-state orbital must have some directionality, or no X-ray birefringence would be observed.

6.4.2 (η^4 -1,3-cyclohexadiene)Fe(CO)₃/thiourea and (η^4 -trimethylene methane)Fe(CO)₃/thiourea

The inclusion compounds (η^4 -1,3-cyclohexadiene)Fe(CO)₃/thiourea (FeTCC) and (η^4 -trimethylene methane)Fe(CO)₃/thiourea (FeTMM) were originally studied, like CrTUIC, with regard to the fact that single crystals exhibit SHG.⁹⁴ Both FeTCC and FeTMM have three carbonyl ligands and another ligand bound to the metal atom by four contacts (Figure 6.2).

The carbonyl ligands are almost equidistant to the iron atom in both FeTCC and FeTMM. FeTCC bonds to the 1,3-cyclohexadiene ligand at four carbon atoms, thus distorting the ring out of plane. FeTMM guest molecules are stacked along the tunnel axis (*c*-axis) in the thiourea inclusion compound similar to CrTCH (Figure 6.13 (b)). In contrast, FeTCC guest molecules are oriented perpendicular to the tunnel, which in this case is aligned along the *a*-axis of the crystal structure (Figure 6.13 (a)). Thus, for FeTMM the reference axis is the crystallographic *c*-axis, while for FeTCC it is the crystallographic *a*-axis. The χ rotation of the crystal refers to the rotation of the reference axis about the incident X-ray beam (*z*-axis), where the reference axis remains in the *xy*-plane. When $\chi = 0^\circ$ the reference axis is parallel to the *x*-axis. The φ rotation refers to rotation of the crystal around the reference axis.

The perpendicular stacking of FeTCC may relate to the metallocenes carbonyl bonding. The iron centre in FeTCC is a d^8 metal and the greater electron density on the metal atom means there is a greater amount of back bonding to the π^* orbital on the carbonyls. Therefore, the oxygen of the carbonyl could be expected to be a better Lewis base and, thus, more likely to hydrogen bond to thiourea. The sideways stacking allows more hydrogen bonding and greater stabilization. FeTMM, on the other hand, has a d^6 metal centre and the lower electron density means that it stacks along the tunnel axis. Carbonyl stretching vibrations indicate more back bonding for FeTCC when compared to FeTMM, lending credence to the above theory.⁹⁴

Tensors based on Fe-C vectors (only bonded Fe-C considered) are shown in Figure 6.13 and Figure 6.14. The tensors for FeTCC and FeTMM are prolate spheroids. The FeTCC tensor long axis is almost perpendicular to the tunnel direction (*x*-axis) due to the orientation of the metallocenes molecules (Figure 6.13). Thus, the FeTCC tensor predicts that there should be quite a strong φ dependence on XBI behavior, i.e., for certain values of φ , significant X-ray birefringence would be observed for a χ -scan, whereas for other values of φ , the tensor would be essentially isotropic and no X-ray birefringence would be observed with rotation in χ .

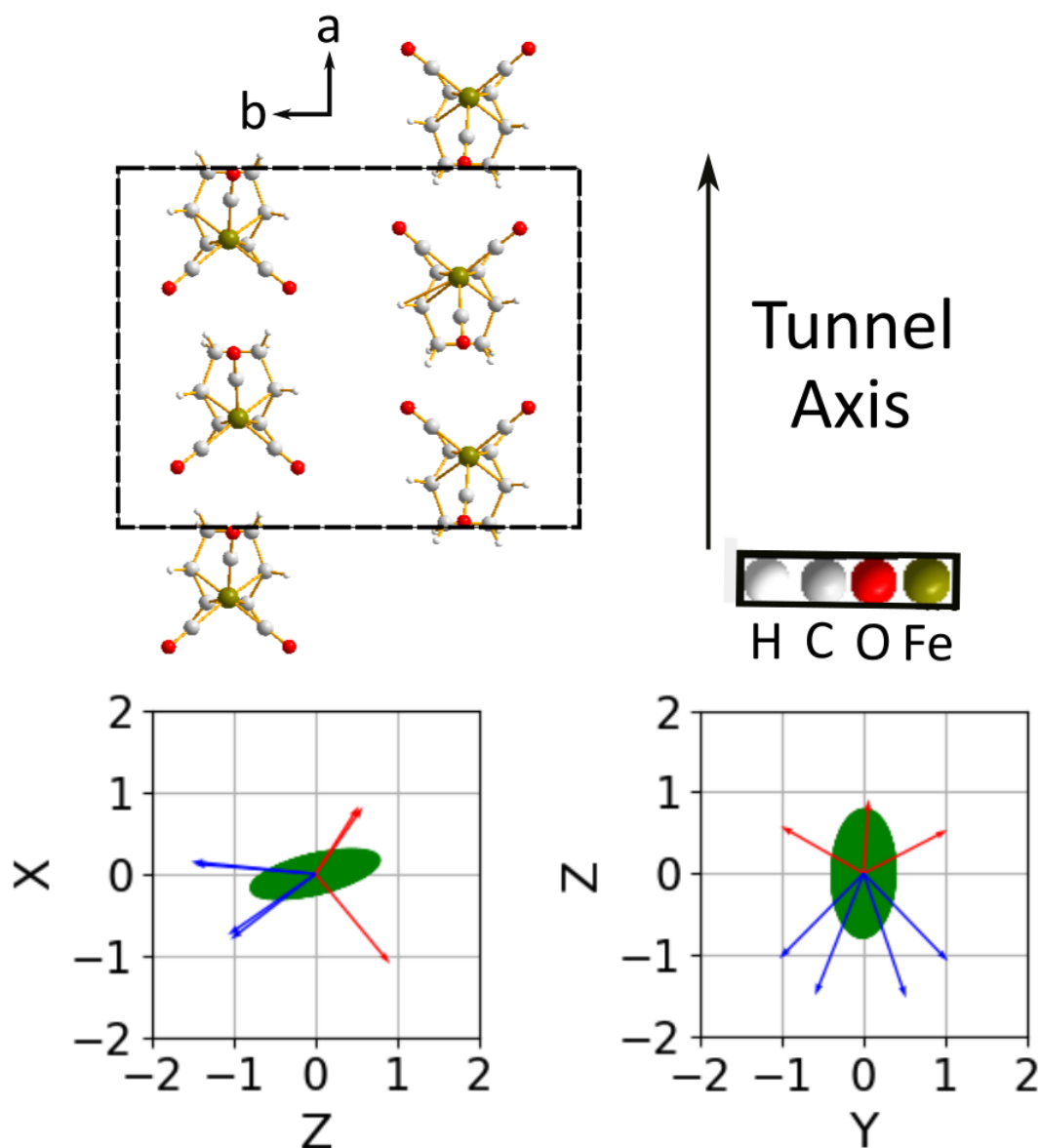


Figure 6.13 Crystal structure of the guest component in FeTCC (thiourea removed for clarity) viewed along the c -axis (structure determined at 173 K). Tensor of a single molecule of $(\eta^4\text{-}1,3\text{-cyclohexadiene})\text{Fe}(\text{CO})_3$ is viewed from two orientations: left along b (y)-axis, right is along a (x)-axis. Note that for this structure the a (x)-axis is parallel to the thiourea tunnel axis.

The tensor for FeTMM is elongated parallel to the tunnel axis (c -axis) and appears isotropic when viewed parallel to the c -axis (Figure 6.14). Therefore, if the assumed tensor is correct then X-ray birefringence should be observed for all orientations in φ .

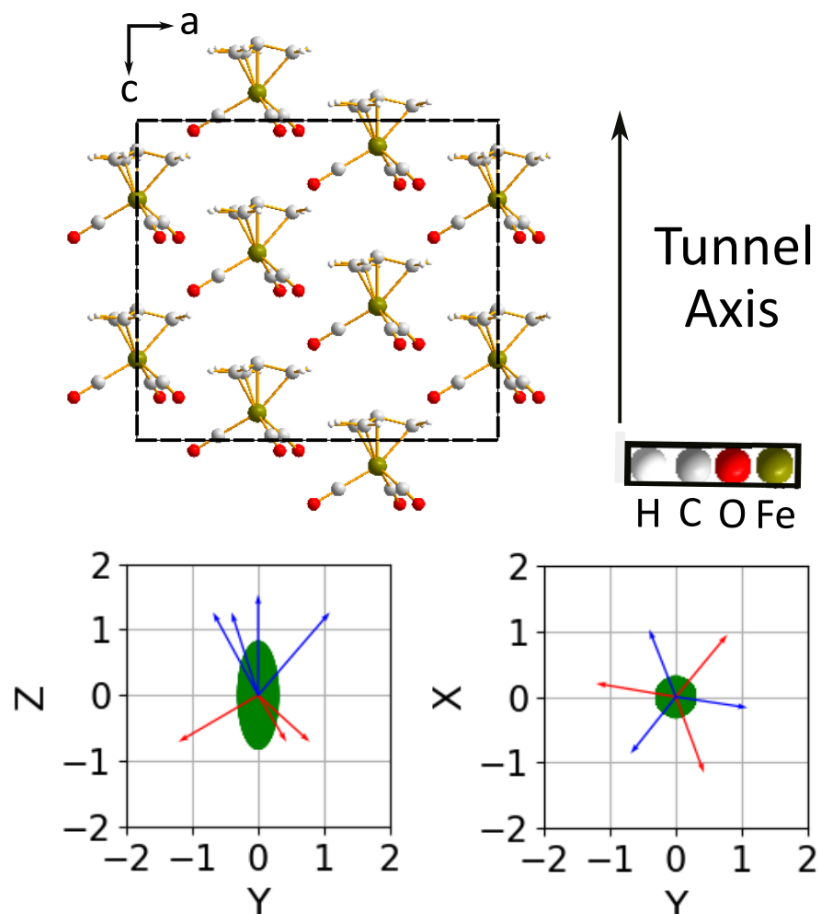


Figure 6.14 Crystal structure of FeTMM (thiourea removed for clarity) determined at 203 K viewed along the b -axis. Tensor of a single molecule of $(\eta^4\text{-trimethylene methane})\text{Fe}(\text{CO})_3$ is viewed from two orientations: left along $a(x)$ -axis, right is along the $c(z)$ -axis. Note that for this structure the $c(z)$ -axis is parallel to the thiourea tunnel axis. The Fe-C bond vectors which were used to determine the tensor can also be seen the carbonyls are depicted in red and the other Fe-C vectors as blue.

X-ray absorption spectra were recorded for a single crystal of FeTCC and a single crystal of FeTMM (Figure 6.15) for two orientations ($\chi = 0^\circ$ and $\chi = 90^\circ$). For the two orientations, there is only a small difference around the K-edge, which is slightly more pronounced for FeTMM (Figure 6.15 (b)). However, the large variations above and below the K-edges, which are almost certainly from systematic errors, make any results difficult to interpret. The magnitude of the systematic errors observed for these two samples means that no further attempts were made to study them using XBI. Other single crystals of the same materials may lead to spectra of higher quality, to give more clarity on the behaviour around the K-edge for different orientations.

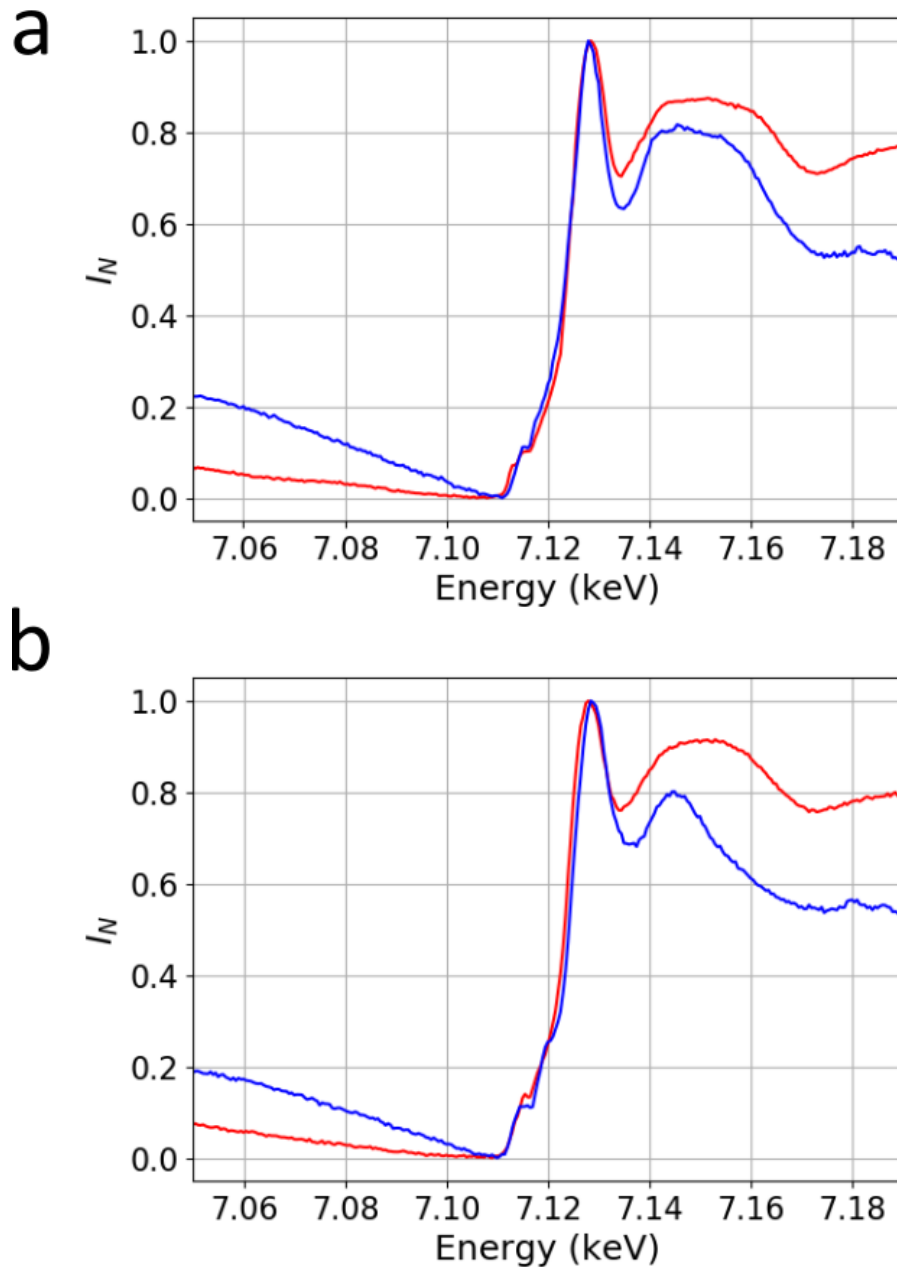


Figure 6.15 (a) X-ray absorption spectra recorded for a single crystal of FeTCC at a fixed angle of $\varphi = -30^\circ$ and two different angles of $\chi = 90^\circ$ (red) and 0° (blue). (b) X-ray absorption spectra recorded for a single crystal of FeTMM at a fixed angle of $\varphi = -30^\circ$ and two different angles of $\chi = 90^\circ$ (red) and 0° (blue). These X-ray absorption scans were normalized to the maximum and minimum values rather than using Equation 6.1 and 6.2 due to the large variations in intensity at high and low energy. These variations most likely caused by a misalignment of the sample or unusual sample morphology.

As the tensor for FeTCC indicates the potential for X-ray birefringence to be observed, at least for certain values of φ , one possibility for the lack of X-ray dichroism in Figure 6.15 (a) is that the crystal orientation (φ value) was such that the tensor is essentially isotropic along the direction of the incident beam and should therefore show no X-ray dichroism as χ is changed. However, this does not explain the lack of X-ray birefringence observed for FeTMM as according to the tensor X-ray dichroism should have been observed in all φ orientations. To assess other reasons for the lack of X-ray dichroism in the experimental data, we must look back at assumptions we made for calculating the tensors. Essentially, to determine the tensors, we assumed that the excited-state orbital has directionality that depends on the Fe-C bond vectors. Clearly the lack of X-ray dichroism observed for these materials suggests that this assumption is incorrect.

For all the metallocenes studied, the tensors upon which our interpretation of results has been based can be considered only a rough approximation. We have assumed that the X-ray dichroism and X-ray birefringence behaviour can be approximated by the consideration of the metal-carbon bond vectors. However, the bonding around the central metal atoms is clearly more complicated, and greater understanding is needed to truly interpret and predict the bonding environment around the metal centre, and the specific excited-state molecular orbitals involved in the electronic transitions at the K-edge. Regardless, the recorded results clearly indicate that at least some of the metallocenes studied have anisotropic local bonding environments and exhibit X-ray dichroism (and hence X-ray birefringence).

6.5 XBI Studies of Copper Dibromide

Copper dibromide (CuBr_2) proved to be a novel material for XBI study as it is feasible to record XBI data at two different absorption edges and it is the first inorganic material to be studied using XBI. As for all the samples in this chapter, the bonding involving the X-ray absorbing atom(s) in CuBr_2 is more complicated than that in brominated organic materials studied previously using XBI at the Br k-edge.

Within the CuBr_2 crystal structure, the Cu-Br bonds give rise to a planar diamond arrangement with the copper and bromine atoms in alternate corners. Each copper atom is part of two of these diamonds, leading to a ribbon-like array. These ribbons propagate infinitely along the b -axis, the plane of the ribbon is in the $(10\bar{1})$ plane. The copper bromine bond length within the ribbon is 2.41 \AA . These ribbons form into layers, with longer contacts between the copper and bromine atoms (3.15 \AA) between layers, essentially showing a Jahn-Teller distortion of bonding around the copper atom (Figure 6.16).^{118,119}

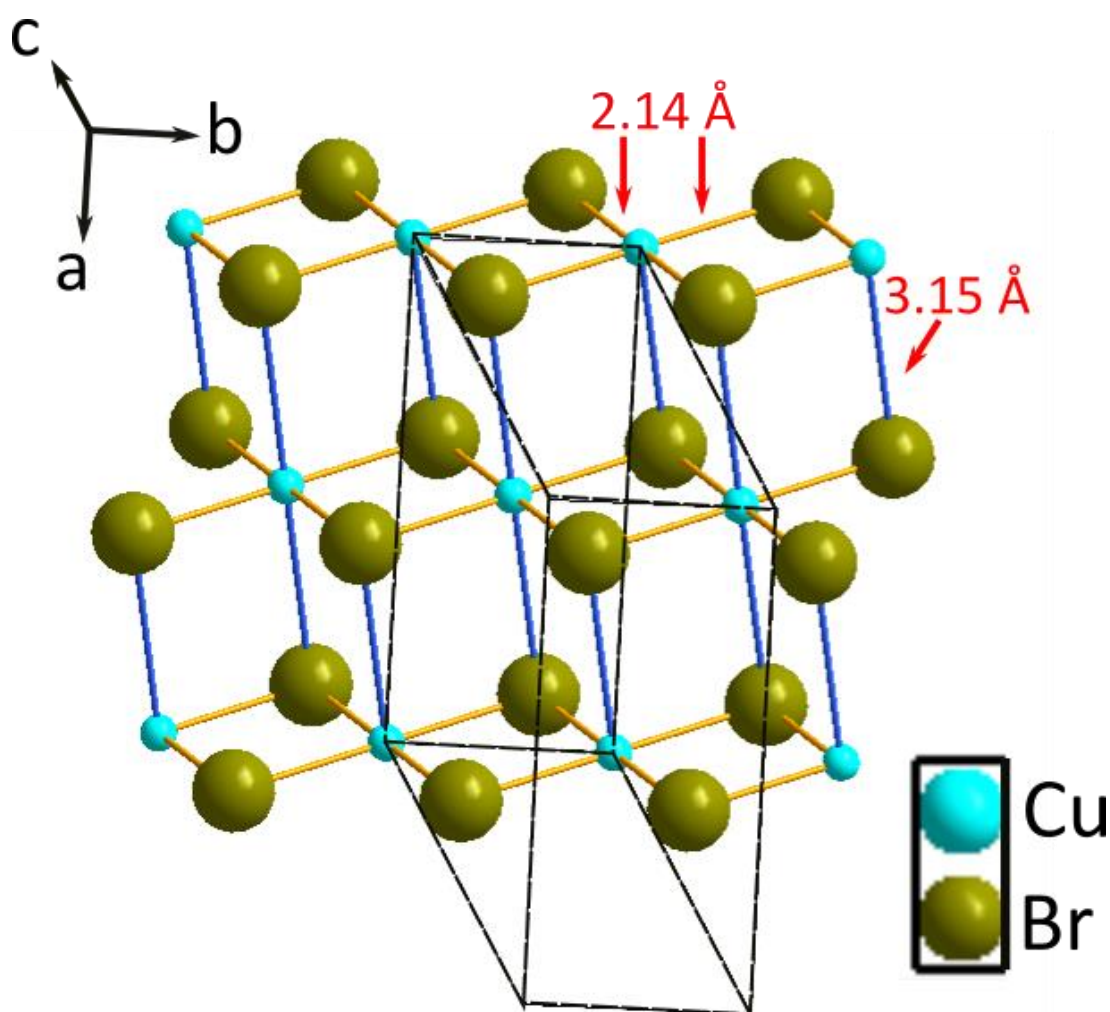


Figure 6.16 The partial unit cell crystal structure of CuBr_2 viewed along, showing three ribbons. Cu-Br bonds of length 2.14 \AA are yellow, Cu-Br bonds of length 3.15 \AA are blue.

Figure 6.17 illustrates the face indexing of the actual crystal used in the XBI studies. Face indexing performed using SCXRD establishes the orientation of the unit cell of the crystal structure relative to the morphology of the single crystal sample. This is of particular importance to XBI in interpreting how the crystal structure is oriented relative to the laboratory reference frame for the XBI experiments, and in particular the specific orientation of the crystal for given values of the crystal orientation angles χ and φ .

The crystals appear as flat, elongated crystals with a rectangular cross-section, and quite pockmarked with an uneven surface. The long axis of the crystals is taken as the reference axis in this case. The χ rotation of the crystal refers to the rotation of the reference axis about the incident X-ray beam (z -axis), with the reference axis maintained in the xy -plane. When $\chi = 0^\circ$ the reference axis is parallel to the x -axis. The φ rotation refers to rotation of the crystal around the reference axis. At $\varphi = 0^\circ$, the incident X-ray beam (z -axis) propagates along the $[78\bar{1}]$ direction in the crystal. The large face of the crystal is close to perpendicular to the $[2\bar{1}3]$ axis and is perpendicular to the incident beam direction when $\varphi = 90^\circ$.

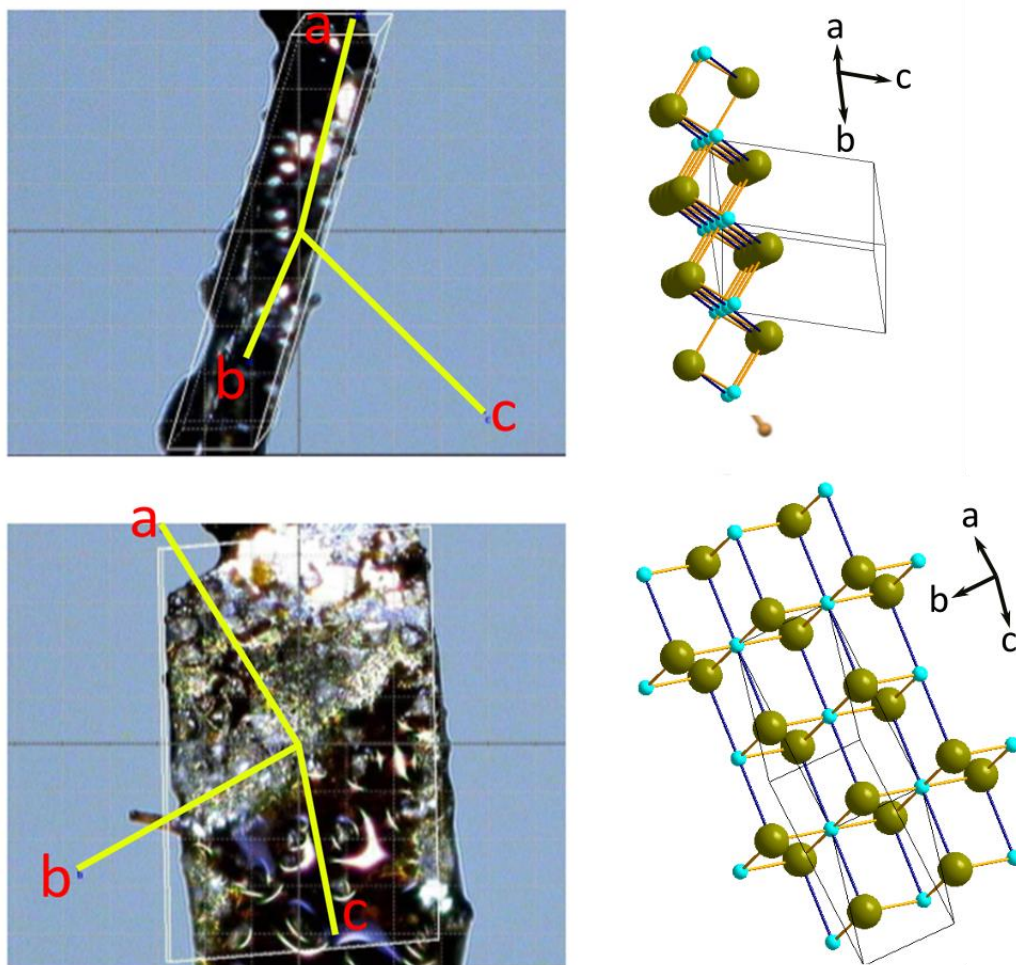


Figure 6.17 Face indexing for the CuBr_2 single crystal used in the XBI measurements. Top shows smallest face of crystal parallel to the long axis, corresponding to viewing the crystal structure along the $[78\bar{1}]$ direction. Bottom shows the largest face of the crystal corresponding to viewing along the $[2\bar{1}3]$ direction.

CuBr_2 was obtained from Sigma Aldrich and recrystallized from water. The solution was left in a fume hood and black crystals of several cm in size formed upon slow evaporation over a week. This produced a number of crystals of varying quality. The crystals themselves are flat elongated rectangles, which are quite soft and easily deformed. A single crystal of good quality was selected for the XBI measurements.

For XBI measurements at the Cu K-edge, the incident X-ray energy was 8.985 keV, and for XBI measurements at the Br K-edge, the incident X-ray energy was 13.474 keV. In this work, the beam dimensions were defined by slits of 4 mm (vertical) and 4 mm (horizontal), and the polarization analyzer reflection was Si (440) for studies at the Cu K-edge and Ge (555) for studies at the Br K-edge. The detector used was the “X-ray eye” (12 bit **CCD** miniFDI camera from Photonic Science Ltd).

Figure 6.18 shows XBI images recorded for a single crystal of CuBr_2 at the Br K-edge and at the Cu K-edge for different crystal orientations specified by χ and ϕ . The XBI images at both the Br and Cu K-edges show the same essential behaviour as a function of crystal orientation. With ϕ fixed at 90° , the crystal is uniformly bright at $\chi = 20^\circ$ and 110° and uniformly dark at $\chi = 65^\circ$ and 155° . With ϕ fixed at -90° , the reverse behaviour is observed, with the crystal bright at $\chi = 65^\circ$ and 155° , and uniformly dark at $\chi = 20^\circ$ and 110° . This similar behaviour for data recorded at the Br K-edge and Cu K-edge is understandable as the measurement at each K-edge involve the same structure and the same bonding environment. However, the images recorded at the copper K-edge are clearly lower in intensity than the images recorded at the bromine K-edge. The difference in observed intensity contrast is most likely a consequence of the different K-edge energies.

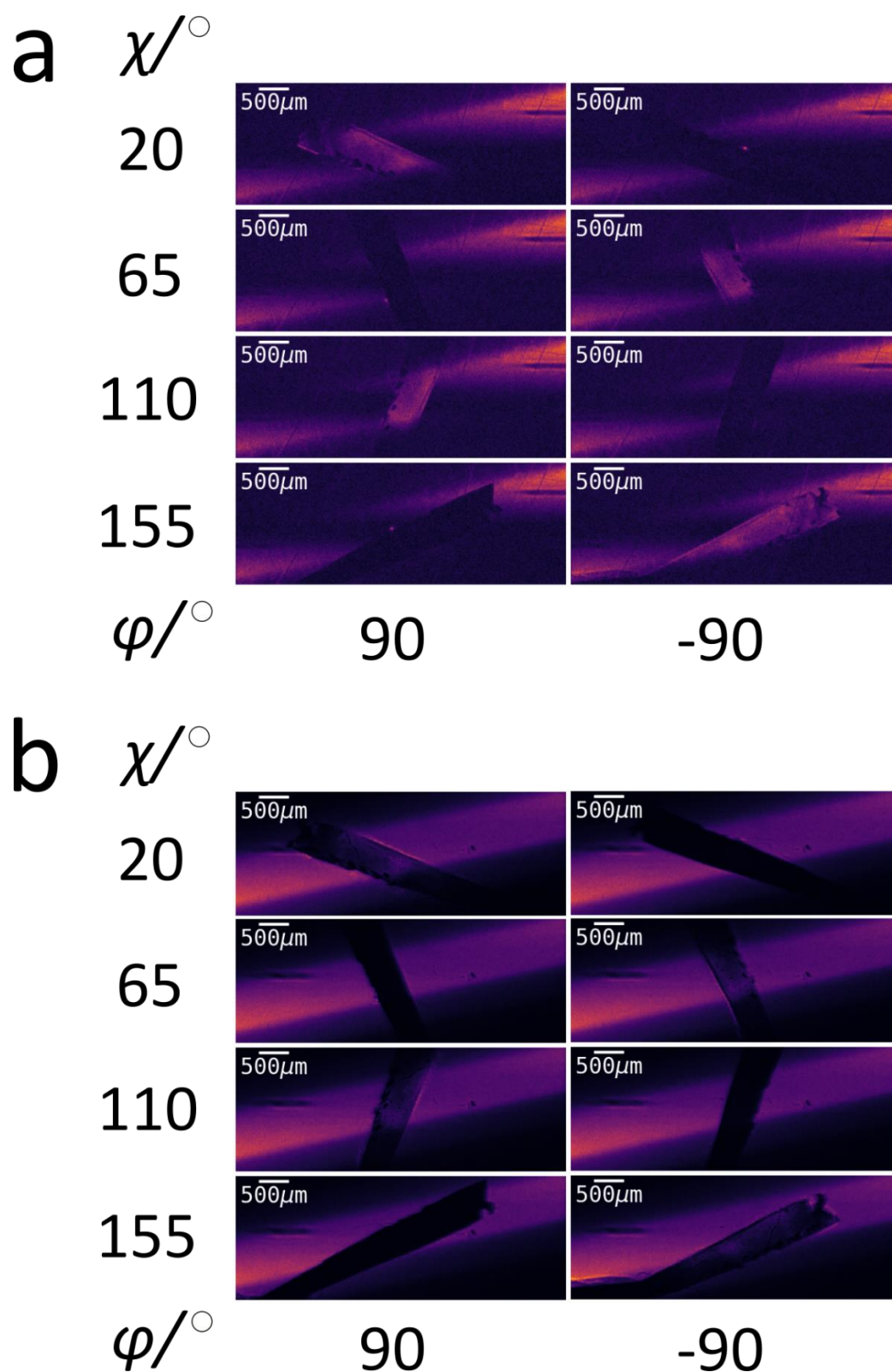


Figure 6.18 XBI images recorded for a single crystal of CuBr_2 at $\chi = 20^\circ, 65^\circ, 110^\circ, 155^\circ$ and $\varphi = 90^\circ, -90^\circ$, using linearly polarized X-rays tuned to (a) the bromine K-edge (13.474 keV) and (b) the copper K-edge (8.985 keV).

The variation in X-ray intensity as a function of orientation of the CuBr₂ single crystal is better observed in Figure 6.19. The intensities in this figure are calculated from the mean intensity of a selected region of the crystal in the XBI images. Figure 6.19 (a) shows this intensity as a function of χ at $\varphi = 90^\circ$ and $\varphi = -90^\circ$ (for these φ values, the incident beam is perpendicular to the two large faces of the crystal, the $(2\bar{1}3)$ and $(\bar{2}1\bar{3})$ faces, which are parallel to each other). The fact that the intensity maxima at $\chi = 20^\circ$ and 110° (at $\varphi = 90^\circ$) have unequal intensity and the intensity maxima at $\chi = 65^\circ$ and 155° (at $\varphi = -90^\circ$) have unequal intensity is a consequence of elliptical polarization in the incident beam (i.e., the sample was not exactly in the beam centre during the XBI measurements).

Figure 6.19 (b) shows contour plots of intensity as function of both χ and φ , for measurements at the Cu K-edge and the Br K-edge. While the χ -dependence is clearly related to X-ray birefringence, the φ -dependence is more complicated. Due to the anisotropy of the crystal morphology, the path length of the X-ray beam through the crystal is clearly different for different values of φ , with maximum path length at $\varphi = 0^\circ$. This large variation in path length will result in a variation in X-ray absorption as a function of φ . X-rays transmitted through a larger path length in the sample will show a proportional decrease in intensity. Understanding the relationship between morphology of the sample and XBI intensity is therefore vital to interpreting XBI results.

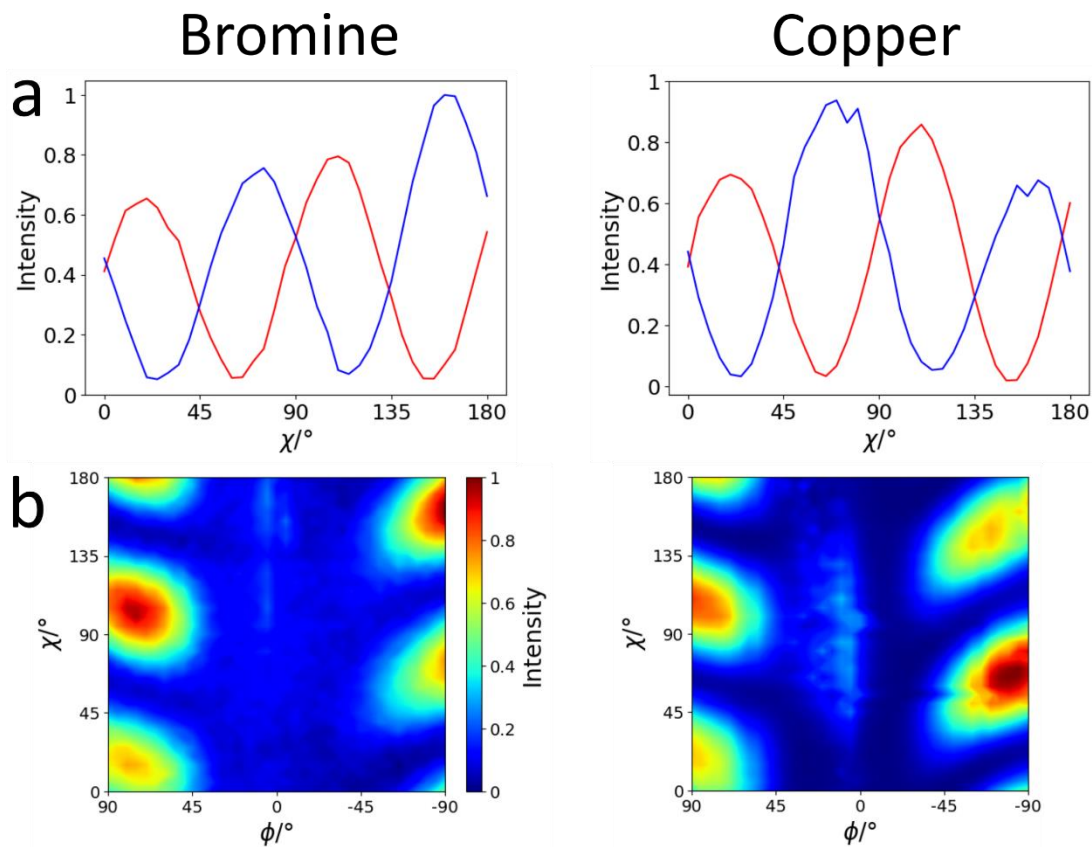


Figure 6.19 XBI intensity for a single crystal of CuBr_2 at the copper K-edge (right) and bromine K-edges (left) (a) as a function of χ with ϕ fixed at $\phi = 90^\circ$ (red) and $\phi = -90^\circ$ (blue). (b) Contour plot showing intensity as a function of both χ and ϕ .

However, the difference in the behaviour of the χ scans at $\phi = 90^\circ$ and $\phi = -90^\circ$ cannot be explained by the sample morphology, as the path length of the X-ray beam through the crystal is the same for $\phi = 90^\circ$ and -90° . As shown in (Figure 6.19 (a)) the intensity maxima observed in the χ scan at $\phi = 90^\circ$ correspond to minima in the χ scan at $\phi = -90^\circ$, and vice versa (both for the Br K-edge and the Cu K-edge). The difference in ϕ of $\Delta\phi = 180^\circ$ between the two scans means that the X-ray beam should travel the same path through the sample, but in the opposite direction. Furthermore, from the intensity contour plots, it is clear that there is a gradual shift in the value of χ corresponding to the intensity maxima as the value of ϕ is changed.

The tensor for CuBr_2 is shown in Figure 6.20 and was calculated using Equation 3.5 from the Cu-Br vectors in the crystal structure of CuBr_2 . The tensor can be described as an oblate spheroid. The tensor is oriented such that none of the tensor axes is aligned to the axes of the experimental reference frame when $\chi = 0^\circ$ and $\varphi = 0^\circ$, which helps to explain the observed XBI behaviour. If we were to rotate by 180° about the long axis of the tensor, there is no change in orientation. If we were to rotate about the long axis of the crystal (x -axis) by 180° , then the resulting orientation of the tensor relative to the experimental reference frame is not the same as the initial orientation. Therefore, the measured X-ray birefringence data would be different.

This XBI behaviour is similar to that for 1,2,4,5-tetrabromobenzene (TBB) discussed in Chapter 5. The XBI behaviour of TBB was modelled and the change in intensity dependence for different values of φ was explained using a similar predicted tensor for which the axes of the tensor are not aligned with the experimental axis system, lending support to our theory. Of course, we note that this analysis makes many assumptions regarding the bonding in the material such as a similar bonding environment for all the Cu-Br bonds, and the directionality of the relevant excited-state orbital relative to the Cu-Br bond direction.

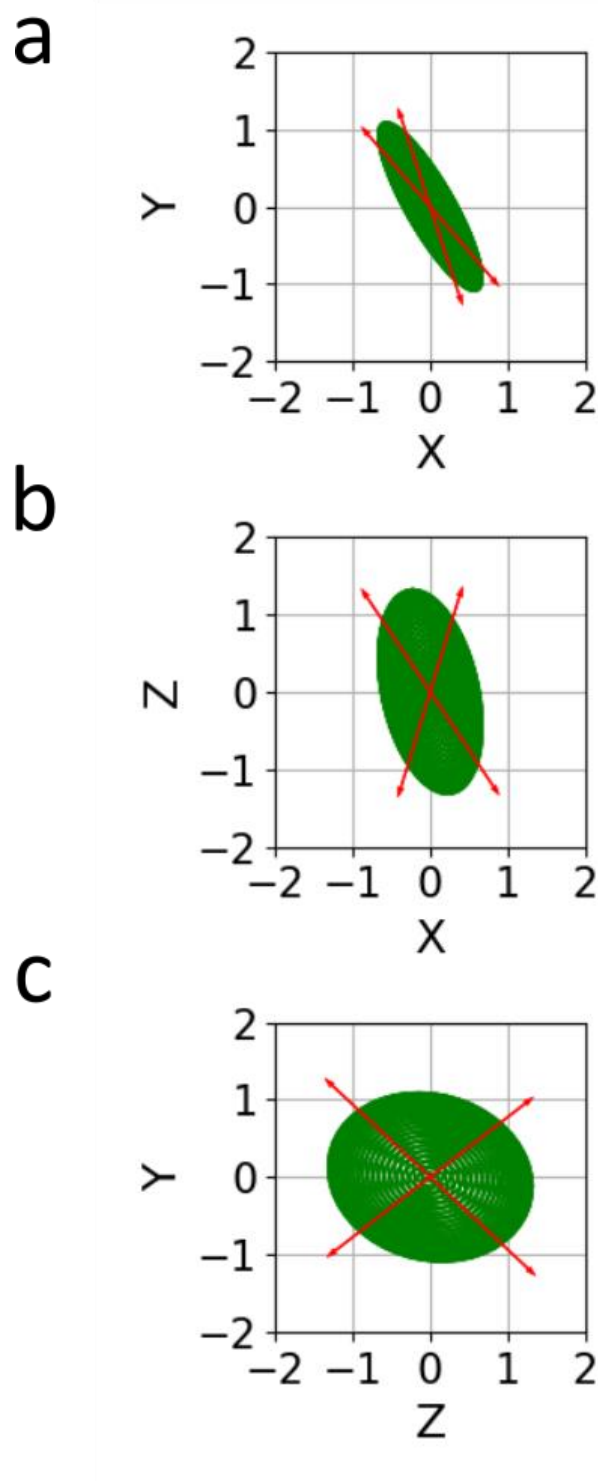


Figure 6.20 Tensor (green) determined from the nearest neighbour Cu-Br bonds (distance 2.14 Å) in the unit cell of CuBr₂ (the bond directions are shown as red vectors), when the single crystal is oriented so that the $[2\bar{1}3]$ axis is parallel to the y-axis and the $[78\bar{1}]$ axis is parallel to the z-axis ($\chi = 0^\circ$ and $\phi = 0^\circ$). Viewed along (a) the z-axis, (b) the y-axis and (c) the x-axis.

6.6 Conclusions

A number of samples were studied, increasing the range of materials that have been studied by XBI on B16 to include the iron and copper K-edges. Furthermore, in principle this means that elements with absorption edges between 7.11 keV (Fe) and 13.47 keV (Br) should also be accessible for XBI study on B16. Experiments on I16 proved the feasibility of observing X-ray birefringence in materials containing sulphur and chromium, although unfortunately I16 cannot be setup for XB measurements in imaging mode (i.e. XBI) at present. Future work to create a working XBI setup on I16 would be beneficial and would vastly increase the range of materials that could be studied.

Of particular interest is the iron K-edge. The presence of iron in haemoglobin, the molecule responsible for the transport of oxygen in blood, is already well established. Furthermore, a change in the local bonding environment of haemoglobin is expected when oxygen is bound compared to unbound, which will also be associated with a change in oxidation state of iron (and hence a change in the Fe K-edge energy). X-ray absorption spectra have already been shown to be sensitive to oxidation state of iron.^{120–123}

The samples studied each proved interesting. The thiourea sample studied on I16 showed strong X-ray dichroism and paved the way to study a range of thiolated materials including polymers¹⁰⁷, self-assembled monolayers^{108,109} and the host structure of thiourea inclusion compounds using XBI. The inclusion compounds CrTUIC and FeTUIC showed nominal X-ray birefringence, indicating some directionality in the excited-state orbital for the metallocenes, while FeTMM and FeTCC showed very little evidence of X-ray birefringence. Possibly this could have been due to the specific crystal orientation studied corresponding to an isotropic direction of the tensor. Changing the orientation (φ) of the crystal could allow this issue to be resolved.

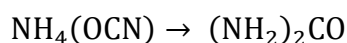
The FerTUIC sample showed slight increase in X-ray birefringence with a decrease in temperature, thus indicating an increase in ordering of the ferrocene molecules, in agreement with previous conclusions from Mössbauer spectroscopy,¹¹² ¹³C NMR,¹¹³ and ²H NMR.¹¹⁴ This observation confirms that X-ray dichroism is sensitive to small changes in orientational ordering.

The CuBr₂ crystal is the only sample discussed in this chapter to actually be studied using XBI measurements. It shows remarkable birefringent behaviour similar to that of TBB. Comparable XBI behaviour was observed at both the copper and bromine K-edges with χ -scans showing sinusoidal variation in transmitted X-ray intensity as a function of χ . However, reversing the direction of propagation of X-rays through the crystal (corresponding to $\Delta\phi = 180^\circ$) led to a change in the observed maxima and minima in the χ scan by $\Delta\chi = 45^\circ$. The XBI behaviour of metallocenes and inorganic materials is clearly quite complicated, depending heavily on the nature of the bonding environment of the X-ray absorbing element. A deeper understanding of the bonding is necessary for further understanding of XBI behaviour, as the technique progresses to study new materials at different absorption edges.

7 PXRD studies of the solid-state transformation of Ammonium Cyanate to Urea

7.1 Introduction

In 1828, Friedrich Wöhler attempted to synthesize ammonium cyanate (AC) from a number of reactions (cyanic acid and ammonia in solution, silver cyanate and ammonium chloride solution, lead cyanate and ammonia), instead forming urea.¹²⁴ Two years later, Wöhler and Liebig discovered the transformation of AC [NH₄(OCN)] into urea [(NH₂)₂CO] at ambient temperature over a period of two days.¹²⁵



Typically, a solid-state synthesis such as the one above would not garner the recognition that Wöhler's synthesis retains to this day. However, during this time-period, a theory known as 'Vitalism' was commonly accepted in the scientific community. Vitalism theorized that organic compounds had a "vital force" only present in living things. Therefore, there was a division between organic and inorganic compounds. AC, an inorganic compound, transforming into urea, an organic compound (extracted from urine in 1799), disproved Vitalism. Whether the reaction actually had much effect in dispelling the belief in Vitalism that existed in this era is debatable. A lot of Wöhler's recognition was posthumous. Regardless, the Wöhler synthesis is one of the first organic solid-state reactions recorded and is embedded in the history of organic chemistry.

The crystal structure of AC was reported only in 1998¹²⁶ and further refined in 2003, as the development of techniques for structure determination from PXRD was necessary.³⁴ Urea was one of the first organic crystals to be studied using X-ray diffraction.^{127,128} It is of chemical importance as a main component in the ultimate product of animal metabolism and used in industry to produce pharmaceuticals and fertilizers. Since the first X-ray diffraction study of urea in 1921, there have been numerous other studies to get a better determination of the crystal structure.^{129–135}

Walker and Wood (1900)¹³⁶ studied the solid-state reaction of AC to urea in detail. AC was observed to melt at 80°C and then solidify, and the resulting solid melted again at 128-130°C (the melting point of urea). Walker and Wood determined that the reaction of AC progressed only when exposed to moisture at moderate temperatures. Increasing the temperature increases the rate of transformation significantly.

While the structure of AC and urea have now been known for a few years, the mechanism by which AC transforms into urea remains unknown. In an attempt to determine the mechanism, more information on the reaction was needed. Thus, we decided to study the kinetics of the transformation. Preliminary powder X-ray diffraction (PXRD) measurements were undertaken on both deuterated (ND_{old}) and non-deuterated (NH_{old}) samples of AC, which had been used previously to determine the crystal structure of AC.^{34,126} In the present work, PXRD patterns were recorded to check if these samples were still monophasic samples of AC. However, upon comparing the PXRD pattern of NH_{old} with that corresponding to the known structure of AC (Figure 7.1 (a)), an additional phase is clearly observed, with peaks that do not correspond to either urea or AC.

The PXRD pattern of ND_{old} is shown in Figure 7.1 (b), with none of the additional phase present at ambient temperature. The only peaks observed correspond to AC and a solitary peak at around $2\theta = 22^\circ$ corresponding to urea, indicating the partial transformation of the ND_{old} sample from AC to urea.

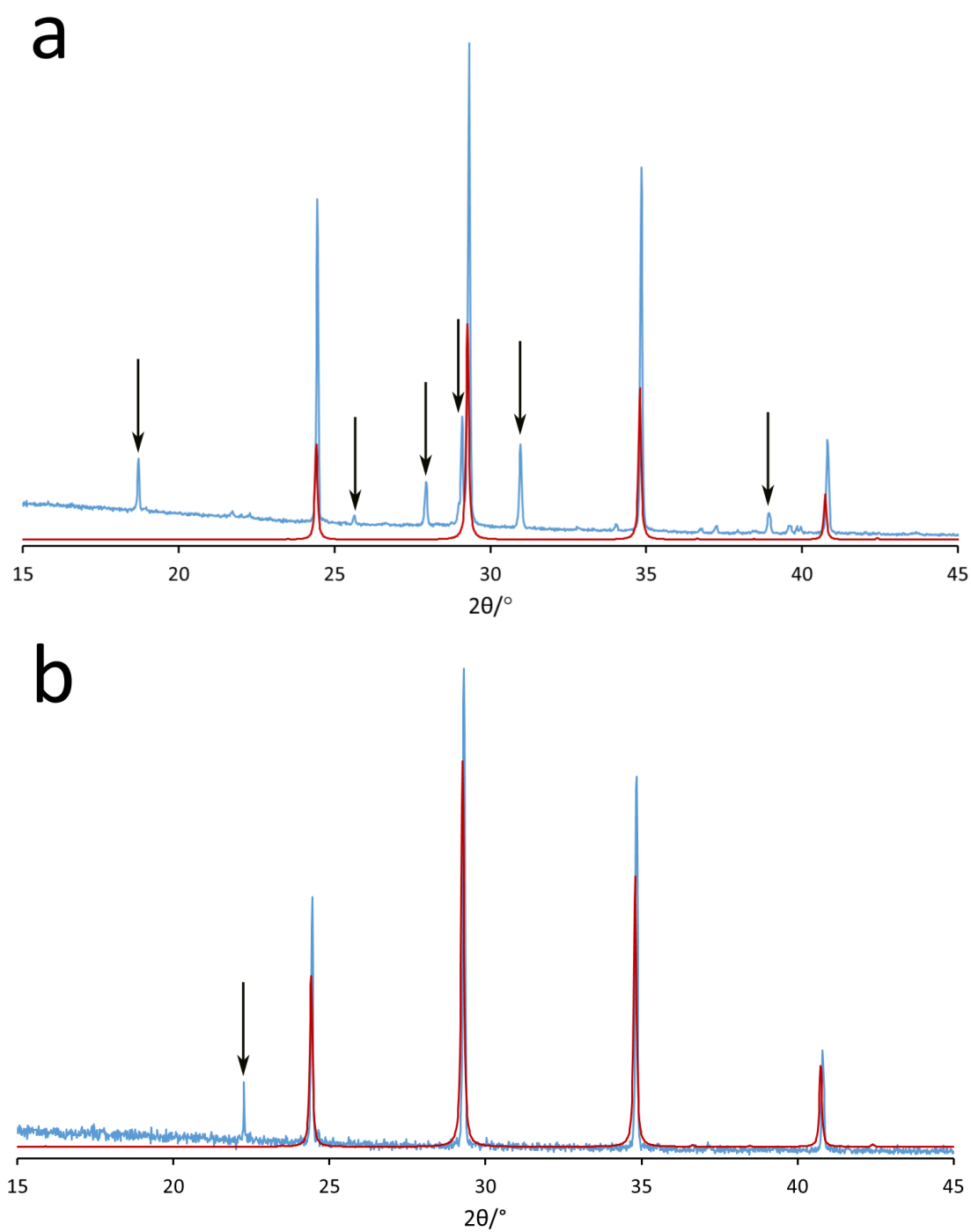


Figure 7.1 PXRD pattern recorded at ambient temperature for (a) NH_{old} (blue); peaks due to the unknown phase are marked with black arrows. (b) ND_{old} (blue); the peak due to urea is marked with the black arrow. In each case, the PXRD pattern of AC simulated for the crystal structure determined at ambient temperature is shown in red.³⁴

Initially, studies of the reaction of AC to urea were studied for ND_{old} by recording powder XRD data as a function of time (at fixed temperature) using a 2D detector (ND_{old} was used rather than NH_{old} , as the sample amount for NH_{old} was very small). A 2D detector is used on the single crystal X-ray diffractometer, which has the variable temperature capability required for these experiments. (Variable temperature is not available on the currently accessible powder X-ray diffractometers.) While the single crystal X-ray diffractometer can be used to record PXRD patterns, the peaks are broader than on the powder XRD instrument, and generally not suitable for structure determination. From analysis of this initial data, we determined that ND_{old} passes through an intermediate phase before transforming fully into urea (Figure 7.2). Moreover, the intermediate phase is identified as the same phase as the additional phase present in the sample of NH_{old} discussed earlier.

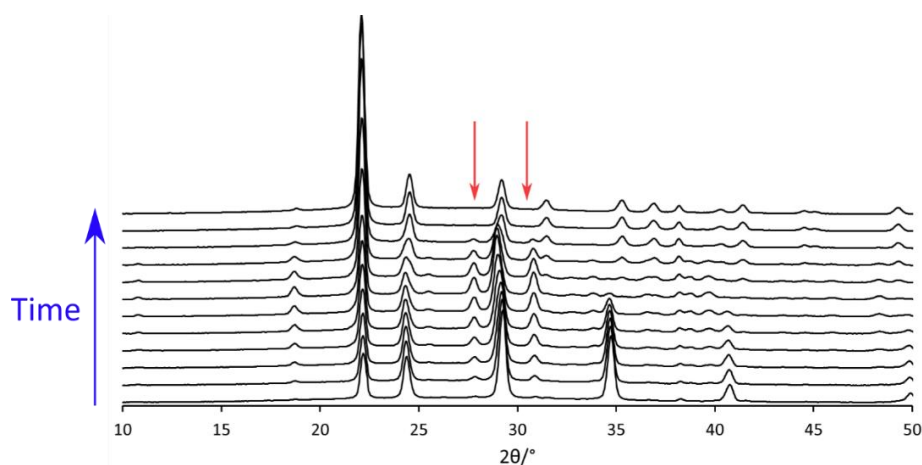


Figure 7.2 Powder X-ray diffraction pattern of ND_{old} recorded every 5 minutes for 1 hour at 340 K on a single crystal diffractometer. The initial PXRD pattern shows only peaks corresponding to AC; red arrows indicate peaks due to the intermediate phase which formed within 5 min and then disappeared at ca. 50 min. Final PXRD pattern shows only peaks corresponding to urea.

The presence of an intermediate crystalline phase in the transformation from AC to urea sheds new light on the potential mechanism of the transformation. For this reason, we focus here on determination of the crystal structure of the intermediate phase, leading to the proposal of a mechanism for the transformation. Furthermore, the kinetics of the AC to urea reaction were studied for ND_{old} and two new samples made in 2018: a non-deuterated sample (NH_{new}) and a deuterated sample (ND_{new}).

7.2 Experimental

The samples of AC from 1998 were made using ion exchange between tetraethylammonium cyanate and ammonium thiocyanate using an altered form of the method described in References 126 and 137.^{126,137} We would like to acknowledge Dr Tanja Miletić and Professor Davide Bonifazi for providing the newer samples of AC.

7.2.1 Powder X-ray diffraction

Synchrotron PXRD data were recorded on beamline I11 at Diamond Light Source¹³⁸ at a wavelength of 0.82578 Å. Borosilicate glass capillaries (0.7 mm) were used to hold the samples and the capillaries were rotated around the long axis to reduce the effects of preferred orientation in the powder XRD data. An Oxford Cryostream Plus was used to control the temperature of the sample.

7.2.1.1 Structure Determination

As the amount of the intermediate phase passes through a maximum partway through the reaction from AC to urea, a sample of ND_{old} was heated at 343 K for 9 min to obtain a sample containing a maximal amount of the intermediate. The sample was immediately cooled to 293 K and the powder XRD pattern was recorded using the Multi-Analyser-Crystal (MAC) detector; step size, 0.001°; 2θ range, 0° to 150°; data collection time, 15 min. The recorded data from the MAC detector was binned to give an effective step size of 0.004° so that it could be used in GSAS. These data were used for structure determination of the intermediate phase.

7.2.1.2 Kinetics of the Solid-State Reaction

Powder XRD data to study the kinetics of the reaction were recorded using a position sensitive detector (PSD) and the following data collection parameters; step size, 0.004°; 2θ range, 2.084° to 92.112°; data collection time ca. 1 s.

T/K	Sample		
	NH _{new}	ND _{new}	ND _{old}
338	✓	✓	
343	✓	✓	✓
348	✓	✓	✓
353	✓	✓	✓
358			✓

Table 7.1 Temperatures at which powder XRD data were recorded as a function of time for samples; NH_{new}, ND_{new} and ND_{old}, using I11 at DLS.

The relative amounts of AC, urea and the intermediate phase for each PXRD pattern were determined from TOPAS fitting of PXRD pattern performed by Dr. Leigh Connor at DLS. The unit cell parameters (a , b , c and V) and the line shape parameters were refined as a function of time to achieve a good fit for each PXRD pattern.

7.2.2 Solid-state NMR

High-resolution solid-state ¹³C NMR data were recorded for a sample of ND_{old} heated at 343 K for 9 min to obtain a sample containing a maximal amount of the intermediate (same sample for which PXRD pattern was recorded for structure determination). The sample was packed inside a standard solid-state NMR rotor. The data were recorded using a Bruker AVANCE III spectrometer at the UK 850 MHz High-Field Solid-State NMR Facility. The ¹³C NMR spectra was recorded using magic-angle spinning (MAS) at 12 kHz at ambient temperature using ¹H→¹³C cross-polarization (CP) with a contact time of 4 ms, a recycle delay of 3 s and 1024 scans.

7.3 Results and Discussion

7.3.1 Structure Determination

The PXRD pattern used for structure determination consists of peaks from the intermediate phase formed in the AC to urea transformation, peaks from the starting material AC and a solitary peak corresponding to urea at $\sim 2\theta = 11^\circ$ (the dominant peak in the powder XRD pattern of urea).

As the intermediate phase is formed during the reaction, a pure sample of this phase is impossible to obtain. This made the indexing of the powder XRD pattern more difficult. Although, the AC crystal structure peaks can be excluded, many of the AC peaks appear to overlap with peaks due to the intermediate phase (Figure 7.3). However, through trial and error, a set of peaks were eventually selected that allowed successful indexing of the intermediate phase.

Certain peaks ($2\theta = 12.3\text{-}13.6^\circ$ and $17.6\text{-}19.4^\circ$) possibly corresponding to AC do not show predicted peak intensities from the AC crystal structure. This could be due to either an overlap with intermediate phase, which is adding intensity to certain peaks, or the existence of preferred orientation in the sample. Preferred orientation occurs when the powder sample does not have a random distribution of crystal orientations, leading to the relative peak intensities in the powder XRD data differing from the intrinsic relative intensities characteristic of the crystal structure; clearly, simulation of powder XRD data for a known crystal structure (generally) assumes that there is no preferred orientation.

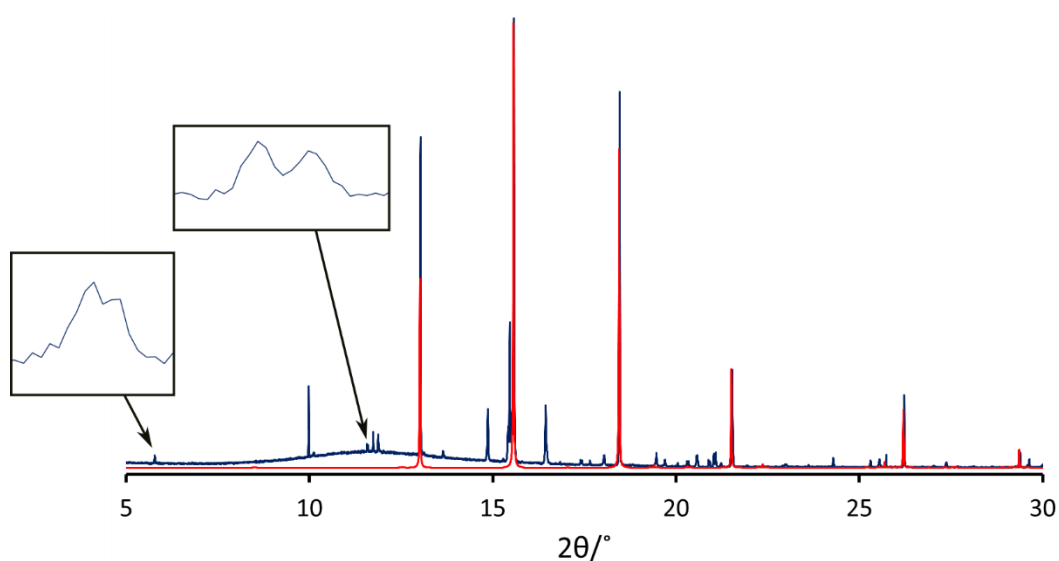


Figure 7.3 PXRD pattern recorded on I11 at DLS for mixture of intermediate phase, AC and urea (blue) used for structure determination (recorded at ambient temperature). Simulated PXRD pattern from the crystal structure of AC (red) determined at ambient temperature.³⁴ Zoomed regions of peaks at $2\theta = 5.779^\circ$ and 11.573° are shown to illustrate the double peaks observed at the (020) and (040) reflection.

The peaks assigned to the intermediate phase were indexed using the LZON¹³⁹ algorithm in the CRYSFIRE³⁶ indexing suite. From the list of potential unit cells the most physically sensible starting point was considered to be a monoclinic cell ($a = 9.356 \text{ \AA}$, $b = 3.707 \text{ \AA}$, $c = 16.382 \text{ \AA}$, $\beta = 90.81^\circ$; $V = 568 \text{ \AA}^3$). However, as the β angle of this unit cell is close to 90° , a Le Bail fit was attempted for an orthorhombic cell with $P222$ symmetry. The orthorhombic cell was eventually determined to be incorrect, as it gives one peak at (020) and (040) reflection, whereas two peaks are observed at each of these positions in the experimental data (Figure 7.3).

As the intermediate crystalline phase is produced on the pathway from AC to urea, the intermediate structure could be made up of just urea, just AC, a mixture of urea and AC or an intermediate chemical entity. To determine the chemical composition high-resolution solid-state ^{13}C NMR spectroscopy was used.

Figure 7.4 shows the high-resolution solid-state ^{13}C NMR spectrum recorded at 293 K (MAS frequency, 12 kHz). Pure AC and urea each give one isotropic peak in the solid-state ^{13}C NMR spectrum (excluding spinning side bands), at 187.5 and 162.3 ppm respectively. Using this information, we can identify two peaks (183.3 and 163 ppm) that potentially correspond to the intermediate phase. Therefore, the peak at 183.3 ppm was assigned as cyanate anions in the intermediate phase and 163 ppm to urea in the intermediate phase. The urea peak at 163 ppm assigned to the intermediate is very close to the value expected for pure urea (162.3 ppm). Typically, pure urea is not observed in solid-state NMR due to its long relaxation time, hence, the decision to assign the peak to the intermediate phase. All, other observed peaks were identified as spinning side bands.

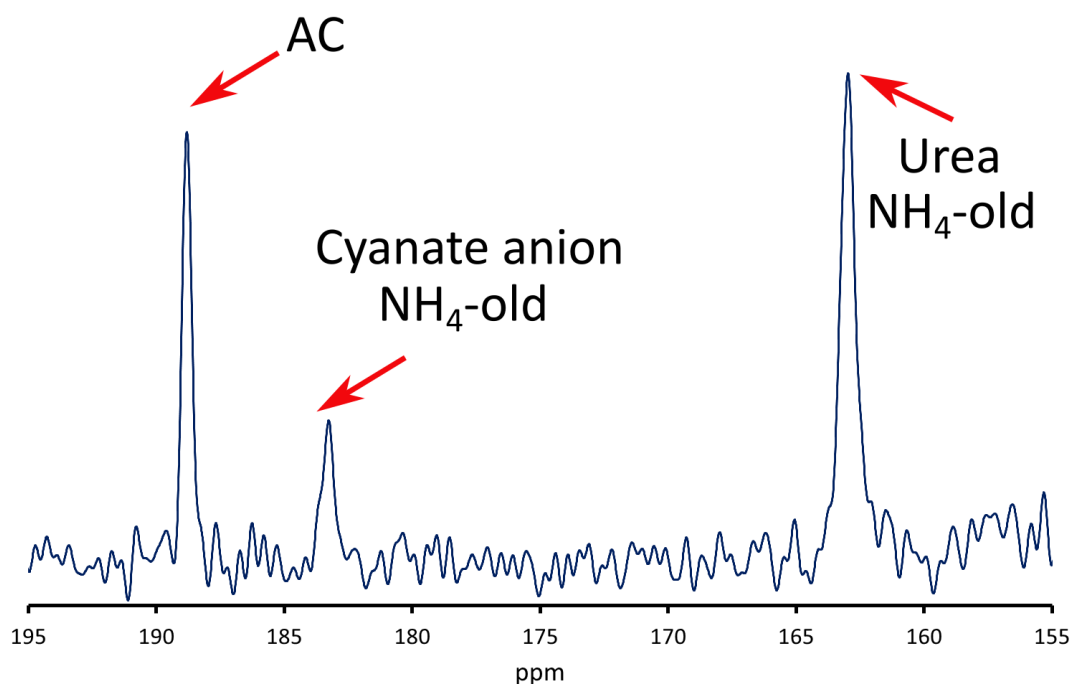


Figure 7.4 High-resolution solid-state ^{13}C NMR data recorded for the intermediate phase at 293 K. The isotropic peaks are labelled according to their corresponding carbon environments.

Therefore, the chemical entities present in the intermediate phase are identified as cyanate anions, ammonium cations and urea molecules, although the solid-state ^{13}C NMR does not allow quantitative assignment of the relative proportions of ammonium cyanate and urea in the intermediate phase. However, we make the assumption at this stage that the urea and ammonium cyanate are present in 1:1 ratio in the intermediate phase. Based on this assumption, the potential space group can be checked using the volume of the prospective unit cell and an expected density.

- Unit cell volume (V) = $5.68 \times 10^{-22} \text{ cm}^3$
- Urea (M_r) = 60.06 g/mol
- Ammonium (M_r) = 18.04 g/mol
- Cyanate (M_r) = 42.02 g/mol
- Avogadro's constant (N_A) = $6.022 \times 10^{23} \text{ mol}^{-1}$

The mass of the formula unit (AC, urea) is calculated from the molecular masses (M_r) and Avogadro's number (N_A).

$$\Sigma M_r / N_A = \text{Mass of formula unit} = M \quad (7.1)$$

$$(60.06 + 18.04 + 42.02) \div (6.022 \times 10^{23}) = 1.995 \times 10^{-22} \text{ g}$$

If there are N formula units in the unit cell, the density of the material is given by the mass of the unit cell contents ($N \times M$) divided by the volume (V) of the unit cell:

$$(N \times M) / V = \text{Density} \quad (7.2)$$

$$\frac{(4 \times (1.995 \times 10^{-22}))}{(5.68 \times 10^{-22})} = 1.408 \text{ g/cm}^3$$

Four formula units in the unit cell gives a final density of 1.408 g/cm^3 . This is sufficiently similar to the density of urea (1.32 g/cm^3) to deduce the most reasonable value is $N = 4$. The density analysis allows us to determine the number of formula units in the unit cell, using this and taking into account systematic absences (see Page 49) the $I2$ space group was selected.

To refine the unit cell and fit the profile of the powder pattern, the Le Bail procedure³⁷ was used as implemented in GSAS using the graphical user interface EXPGUI¹⁴⁰ ($I2$, $R_{wp} = 5.07\%$, $R_p = 3.70\%$, Figure 7.5). In the powder XRD pattern, the majority of the peaks are due to the intermediate phase and AC; therefore, the unit cells for both the intermediate phase and AC were included. As the structure for AC is already known, Rietveld refinement⁴² was performed on the AC phase rather than Le Bail. The peak due to urea is present between $2\theta = 11.828^\circ$ and 11.924° was removed from the powder XRD pattern for the Le Bail fitting and the intensity was excluded between these 2θ values. This is the only urea peak observed in the diffraction pattern.

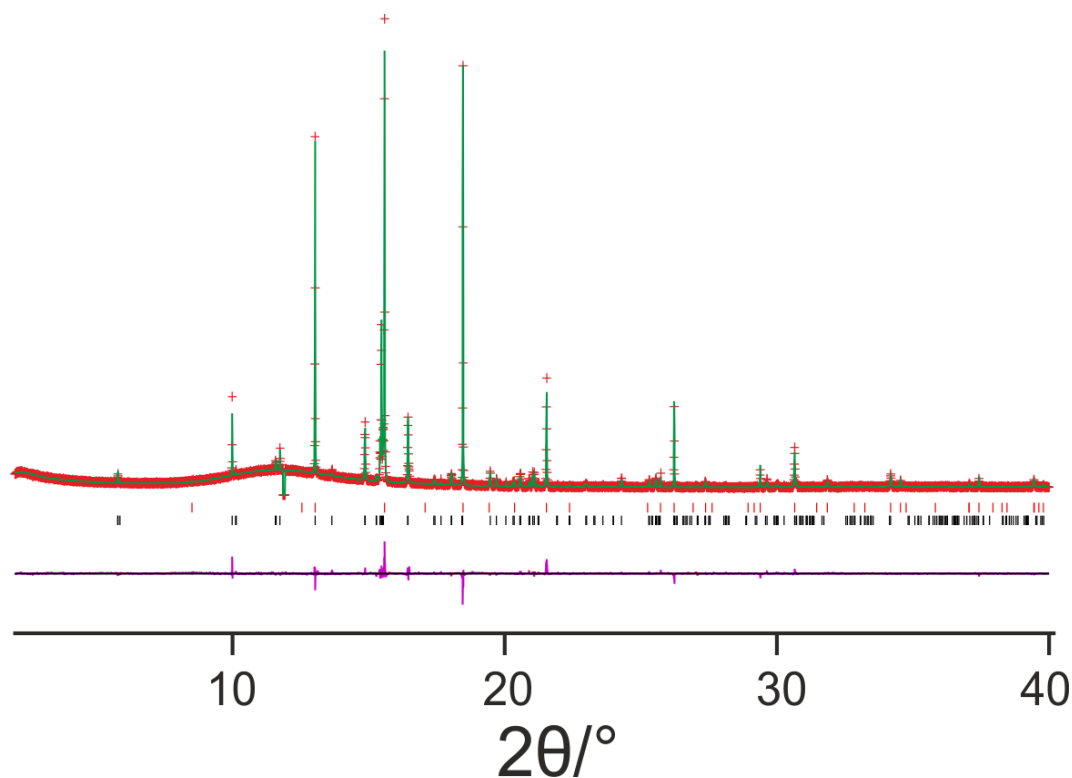


Figure 7.5 Le Bail profile fit of the powder XRD pattern containing the intermediate phase and AC, using the *I2* space group. Shown on the plot are: experimental data (red crosses), calculated data (green line), background intensity (black line), peak positions (red = AC, black = intermediate phase), difference between experimental data and fit (magenta line). A peak corresponding to urea has been excluded between $2\theta = 11.828^\circ$ and 11.924° .

In spite of the fact that the Le Bail profile fit had to cope with multiple phases as well as unusual line shapes (Le Bail struggles to fit powder X-ray data recorded at the synchrotron rather than lab based diffractometer data due to the different peak shapes characteristic to each X-ray source), a good quality fit was achieved. The unit cell and profile parameters for the intermediate phase refined for the *I2* space group using Le Bail profile fitting were used in subsequent structure solution calculations. Structure solution was carried out from the PXRD data using a direct-space genetic algorithm³⁸⁻⁴⁰ in the program EAGER. The number of molecules in the formula unit has already been determined from solid-state NMR, and checked using the calculated volume of the unit cell and expected density of urea.

As four formula units are expected in the unit cell accounting for density and the *I2* space group similarly has four asymmetric units in the unit cell, the structure solution calculations were carried out using the *I2* space group with one ammonium cation, one cyanate anion and one urea molecule in the asymmetric unit. In EAGER, each fragment in the asymmetric unit was defined by 6 structural variables: 3 positional variables and 3 orientational variables. The cyanate anion was additionally restrained to prevent it from rotating about the long axis, as this would not change in the crystal structure.

In total, 40 independent structure solution calculations were carried out on Hawk, the SCW supercomputer. In each calculation, the population comprised 100 trial structures and the calculation was run for 100 generations, with 10 mating operations and 50 mutation operations carried out per generation. GSAS used in the Le Bail fitting has the capability to fit more than one phase, which is useful when dealing with multi-phase samples. EAGER does not have this capability, therefore it was decided that the peaks in the powder pattern corresponding to AC would be removed from the experimental powder XRD data for the EAGER calculation (for peak positions see Appendix I).

However, as seen in Figure 7.3, the relative intensity between the powder pattern produced from the simulated structure for AC and the experimentally recorded powder pattern (comprising the intermediate, AC and urea) suggest that some peaks of the intermediate phase overlap with peaks due to AC. This is most evident for the peak between $2\theta = 12.99^\circ$ and 13.07° . It was determined that this peak has intensity contributions from both phases. Rather than removing this peak, it was scaled to remove the contribution to the intensity from AC. To assess the degree of scaling needed, the simulated powder pattern was scaled so that peaks due to AC had the same relative intensities in both diffraction patterns. When overlaid, we determined that, for the peak between $2\theta = 12.99^\circ$ and 13.07° , the intermediate phase contributes 40% of the total peak intensity. The modified PXRD pattern used as input to EAGER is shown in Figure 7.6.

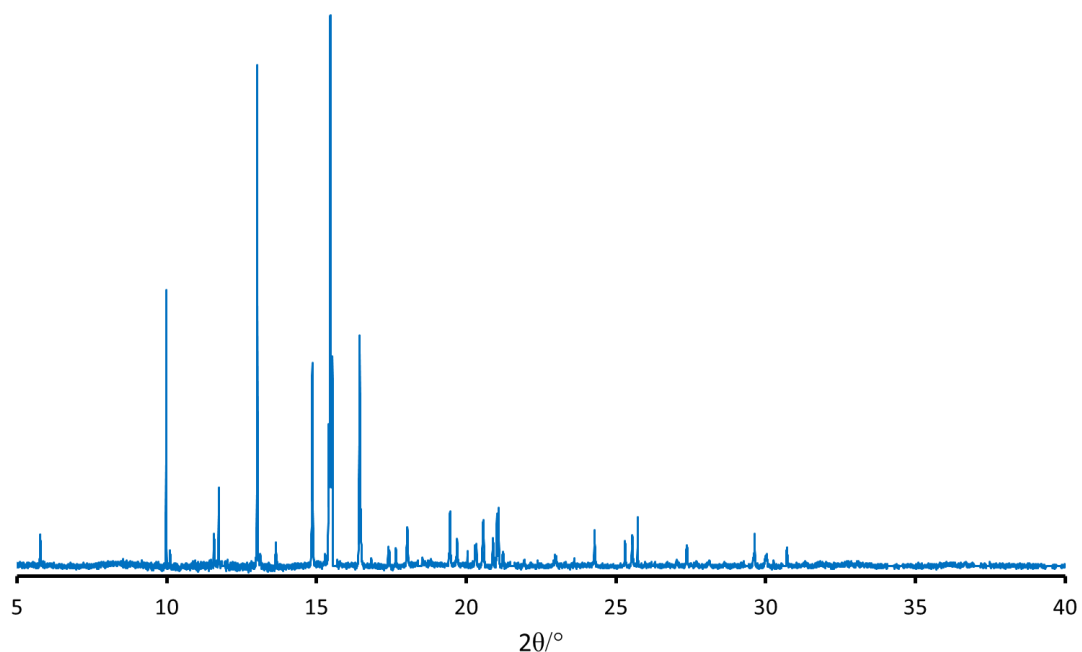


Figure 7.6 The modified PXRD pattern used in structure solution from EAGER, with the contribution from AC removed.

The EAGER calculation that produced the structure with the lowest R_{wp} (best fit between experimental and calculated powder XRD data), was chosen as the initial structure for Rietveld refinement. The Rietveld refinement, like the Le Bail fit, was performed in GSAS. Standard restraints were applied to bond lengths, bond angles and planar restraints were applied to the urea molecule. A common isotropic displacement parameter was refined for all non-hydrogen atoms; for the hydrogens, this parameter was set to 1.2 times the refined isotropic displacement parameter for the non-hydrogen atoms. To optimize the hydrogen bonding geometries, intermolecular distance restraints were used. Rietveld refinement gave a good fit from the powder XRD pattern ($R_{wp} = 5.15\%$, $R_p = 3.76\%$).

Periodic DFT calculations for geometry optimization were carried out on the structure obtained in the Rietveld refinement using CASTEP¹⁴¹. Calculations were carried out with a basis set endpoint energy of 700 eV, fixed unit cell, preserved space group symmetry, ultrasoft pseudopotentials, PBE functional, TS correction scheme and periodic boundary conditions.

The structure produced from CASTEP led to distortion of the urea molecule, with the hydrogens moving out of the plane of the rest of the molecule. A further Rietveld refinement was carried out using the structure from CASTEP but with the hydrogen atoms of the urea molecule moved back into the molecular plane. Additional restraints were added for H-N-H bond angles in the ammonium cation, bond restraint between the nitrogen and the oxygen of the cyanate anion (N \cdots O) and restraints for hydrogen bonding.

The structure was refined as stated above until minima for the fit for as many possible parameters had been achieved. Attempting to refine the ammonium cation with individual atom positions made the fit unstable. Therefore, the ammonium cation was redefined as a rigid body in GSAS, with the ammonium cation translated and rotated as one unit. This of course means that the intermolecular restraints for ammonium are no longer necessary.

Redefining the ammonium cation as a rigid body proved beneficial, allowing the refinement to proceed successfully. In this case, the ammonium rigid body was allowed to translate but not rotate, as the rotation interfered with the hydrogen bond restraints. The final Rietveld refinement gave a good fit to the powder XRD pattern ($R_{wp} = 5.16\%$, $R_p = 3.80\%$), with the following refined parameters: $a = 9.48705(10)$ Å, $b = 3.73385(4)$ Å, $c = 16.14188(15)$ Å, $\beta = 90.1433(7)^\circ$; $V = 571.795(11)$ Å³ (2θ range, 2° - 40° ; 9501 profile points; 72 refined variables (Figure 7.7).

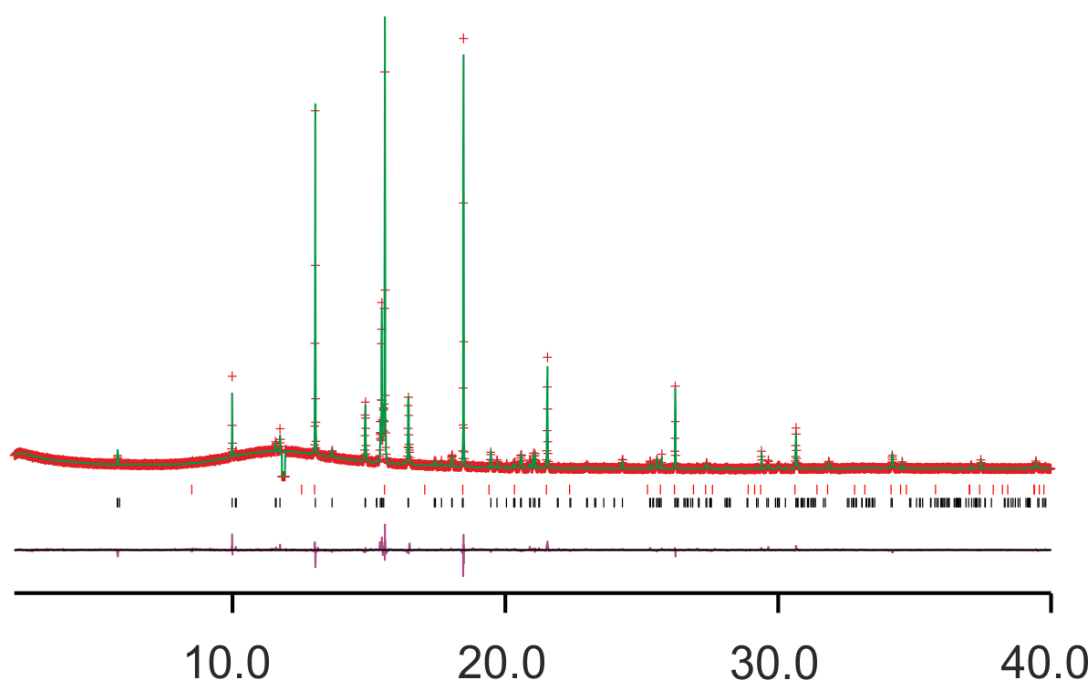


Figure 7.7 Final Rietveld refinement of the intermediate phase, showing: experimental data (red crosses), calculated data (green line), background intensity (black line), peak positions (red = AC, black = intermediate phase), difference between experimental data and fit (magenta line).

Problems associated with this PXRD pattern such as multiple phases, overlapping peaks and the abnormal line shape associated with synchrotron data clearly introduce significant challenges in the Rietveld refinement. The fit observed between the experimental and calculated PXRD data is a good indication of a correct crystal structure.

The crystal structure for the intermediate phase is shown in Figure 7.8, viewed along the three unit cell axes. The asymmetric unit comprises of a single molecule of urea, an ammonium cation and a cyanate anion. The urea molecules are almost planar (lying parallel to the *ac*-plane) while the cyanate anions are aligned close to the *a*-axis although tilted out of the *ac*-plane. Extensive hydrogen bonding is observed in the crystal structure, the ammonium cations form four hydrogen bonds, two to the oxygen on the carbonyl on urea and two to the nitrogen on cyanate anions.

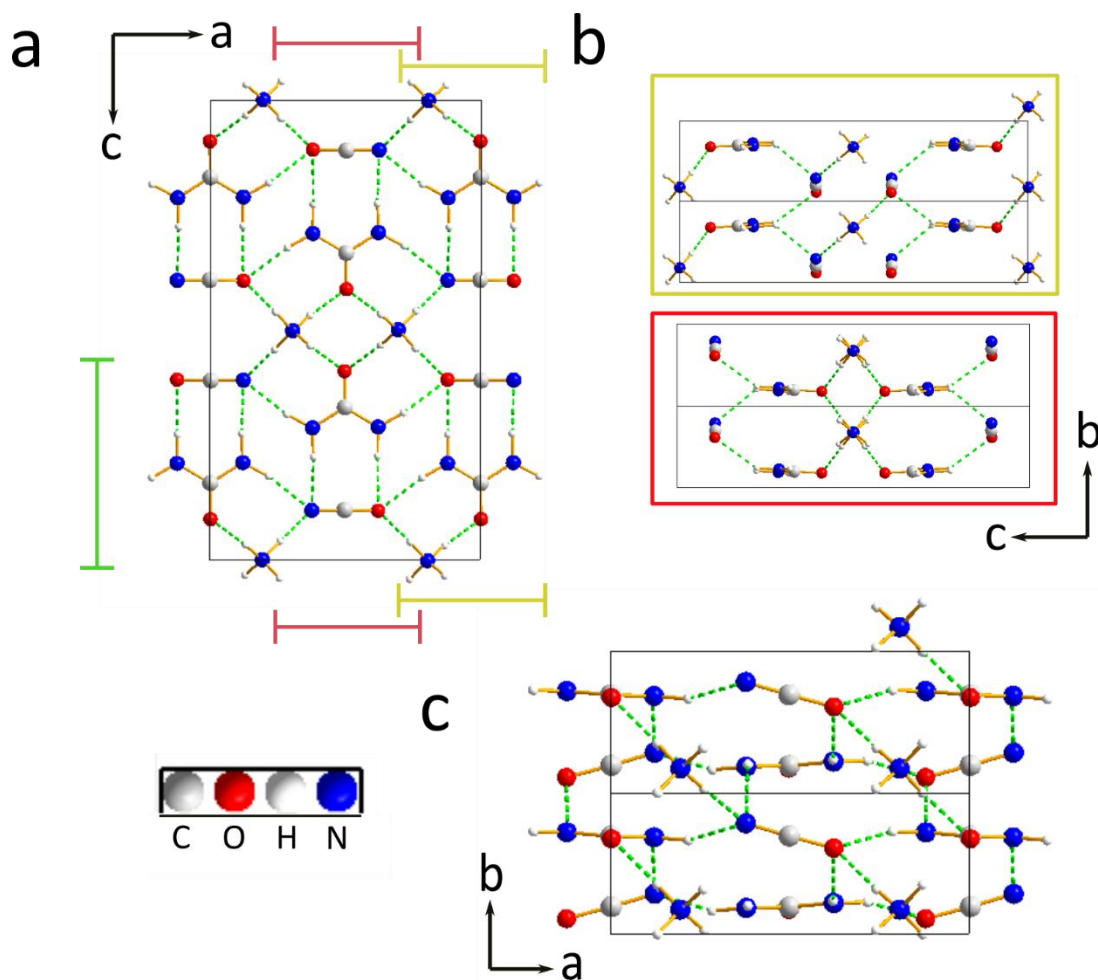


Figure 7.8 Crystal structure of the intermediate phase (the unit cell is doubled along the b-axis) viewed along the (a) b-axis, (b) a-axis and (c) c-axis. The hydrogen bonds are shown as green dotted lines. Two images are shown for clarity in (b), which correspond to different regions of the unit cell along the a-axis. Only half of the unit cell along the c-axis is shown in (c).

7.3.2 Proposed Mechanism for the Transformation from AC to Urea

The proposed mechanism for transformation of AC to urea incorporating the intermediate phase can now be discussed. The unit cell information for the three crystal structures involved is shown in Table 7.2.

		AC	Intermediate	Urea
Crystal System		Tetragonal	Monoclinic	Tetragonal
Space Group		$P4/nmm$	$I2$	$P\bar{4}2_1m$
Cell Parameters	a (Å)	5.1525	9.48705	5.645
	b (Å)	5.1525	3.73385	5.645
	c (Å)	5.5712	16.14188	4.704
Cell Volume (Å ³)		147.91	571.795	149.90
Temperature (K)		288	293	283-303

Table 7.2 Crystal structure information for AC, urea and the intermediate phase.^{34,142}

The crystal structure information for AC and urea is very similar, while the intermediate phase has very different values for its unit cell. Notably the cell volume for the intermediate phase is roughly twice the size of either the AC or urea unit cells.

The crystal structure of AC has two formula units NH_4OCN in the unit cell. In the AC crystal structure, the linear cyanate anions are aligned parallel to the c -axis. The two cyanate anions present within the unit cell have opposite orientations along the c -axis. The ammonium cation is tetrahedral, sitting on a site of $\bar{4}$ symmetry, while the cyanate anion is linear and lies along a 4-fold axis. Each ammonium cation is surrounded by eight cyanate anions forming a distorted cube with oxygen atoms and nitrogen atoms occupying alternate corners of the “cube”. The ammonium cation forms four $\text{N-H}\cdots\text{N}$ hydrogen bonds to the nitrogen of the cyanate anions at four corners of the distorted cube (Figure 7.9).

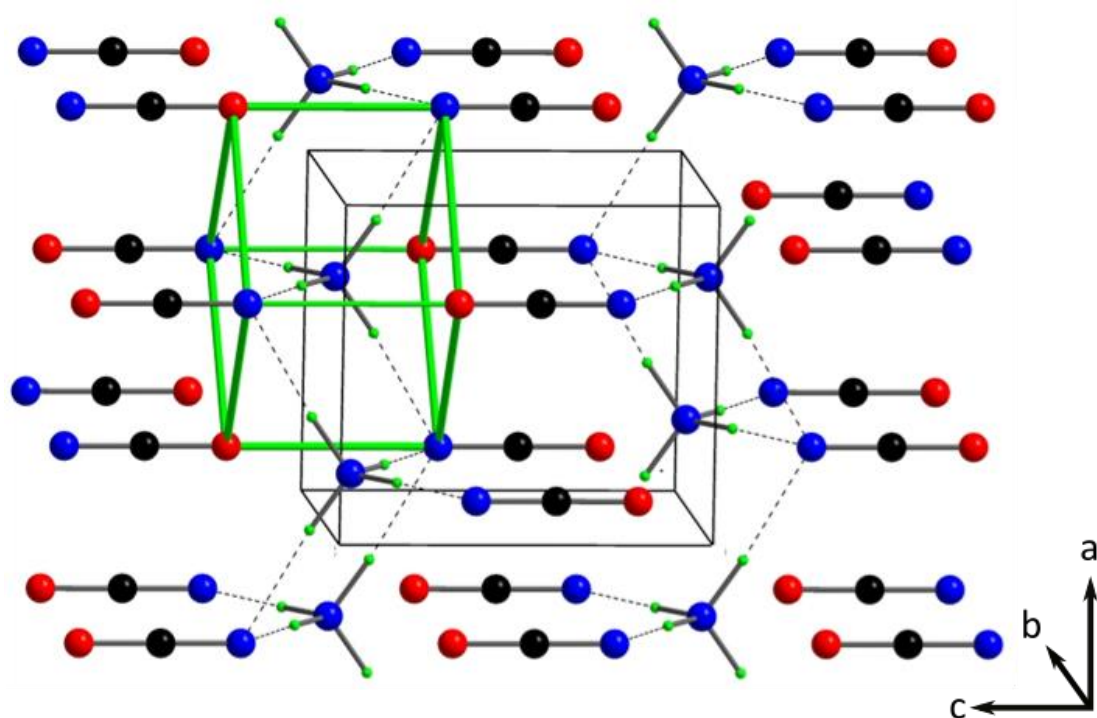


Figure 7.9 Crystal structure of AC showing the distorted cube outlined in green. The hydrogen bonding between the ammonium cation and nitrogen atoms of the cyanate anions is shown (grey dashed lines).

To identify a potential mechanism by which AC transforms into the intermediate phase, we identify the “unreacted” and “reacted” regions in the crystal structure of the intermediate phase. Figure 7.10 shows the parts of the crystal structure of the intermediate phase containing ammonium cyanate (the “unreacted” regions) and the parts containing urea (the “reacted” regions), together with the corresponding regions in the crystal structure of AC (before reaction).

The unreacted regions are represented by cylindrical columns along the [010] direction in the intermediate phase and along the [110] direction in AC. The reacted regions, where urea is produced, comprise “corrugated” layers again forming columns along the [010] and [110] axes in the intermediate phase and AC respectively. Distances between the carbons of cyanate anions in each crystal structure are shown in Figure 7.10. The distances are similar, although the intermediate phase appears to be condensed compared to the AC structure.

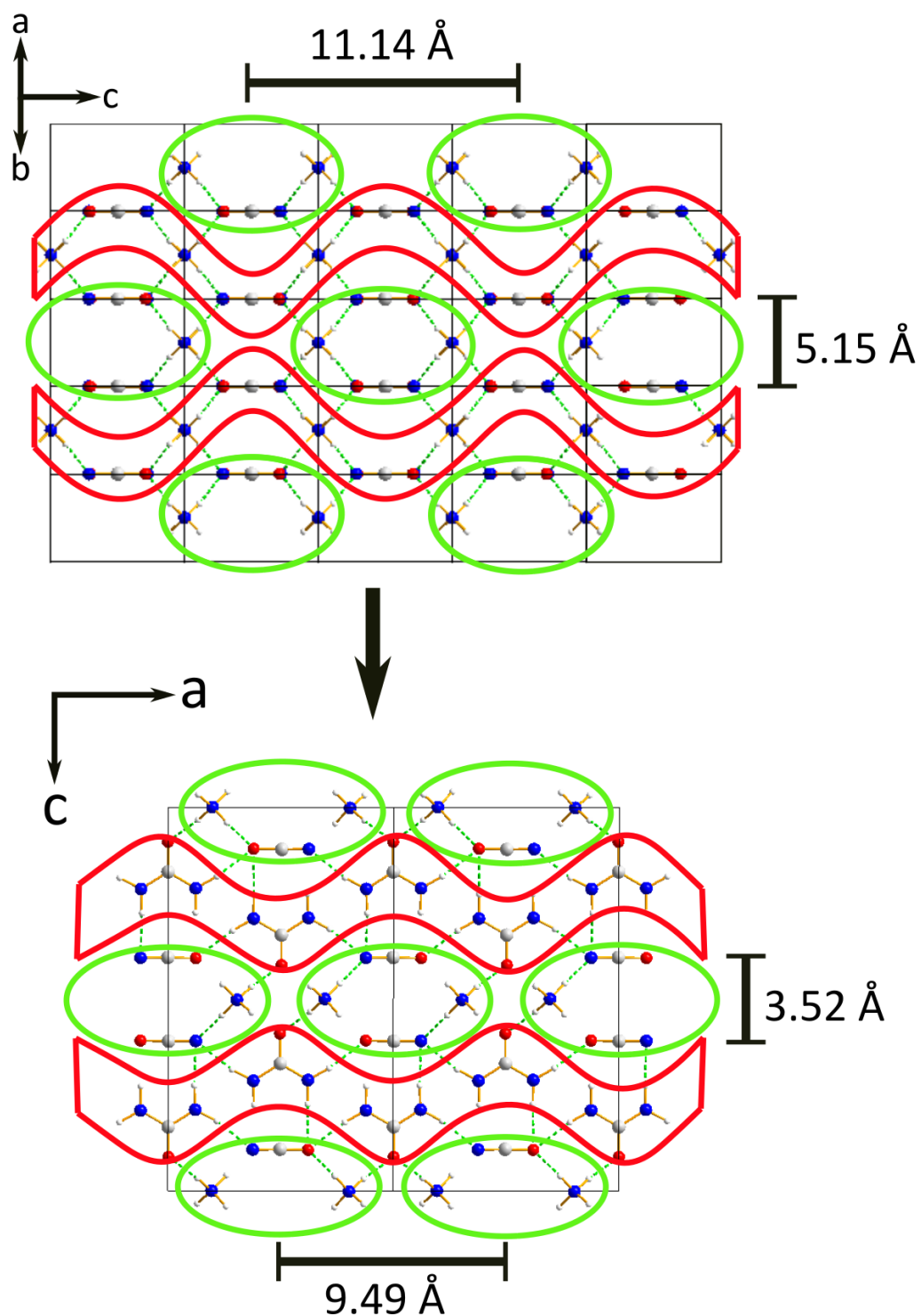


Figure 7.10 Crystal structures of AC and the intermediate phase viewed along the [110] and [010] axes respectively. Corrugated layers in red are selected in both structures, which indicate the regions in which reaction occurs in AC to form the urea molecules in the intermediate phase. Regions highlighted in green remain unreacted.

In Figure 7.11 (a), the transformation of AC to the intermediate phase is again shown but viewed along the [001] and [100] axes respectively. Figure 7.11 (b) shows a single corrugated layer (viewed perpendicular to the layer) in the crystal structure of AC, and a proposed mechanism for the reaction. Most probably, the solid-state transformation occurs via a proton jump from the ammonium cation to the cyanate anion along an N-H...N hydrogen bond. Simultaneously, the carbon atom experiences a nucleophilic attack by the NH₃. Thus, the transformation would proceed diagonally across the “corrugated” layer.

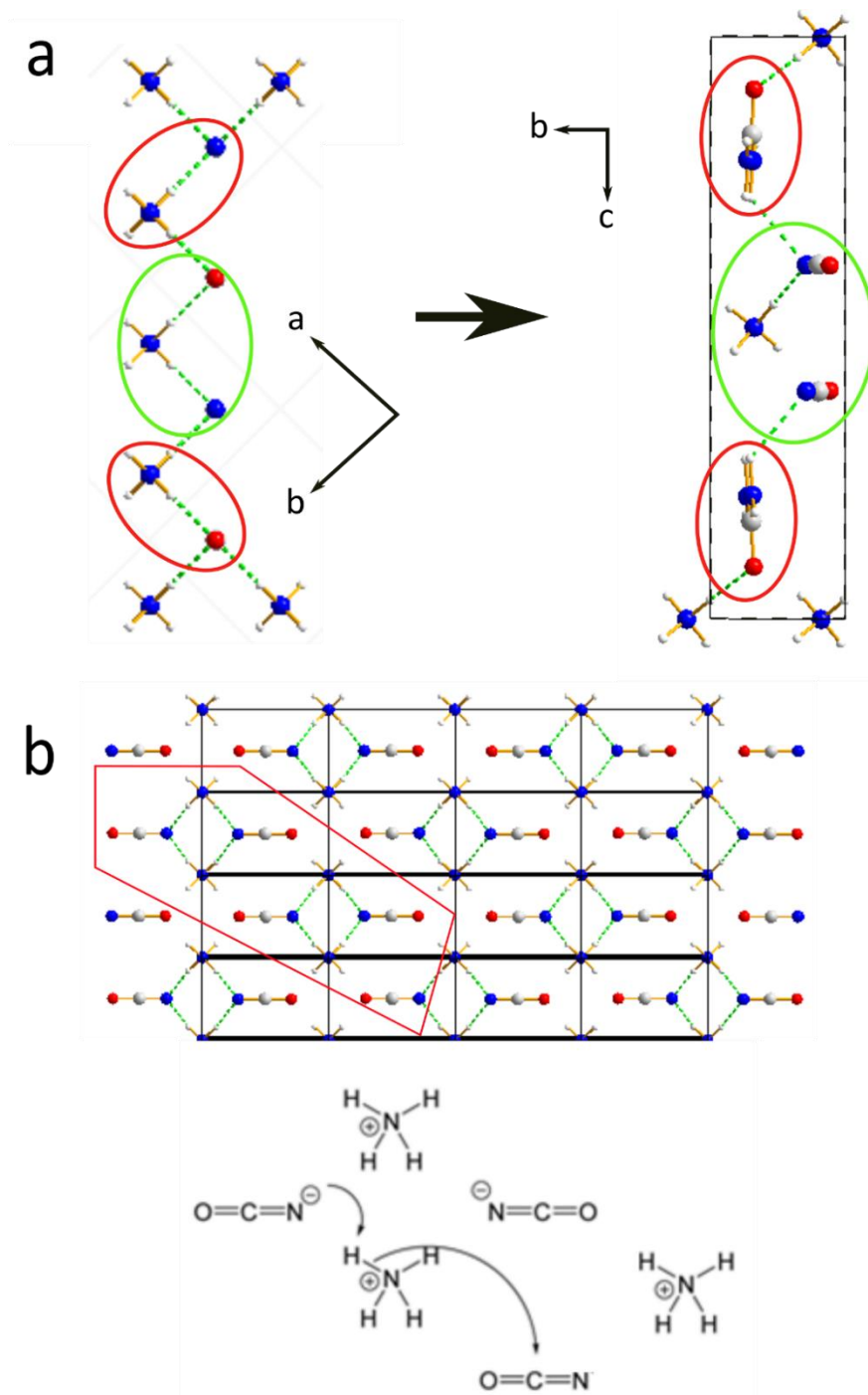


Figure 7.11 (a) Reaction of AC to the intermediate phase viewed along the [001] and [100] axes respectively. The intermediate phase contains only part of the unit cell along the [100] direction for clarity. Regions highlighted in red undergo reaction from ammonium cyanate to urea molecules. Regions highlighted in green remain unreacted. (b) The corrugated layer of AC highlighted in red in Figure 7.10 (a) viewed perpendicular to the layer. The region selected in red is shown in (c) with a proposed reaction mechanism.

The second stage of the reaction now progresses, transforming the intermediate phase into the pure crystalline phase of urea. The urea crystal structure consists solely of urea molecules in two orientations. Each urea molecule is planar, with the C=O bond lying on a two-fold rotation axis and with the molecule in a mirror plane. The carbonyl bond in the urea molecule, like the C=O bond in AC, lies along the [001] axis. The planes of the urea molecules lie in two different planes, as seen in Figure 7.12 (c). The molecular planes are perpendicular to each other and lie in the (110) and the ($1\bar{1}0$) planes. The C=O bond of the urea molecules in one plane are aligned along the positive *c*-axis, while the C=O bond of the urea molecules in the other plane is aligned along the negative *c*-axis.

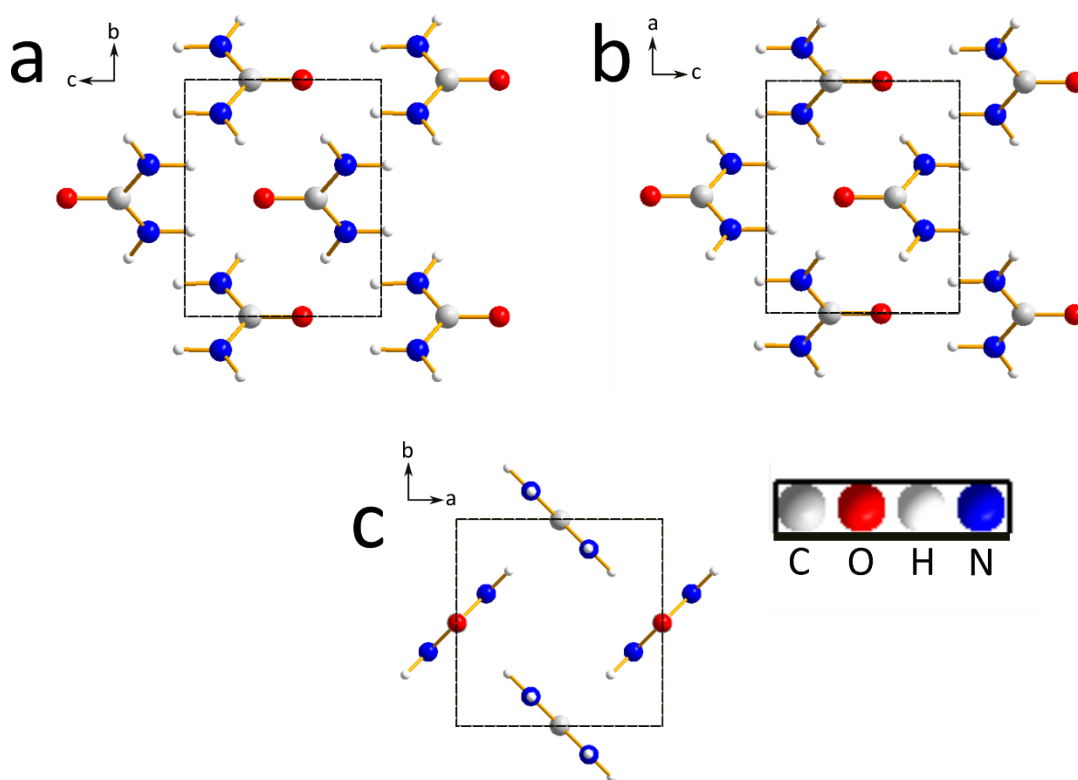


Figure 7.12 Crystal structure of urea viewed along the (a) *a*-axis, (b) *b*-axis, and (c) *c*-axis.¹⁴²

In the unreacted regions of the intermediate phase seen in Figure 7.10 (a), the ammonium cations and cyanate anions are located in “cylindrical” columns, which run into the page. The unreacted cylindrical columns are viewed along the [001] axis in Figure 7.13 (i.e. perpendicular to the view in Figure 7.10 (a)).

Thus, we can see two hydrogen bonding chains, where a proton from the ammonium cation can transfer to a cyanate anion, the carbon atom of which is simultaneously attacked (nucleophilic attack) by the nitrogen atom of a deprotonating ammonium cation in the same chain.

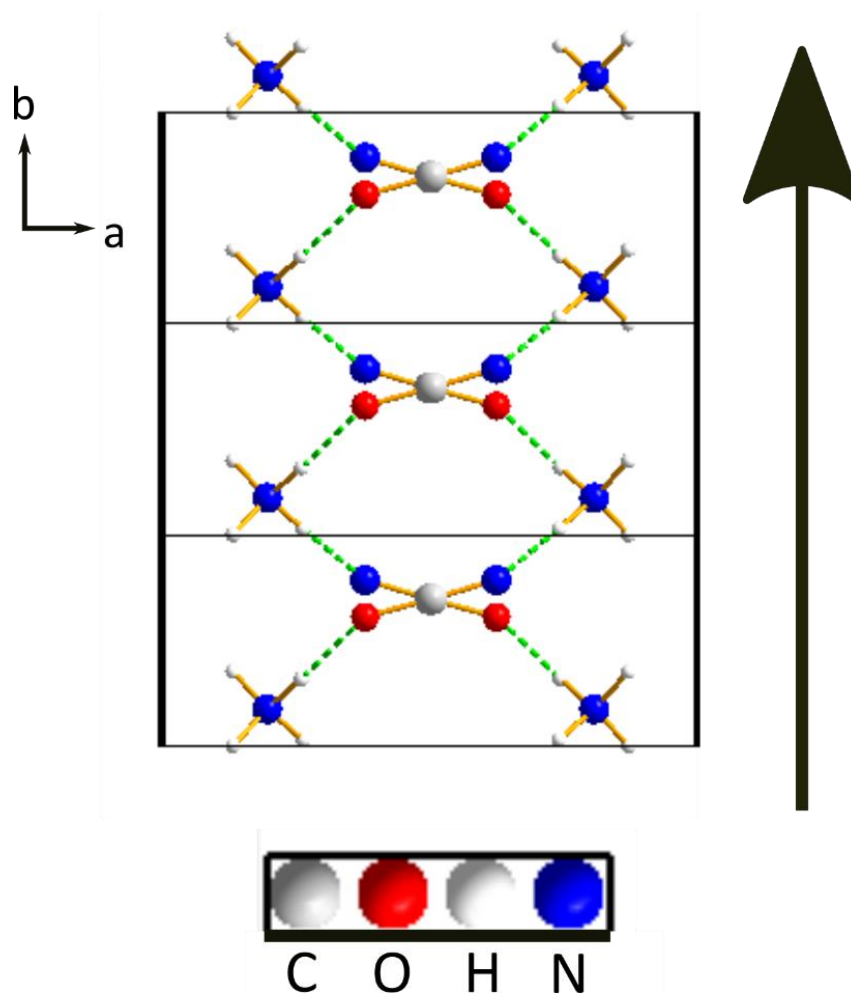


Figure 7.13 Unreacted region of the intermediate phase viewed along the $[001]$ axis. The reaction occurs along the two hydrogen-bonded chains (green).

The resemblance between the crystal structure of the intermediate phase and the urea crystal structure is not obvious at first glance. Urea has molecules arranged with opposite parity and in perpendicular planes. In contrast, the urea molecules in the intermediate phase lie in parallel planes, and with pairs of urea molecules that have their carbonyl bonds oriented towards each other. It is clear that significant structural reorganization occurs upon reaction in the intermediate phase, resulting in the crystal structure of urea as the final product.

7.3.3 Kinetics for the Transformation from AC to Urea

The rate of a chemical reaction is determined by the rate at which reactants are consumed or, equivalently, the rate at which a product is formed. If the reaction has multiple steps, then the kinetics of the reaction can become quite complex. We first look at the relative amounts of the crystalline phase of AC, the intermediate phase and crystalline urea present as a function of time during the reaction, at each temperature studied. These fits were performed using an earlier form of the intermediate crystal structure ($P2_1/n$, $a = 9.488 \text{ \AA}$, $b = 3.734 \text{ \AA}$, $c = 16.143 \text{ \AA}$, $\beta = 90.143^\circ$; $V = 571.87 \text{ \AA}^3$) so the results discussed in this section are preliminary and work is ongoing.

The time for complete transformation from AC to urea (encompassing the formation of the intermediate phase) was determined by recording PXRD patterns on I11 at DLS for a variety of temperatures (for full experimental details see Section 7.2.1). Three samples were studied, an old deuterated sample (ND_{old}), a new deuterated sample (ND_{new}) and a new undeuterated sample (NH_{new}).

Representative plots showing the relative amounts of each phase present as a function of time are shown in (Figure 7.14). It is clear that only the ND_{old} sample shows a large amount of the intermediate phase during the reaction. The plots of amount vs. time in Figure 7.14 for samples NH_{new} and ND_{new} indicate an induction time before any significant amount of reaction is evident. The induction time is the time for nucleation to occur. The ND_{old} sample had already nucleated as it already contains a significant amount of the intermediate phase.

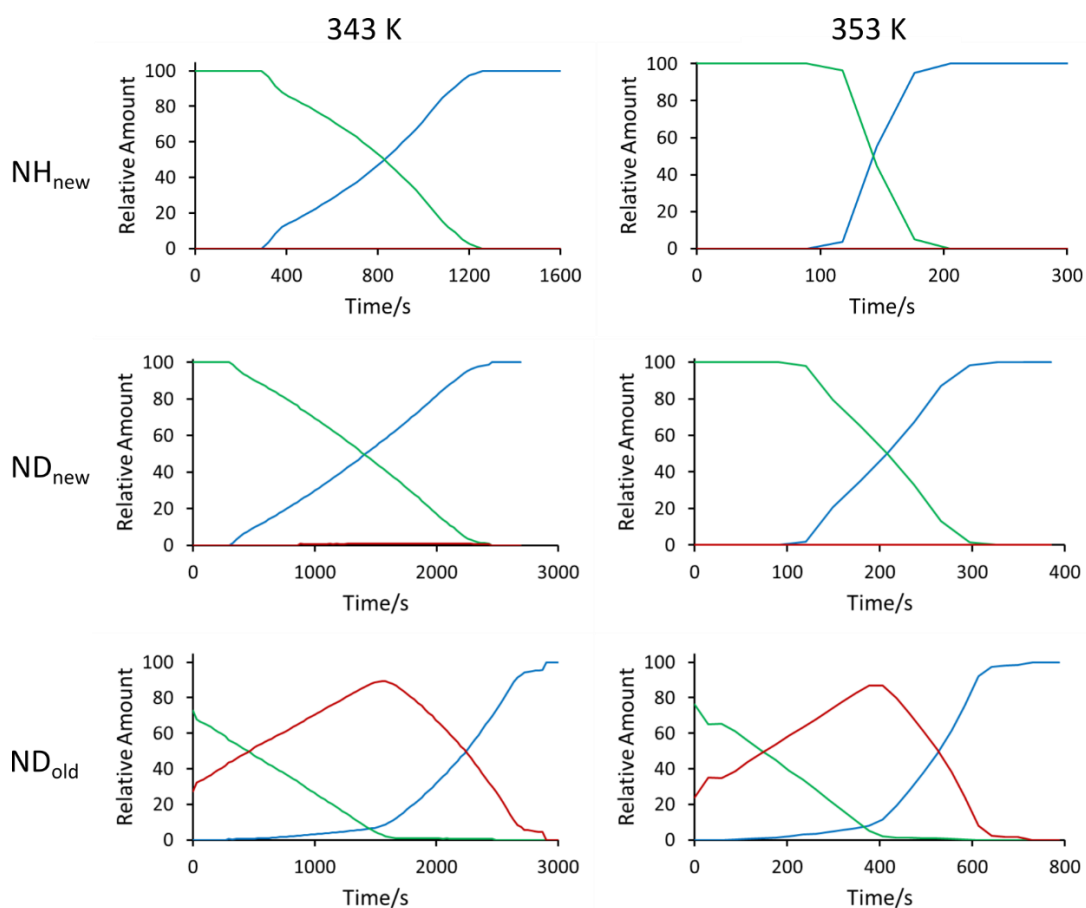


Figure 7.14 Relative amounts of crystalline AC (green), crystalline urea (blue) and intermediate phase (red) as a function of time at 343 K and 353 K, for samples NH_{new} , ND_{new} and ND_{old} .

As the plots do not appear to show any significant change in the amounts of product and reactant during the induction time, the rates were only calculated for the period of the reaction after the induction time Figure 7.14. The rates for each of the reactions are shown in Table 7.3.

The kinetics of sample ND_{old} are more difficult to determine, due to the presence of the intermediate in the initial sample. The initial sample was not pure and instead consisted of crystalline AC and the intermediate phase. The formation of the intermediate phase is clearly seen in ND_{old} reaching close to a 100% conversion, before transforming to crystalline urea. The reaction of ND_{old} (AC, urea and intermediate) can be studied in terms of two distinct stages: reaction from AC to intermediate phase (superscript f) and reaction from intermediate phase to urea (superscript l).

For NH_{new} and ND_{new} samples, the formation of the intermediate phase is much less obvious. There is some evidence of the intermediate phase in the reaction of ND_{new} , although at much smaller amounts, ca. 1% (Figure 7.15). Therefore, for the purpose of determination of the rates of reaction, the formation of the intermediate was ignored for ND_{new} . The presence of the intermediate phase was not observed for NH_{new} .

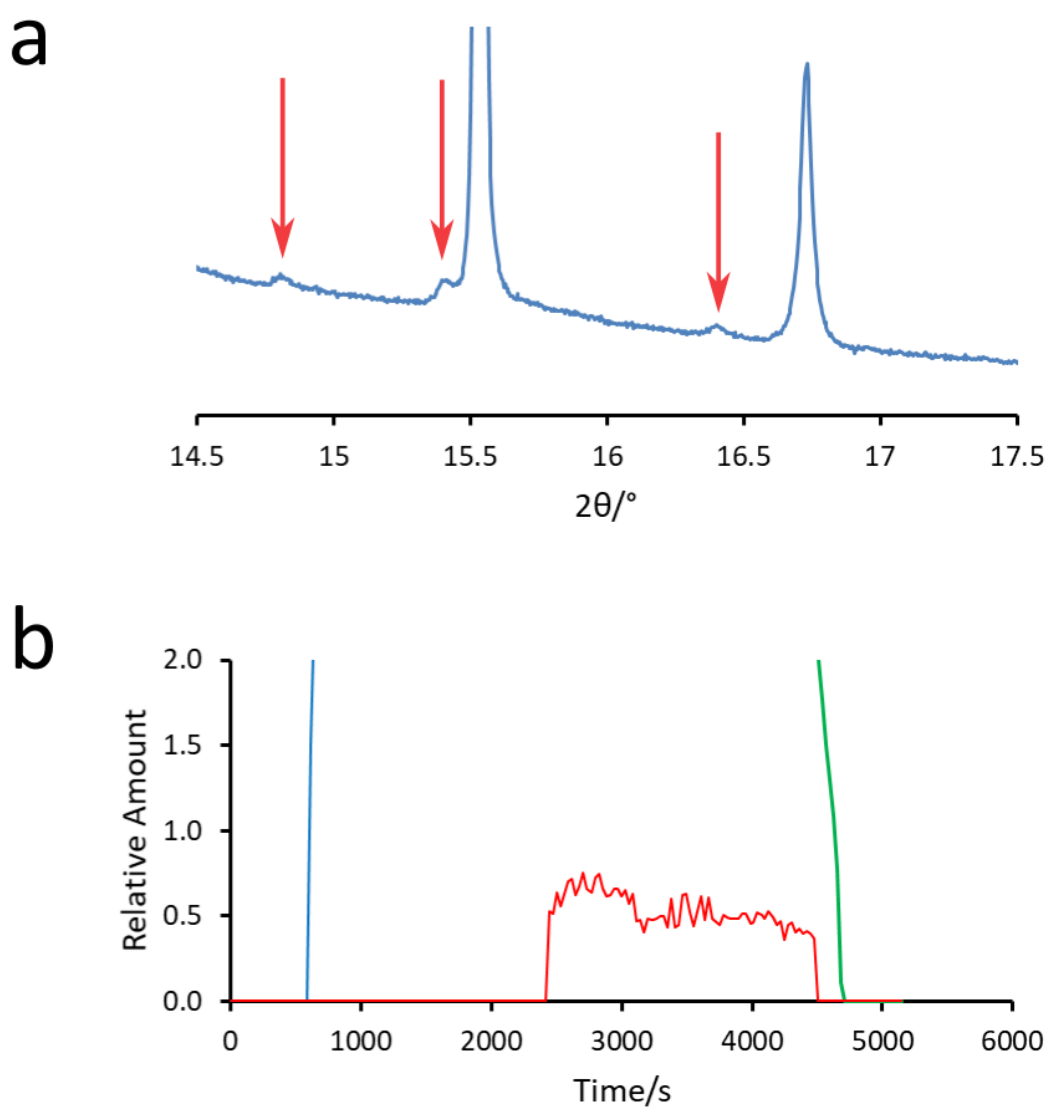


Figure 7.15 (a) PXRD pattern recorded at 614 s in the reaction of AC to urea at 348 K. Red arrows highlight the peaks corresponding to the intermediate phase. (b) Zoomed region of the plot showing relative amounts of different phases as a function of time for ND_{new} at 348 K. The intermediate phase is detected between ~2500-4500 s.

		Rate/s ⁻¹				
		338 K	343 K	348 K	353 K	358 K
NH_{new}	AC	0.0463	0.1034	0.2155	0.8621	
ND_{new}	AC	0.0242	0.0464	0.1490	0.4237	
ND_{old}	AC^f		0.0427	0.1009	0.1817	0.5382
	Inter^f		0.0375	0.0878	0.1492	0.4831
	Inter^l		0.0722	0.1581	0.3586	0.9279
	Urea^l		0.0749	0.1663	0.3670	1.0044

Table 7.3 Rates determined from experimental data for NH_{new} , ND_{new} , and ND_{old} at the different temperatures recorded.

As the rates of reaction have been determined at a few different temperatures, activation parameters for the reaction can be determined using the Arrhenius equation. From the rates (k) calculated at each temperature (T), the Arrhenius equation was used to determine the activation energy (E_a) and frequency factor (A), where R is a constant ($8.314 \text{ Jmol}^{-1}\text{K}^{-1}$).

$$k = Ae^{-E_a/RT} \quad (7.3)$$

The Arrhenius Equation describes the typical temperature-dependences of the rates of reactions. The activation energy (E_a) denotes the energy difference between the reactants and the transition state of the reaction (Figure 7.16). Thus, it gives information on the energy barrier to the reaction.

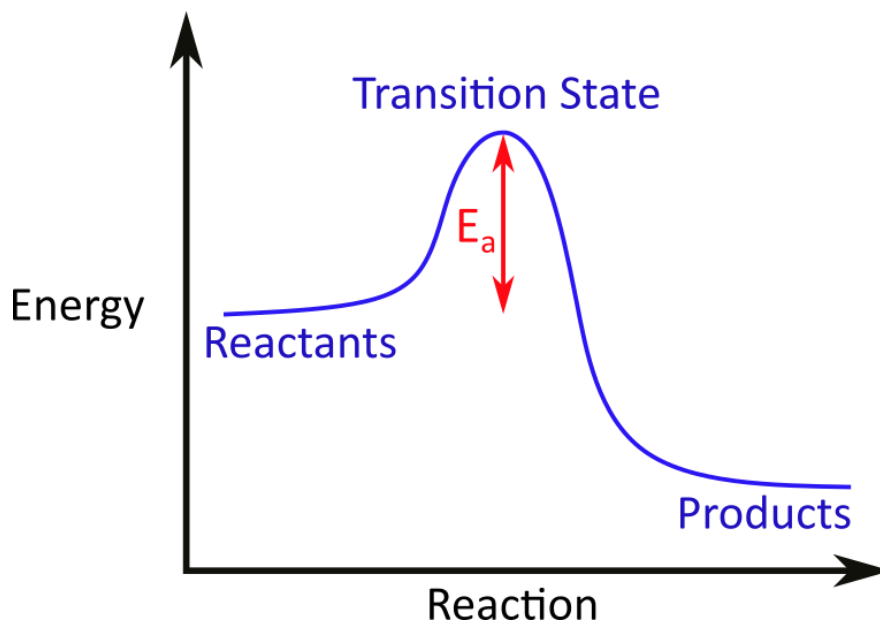


Figure 7.16 The respective energies for reactants and products in a reaction. The activation energy (E_a) denotes the energy required to reach the transition state (i.e., the energy barrier that must be surmounted for the reaction to occur).

To determine the activation energy, a plot of $\ln(k)$ vs. $1/T$ (Arrhenius plot) is required. The line plotted has an intercept of $\ln(A)$ and a gradient of $-E_a/R$. Figure 7.17 (a) shows Arrhenius plots for the loss of AC in each sample, it is not possible to determine much difference in gradient between the samples by eye, indicating the difference in activation energy is not significant.

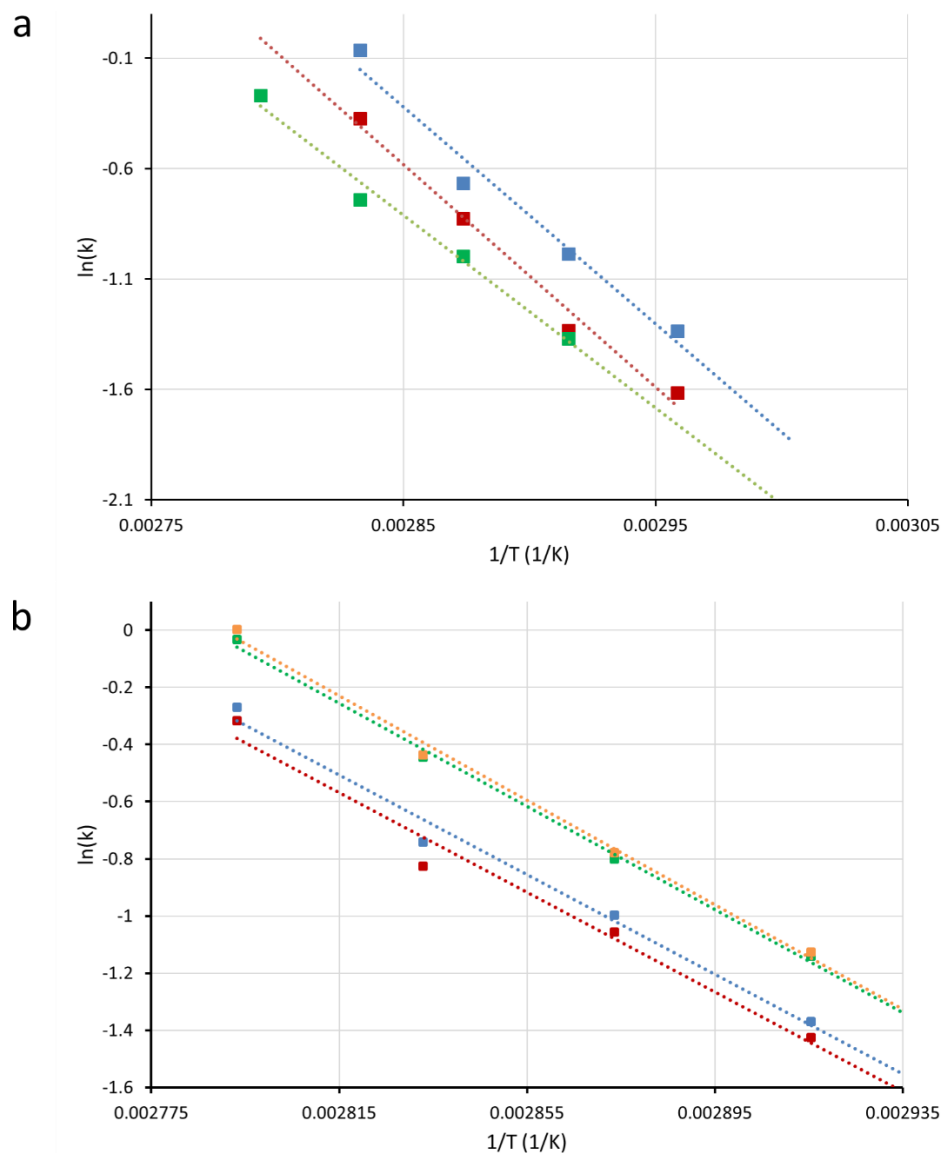


Figure 7.17 (a) Arrhenius plot for the rate of loss of crystalline AC in NH_{new} (blue), ND_{new} (red) and ND_{old} (green). (b) Arrhenius plots for ND_{old} , showing the rate of loss of AC in blue, and the rate of formation of the intermediate phase in red, the rate of loss of the intermediate phase in green, and the rate of formation of crystalline urea in yellow.

Figure 7.17 (b) shows Arrhenius plots for the kinetic data determined for ND_{old} . It is quite apparent that the transformation in this case can be separated into two distinct stages, which have similar activation energies: conversion of crystalline AC to the intermediate phase, and conversion of the intermediate phase to crystalline urea. Values for the activation energy for each of the stages are in Table 7.4. The gradient in each case was determined by using a line of best fit.

		E_a/kJmol^{-1}	Rate at 293 K/ s^{-1}
NH_{new}	AC	81.75	0.00287
ND_{new}	AC	83.92	0.00191
ND_{old}	AC^f	72.59	0.00326
	Inter^f	72.59	0.00306
	Inter^l	75.15	0.00349
	Urea^l	76.04	0.00335

Table 7.4 Activation energies and rates at 293 K for the reactions of NH_{new} , ND_{new} and ND_{old} .

For NH_{new} and ND_{new} only the activation energy for the loss of AC is shown, the activation energy for the formation of urea is identical, as the analysis has considered the process to be a direct conversion from AC to urea, given that only very small amounts of the intermediate phase are detected. The activation energy is lower for NH_{new} than ND_{new} , indicating that the reaction rates for NH_{new} will show a greater increase with temperature than ND_{new} , consistent with the observed rates in Table 7.3. Furthermore, the times taken for complete conversion of AC to urea shown in Table 7.5, where ND_{new} consistently took a longer time to undergo complete conversion from AC to urea than NH_{new} .

Understanding the kinetics of ND_{old} is more complicated. The reaction of ND_{old} can clearly be considered in two distinct stages: conversion of AC into the intermediate phase, and conversion of the intermediate phase to urea. The activation energies for the loss of AC and the formation of the intermediate phase are the same. The activation energies for the loss of the intermediate phase and the formation of urea are effectively equivalent, i.e., they correspond to the same reactions, thus indicating that there is no direct conversion of AC to urea but instead, for ND_{old} , AC is converted to the intermediate, which then transforms into urea. The time taken for complete conversion of ND_{old} is greater than for the other two samples, as the two stages of the reaction are combined.

Temperature/K	Time for Complete Conversion (s)		
	NH _{new}	ND _{new}	ND _{old}
338	2685	4769	
343	1289	2485	2930
348	641	818	1268
353	235	327	729
358			289

Table 7.5 Time taken for complete conversion of AC to urea for NH_{new}, ND_{new} and ND_{old}.

The differences in kinetics between ND_{new} and NH_{new} and the fact that the intermediate is only observed for ND_{new} could be due to the difference in isotope, although this requires more investigation. It will also be interesting to determine if the conclusions drawn in this section remain the same when the fitting for the kinetic data is repeated using the crystal structure of the intermediate phase detailed in Section 7.3.1.

7.4 Conclusions

We have identified the presence of an intermediate phase in the solid-state reaction of crystalline AC to crystalline urea. Furthermore, the crystal structure of the intermediate phase has been determined despite the multi-phase nature of the sample used to record the PXRD pattern used for structure determination. The intermediate phase has been observed under only certain sample conditions; the greatest relative amount of intermediate phase was observed in samples stored in a freezer (at ca. -18 °C), for close to two decades. A freshly prepared deuterated sample of AC showed some evidence of the intermediate phase during the reaction to urea, but in much smaller relative amount. A freshly prepared sample of AC at natural isotropic abundance showed no evidence of the intermediate phase during the reaction to urea.

A mechanism for the conversion of crystalline AC to the intermediate phase has been proposed based on the crystal structures. Preliminary analysis for the kinetics of the reaction have been undertaken, from time-resolved powder XRD data, albeit based on a crystal structure of the intermediate phase that is only approximately correct. The preliminary kinetic data indicates that for ND_{old} , the overall reaction can be described in two stages: conversion from AC to intermediate phase and then the conversion of the intermediate phase to urea. According to activation energies, NH_{new} reacts the quickest. At a given temperature, the rate of reaction is faster for NH_{new} than ND_{new} , suggesting a kinetic isotope effect.

The results discussed in this chapter have shed new light on Wöhler's reaction. However, more work needs to be carried out before our understanding of the reaction can be considered complete.

8 Conclusion

X-ray birefringence imaging (XBI) is a relatively new technique enabling spatially resolved mapping of the orientational properties of the bonding environment around an X-ray absorbing element. Previous work established the usefulness of the XBI technique in determining the orientations of individual molecules and the characterization of phase transitions within solid materials as well as liquid crystalline materials oriented in a magnetic field. XBI is of particular interest for the structural characterization of materials for which X-ray diffraction is not applicable, such as liquid phases, amorphous materials, twinned crystals, and the imaging of domains and domain boundaries. The time to record XBI images is relatively fast (1 - 2 s), which can be exploited in time-resolved experiments. The research in this thesis aimed to explore a variety of materials to advance the frontiers of XBI analysis and to expand the applicability of the XBI technique.

The first chapter describing new research (Chapter 4) is focused on mechanically deformable crystals, specifically hexabromobenzene (HBB) and copper acetyl acetonate (CuAcAc). Mechanically deformable crystals are fascinating due to their varying physical and chemical properties,⁵⁸ which are critical in understanding the processing of pharmaceuticals and the potential uses of deformable crystals as actuators or molecular machines.^{49,50,54,59-70} The exploration of the capability of XBI to study in-situ bending of crystals is particularly important for materials such as HBB for which bending occurs only above a certain temperature and thus, demonstrating the potential to apply XBI for imaging of dynamic processes. Halogenated benzenes exhibit several interesting physical properties such as phase transitions, bending and shearing,^{71,80} and the easy accessibility of XBI measurements at the bromine K-edge greatly facilitates the characterization of these materials using the XBI technique.

The bending crystal CuAcAc has been particularly important in expanding the theoretical calculation of XBI behaviour. The specific bonding environment of a single copper atom bonded to four oxygen atoms provides an interesting challenge compared to previous theoretical work which focused exclusively on single C-Br bonds and facilitated the development of a matrix-based formalism for calculating the XBI properties for such bonding environments.

Further expansion of the theoretical framework of XBI included a method to determine anisotropic and isotropic absorption coefficients from experimental data, leading to more accurate prediction of XBI intensities. The next step for XBI theoretical calculations is to determine an accurate way to incorporate the varying path length of X-rays through samples for which the sample thickness along the X-ray beam direction varies significantly upon ϕ -rotation.

An in-depth XBI study was carried out on 1,2,4,5-tetrabromobenzene (TBB) due to its fascinating physical properties. The results are exceedingly interesting, as single crystals of TBB exhibit XBI behaviour that has not been observed previously for other brominated materials (specifically, when ϕ is changed by 180° , the positions of the intensity maxima and minima as a function of χ are different). Theoretical XBI calculations showed that this unusual XBI behaviour arises when the 3D tensor describing the X-ray absorption of the C-Br bonds does not coincide with the laboratory coordinate system.

Furthermore, TBB was the first instance of using XBI to image twinned crystals in detail, remarkable in that a clear difference in intensity is observed between the two twin components. More work needs to be carried out on twinned crystals to fully exploit the potential to interpret the intensity differences between the twin components, to give information on relative orientations of the unit cells within each component. TBB has also been shown to act as a 'bimetallic strip', which would be particularly amenable to in-situ XBI imaging.

Another unforeseen aspect of TBB is the observation that some crystals contain 'hourglass' shaped domains. Within the 'hourglass', typical XBI behaviour of a single crystal of TBB is observed, while the intensity outside the 'hourglass' is zero, suggesting that this region of the crystal either has a different non-birefringent structure or is polycrystalline. Further studies are required to understand how these 'hourglass' crystals are formed, and to establish the structure composition of the domains.

XBI has been demonstrated to be a reliable method for imaging the distribution of orientations of C-Br bonds in materials through studies at the bromine K-edge, with considerable potential to expand XBI studies to a wider range of X-ray absorption edges. Chapter 6 is focused on expanding the application of XBI to studies at the S, Cr, Fe and Cu K-edges. Initially, X-ray dichroism measurements were carried out, allowing a straightforward assessment of whether X-ray birefringence studies on the same material would be promising. These studies confirm the potential to carry out XBI studies at the Fe K-edge (7.11 KeV) and higher energy K-edges on beamline B16 at Diamond Light Source. A fascinating future XBI study would be to explore the iron present in haemoglobin, which changes oxidation state and local bonding environment depending on whether oxygen is bound or unbound to the molecule.

X-ray dichroism measurements were also carried out on beamline I16, which can access lower K-edge energies. Showcasing the accessibility of the sulphur K-edge and demonstrating the X-ray dichroic properties of single crystals of thiourea. Thus, there is considerable potential for XBI studies of a variety of thiolated materials including polymers¹⁰⁷ and self-assembled monolayers^{108,109} on beamline I16 in the future. However, such experiments are not feasible at present, as significant modifications to the beamline would be required to make I16 suitable for XBI experiments.

As discussed in Chapter 6, CuBr_2 is the first sample to be studied by XBI at two different X-ray absorption edges (Br K-edge and Cu K-edge). At each absorption edge, the XBI behaviour is similar to single crystals of TBB (i.e. when ϕ is changed by 180° , the positions of the intensity maxima and minima as a function of χ are different). The bonding in inorganic materials and metallocenes around the X-ray absorbing element is evidently complex and greater insights are needed before understanding the observed XBI behaviour.

Chapter 7 contains the only experimental results not concerned with XBI, focusing instead on structure determination from powder XRD data. While investigating the mechanism of the solid-state reaction from ammonium cyanate to urea an intermediate phase was identified.

In this work, the crystal structure of the intermediate phase is determined from powder XRD data, in spite of the multi-phase nature of the powder sample (which, at an intermediate stage of the reaction, contains ammonium cyanate, the intermediate phase and urea). Furthermore, the reaction mechanisms for the conversion of ammonium cyanate to the intermediate phase and for the conversion of the intermediate phase to urea are suggested. Although, the work discussed in this chapter is preliminary it has already shed new light on Wöhler's reaction.

The aim of the research in this thesis was to further advance the XBI technique through studies of materials that highlight new and exciting applications of the technique. The work has demonstrated the capability of XBI for imaging local orientational properties of materials and for observing small changes in orientations of bonds associated with dynamic processes. The potential of the XBI technique will surely only increase as more experiments are carried out and as the capabilities of the technique become better understood.

9 References

1. Hegedüs, R., Åkesson, S., Wehner, R. & Horváth, G. Could Vikings have navigated under foggy and cloudy conditions by skylight polarization? On the atmospheric optical prerequisites of polarimetric Viking navigation under foggy and cloudy skies. *Proc. R. Soc. A* **463**, 1081–1095 (2007).
2. Ropars, G., Gorre, G., Le Floch, A., Enoch, J. & Lakshminarayanan, V. A depolarizer as a possible precise sunstone for Viking navigation by polarized skylight. *Proc. R. Soc. A* **468**, 671–684 (2011).
3. Hughes, L., Archer, C. & ap Gwynn, I. The Ultrastructure of Mouse Articular Cartilage: Collagen Orientation and Implications for Tissue Functionality. A Polarised Light and Scanning Electron Microscope Study and Review. *Eur. Cell. Mater.* **9**, 68–84 (2005).
4. Varghese, B. *et al.* Quantitative Assessment of Birefringent Skin Structures in Scattered Light Confocal Imaging Using Radially Polarized Light. *Sensors* **13**, 12527–12535 (2013).
5. Khan, K. M., Cook, J. L., Bonar, F., Harcourt, P. & Astrom, M. Histopathology of Common Tendinopathies. Update and Implications for Clinical Management. *Sports Med.* **27**, 393–408 (1999).
6. Neves, N. M., Pouzada, A. S., Voerman, J. H. D. & Powell, P. C. The use of birefringence for predicting the stiffness of injection molded polycarbonate discs. *Polym. Eng. Sci.* **38**, 1770–1777 (1998).
7. Iverson, I. K. & Tam-Chang, S.-W. Cascade of Molecular Order by Sequential Self-Organization, Induced Orientation, and Order Transfer Processes. *J. Am. Chem. Soc.* **121**, 5801–5802 (1999).
8. Zhou, Y. *et al.* Spatially resolved mapping of phase transitions in liquid-crystalline materials by X-ray birefringence imaging. *Chem. Sci.* **10**, 3005–3011 (2019).

9. Jenkins, F. A. & White, H. E. Fundamentals of Physical Optics. in 316–319 (McGraw, 1937).
10. Daintith, J. D. Nicol prism. in *A Dictionary of Chemistry* (ed. Daintith, J.) (Oxford University Press, 2008).
11. Land, E. H. Light polarizer and process of manufacturing the same. (1941).
12. NIST: X-Ray Mass Attenuation Coefficients - Table 3. <https://physics.nist.gov/PhysRefData/XrayMassCoef/tab3.html>.
13. Evans, J. Figure 4.38. in *X-ray Absorption Spectroscopy for the Chemical and Materials Sciences* (Wiley, 2018).
14. Brouder, C. Angular dependence of X-ray absorption spectra. *J. Phys. Condens. Matter* **2**, 701–738 (1990).
15. van der Laan, G., Schofield, P. F., Cressey, G. & Henderson, C. M. B. Natural linear dichroism at the Fe 2p absorption edge of gillespite. *Chem. Phys. Lett.* **252**, 272–276 (1996).
16. Collins, S. P. *et al.* X-ray linear dichroism in an α,ω -dibromoalkane/urea inclusion compound and its application to polarization analysis of magnetic diffraction. *J. Phys. Condens. Matter* **14**, 123–134 (2001).
17. Chao, M.-H., Kariuki, B. M., Harris, K. D. M., Collins, S. P. & Laundy, D. Design of a Solid Inclusion Compound with Optimal Properties as a Linear Dichroic Filter for X-ray Polarization Analysis. *Angew. Chem. Int. Ed.* **42**, 2982–2985 (2003).
18. Mertins, H.-Ch. *et al.* X-ray natural birefringence in reflection from graphite. *Phys. Rev. B* **70**, 235106 (2004).
19. Lovesey, S. W. & Collins, S. P. X-ray birefringence and dichroism obtained from magnetic materials. *J. Synchrotron Rad* **8**, 1065–1077 (2001).

20. Sauvage, M., Malgrange, C. & Petroff, J.-F. Rotatory power measurements in the X-ray range with synchrotron radiation: Experimental set-up and preliminary results for NaBrO₃ single crystals. *J. Appl. Cryst* **16**, 14–20 (1983).
21. Ade, H. & Hsiao, B. X-ray Linear Dichroism Microscopy. *Science* **262**, 1427–1429 (1993).
22. Bannister, N. P. *et al.* Dichroic Filters For Astronomical X-Ray Polarimetry. *Exp. Astron.* **21**, 1–12 (2006).
23. Palmer, B. A., Morte-Ródenas, A., Kariuki, B. M., Harris, K. D. M. & Collins, S. P. X-ray Birefringence from a Model Anisotropic Crystal. *J. Phys. Chem. Lett.* **2**, 2346–2351 (2011).
24. Palmer, B. A. *et al.* X-ray Birefringence: A New Strategy for Determining Molecular Orientation in Materials. *J. Phys. Chem. Lett.* **3**, 3216–3222 (2012).
25. Sawhney, K. J. S. *et al.* A Test Beamline on Diamond Light Source. *AIP Conf. Proc.* **1234**, 387–390 (2010).
26. Macrander, A. T. & Huang, X. Synchrotron X-Ray Optics. *Annu. Rev. Mater. Res.* **47**, 135–152 (2017).
27. 1005. <https://www.xhuber.com/en/products/4-accessories/40-goniometer-heads/manual-versions/1005/>.
28. Palmer, B. *et al.* Theoretical analysis of the background intensity distribution in X-ray Birefringence Imaging using synchrotron bending-magnet radiation. *J. Appl. Phys.* **117**, 164902 (2015).
29. John David Jackson. *Classical Electrodynamics, 2nd Edition.* (Wiley, 1975).
30. Sutter, J. P. *et al.* Novel technique for spatially resolved imaging of molecular bond orientations using x-ray birefringence. *AIP Conf. Proc.* **1741**, 050009 (2016).

31. Sanchez del Rio, M., Canestrari, N., Jiang, F. & Cerrina, F. SHADOW3: a new version of the synchrotron X-ray optics modelling package. *J. Synchrotron Radiat.* **18**, 708–716 (2011).
32. Palmer, B. A. *et al.* X-ray Birefringence Imaging of Materials with Anisotropic Molecular Dynamics. *J. Phys. Chem. Lett.* **6**, 561–567 (2015).
33. Palmer, B. A. *et al.* X-ray birefringence imaging. *Science* **344**, 1013–1016 (2014).
34. MacLean, E. J. *et al.* Ammonium cyanate shows N-H...N hydrogen bonding, not N-H...O. *J. Am. Chem. Soc.* **125**, 14449–14451 (2003).
35. Harris, K. D. M. Powder diffraction crystallography of molecular solids. *Top. Curr. Chem.* **315**, 133–177 (2012).
36. Shirley, R. Accuracy in Powder Diffraction. in vol. 567 361–382 (NBS Spec. Publ., 1980).
37. Bail, A. L. Whole powder pattern decomposition methods and applications: A retrospection. *Powder Diffr.* **20**, 316–326 (2005).
38. Kariuki, B. M., Serrano-González, H., Johnston, R. L. & Harris, K. D. M. The application of a genetic algorithm for solving crystal structures from powder diffraction data. *Chem. Phys. Lett.* **280**, 189–195 (1997).
39. Harris, K. D. M., Johnston, R. L. & Kariuki, B. M. The Genetic Algorithm: Foundations and Applications in Structure Solution from Powder Diffraction Data. *Acta Cryst* **A54**, 632–645 (1998).
40. Kariuki, B. M., Calcagno, P., Harris, K. D. M., Philp, D. & Johnston, R. L. Evolving Opportunities in Structure Solution from Powder Diffraction Data—Crystal Structure Determination of a Molecular System with Twelve Variable Torsion Angles. *Angew. Chem. Int. Ed.* **38**, 831–835 (1999).
41. Harris, K. D. M. & Cheung, E. Y. How to determine structures when single crystals cannot be grown: opportunities for structure determination of molecular materials using powder diffraction data. *Chem. Soc. Rev.* **33**, 526–538 (2004).

42. Rietveld, H. M. A profile refinement method for nuclear and magnetic structures. *J. Appl. Cryst* **2**, 65–71 (1969).
43. Collins, S. P. *et al.* X-ray Birefringence in highly Anisotropic Materials. *J. Phys. Conf. Ser.* **425**, 132015 (2013).
44. Detlefs, C., Sanchez del Rio, M. & Mazzoli, C. X-ray polarization: General formalism and polarization analysis. *Eur. Phys. J. Spec. Top.* **208**, 359–371 (2012).
45. Lovesey, S. W. Photon scattering by magnetic solids. *Rep. Prog. Phys.* **56**, 257–326 (1993).
46. Sands, D. E. *Introduction to Crystallography*. (Courier Corporation, 1993).
47. Malla Reddy, C. *et al.* Structural basis for bending of organic crystals. *Chem. Commun.* **0**, 3945–3947 (2005).
48. Sun, J.-K. *et al.* Photoinduced Bending of a Large Single Crystal of a 1,2-Bis(4-pyridyl)ethylene-Based Pyridinium Salt Powered by a [2+2] Cycloaddition. *Angew. Chem. Int. Ed.* **52**, 6653–6657 (2013).
49. Bushuyev, O. S., Singleton, T. A. & Barrett, C. J. Fast, Reversible, and General Photomechanical Motion in Single Crystals of Various Azo Compounds Using Visible Light. *Adv. Mater.* **25**, 1796–1800 (2013).
50. Koshima, H. & Ojima, N. Photomechanical bending of 4-aminoazobenzene crystals. *Dyes Pigments* **92**, 798–801 (2012).
51. Chou, C.-M. *et al.* Highly bent crystals formed by restrained π -stacked columns connected via alkylene linkers with variable conformations. *Chem. Sci.* **6**, 2354–2359 (2015).
52. Pejov, L., Panda, M. K., Moriwaki, T. & Naumov, P. Probing Structural Perturbation in a Bent Molecular Crystal with Synchrotron Infrared Microspectroscopy and Periodic Density Functional Theory Calculations. *J. Am. Chem. Soc.* **139**, 2318–2328 (2017).

53. Kim, T., Zhu, L., Al-Kaysi, R. O. & Bardeen, C. J. Organic Photomechanical Materials. *ChemPhysChem* **15**, 400–414 (2014).
54. Koshima, H., Ojima, N. & Uchimoto, H. Mechanical Motion of Azobenzene Crystals upon Photoirradiation. *J. Am. Chem. Soc.* **131**, 6890–6891 (2009).
55. Nath, N. K. *et al.* Model for Photoinduced Bending of Slender Molecular Crystals. *J. Am. Chem. Soc.* **136**, 2757–2766 (2014).
56. Shtukenberg, A. G., Punin, Y. O., Gujral, A. & Kahr, B. Growth Actuated Bending and Twisting of Single Crystals. *Angew. Chem. Int. Ed.* **53**, 672–699 (2014).
57. Maahs, A. C., Ignacio, M. G., Ghazzali, M., Soldatov, D. V. & Preuss, K. E. Chiral Crystals of an Achiral Molecule Exhibit Plastic Bending and a Crystal-to-Crystal Phase Transition. *Cryst. Growth Des.* **17**, 1390–1395 (2017).
58. Boldyrev, V. V. & IUPAC. *Reactivity of solids : past, present, and future.* (Blackwell Science, 1996).
59. Reddy, C. M., Krishna, G. R. & Ghosh, S. Mechanical properties of molecular crystals—applications to crystal engineering. *CrystEngComm* **12**, 2296–2314 (2010).
60. Ghosh, S. & Reddy, C. M. Elastic and Bendable Caffeine Cocrystals: Implications for the Design of Flexible Organic Materials. *Angew. Chem. Int. Ed.* **51**, 10319–10323 (2012).
61. Kobatake, S., Takami, S., Muto, H., Ishikawa, T. & Irie, M. Rapid and reversible shape changes of molecular crystals on photoirradiation. *Nature* **446**, 778–781 (2007).
62. Al-Kaysi, R. O., Müller, A. M. & Bardeen, C. J. Photochemically Driven Shape Changes of Crystalline Organic Nanorods. *J. Am. Chem. Soc.* **128**, 15938–15939 (2006).

63. Terao, F., Morimoto, M. & Irie, M. Light-Driven Molecular-Crystal Actuators: Rapid and Reversible Bending of Rodlike Mixed Crystals of Diarylethene Derivatives. *Angew. Chem. Int. Ed.* **51**, 901–904 (2012).
64. Kim, T., Zhu, L., Mueller, L. J. & Bardeen, C. J. Dependence of the solid-state photomechanical response of 4-chlorocinnamic acid on crystal shape and size. *CrystEngComm* **14**, 7792–7799 (2012).
65. Good, J. T., Burdett, J. J. & Bardeen, C. J. Using Two-Photon Excitation to Control Bending Motions in Molecular-Crystal Nanorods. *Small* **5**, 2902–2909 (2009).
66. Koshima, H., Takechi, K., Uchimoto, H., Shiro, M. & Hashizume, D. Photomechanical bending of salicylideneaniline crystals. *Chem. Commun.* **47**, 11423–11425 (2011).
67. Sahoo, S. C. *et al.* Kinematic and Mechanical Profile of the Self-Actuation of Thermosensitive Crystal Twins of 1,2,4,5-Tetrabromobenzene: A Molecular Crystalline Analogue of a Bimetallic Strip. *J. Am. Chem. Soc.* **135**, 13843–13850 (2013).
68. John, G., Jadhav, S. R., Menon, V. M. & John, V. T. Flexible Optics: Recent Developments in Molecular Gels. *Angew. Chem. Int. Ed.* **51**, 1760–1762 (2012).
69. Fratzl, P. & Barth, F. G. Biomaterial systems for mechanosensing and actuation. *Nature* **462**, 442–448 (2009).
70. Lv, S. *et al.* Designed biomaterials to mimic the mechanical properties of muscles. *Nature* **465**, 69–73 (2010).
71. Reddy, C. M., Padmanabhan, K. A. & Desiraju, G. R. Structure–Property Correlations in Bending and Brittle Organic Crystals. *Cryst. Growth Des.* **6**, 2720–2731 (2006).
72. Panda, M. K. *et al.* Spatially resolved analysis of short-range structure perturbations in a plastically bent molecular crystal. *Nat. Chem.* **7**, 65–72 (2015).

73. Takamizawa, S. & Miyamoto, Y. Superelastic Organic Crystals. *Angew. Chem. Int. Ed.* **53**, 6970–6973 (2014).
74. Saha, S. & Desiraju, G. R. Crystal Engineering of Hand-Twisted Helical Crystals. *J. Am. Chem. Soc.* **139**, 1975–1983 (2017).
75. Takamizawa, S. & Takasaki, Y. Superelastic Shape Recovery of Mechanically Twinned 3,5-Difluorobenzoic Acid Crystals. *Angew. Chem. Int. Ed.* **54**, 4815–4817 (2015).
76. Ghosh, S., Mishra, M. K., Kadambi, S. B., Ramamurty, U. & Desiraju, G. R. Designing Elastic Organic Crystals: Highly Flexible Polyhalogenated N-Benzylideneanilines. *Angew. Chem. Int. Ed.* **54**, 2674–2678 (2015).
77. Zhou, Y. Advancing fundamentals and applications of X-ray birefringence imaging. (Cardiff University, 2018).
78. Worthy, A. *et al.* Atomic resolution of structural changes in elastic crystals of copper(II) acetylacetonate. *Nat. Chem.* **10**, 65–69 (2018).
79. Brezgunova, M. E. *et al.* Charge Density Analysis and Topological Properties of Hal3-Synthons and Their Comparison with Competing Hydrogen Bonds. *Cryst. Growth Des.* **12**, 5373–5386 (2012).
80. Reddy, C. M., Kirchner, M. T., Gundakaram, R. C., Padmanabhan, K. A. & Desiraju, G. R. Isostructurality, Polymorphism and Mechanical Properties of Some Hexahalogenated Benzenes: The Nature of Halogen···Halogen Interactions. *Chem. - Eur. J.* **12**, 2222–2234 (2006).
81. Baharie, E. & Pawley, G. S. The crystal structure of hexabromobenzene: constrained refinement of neutron powder diffraction data. *Acta Cryst* **A35**, 233–235 (1979).
82. Sahoo, S. C., Panda, M. K., Nath, N. K. & Naumov, P. Biomimetic Crystalline Actuators: Structure–Kinematic Aspects of the Self-Actuation and Motility of Thermosalient Crystals. *J. Am. Chem. Soc.* **135**, 12241–12251 (2013).

83. Lieberman, H. F., Davey, R. J. & Newsham, D. M. T. Br \cdots Br and Br \cdots H Interactions in Action: Polymorphism, Hopping, and Twinning in 1,2,4,5-Tetrabromobenzene. *Chem. Mater.* **12**, 490–494 (2000).
84. Gafner, G. The crystal and molecular structures of overcrowded halogenated compounds. II. β -1:2-4:5-Tetrabromobenzene. *Acta Crystallogr.* **13**, 706–716 (1960).
85. Gafner, G. The crystal and molecular structures of overcrowded halogenated compounds. V. γ -1,2:4,5-Tetrabromobenzene. *Acta Crystallogr.* **17**, 982–985 (1964).
86. Johnson, F. B. Phase-Change in 1,2,4,5-Tetrabromobenzene investigated by Pure Quadrupole Resonance. *Nature* **178**, 590–590 (1956).
87. Zakharov, B. A., Michalchuk, A. A. L., Morrison, C. A. & Boldyreva, E. V. Anisotropic lattice softening near the structural phase transition in the thermosalient crystal 1,2,4,5-tetrabromobenzene. *Phys. Chem. Chem. Phys.* **20**, 8523–8532 (2018).
88. Ko, J.-H., Lee, K.-S., Chandra Sahoo, S. & Naumov, P. Isomorphous phase transition of 1,2,4,5-tetrabromobenzene jumping crystals studied by Brillouin light scattering. *Solid State Commun.* **173**, 46–50 (2013).
89. White, K. M. & Eckhardt, C. J. Assignment of the Raman active lattice vibrations in various phases of 1,2,4,5-tetrabromobenzene and 1,2,4,5-tetrachlorobenzene crystals. *J. Chem. Phys.* **90**, 4709 (1989).
90. Krafczyk, S., Jacobi, H. & Follner, H. Twinning of crystals as a result of differences between symmetrical and energetical most favourable structure arrangements. *Cryst. Res. Technol.* **29**, 623–631 (1994).
91. Gas Filter Transmission. http://henke.lbl.gov/optical_constants/gastrn2.html.
92. Lenné, H.-U. Röntgenographische Strukturuntersuchungen hexagonaler Einschlussverbindungen des Thioharnstoffs. *Acta Crystallogr.* **7**, 1–15 (1954).

93. Harris, K. D. M. & Thomas, J. M. Structural aspects of the chlorocyclohexane/thiourea inclusion system. *J. Chem. Soc. Faraday Trans.* **86**, 1095–1101 (1990).
94. Tam, W. *et al.* Channel inclusion complexation of organometallics: dipolar alignment for second harmonic generation. *Chem. Mater.* **1**, 128–140 (1989).
95. Harris, K. D. M. Structural and dynamic properties of urea and thiourea inclusion compounds. *J. Mol. Struct. THEOCHEM* **374**, 241–250 (1996).
96. George, A. R. & Harris, K. D. M. Representing and understanding geometric features of one-dimensional tunnel structures in solid inclusion compounds. *J. Mol. Graph.* **13**, 138–141 (1995).
97. Schiessler, R. W. & Flitter, D. Urea and Thiourea Adduction of C5—C42-Hydrocarbons. *J. Am. Chem. Soc.* **74**, 1720–1723 (1952).
98. Harris, K. D. M. Towards a Fundamental Understanding of Urea and Thiourea inclusion Compounds. *J. Chin. Chem. Soc.* **46**, 5–22 (1999).
99. Hough, E. & Nicholson, D. G. X-Ray crystallographic studies on ferrocene included in a thiourea host lattice. *J. Chem. Soc. Dalton Trans.* 15–18 (1978).
100. Lorson, L. C., Tai, O. & Foxman, B. M. Use of Topotactic Phase Transformations To Obtain Solutions of the Crystal Structures of Highly Disordered Materials. *Cryst. Growth Des.* **18**, 409–415 (2018).
101. Rogalev, A. *et al.* Element selective X-ray magnetic circular and linear dichroisms in ferrimagnetic yttrium iron garnet films. *J. Magn. Magn. Mater.* **321**, 3945–3962 (2009).
102. Ovchinnikova, E. N. *et al.* X-ray natural circular dichroism in copper metaborate. *J. Exp. Theor. Phys.* **123**, 27–32 (2016).
103. Nielson, D., Boone, D. & Eyring, H. Magnetic circular dichroism of ferrocene and substituted ferrocenes. d-d Transitions. *J. Phys. Chem.* **76**, 511–515 (1972).

104. Truter, M. R. Comparison of photographic and counter observations for the X-ray crystal structure analysis of thiourea. *Acta Crystallogr.* **22**, 556–559 (1967).
105. Elcombe, M. M. & Taylor, J. C. A neutron diffraction determination of the crystal structures of thiourea and deuterated thiourea above and below the ferroelectric transition. *Acta Cryst* **A24**, 410–420 (1968).
106. Mullen, D., Heger, G. & Treutmann, W. Refinement of the structure of thiourea: A neutron diffraction study at 293 K. *Z. Für Krist. - Cryst. Mater.* **148**, 95–100 (1978).
107. Goethals, E. J. Sulfur-Containing Polymers. *J. Macromol. Sci. Part C* **2**, 73–144 (1968).
108. Bürgi, T. Properties of the gold–sulphur interface: from self-assembled monolayers to clusters. *Nanoscale* **7**, 15553–15567 (2015).
109. Vericat, C. *et al.* Self-assembled monolayers of thiolates on metals: a review article on sulfur-metal chemistry and surface structures. *RSC Adv.* **4**, 27730–27754 (2014).
110. Haaland, A. & Nilsson, J.-E. The determination of the barrier to internal rotation in ferrocene and ruthenocene by means of electron diffraction. *Chem. Commun. Lond.* 88–89 (1968).
111. Dunitz, J. D., Orgel, L. E. & Rich, A. The crystal structure of ferrocene. *Acta Crystallogr.* **9**, 373–375 (1956).
112. Gibb, T. C. Anisotropic relaxation of the electric field gradient tensor in the ^{57}Fe Mossbauer spectra of a thiourea-ferrocene clathrate. *J. Phys. C Solid State Phys.* **9**, 2627–2642 (1976).
113. Nakai, T., Terao, T., Imashiro, F. & Saika, A. A ^{13}C NMR study of the dynamic structure of the thiourea-ferrocene inclusion compound. *Chem. Phys. Lett.* **132**, 554–557 (1986).

114. Lowery, M. D., Wittebort, R. J., Sorai, M. & Hendrickson, D. N. Dynamics of ferrocene in a thiourea inclusion matrix. *J. Am. Chem. Soc.* **112**, 4214–4225.
115. Clément, R., Gourdji, M. & Guibé, L. Molecular motions in the thiourea-d₄-ferrocene inclusion compound. *Chem. Phys. Lett.* **72**, 466–468 (1980).
116. Clement, R., Claude, R. & Mazieres, C. Clathration of ferrocene and nickelocene in a thiourea host lattice. *J. Chem. Soc. Chem. Commun.* 654–655 (1974).
117. Heyes, S. J., Clayden, N. J. & Dobson, C. M. Ferrocene molecular reorientation in the (thiourea)₃·ferrocene inclusion compound as studied by deuterium NMR spectroscopy. *J. Phys. Chem.* **95**, 1547–1554 (1991).
118. Wyckoff, R. W. G. & Posnjak, E. THE CRYSTAL STRUCTURES OF THE CUPROUS HALIDES. *J. Am. Chem. Soc.* **44**, 30–36 (1922).
119. Oeckler, O. & Simon, A. Redetermination of the crystal structure of copper dibromide, CuBr₂. *Z. Für Krist. - New Cryst. Struct.* **215**, 13–13 (2000).
120. Everett, J. *et al.* Ferrous iron formation following the co-aggregation of ferric iron and the Alzheimer's disease peptide β -amyloid (1–42). *J. R. Soc. Interface* **11**, (2014).
121. Bajt, S., Sutton, S. R. & Delaney, J. S. X-ray microprobe analysis of iron oxidation states in silicates and oxides using X-ray absorption near edge structure (XANES). *Geochim. Cosmochim. Acta* **58**, 5209–5214 (1994).
122. Pin, S., Alpert, B. & Michalowicz, A. An investigation by iron K-edge spectroscopy of the oxidation state of iron in hemoglobin and its subunits. *FEBS Lett.* **147**, 106–110 (1982).
123. Wilson, S. A. *et al.* X-ray absorption spectroscopic investigation of the electronic structure differences in solution and crystalline oxyhemoglobin. *Proc. Natl. Acad. Sci. U. S. A.* **110**, 16333–16338 (2013).

124. Wöhler, F. Ueber künstliche Bildung des Harnstoffs. *Ann. Phys.* **88**, 253–256 (1828).
125. Liebig, J. & Wöhler, F. Untersuchungen über die Cyansäure. *Ann. Phys.* **96**, 369–400 (1830).
126. Dunitz, J. D. *et al.* New Light on an Old Story: The Solid-State Transformation of Ammonium Cyanate into Urea. *J. Am. Chem. Soc.* **120**, 13274–13275 (1998).
127. Becker, K. & Jancke, W. Röntgenspektroskopische Untersuchungen an organischen Verbindungen. I. *Z. Für Phys. Chem.* **99U**, 242–266 (1921).
128. Becker, K. & Jancke, W. Röntgenspektroskopische Untersuchungen an organischen Verbindungen. II. *Z. Für Phys. Chem.* **99U**, 267–274 (1921).
129. Mark, H. & Weissenberg, K. Röntgenographische Bestimmung der Struktur des Harnstoffs und des Zinntetraiodids. *Z. Phys.* **16**, 1–22 (1923).
130. Hendricks, S. B. THE CRYSTAL STRUCTURE OF UREA AND THE MOLECULAR SYMMETRY OF THIOUREA. *J. Am. Chem. Soc.* **50**, 2455–2464 (1928).
131. Wyckoff, R. W. G. 35. A Powder Spectrometry Study of the Structure of Urea. *Z. Für Krist. - Cryst. Mater.* **75**, 529–537 (1930).
132. Wyckoff, R. W. G. & Corey, R. B. Spectrometric Measurements on Hexamethylene Tetramine and Urea. *Z. Für Krist. - Cryst. Mater.* **89**, 462–468 (1934).
133. Vaughan, P. & Donohue, J. The structure of urea. Interatomic distances and resonance in urea and related compounds. *Acta Crystallogr.* **5**, 530–535 (1952).
134. Worsham, J. E., Levy, H. A. & Peterson, S. W. The positions of hydrogen atoms in urea by neutron diffraction. *Acta Crystallogr.* **10**, 319–323 (1957).
135. Sklar, N., Senko, M. E. & Post, B. Thermal effects in urea: the crystal structure at –140°C and at room temperature. *Acta Crystallogr.* **14**, 716–720 (1961).

136. Walker, J. & Wood, J. K. III.—The preparation and properties of solid ammonium cyanate. *J. Chem. Soc. Trans.* **77**, 21–33 (1900).
137. Dieck, R. L. *et al.* Tetraethylammonium, Tetraphenylarsonium, and Ammonium Cyanates and Cyanides. in *Inorganic Syntheses* 131–137 (John Wiley & Sons, Ltd, 2007).
138. Thompson, S. P. *et al.* Beamline I11 at Diamond: a new instrument for high resolution powder diffraction. *Rev. Sci. Instrum.* **80**, 075107 (2009).
139. Shirley, R. & Louër, D. New powder indexing programs for any symmetry which combine grid-search with successive dichotomy. *Acta Crystallogr. Sect. A* **A34**, S382 (1978).
140. Toby, B. H. EXPGUI, a graphical user interface for GSAS. *J. Appl. Crystallogr.* **34**, 210–213 (2001).
141. Clark, S. J. *et al.* First principles methods using CASTEP. *Z. Für Krist. - Cryst. Mater.* **220**, 567–570 (2005).
142. Guth, H., Heger, G., Klein, S., Treutmann, W. & Scheringer, C. Strukturverfeinerung von Harnstoff mit Neutronenbeugungsdaten bei 60, 123 und 293 K und X–N- und X–X(1s₂)-Synthesen bei etwa 100 K. *Z. Für Krist. - Cryst. Mater.* **153**, 237–254 (1980).

10 Appendices

10.1 Appendix I

Peaks in the experimental powder XRD pattern corresponding to AC which are removed for the EAGER calculation.

$2\theta = (15.55^\circ, 15.68^\circ), (18.40^\circ, 18.52^\circ), (21.48^\circ, 21.6^\circ), (26.19^\circ, 26.27^\circ), (29.32^\circ, 29.43^\circ), (30.57^\circ, 30.69^\circ), (31.83^\circ, 31.89^\circ), (34.07^\circ, 34.27^\circ), (34.47^\circ, 34.57^\circ), (36.97^\circ, 37.17^\circ), (37.37^\circ, 37.47^\circ), (39.37^\circ, 39.57^\circ), (39.72^\circ, 39.8^\circ).$